TECHNISCHE UNIVERSITÄT DRESDEN

Institut für Geotechnik

MITTEILUNGEN
HEFT 27

Experimental analysis of the evolution of fabric in granular soils upon monotonic loading and load reversals

Experimentelle Untersuchung der Strukturentwicklung in granularen Böden bei monotoner Belastung und Lastwechseln

von
Max Wiebicke

DRESDEN 2020

Mitteilungen – Institut für Geotechnik, Technische Universität Dresden
ISSN 1434-3053
Herausgeber: Univ.-Prof. Dr.-Ing. habil. I. Herle

Briefanschrift:
Institut für Geotechnik
TU Dresden
01062 Dresden

Besucheradresse:
Neuffer-Bau
George-Bähr-Straße 1a
01069 Dresden

Telefon: 03 51/46 33 42 48
Fax: 03 51/46 33 41 31
E-Mail: geotechnik@mailbox.tu-dresden.de

Abstract

The majority of constitutive models, that are used nowadays to describe the behaviour of granular materials such as sands, are continuum models based on phenomenological approaches. In order to describe some of the phenomena occurring on the macroscopic scale, *e.g.*, the abrupt change of stiffness due to a load reversal, constitutive models use phenomenological state variables (*e.g.*, the inter-granular strain concept for hypoplasticity). These often lack a clear physical meaning. The mechanisms that control the macroscopic behaviour must be sought at the grain-scale with the interactions of individual particles playing the key-role. To access that scale and describe the fabric of granular assemblies, x-ray μ-computed tomography is used in this thesis for full-field measurements during monotonic and cyclic experiments. This non-destructive technique allows to acquire 3D images at various stages of the loading and thus, a tracking of the evolution of the fabric.

The spatial resolution of such tomographies is limited as the specimen has to be mechanically representative and at the same time sufficiently small to identify individual grains in the images. Different image analysis techniques can be used to extract information on the fabric of the granular material, but they all lack a thorough metrological characterisation, especially regarding the limited spatial resolution. Therefore, it was necessary to study the different techniques and determine their uncertainties before running the experiments and evaluating the tomographies. Artificial as well as high resolution images serve as the basis of the metrological analysis which showed that the standard approaches for the analysis of contact orientations, implemented in most commercial software, strongly suffer in accuracy and often introduce huge artefacts. New techniques to refine these measures are proposed and validated on the same images.

Monotonic triaxial compression tests on two different sands are studied re-

garding the localisation of deformation in terms of the contact fabric. The complete fabric tensor is determined inside and outside of the developing shear band throughout the experiment. Its evolution is expressed by the anisotropy and related to the macroscopic response. The specimen appears to behave homogeneously in the different zones until the onset of the localisation at which the fabric diverges. Outside of the shear band it stays relatively constant whereas it seems directly related to the stress ratio inside the shear band. The anisotropy captures the characteristic evolution of the stress response, such as peak states and softening.

A series of triaxial compression tests with load reversals has been conducted on specimens consisting of sand grains and glass beads. To capture the fabric response to the cycles, tomographies have been acquired before and after unloading and after reloading. As opposed to numerical simulations, no large changes of the fabric during the load cycles could be observed. Qualitatively, the fabric changes similar to the numerical simulations: the anisotropy decreases upon unloading and increases upon reloading. The incremental response to each reversal is compared to the numerical simulations and the evolution of the inter-granular strain tensor for similar conditions. The latter is determined by a simplified element test with the aim of possibly relating this phenomenological variable to a truly structural one. The comparison of the evolution of the fabric and the inter-granular strain, however, showed major differences, based on which such a relation is not possible. The fabric evolves at a slower rate than the state variable and continues to evolve even throughout monotonic loading situations.

Kurzfassung

Der Großteil der Stoffmodelle, die heutzutage zur Beschreibung des Verhaltens von granularen Materialien wie Sanden verwendet werden, sind Modelle im Kontinuum, die auf phänomenologischen Ansätzen basieren. Diese Stoffmodelle nutzen oft phänomenologische Zustandsvariablen (z.B. die intergranulare Dehnung in der Hypoplastizität), um Phänomene, die auf makroskopischer Ebene beobachtet werden können, wie z.B. ein abrupter Wechsel der Steifigkeit bei Lastumkehr, zu beschreiben. Der Großteil dieser Zustandsvariablen ist aus theoretischen Konzepten hervorgegangen, die bisher noch nicht auf experimentelle Grundlagen gestellt werden konnten. Die Mechanismen, die das makroskopische Verhalten und die Phänomene auf dieser Ebene kontrollieren, müssen auf der Kornskala gesucht werden, da die Interaktionen von individuellen Körnern die Schlüsselrolle spielen. Um die Struktur von Granulaten auf dieser Skala beschreiben zu können, kommt die Röntgen Computertomographie in dieser Arbeit zum Einsatz. Diese erlaubt es 3D Bilder von Proben während einer makroskopischen Belastung zu erstellen und somit Strukturänderungen zu verfolgen.

Hierbei ist es wichtig, zu beachten, dass die räumliche Auflösung der Tomographien limitiert ist, da mechanisch repräsentative Proben untersucht werden sollen. Mit verschiedenen Bildbearbeitungstools können aus diesen Bildern Informationen zur Struktur der Proben gewonnen werden. Aufgrund der limitierten Auflösung und unzureichenden, bisher durchgeführten Studien war es notwendig, diese Tools auf ihre Genauigkeit zu untersuchen. Mit Hilfe von synthetischen Bildern und hochauflösenden Nano-Tomographien, die als Basis für diese Analyse dienten, konnte festgestellt werden, dass Standardverfahren, die auch in kommerziellen Programmen implementiert sind, eine unzureichende Genauigkeit aufweisen. Aus diesem Grund wurden fortgeschrittene Verfahren hinsichtlich ihrer Genauigkeit und Verwendbarkeit untersucht und Verfeinerungen der Standardverfahren vorge-

schlagen. Es konnte gezeigt werden, dass diese Verbesserungen eine wesentlich höhere Genauigkeit hinsichtlich der zu bestimmenden Strukturgrößen aufweisen.

Mit diesen optimierten Verfahren wurde die Lokalisierung von Verformungen in monotonen Triaxialversuchen an zwei verschiedenen Sanden untersucht. Dazu wurde die Struktur innerhalb und außerhalb eines sich entwickelnden Scherbandes bestimmt und über einen Strukturtensor dargestellt. Die Proben verhalten sich relativ homogen bis zum Anfang der Lokalisierung. Danach wird die Struktur innerhalb des Scherbandes zunehmend anisotroper, indem sich die Kontakte immer weiter in Richtung der größten Hauptspannung ausrichten. Außerhalb des Scherbandes verändert sie sich kaum. Die Anisotropie des Strukturtensors bildet die Entwicklung des Spannungsdeviators dabei sehr gut ab.

Um die abrupte Änderung der Steifigkeit bei Lastumkehr zu untersuchen, wurden Experimente an Sand- und Glaskugelproben durchgeführt, bei denen die Lastrichtung zu unterschiedlichen Zuständen umgekehrt wurde. Dabei wurden Tomographien von der Probe inbesondere vor und nach der Entlastung sowie nach der Wiederbelastung erstellt. Im Gegensatz zu Untersuchungen mit der DEM, entwickelt sich die Struktur in diesen Experimenten nur sehr gering. Qualitativ sind die Änderungen aber ähnlich mit denen aus den numerischen Simulationen: die Anisotropie verringert sich bei Ent- und vergrößert sich bei Wiederbelastung. Die inkrementelle Änderung der Anisotropie bei Lastumkehr wurde mit den Ergebnissen aus den numerischen Simulationen sowie der Entwicklung der intergranularen Dehnung verglichen. Mit dem Ziel dieses phänomenologische Konzept auf experimentelle Grundlagen zu stellen, wurde die intergranulare Dehnung in einer Simulation bei ähnlichen Bedingungen ermittelt. Eine experimentelle Erklärung dieses Konzeptes ist zumindest mit der Kontaktstruktur nicht möglich, da sich beide Variablen unterschiedlich entwickeln. Die Struktur entwickelt sich langsamer als die Zustandsvariable und weit über die Lastumkehr hinaus.

Résumé

La majorité des modèles constitutifs, utilisés aujourd'hui pour décrire le comportement de matériaux granulaires, sont des modèles de continuum basés sur des approches phénoménologiques. Afin de décrire certains des phénomènes qui se produisent à l'échelle macroscopique, par exemple: le changement brusque de rigidité à une inversion de charge, les modèles constitutifs utilisent des variables d'état phénoménologiques (par exemple: le concept de déformation intergranulaire pour l'hypoplasticité). Ces modèles manquent souvent d'une signification physique. Les mécanismes qui contrôlent le comportement macroscopique doivent être étudiés à l'échelle du grain, car les interactions des particules jouent un rôle essentiel. Pour accéder à cette échelle et décrire la structure des assemblages granulaires, la tomographie par rayons X est utilisée dans ces travaux de thèse.

La résolution spatiale de telles tomographies est limitée car le spécimen doit avoir une taille mécaniquement représentative et en même temps doit être suffisamment petit pour identifier les grains individuels dans les images. Différentes techniques d'analyse d'images peuvent être utilisées pour extraire des informations sur la structure du matérial granulaire, mais elles manquent toutes d'une caractérisation métrologique approfondie.Donc, il était nécessaire d'étudier les différentes techniques et de déterminer leurs incertitudes. Les images artificielles ainsi que les images haute résolution servent de base à l'analyse métrologique, qui a montré que les approches standard pour l'analyse des orientations de contact, mises en œuvre dans la plupart des logiciels commerciaux, sont inexacts et entraînent souvent d'importants artefacts. De nouvelles techniques pour affiner ces mesures sont proposées et validées sur les mêmes images.

Des essais de compression triaxiaux monotoniques sur deux sables différents sont étudiés en ce qui concerne la localisation de la déformation par rapport au structure de contact. Le tenseur de structure complet est déterminé

à l'intérieur et à l'extérieur de la bande de cisaillement en développement tout au long de l'expérience. Son évolution est exprimée par l'anisotropie et liée à la réponse macroscopique. Le spécimen semble se comporter de manière homogène dans les différentes zones jusqu'au début de la localisation à laquelle le tissu diverge. En dehors de la bande de cisaillement, il reste relativement constant alors qu'il semble directement lié au taux de contrainte à l'intérieur de la bande de cisaillement. L'anisotropie capture l'évolution caractéristique de la réponse a la contrainte, telle que les états de pic et le ramollissement.

Une série d'essais de compression triaxiale avec inversion de charge a été réalisée sur des échantillons constitués de grains de sable et de billes de verre. Pour capturer la réponse de la structure aux cycles de charge, des tomographies ont été acquises avant et après le déchargement et après le rechargement. Contrairement aux simulations numériques, aucun changement important du tissu au cours de ces cycles n'a pas pu être observé. Qualitativement, les changements de structure ressemblent à ceux des simulations numériques: l'anisotropie diminue au déchargement et augmente au rechargement. La réponse incrémentale à chaque inversion est comparée aux simulations numériques et à l'évolution du tenseur de déformation intergranulaire sous des conditions similaires. La déformation intergranulaire est déterminée par un test élémentaire simplifié dans le but de relier éventuellement cette variable phénoménologique à une variable véritablement structurelle. La comparaison de l'évolution du tissu et de la déformation intergranulaire a toutefois révélé des différences majeures, sur la base desquelles une telle relation n'est pas possible. La structure évolue à un taux plus lent que la variable d'état et continue d'évoluer même dans les situations de chargement monotone.

Vorwort des Herausgebers

Lange Zeit hat man Stoffmodelle nur auf der Basis von Auswertungen der sog. Elementversuche entwickelt. Die Spannungen in der Probe wurden aus den auf die Oberfläche der Probe wirkenden Kräften und die Dehnungen aus den Randverschiebungen bestimmt. Dies entspricht der Annahme, dass die Probe mit einem homogenen Kontinuum gleichgesetzt werden kann. Obwohl es allmählich klar wurde, dass durch die Entstehung von Scherzonen die Deformation lokalisiert wird und diese Lokalisierung schon in den früheren Phasen der Elementversuche stattfindet, gab es experimentell keine Möglichkeit, in die Proben während des Versuchsverlaufs hineinzuschauen.

Darüber hinaus waren und sind die fortgeschrittenen Stoffmodelle keine reine Spannung-Dehnungsbeziehungen. Sie enthalten in der Regel weitere Zustandsvariablen, die die Bodenstruktur – d.h. den Aufbau des Korngerüstes – charakterisieren. Diese Zustandsvariablen sind häufig nicht direkt messbar und dementsprechend nur mit verschiedenen Hypothesen begründet.

Der Einsatz der Computer Tomographie (CT) für die Bodenuntersuchungen hat unerahnte Möglichkeiten für die Erforschung des Bodenverhaltens eröffnet. Mit der aus der Medizin stammenden Methode können einzelne Körner identifiziert und während der Probendeformation verfolgt werden. Es können die gegenseitigen Kornkontakte im Korngerüst lokalisiert und ihre Verteilungen und räumliche Orientierungen dargestellt werden. Kommt jetzt also endlich die Zeit, dass die Stoffmodelle mit dem Verhalten der Körner der gesamten Probe überprüft bzw. neu definiert werden können?

Der Enthusiasmus in diese Richtung war am Anfang der Forschung von Max Wiebicke sehr groß. Noch größer war allerdings seine Ernüchterung, als er festgestellt hat, dass über die Genauigkeit der CT-Methode eigentlich so gut wie nichts bekannt ist. Bezogen auf die Kornkontakte hat sich

zum Beispiel herausgestellt, dass die Standardauswertung Kornkontakte dort liefert, wo in Wirklichkeit keine sind. Die Festellung solcher massiven Defizite hat Max zu echten Pionierschritten veranlasst. Er hat neue Verfahren für die Auswertung der CT für Bodenanalyse vorgeschlagen, algorithmisiert, programmiert und den Wissenschaftlern in der ganzen Welt zur Verfügung gestellt. Auf Basis dieser Verfahren konnte er anschließend neue Einblicke in das Bodenverhalten liefern. Dazu gehört die Entwicklung von Kornkontakten innerhab und außerhalb von Scherzonen oder die Widerlegung der für die Formulierung von sog. *intergranularen Dehnungen* aufgestellten Hypothese. Und, nicht zu vergessen, eine wesentliche, auf Experimenten aufgestellte Kritik der heute besonders populären Diskreten Elementen Methode (DEM). Seine Veröffentlichungen in den besten internationalen Forschungszeitschriften belegen die Anerkennung seiner Ergebnisse in der Fachwelt.

Die wissenschaftliche Motivation, ideenreiche Innovation, der Arbeitseinsatz und die natürliche Intelligenz waren und sind bei Max Wiebicke beispiellos, wobei auch die menschlichen Komponenten seiner Persönlichkeit, wie die Hilfsbereitschaft für alle, die sich an ihn wenden, herausragend sind. Ich war glücklich, mit Max diskutieren und seine Arbeit betreuen zu können.

Die Unterstützung der Deutschen Forschungsgemeinschaft und die konstruktive Bewertung des Projektantrags (HE-2933/8) durch die Gutachter soll hier ebenfalls gewürdigt werden.

Ivo Herle

Acknowledgements

This work was carried out during 2014 and 2019 at both, the Institute of Geotechnical Engineering at the TU Dresden and Laboratoire 3SR in Grenoble. I am deeply thankful to my three supervisors: Ivo, Cino and Eddy, in no particular order at all. My journey into the challenging and humbling world of research started when Ivo encouraged me to participate in Cino's Master's course in Grenoble. The decision to do so changed my life for the better in spite of the doubts I had before leaving to France. I really would like to see the expression on the faces of my French teachers from high school if they would learn about me living in France for such a substantial time. I am grateful for this opportunity and even more so for what came after: both, Ivo and Cino, wanted to continue to work with me.

Unfortunately, a bilateral research programme between France and Germany stopped their funding just before we wanted to start our cooperation and we had to start a long process of applying. This, however, taught me right from the beginning, what it means to apply for research funding – again, thanks to Ivo who entrusted me with that task. Thanks to the German Research Foundation (DFG) for funding our two projects that permitted me to work on this thesis.

No thanks, whatsoever, to the French bureaucracy. I really thought that we in Germany know what super complicated filling of forms that themselves are needed to get other forms, you get the idea, means, but I was totally wrong. Doing a co-operational thesis is great from the scientific side, but not at all from the organisational one. I have never ever filled so many useless forms, with so many redundant information and taken out redundant insurances than for the école doctoral. Thanks to Bernard Penz and Gaël Combe for making my life less complicated on these matters and being very helpful.

I got super lucky with my three supervisors. Thank you, Eddy, for introducing me to the world of open source and helping me with so many details on implementation, for spending so much time with me on the experiments and for teaching me the operation of the x-ray tomograph. I truly enjoyed the time we spend on scientific discussions as well as thinking about sustainable life styles and sharing ideas on various books. Thank you, Cino, for always motivating me. No matter the mood I was in when we had a meeting, I was always super motivated when we finished our discussions. You really have a special way of motivating me, and probably all students that have the pleasure to work with you. Thank you, Ivo, for your guidance and for always putting everything in perspective. You always were a step ahead and thought about the bigger picture, when I was still focused on how to improve on the details. If you had not infected me with your passion on the very weird behaviour of soils in my first course on soil mechanics, I would probably have followed a different path. Would you have focused on codes instead of mechanics as so many others, I would not have continued that road. And also thank you for giving me so many opportunities during my work in your institute. The most impactful was cooperating with Prof. Itai Einav and his group, which truly challenged and also formed me. It has to be noted, that both, Cino and Ivo, additionally took on high, immensely time-consuming administrative positions during my thesis, but nevertheless, always had time for my problems. You taught me what being a passionate teacher (or supervisor) means.

I have had the pleasure of spending a lot of time in very different research environments, mostly in Dresden and Grenoble. Thanks to my group in Dresden and also to the Geomecanique team. Thanks to Pascal and Erminio for helping me a lot with setting up my experiments and creating the specimen; this can be so upsetting. Thanks Václav for introducing me to discrete element modelling, helping me with my problems in implementations and being the most impressive coder I have ever seen. Although it sounds like a lot of fun to travel so much, it was personally really tough to switch home in such short periods. I think my maximum was switching home for 8 times in a year. Without my friends that would not have been possible and I would have suffered too much. Thank you for making both, Grenoble and Dresden, my two homes.

I am deeply grateful for my family for being as supportive and loving as they are. Without them, I would not be where and who I am right now. Thank you, Maria, for suffering during the time I spent writing this thesis,

I know that it was tough and I was not very pleasant at times.

Max Wiebicke

Contents

List of Abbreviations and Symbols

Abbreviations

μCT	Micro focus computed tomography, page 31
2D	Two dimensional ...
3D	Three dimensional ...
COM	Centre of mass, page 49
DEM	Discrete element method, page 21
EDM	Euclidean distance map, page 174
FEM	Finite element method
MOI	Moment of inertia, page 81
PCA	Principal component analysis, page 37
PVE	Partial volume effect, page 34

Symbols

$\boldsymbol{\delta}$	Inter-granular strain tensor, page 6
ϵ_i	Principal strains with $i \in$ [1,2,3]
ϵ_v	Volumetric strain
$\mathbf{D}$	Deviatoric fabric tensor, see equation (7.7), page 136
$\mathbf{E}$	Strain rate tensor, see equation (1.1), page 6
$\mathbf{I}$	Second order identity tensor, see equation (7.7), page 136
$\mathbf{M}$	Moment of inertia tensor, see equation (4.1), page 81

$\mathbf{N}$	Fabric tensor of the first kind, see equation (1.2), page 13
$\mathbf{o}$	Individual Orientation (Vector)
$\mathcal{I}$	Fourth order identity tensor, see equation (1.1), page 6
ρ	Normalised magnitude of the inter-granular strain tensor $\boldsymbol{\delta}$, see equation (1.1), page 6
ρ_d	Dry density, *i.e.*, the density of the specimen, see equation (9.1), page 193
ρ_s	Specific density, *i.e.*, the density of the individual grains, see equation (9.1), page 193
σ_i	Principal stresses with $i \in$ [1,2,3]
θ	Inclination in the spherical coordinate system, see equation (7.11), page 137
φ	Azimuth in the spherical and radial coordinate system, see equation (7.11), page 137
a	Scalar anisotropy factor, see equation (7.8), page 136
e	Void ratio
I_D	Relative density, page 252
p	Mean stress, $(\sigma_1 + 2\sigma_3)/2$ in axially-symmetric conditions
q	Deviatoric stress, $\sigma_1 - \sigma_3$
N_c	Number of contacts
N_p	Number of particles

Part I

Introduction and state of the art

1 Motivation

One of the main tasks of geotechnical engineering is to predict the deformations of structures that are either connected to the ground, such as buildings and bridges, or consist solely of the ground, such as dams and slopes. This has changed over the last decades, as the original goal was rather to predict failure states and design structures that are far from those. In order to make reliable predictions, models must capture the fundamental behaviour of the geomaterials with all their phenomena. The latter are manifold depending on different factors, such as the loading applied to the ground, the state of the ground, the loading history, *etc.* This work focuses on sand as a granular (geo)material and its behaviour upon load reversal.

Soil is not an elastic material and almost all loading involves irreversible deformations. One phenomenon associated to that is its behaviour upon load reversal: if soil is undergoing a certain loading and the direction of the loading is suddenly changed, or even reversed (unloading), its stiffness changes abruptly to a significantly higher value. Macroscopically, this phenomenon is explained by considering the loading history as the soil has once already experienced a different loading. It is not clear, however, which grain scale mechanisms control this behaviour. In other words, *how* and *where* the loading history is recorded in the structure of the material.

This might not effect very simple monotonic loadings of for example shallow foundations, but come into play when more complex problems are to be predicted. The installation of retaining walls is one those problems. Herle and Mayer [HM09] published *in situ* measurements and a finite element simulation on the installation process of an underwater excavation with an anchored retaining wall. Such simulations enable to access information of the whole field that was simulated based on the chosen discretisation. Using these information, they found that the soil close to the wall and at the bottom of the excavation undergoes very complex loading paths with sev-

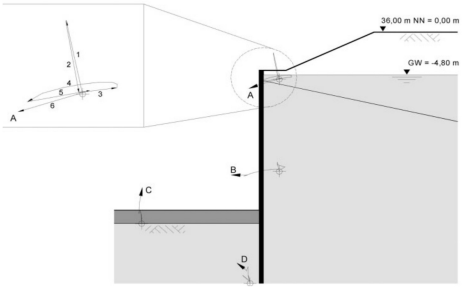

(a) Displacement paths during an excavation from [HM09]

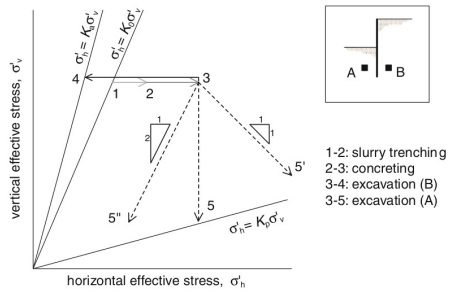

(b) Stress paths from [CSV12]

Figure 1.1: Information on deformation and stress paths from numerical simulations of the installation of retaining walls in [HM09, CSV12]. The paths show that the material undergoes various changes in the loading direction.

eral changes in the loading direction. Figure 1.1a shows the displacement paths for several points around the excavation. A realistic prediction was only possible by using soil parameters that account for the change of stiffness upon load reversal. Going into the same direction, Conti et al [CSV12] simulated the installation process of a diaphragm wall. The resulting complex stress paths from their analysis are depicted in Figure 1.1b. They assessed different modelling approaches to deal with the complex loading of this boundary value problem, and concluded that a realistic prediction of the deformation is only possible by considering the behaviour for load reversals and the accompanying stiffness changes accordingly. In particular the vertical deformation can be predicted totally wrong when the constitutive models are not able to grasp the load reversals. Another example is the excavation of slopes where certain parts of the soil undergo changes in the loading direction. Neglecting an adequate modelling of the behaviour upon such changes could lead to completely unrealistic predictions [Nit16].

A special form is the repeated application of load reversals, *i.e.*, cyclic loading. One of the problems that manifests on the soil scale for this specific loading is the accumulation of deformation [WT04], known as ratcheting. Capturing this effect on the material scale is crucial for the prediction of high speed railways [Weg13] or foundations of wind turbines [WTCZ17] which undergo thousands of load cycles during their life time.

Based on these few examples (and there are many more) it must be acknowl-

edged that the models that are employed for predicting the construction or other aspects of geotechnical structures need to consider the soil behaviour at the material scale accurately. Otherwise, these predictions can go completely wrong.

1.1 Modelling soil behaviour

Most constitutive models developed for soils can be divided into two frameworks: elasto-plasticity and hypoplasticity. The first divides the strains into reversible (elastic) and irreversible (plastic) strains to model the yielding of the material. This is achieved by defining a yield criterion in the stress space: whenever this criterion is met and the loading direction points outward of the yield surface, plastic strains occur, but only elastic strains develop when it is not. The simplest version of such a model is linear elastic and perfectly plastic and often called Mohr-Coulomb model, as it uses the failure surface in the stress space defined by Mohr-Coulomb as a yield function. These kinds of simple models, however, bring many deficiencies: the parameters for the deformational behaviour, *i.e.*, the elastic parameters, are constants that do not consider the dependence on density and the mean stress state, which for example requires a different set of parameters for the same soil in a dense and a loose state. Furthermore, the same stiffness is used for loading and unloading before yielding, as the behaviour is purely elastic. These problems can be overcome by incorporating the critical state concept [SW68] and with that growing yield surfaces, *e.g.*, in the Cam Clay model. But even these models cannot realistically describe the behaviour upon load reversals, as once the material is unloaded, it is in the elastic regime and no irreversible deformations occur.

The hypoplastic models were initially proposed by Kolymbas [Kol91]. They are incrementally non-linear, *i.e.*, non-linear functions of the stress and strain rates, and do not distinguish between elastic and plastic strains. The difference in loading and unloading is modelled by including the norm of the deformation rate which adjusts the incremental stiffness to the loading direction. These models were modified to include the various requirements of soil behaviour, *i.e.*, dependence on density, stress level, *etc.* The most commonly used versions are probably the one proposed by von Wolffersdorff for sands [vW96] and by Mašín for clays [Maš05]. These models, however, are also not capable of modelling the behaviour upon load cycles. Due to the formulation, the stiffness in reloading is similar to the stiffness upon an

initial loading in the same state (density, stress) although it should consider the previously experienced stress history and thus, be closer to the stiffness in unloading.

In order to enhance the capabilities of these constitutive models to capture the behaviour upon cyclic loading, both frameworks were equipped with phenomenological approaches. In elasto-plasticity this was achieved by introducing one more surface in the stress space and called kinematic hardening. This hardening surface defines a smaller elastic region in the stress space and evolves upon loading and unloading, which enables to also produce yielding and plastic strain upon reloading. One established model for sand is for example the Severn Trent Sand model [WG99].

Niemunis and Herle [NH97] implemented a further state variable, the so-called inter-granular strain $\boldsymbol{\delta}$, into hypoplasticity, to remedy the artificial ratcheting upon cyclic loading. In contrary to the former example, this concept is formulated in the strain space and introduces a quasi-elastic range. The evolution equation of the inter-granular strain reads:

$$\mathring{\boldsymbol{\delta}} = \begin{cases} \left(\mathcal{I} - \hat{\boldsymbol{\delta}}\hat{\boldsymbol{\delta}}\rho^{\beta_r}\right) : \mathbf{E} & \text{for} \quad \hat{\boldsymbol{\delta}} : \mathbf{E} > 0 \\ \mathbf{E} & \text{for} \quad \hat{\boldsymbol{\delta}} : \mathbf{E} \leq 0 \end{cases} \tag{1.1}$$

with $\hat{\boldsymbol{\delta}}$ being the direction of $\boldsymbol{\delta}$ and $\mathbf{E}$ the strain rate[1]. In the case of a load reversal, the direction of the strain changes, whereas the inter-granular strain is still pointing in the same direction as in the previous step. Hence, the second criterion $\hat{\boldsymbol{\delta}} : \mathbf{E} \leq 0$ is valid and the $\boldsymbol{\delta}$ evolves similar to the strain rate. In this case, a substantially higher stiffness is assigned to the material. Upon further loading, both are aligned ($\hat{\boldsymbol{\delta}} : \mathbf{E} > 0$) and the evolution of $\boldsymbol{\delta}$ decreases until $||\boldsymbol{\delta}||$ reaches its extremum. This goes along with a reduction of the stiffness to the basic hypoplastic stiffness once the extremum of $\boldsymbol{\delta}$ is reached. The inter-granular strain, thus, acts as a history variable that saves the previous loading direction.

To showcase the evolution of the inter-granular strain, a simple simulation of a triaxial compression test with several load and unload cycles is carried out using the hypoplastic model of von Wolffersdorff [vW96] with the inter-granular strain extension [NH97][2]. The parameters for Hochstetten sand

[1] ρ, β_r and $\mathcal{I}$ are the normalised magnitude of $\boldsymbol{\delta}$, a material parameter and a fourth order identity tensor.

[2] The simulation is carried out using the finite element software *tochnog* [Com16]. The experiment is simulated using a single element and simplified boundary conditions: constant radial stress and a loading by constant velocity in the axial direction (z).

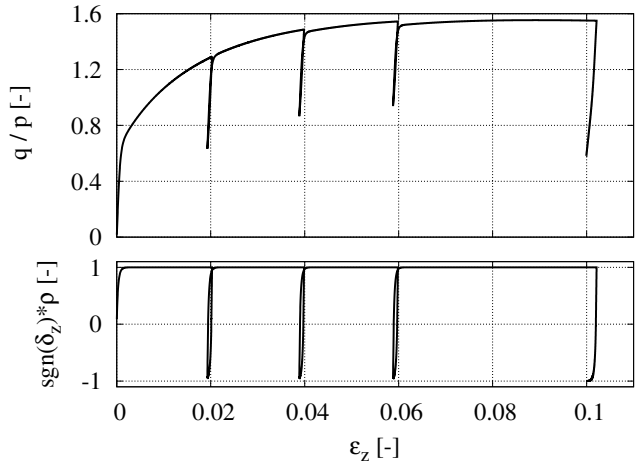

(a) Macroscopic response.

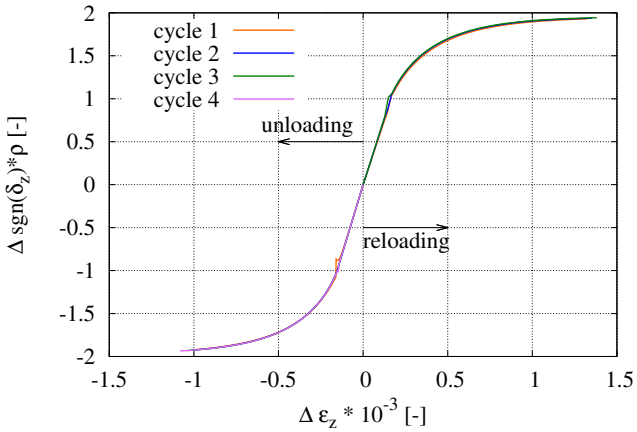

(b) Incremental evolution of ρ.

Figure 1.2: Simulation of a triaxial compression test with Hypoplasticity and the inter-granular strain extension. Left: Macroscopic response and the evolution of the normalised magnitude ρ of the inter-granular strain tensor. It is multiplied by the sign of δ_z to account for the direction. Right: Incremental evolution of ρ in every unloading and reloading step.

given in [NH97] are adopted for this simulation. Only the parameter R is slightly changed and set to $R = 2 \times 10^{-4}$ in order to account for larger cycles than carried out in the original study. The macroscopic response and the evolution of the inter-granular strain tensor in terms of its normalised magnitude ρ are plotted in Figure 1.2a. ρ is multiplied with the sign of the vertical component of the inter-granular strain tensor δ_z to assign a direction to the magnitude. To clearly observe how this variable is evolving, its change $\Delta \mathrm{sgn}\,(\delta_z)\,\rho$ is plotted for the unloading $\Delta\epsilon_z < 0$ and the reloading part $\Delta\epsilon_z > 0$ of every cycle separately in Figure 1.2b. Upon every load reversal, ρ changes linearly before asymptotically approaching its maximum value and with that the classic hypoplastic behaviour.

All of the mentioned concepts are phenomenological in nature, *i.e.*, they are derived to model the observed behaviour, in this case by considering the recent loading history of the material. This history, however, must be engrained somewhere in the material, as the material itself does not use continuum variables to remember what happened recently, but rather arranges itself to sustain the applied loads optimally under given conditions. And this is where fabric might come into play. But let us clarify which role fabric might have on the macroscopic behaviour, what fabric might actually be and dig into past research on how it can help us to understand the complex macroscopic behaviour better and maybe physically more correct.

1.2 Fabric

One of the first effects of fabric to be noticed on the macroscopic scale was the anisotropic behaviour of granular materials. Under certain conditions, specimens of granular materials respond anisotropically although loaded isotropically. Biarez and Wiendieck [BW62] prepared rectangular specimen of either glass beads or sand by pluviation. They compressed the specimen of glass beads by applying an isotropic stress cyclically and measured the deformation of each plane (H,D_V,D_H). The results are plotted in Figure 1.3a and show very different results for each direction. The specimen behaves linear elastically in the direction of pluviation (D_V) whereas it responds softer and non-linear in the other two directions and further experiences irreversible deformation. The sand specimen was initially compressed uniaxially in a direction (H) perpendicular to the direction of pluviation (D_V) and deforms very different in the directions perpendicular to the loading (D_V, D_H) as shown on the left in Figure 1.3b. Afterwards, this specimen

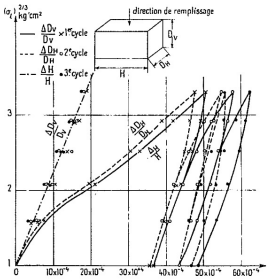

Fig. 2.

(a) Experiment on glass beads

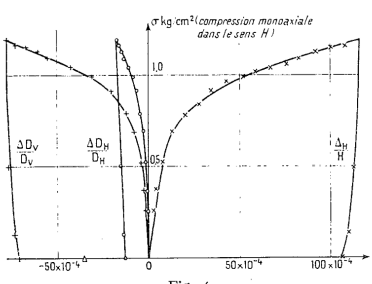

Fig. 4.

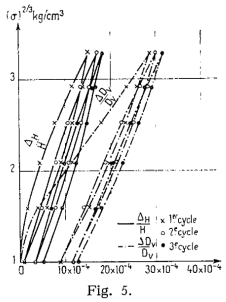

Fig. 5.

Fig. 4. — Écrasement axial sous $\sigma_i = 1$ kg/cm² (sable : 0,1 mm).
Fig. 5. — Cycles de pression uniforme après déviateur : $\Delta H/H = 1{,}2$ %.

(b) Experiments on sand

Figure 1.3: Experiments on a glass beads and a sand specimen showing an anisotropic behaviour from [BW62]. Stress is depicted on the vertical axis and strain on the horizontal axes. Left: Cyclic isotropic compression test on glass beads. The specimen is stiffer in the direction of pluviation (D_V). Right: The left figure shows a uniaxial compression of the sand specimen perpendicular to the direction of pluviation. The subsequent cyclic, isotropic compression is plotted in the right figure and shows that the direction of the preceding uniaxial compression (H) is now the stiffest.

was compressed similar to the specimen of glass beads by cyclic isotropic compression. But on the contrary to the glass beads, the sand behaves softer in the direction of pluviation and stiffer in the direction of the applied shear in the preceding loading as plotted on the right of Figure 1.3b. These results are evidence that the arrangement of particles must play a role on the macroscopic behaviour as the preparation of the specimens and the loading history have a strong impact. This is an experimental prove for the existence of an inherent anisotropy, that is caused by the creation of the sample, and an induced anisotropy, which is due to the loading history[3].

Along the same lines, Oda [Oda72a] prepared sand specimens with different particle arrangements but identical void ratios by pouring them under water and changing the bedding plane. These specimens were sheared in triaxial compression tests under the same confinement pressures. Following conventional theories, the specimens should behave similarly because the standard state variables (stress, strain, strain rate, void ratio) and the

[3]Note that according to Arthur [AM72], the terms inherent and induced anisotropy were initially defined by Casagrande in [Cas44]. The author, however, could not access this paper for verification.

loading conditions are identical. But the opposite occurred as the bedding plane was observed to have a large influence on the macroscopic behaviour, especially the maximum deviatoric stress, the stiffness in form of the secant modulus and the stress ratio at failure. The effects of these initial particle arrangements were found to be more pronounced for angular than for round sands.

Arthur further investigated the two phenomena observed in these experiments: the inherent as well as the induced fabric of granular materials. To investigate the inherent anisotropy he used a true triaxial apparatus which is able to control all three principal stress directions on sands with different bedding planes prepared by dry pluviation [AM72]. The pre-failure behaviour was shown to be largely dependent on the initial fabric supporting the observations of Oda [Oda72a]. Later, he developed a plane strain apparatus that is able to apply a rotation of the principal stress directions. The samples were loaded in a specific direction, unloaded and subsequently reloaded at rotated principal stress directions. Induced anisotropy was found to have no significant influence on the macroscopic friction, but a large impact on stiffness. The stiffness was observed to be maximal in the direction of the previously applied stress.

These pioneering works, among some others, have shown that fabric indeed has a strong influence on the macroscopic behaviour of granular materials. To follow that up, a concept of what the broad term fabric might represent is outlined in the following.

1.2.1 What is fabric?

The word fabric has a rather general meaning in the mechanics of granular materials and is not necessarily used to describe the same things throughout our community. In this work, it is understood as a snapshot of a material that describes its complete state. It can be divided into a statical and a structural part, as *e.g.*, done in [TB86]. Furthermore, there are at least two scales at which a granular material can be characterised: at the continuum scale (macro scale), *e.g.*, using stress, strain and density, as presented in the previous section and at the grain scale (micro scale) using inter-particle forces, deformations of particles, *etc.*

The statical part consists of the macroscopic stress state and the microscopic inter-particle forces. The structural part is defined purely by geometric en-

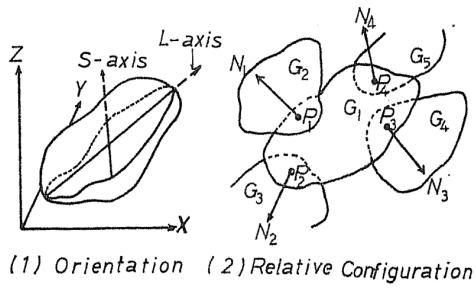

(a) Particle and contact orientations

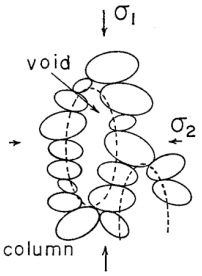

(b) Void orientations

Figure 1.4: Illustration of three structural (geometric) fabric entities. Left: Particle and contact orientations from [Oda72a]. Right: Void orientations from [ONNK85].

tities, *i.e.*, the void ratio (or porosity) macroscopically and various entities at the grain scale. Figure 1.4 visualises the latter using the sketches of Oda, who is one of the pioneers working on that subject. The entity at the micro scale, that was investigated at the beginning, is the contact normal orientation [BW63, Oda72a]. It was probably the first, because forces are transmitted through the contacts, which is why they must contain geometric information that affects the macroscopic behaviour, at least to a certain amount. Contacts contain two important geometric information: their orientations and thus, their spatial distribution as well as their density. The contact density measures the amount of contacts in a granular assembly and is commonly expressed as the average number of contacts per particle, *i.e.*, the coordination number. It is thus, a scalar volumetric measure like the void ratio. Another quantity related to contacts is the branch vector, which is the vector connecting the centres of mass of two contacting particles. In the special case of spherical particles, its direction is identical to the contact orientation. For more complex shapes, however, it is hard to say whether this entity, that somehow describes the arrangement of particles to each other, is physically relevant if information on the contact network can be accessed at the same time. It must be noted already, that accessing the branch vector fabric is far simpler than determining contact orientations, which is why the branch vectors are sometimes used in experimental studies to bypass metrological problems [CW18, CW19].

Another geometric entity is the orientation of a particle, which can for example be described by the direction of its principal axis, *i.e.*, long and short

axes. Note that spheres cannot be described using particle orientations, because their shape is isotropic. Especially in three dimensions, it becomes crucial to consider the particle shape when choosing the principal orientation. Consider for example ellipsoidals: they can either have two long and one short axes or vice-versa. In the first case, the short axis would be the most representative and the latter case the long axis. This is explained further and discussed in the light of their measurement from images in section 4.3. Oda introduced the void shape as a third vectorial entity in [ONNK85]. In contrast to particle and contact orientations, which are defined on an individual (per particle) basis, the void shape is determined overall and describes the amount of void space in all spatial dimensions.

In this work, only contact and particle fabric will be investigated and discussed and the word fabric will thus, mostly be used to describe these structural microscopic entities. The orientations were originally plotted using so-called Rose-Diagrams, that show the frequency of the orientations in the spatial directions. As the research in the first decades was carried out on two-dimensional data, plotting and understanding these histograms was simple. With three-dimensional data, the histograms have to be either plotted in 3D, which can become complex to understand, or by a projection in 2D. The latter is chosen here using a Lambert azimuthal equal-area projection, which is explained in section 7.2.1.

1.2.2 Statistical description of fabric

The contact density as a scalar measure is simple to relate to the macroscopic behaviour, whereas the information on the orientational fabric is available as vectors and their distribution, which complicates their mathematical depiction. These distributions contain valuable information, but are therefore not suited for relating the micro with the macro scale. The common way of capturing these distributions statistically is with the help of a fabric tensor. Oda [Oda72a] started to describe the orientations with a probability density function which was then put into a framework for fabric tensors by Kanatani [KI84]. Generally, these tensors are a statistical descriptions to a certain degree of approximation. This degree can be chosen by the order of the fabric tensor, which is set to two in most applications. The classic and most commonly used formulation for a second order fabric

tensor $\mathbf{N}$ reads [KI84]:

$$\mathbf{N} = \frac{1}{N} \sum_{\alpha=1}^{N} \mathbf{o}^{\alpha} \otimes \mathbf{o}^{\alpha} \tag{1.2}$$

with N being the number of orientations and $\mathbf{o}$ an individual orientation, *e.g.*, a particle or a contact orientation. The main difference of most formulations is the way to normalise the tensor as the orientations are usually treated in the same way. In this formulation and throughout this work, the tensor is normalised by the number of orientations, which causes it to always have a norm of one as the orientations are unit vectors. It is the most common way of normalisation in the literature, see *e.g.*, [ONNK85, FOCL13, FNRA+16, IDA18]. The summation can also be multiplied by the contact density and the average branch vector length as done in [ONMM82, TB86] in order to additionally contain information on the packing density. There are various other ways to normalise the fabric tensor such that it has more properties, *e.g.*, its trace giving information on the contact density or formulations that involve the particle size distribution [MTLL04, PKW18]. Its norm would, thus, correspond to the coordination number. Void orientations have to be handled differently, but are not discussed further in this work. More information on their statistical description can be found for example in [ONNK85, TVD17].

There are more complex definitions of such tensors that incorporate, *e.g.*, volumetric information, to weight the individual entities and associate them to volumes [MTLL04, GDL10]. Using such approaches might facilitate a possible implementation in thermodynamic frameworks, *e.g.*, [JL09].

1.3 How could information on fabric be used?

Assuming that there is no problem in gaining information on the fabric at the grain-scale, the following question can be raised: What are we going to do with such information and its effects on the macroscopic behaviour? Some examples on how to work with links between the micro and macro scale are presented here.

Based on his experimental work, that will be described hereafter, Oda concludes in [OKNN80] that the *granular fabric [...] changes continually in order to increase the ability of the material to withstand the increased applied*

stresses and that this change *is responsible for the hardening (or softening) of granular materials.* He proposes to model the effects of fabric on the macroscopic behaviour by incorporating a fabric based state variable that is similar to the stress tensor into the constitutive models. Arthur goes into the same direction emphasising on two properties that such a state variable should possess: its initial value should have a strong effect on the pre-failure stress-strain behaviour and thus, consider an inherent anisotropy [AM72]. Furthermore, such a variable should be able to evolve and hence, reflect the loading history of the material that was found to induce anisotropy in the behaviour [ADC77]. Considering cyclic loading, Alonso-Marroquin [AMH04] found evidence that the evolution of the microstructure strongly influences the accumulation of deformation, known as ratcheting, and proposed to add a further state variable that is built on the responsible part of the fabric.

Several constitutive models were developed in the last decades that account for anisotropic behaviour by using a fabric related state variable [RRD17], such as *e.g.*, the fabric tensor defined in Equation (1.2). One example is the family of elasto-plastic models for sands called SANISAND developed by Dafalias and co-workers. At first, he included the effect of inherent anisotropy into an elasto-plastic framework by introducing an anisotropic state parameter that was derived from the direction of fabric with respect to the stress and considered Lode's angle [DPL04]. The fabric itself stayed constant in this model and is based on particle orientations which were found not to change extensively during shearing in experiments. As this formulation leads to non unique critical state lines, he introduced the evolution of the fabric in [DM04], which is controlled by the plastic strain. This is generally similar to the model of Nemat-Nasser [NN00].

Numerical simulations of large shear tests, that investigated the critical state for granular materials, found that not only the deviatoric stress and the volume are unique and constant at critical state, but also the fabric of the material [FD11, GZ13]. The investigated fabric measures tended to unique values at critical state independent of the initial conditions. Assuming that the critical state theory is not sufficient, Li and Dafalias created the anisotropic critical state theory (ACST) by adding a further constraint of a critical fabric that must be met to reach and maintain the critical state [LD11]. The assumption of the non-uniqueness of the conventional critical state theory was later validated with the numerical simulation of a clever mind experiment by Theocharis et al. [TVDP16]. This ACST was then

implemented into the SANISAND model by implementing the deviatoric fabric into the yield condition. The model was further modified several times and is now, in its most recent formulation, able to account for the rotation of the principal stress directions [PDP19].

Another approach is to explore the relationship of the macroscopic stress to the inter-particle forces (statical fabric) and the structural fabric. These are called stress-force-fabric relationships. The contact forces alone are not sufficient to derive the macroscopic stress which means that the structural fabric must also play a crucial role in controlling the macroscopic behaviour. Christoffersen et al [CMNN81] derived the stress from the inter-granular forces and the branch vectors of contacting particles based on the principal of virtual work and formulated constitutive equations, *e.g.*, a dilatancy equation. The arising constitutive parameters, thus, have clear physical meaning based on the micro-mechanics. Further investigation of this relationship can reveal to which extent and effect which fabric entity is responsible for the macroscopic behaviour. The different sources for anisotropy are for example split into contact normal and tangential forces, contact normal orientations and branch vectors [OR01, GZ13]. These underlying mechanics at the grain-scale can then be used to formulate according constitutive equations.

The major shortcoming with these works is their foundation. They are mostly built on either extremely simplified experimental approaches or on numerical simulations that rely on assumptions concerning their constitutive relations. The ability to extract information on the fabric of natural granular materials directly from experiments became accessible only recently, but their reliability still remains questionable. Some of the approaches to gain information on the particle scale and their results are presented in the following chapters.

1.4 Structure of the thesis

This thesis is structured slightly differently compared to the standard monograph. It consists of three parts of which the first two tell the main story of this work. Part I describes the history of accessing the particle-scale of granular materials and the state of the art using either experimental or numerical approaches. The actual story developed in this dissertation unfolds in Part II. At first, the methodology to study the metrology of im-

age analysis approaches to measure the fabric from x-ray tomographies is described and the main results are pointed out. This investigation starts from individual and finishes with bulk measurements. Then, the experimental campaign is explored and the granular fabric is accessed and followed throughout these tests. The main focus in these parts is the presentation of the methodology and the main results from the analyses. All details, formulations and implementations are then given in Part III. The idea is that the individual sections in this last part can be used as technical notes on the different subjects.

2 History of accessing fabric information

The micro-mechanical behaviour of granular soils has been of interest for a very long time. Due to its inaccessibility, most theories, however, were developed by assuming soil to be a continuous material, *e.g.*, by Coulomb when he developed his earth pressure framework. Already in the 1920's, Terzaghi, the father of soil mechanics, stated that this assumption hinders soil mechanics from developing further [vT20]: *Coulomb's idea proved very useful as a working hypothesis [...], but it developed into an obstacle against further progress as soon as its hypothetical character came to be forgotten by Coulomb's successors.* He wrote that research must start from the grain-scale: *The way out of the difficulty lies in dropping the old fundamental principles and starting again from the elementary fact that sand consists of individual grains. [...]*

It took a few more decades for this message to be heard and bear fruits, before the first pioneers started to look at idealised granulates and tried to access the particle scale. Some of these early works are summarised in the following sections, followed by the first numerical approaches that were developed after computational power became more accessible. Substantial work has also been done on grain-scale kinematics of soils, but this review is mainly dealing with research on the fabric of granular materials.

2.1 Experimental studies

Two of the first pioneers that tried to access the grain scale were Biarez and Wiendieck. After reporting on the mechanical anisotropy of sands in

[BW62][1], they tried to trace this macroscopic phenomenon to the grain-scale. They carried out experiments on idealised two-dimensional materials[2] in order to place them in a biaxial loading apparatus and take photos from one side that was chosen to be transparent [BW62]. The photos were acquired at chosen stages of the biaxial loading and allowed to determine contact properties such as the amount of contacts and their orientations throughout the experiment. Using these information, they related the contact fabric to the macroscopic properties such as strain and void ratio. The distribution of orientations followed the macroscopic deformation, *i.e.*, if the biaxial specimen compressed horizontally, more contacts formed in the vertical direction. The anisotropy of these distributions was found to react immediately to the applied macroscopic strain before tending to asymptotic values. These experiments were carried out on either cylinders to obtain irregular, more isotropic initial packings [BW62], and coins [Wie67] that tend to form regular packings with a strong bias towards certain axes. A linear relation between the anisotropy and the void ratio was observed for different initial states created using the coins.

Along the same lines, a biaxial apparatus called 1γ-2ϵ was built in Grenoble to apply various loading paths to granular assemblies allowing photographies of the grains to be acquired during the experiment [JLDF92]. The dimensions of the apparatus allowed for many more particles to be tested compared to the studies by Biarez and Wiendieck [Wie67]. As the experiments on this machine were carried out 3 decades after the pioneering work, the photographs could be evaluated automatically by computer programs. The photos still had to be acquired analogously, but could be digitized with a stereo device. This technique, called stereo-photogrammetry, was employed to great success in Grenoble to study localisation phenomena in geomaterials [DV04], which, however, will not be discussed here. Calvetti, Combe and Lanier conducted a series of experiments on an idealised 2D material in [CCL97]. They tracked the displacements and rotations of the individual particles and measured strain locally based on these deformations. Using these measures, they observed shear banding in zones that had the size of two to three particles. Furthermore, the contact fabric was measured and a substantial rearrangement was found during the loading. A

[1] The experiments are described in section 1.2 and plotted in Figure 1.3. The anisotropy observed on the macroscopic scale was caused by the preparation of specimens and the deformation history.

[2] Two-dimensional materials are of course three-dimensional. Their shape in the third dimension is simply constant and thus, does not play any role for imaging these materials in this direction. They are also called Schneebeli materials.

second order tensor was employed to statistically capture the distribution of orientations. It was observed to be proportional to the imposed incremental strain, which explains the measured fabric changes.

Additional information from such plane strain (or plane stress) experiments can be gained by exploiting the photo-elastic effect of birefringent materials. Drescher and de Josselin de Jong [Dd72] for example used two dimensional discs and loaded the material in shear. Taking photos under polarised light reveals the stress distribution inside the particles (if the particles are resolved sufficiently clear in the photos). Inter-particle forces can then be determined from the information close to the contacts and thus, open the access to the statical fabric where before only the structural one could be assessed. These and other experiments, *e.g.*, [OKNN80], revealed that the applied stress is carried by a selected network of contacts, which are called force chains, rather than the complete structure of the assembly. Majmudar and Behringer [MB05] determined the inter-particle force distributions for two different systems: an isotropically compressed and a sheared specimen of circular discs. The induced anisotropic stress state in the latter is carried by long force chains that are all aligned in a specific direction. These force chains are probably supported against buckling by contacts in their vicinity that transfer less than the average force. Additional to these observations, Oda [OKNN80] determined the particle, contact and void fabric of such a two-dimensional, photoelastic material and found that especially the contact fabric plays an important role if compared with the overall stress development[3]. Void fabric was not observed to have a major contribution, but was postulated to be linked to the volumetric behaviour. Changes in the particle fabric were insignificant. Such systems are thus, not only structurally anisotropic, but also statically which requires to consider also contact forces when describing stress induced anisotropy.

All the aforementioned work was carried out on idealised two-dimensional materials, which was necessary in order to image the assemblies and extract information on the fabric. At that time, it was simply impossible to acquire full field measurement of natural granular materials and determine information on the fabric. A different approach was to use natural materials, but to simplify the imaging. In soil mechanics, that was pioneered by Oda who carried out an immense amount of work using such approaches [IO99]. Generally, the procedure can be summarised as follows [Oda72a]: a specimen is brought to a chosen state, that might be either

[3]Note that he experimented on oval particles, which thus have a distinct shape

an unloaded state or a state after applying a certain loading. The structure of the specimen is then fixed by injecting a polyester resin. In this way, it cannot be disturbed while manually working on the specimen. Thin sections from interesting regions in the specimen are then cut and imaged under an optimal microscope. At first, Oda [Oda72a] investigated the effects of initial fabric, *i.e.*, inherent anisotropy, by producing specimen with a similar conventional macroscopic state, *i.e.*, void ratio and mean stress, and testing them under the same conditions in triaxial compression. The different initial fabric states were created by preparing the specimen under water with varying bedding planes, as already mentioned in the previous chapter. He found that the initial fabric strongly affects the stiffness pre stress peak, the amount of the stress peak and the stress ratio at failures. These effects were more pronounced for angular than round particles. In his following work [Oda72b], Oda tried to follow the evolution of the fabric by preparing several initially identical specimen and testing them in identical conditions in triaxial compression[4]. The tests were halted at different axial strains, and microscopic images were acquired as described above. It was found that the ratio of contact fabric anisotropy has close relations to the mobilized stress ratio and the dilatancy rate and that the particle long axis evolve preferentially into a perpendicular direction to the major principal stress. Furthermore, the contact fabric evolved continuously for the monotonic triaxial tests. To describe the fabric state analogously to the stress and strain, Oda et al [OKNN80] applied a second order fabric tensor to the distributions of orientations. The principal axes of the contact normal fabric tensor were observed to align with the principal axis of the stress until they become coaxial.

These works prove the assumption that the structural fabric contributes essentially to the macroscopic behaviour. The fabric is both inherent to the specimen and induced by the loading as it rearranges to withstand the loading. Upon monotonic shear, the fabric becomes coaxial with the stress and its anisotropy can be closely related to the mobilised stress ratio. The major contribution of the structural fabric seems to come from the contact fabric. These findings are crucial for a better understanding of the macroscopic behaviour, but they suffer from two major drawbacks. The first is being post-mortem: all the information of the evolution of the fabric is gained from different specimens, that are tested and prepared in the same way. It is at best a strong assumption that their initial fabric is identical

[4]Note that he did not use de-aired water as pore fluid, but a water resin to facilitate the manual work on the specimen after stopping the test.

and behaves in the same way. The second is the evaluation of the images as they are only two-dimensional, but picture a three-dimensional material. It cannot be reliably said that a contact truly exists from the observed 2D slices and how it is oriented in space as the information in the third direction is missing. Furthermore, the definition of a particle long axis is very error-prone, as the true shape cannot be known from a 2D cut through the grains. The long axes can also be oriented in the direction of observation.

2.2 Numerical approaches

There are several numerical methods that can be used to investigate the discrete behaviour of granular materials. Most notably, at least for this work, is the Discrete Element Method (DEM) which was created by Cundall and Strack [CS79]. Every particle is explicitly considered in this approach, which makes it simple to continuously extract information from the particle scale and relate it to the macroscopically imposed conditions. The behaviour of the granulate is modelled by imposing the constitutive model at the contact level. Most commonly, the particles are considered to be spherical, because this facilitates the detection of contacts which can get rather complicated and computationally expensive for more complex shapes. A contact force is calculated from the overlap of two contacting particles based on the constitutive model, *i.e.*, the stiffness of the material. The simplest contact model that is able to create a somehow realistic macroscopic behaviour consists of a linear spring in the contact normal and a frictional slider in the tangential direction, that allows for slipping to occur. Note that due to limited computational power only two-dimensional simulations were carried out in the beginning before three-dimensional computations became feasible.

There is a shear incredible amount of work on granular materials using DEM published, which is why only several chosen contributions are mentioned in this section. Most of these contributions simulate sphere packings which is why they are only concerned with contact fabric and not particle fabric[5]. One of the first applications of this technique that accessed the fabric of an assembly was carried out on 2D disks by Thornton et al. [TB86]. He distinguished between structural and statical anisotropy. The first being the fabric from the geometry, *i.e.*, contact orientations (or branch vectors, which

[5] A particle orientation does not exist for the isotropic shape of a sphere. It does, however, for ellipses or ellipsoids that are used in some simulations.

are identical for discs and spheres), and the latter from the inter-particle force orientations. The structural fabric is more important regarding this work, because it is measurable in experiments, whereas the inter-particle forces still remain inaccessible[6]. It was observed that the evolution of the structural anisotropy is negligible at small strains at which the behaviour is mainly controlled by forces that orientate in the direction of the major stress. At larger strains, however, the increase in deviatoric stress is mainly driven by a changing structural anisotropy.

These findings were validated by the same author for spheres, *i.e.*, in three dimensions, and extended to general loading conditions with special emphasise on a macroscopic critical state [Tho00]. To impose more general loading conditions in such simulations is far easier than in the lab, *e.g.*, in a true triaxial apparatus. He found correlations between the evolution of the deviatoric stress and the deviatoric part of the structural fabric. Furthermore, at the critical state [SW68], *i.e.*, continuing deformation at constant volume and constant deviatoric stress, the mechanical coordination number and the structural anisotropy are observed to also be constant. Similar critical fabric values are found for specimen with different initial densities, which is consistent with macroscopic observations in the critical state soil mechanics such as a critical void ratio. Thus, they seem to tend to critical values for ongoing shear loading. These values appear to be dependent on the contact friction that is imposed in the constitutive model.

The investigation on the fabric evolution of specimens going towards the critical state were continued by Fu and Dafalias [FD11] who carried out 2D DEM simulations on ellipsoids that were sheared to large strains. All simulations started at different fabric states, but reached a unique critical state in terms of both, particle and contact fabric, which was largely independent of the mean stress (in contrast to the void ratio). The evolution of the fabric, however, was strongly dependent on the initial state.

In his 3D DEM simulations on the relationship of stiffness anisotropy to statical and geometrical fabric anisotropy, Gu et al [GHH17] found a threshold of the stress ratio that indicates a change of microscopic behaviour. If the stress ratio is smaller than the threshold, the stiffness anisotropy is mainly controlled by the contact forces and if it is larger both contact force and contact normal orientations contribute.

[6] With some exceptions on either idealised materials or using further assumptions on the material to indirectly measure forces. See *e.g.*, [AA11, Wie12, HMRA14]

Radjai observed a bimodal character of the force network and started to split contact forces into weak and strong networks [RJMR96]: the weak force network is formed by forces less than the average one and the the strong network vice-versa. Many works used this division of force networks to trace different macroscopic phenomena to the corresponding contact networks [GZ13, MCT14]. Thornton, among those works, split the force networks in his work accordingly and was able to directly relate the strong network to the deviatoric stress [TZ10]. The weak network was found to be responsible for the volumetric behaviour and the stability of force chains against buckling. Furthermore, he plotted the stress and the fabric response envelops for different states and observed that they are correlated and agree with Lade's surface [LD75]. Although, this surface was formulated as a failure criterion, it can apparently also be used for modelling the pre-failure behaviour.

Non-smooth particle shapes can also be considered in discrete element simulations, such as in the work on two-dimensional polygons in [AMLHV05]. The particles are rigid and contact forces are calculated from the virtual overlap at the contact, similar to the original method [CS79]. It has to be noted that the polygons were created to an initial void ratio of zero and are thus, infinitely densely packed. Although it compares better to marble than to natural sands, some conclusions can still be drawn for this work: contacts were distinguished into sliding and non-sliding contacts which allowed to relate both to different phenomena: sliding contacts were related to the plasticity, *i.e.*, the flow rule. Overall, the anisotropic stiffness could be related linearly with different measures of the contact fabric anisotropy. In contrast to most other studies, the contact orientation is measured as the vector from the centre of mass of a particle to its contact point. Furthermore, the authors investigated the incremental response of these specimen by strain probing and validated the existence of a non-associated plastic flow. They assume this phenomena to be caused by sliding contacts that are present even in incremental loading steps. This leads to vanishingly small elastic regions which cannot be explained by classic elasto-plasticity.

Based on Oda's experimental work, Iwashita and Oda [IO00] investigated the phenomenon of strain localisation using a 2D DEM model that includes a rolling resistance at the contacts. They observed the micromechanic processes that cause a strain localisation during a biaxial compression test on a polydisperse sample of discs. Initially, during the hardening up to the stress peak, force chains form in the direction of principal stress. This causes the

voids to elongate between neighbouring chains and the contact network to become anisotropic. Contacts that are not directly involved in the force chains, but provide lateral support, are then lost, which makes the contact network increasingly unstable. During the following strain softening, the force chains buckle, the shear strain increasingly localises and large voids form in the shear band. At the residual state, the volumetric strain stays constant in dilation in what the authors call a dynamically stable state, *i.e.*, the newly developing structure is balanced with a already existing one. The main changes to the fabric of the specimen are found to occur within the developing shear band.

Zhao and Guo [ZG15] used a coupled FEM-DEM framework to study strain localisation with emphasis on the fabric. 2D DEM packings of eloganted particles, *i.e.*, clumps of circles, are embedded in the Gauss points of the FE model to replace the classic constitutive model. As the particles are non-circular, the particle fabric can also be investigated by its long axis. The contact fabric was found to evolve almost immediately after applying the biaxial loading to the rectangular specimen whereas the particle fabric requires larger shear and dilation to be changed. Due to their framework, they were able to distinguish between regions inside and outside of the evolving shear band and found that the fabric inside evolves significantly stronger than outside where the specimen is reaching either a steady state or even unloads.

Another major aim of the DEM community working on linking the microscopic with the macroscopic behaviour is to draw a relationship between the stress on the macroscopic and the force and fabric on the microscopic side, the so-called stress-force-fabric relationship. Christoffersen established the first formula to calculate the stress based on the contact forces and the branch vectors [CMNN81], *i.e.*, the vector between the centres of contacting particles. A lot of contributions tried to understand this relationship in more depth and trace the importance and effects of different fabric components to their corresponding actions on the macroscopic scale. In his 3D DEM simulations on spheres, Guo et al [GZ13] split the fabric into four different parts: two from the statical fabric, *i.e.*, normal and tangential contact forces, as well as two from the geometric fabric, *i.e.*, branch vectors and contact normals. Overall, the major contribution to the stress-force-fabric relationship comes from the contact force anisotropy, followed by contact normal orientations, the tangential force anisotropy and almost negligible, the branch vectors. Geometric anisotropy requires larger defor-

mation whereas force anisotropy is mobilised much quicker. However, the geometric fabric gets more important than the statical fabric at liquefaction. They found that sliding contacts from the weak contact network might be an indicator of liquefaction. At critical state, they further observed a striking correlation between critical contact fabric anisotropy and the mean stress. In [ZG13] they defined a parameter for the fabric anisotropy that was uniquely related to the mean stress and thus, proposed an extension of the critical state formulation. They also validated the previous findings on the tendency of the fabric to become coaxial with the applied stresses.

The small strain shear modulus is an important parameter to be considered for the modelling of load reversals, as outlined in the previous chapter. Most commonly it is related to the mean stress and the void ratio, but Zeghal and Tsigginos [ZT15] observed in their simulations that this these correlations might not be sufficient. They simulated a 3D assembly of non-spherical particles[7] and created specimen with varying initial fabric states that were subsequently loaded isotropically. Different small strain shear moduli were observed for identical conventional state variables, *i.e.*, void ratio and mean stress in this case, but a striking, possibly unique relationship was identified if the coordination number and the particle shape are added to the relation. The fabric anisotropy did not play any role for these conditions as the specimen was not sheared and the fabric remained isotropic.

So far, only works on monotonic loading have been described, but one of the aims of this work is to observe particle-scale behaviour for macroscopic load cycles. The simulations presented in the following are quasi-static in order to relate to the experiments carried out in this work and neglect dynamic effects. Using the same approach as described above [AMLHV05], Alonso-Marroquin et al [AMH04] used their 2D DEM simulations of polygons to investigate the cyclic load-unload phenomena known as ratcheting. Even for very small stress cycles they could not identify an elastic regime, as plastic deformation always occurred. During monotonic loading in shear, the amount of sliding contacts increases which leads to a decrease in the macroscopic stiffness. Upon load reversal, this number of sliding contacts abruptly reduces and can explain the discontinuity of the macroscopic stiffness, *i.e.*, a jump to a substantially higher stiffness in the unloading and reloading regime. They propose to formulate a fabric tensor that differentiates between sliding and non-sliding contacts in order to capture this apparently important measure.

[7] The particles are formed by clumps of spheres.

3D DEM simulations on sphere packings with a special emphasis on load reversals were carried out by O'Sullivan et al [OC09]. They created a very detailed simulation of a real triaxial compression test by taking care of the boundary conditions such as the membrane. In order to validate their model, they conducted an accompanying triaxial test on metal spheres and found that macroscopically their model can capture the behaviour. The unloading was mainly carried by a redistribution and a decrease of the inter-particle forces and only negligible reorientation of contacts, which is an apparently elastic response during the load reversals. They state that the coordination number and the fabric tensor change only slightly during the load reversals, although changes of about 50 % can be observed from their Figures[8].

Jiang et al [JZL19] investigated the evolution of the fabric of sphere packings for many cycles in triaxial loading conditions. They were able to reproduce the different cyclic modes[9] with their model. For single load reversals they confirmed the results obtained in [OC09], *i.e.*, a decrease of contact fabric anisotropy and coordination number when unloading, and extended them for different initial packing densities: the contact fabric tends to undergo larger changes in dense specimen. In monotonic as well cyclic loading the stiffness of the specimen is closely related to the coordination number as well as the fabric anisotropy. However, a unique relation could only be found between the stresses and the strong contact force network, but not the complete contact fabric. They further validate the existence of a critical coordination number that is reached at critical state as found in [Tho00, GZ13]. Even for complete unloading to an isotropic stress state, the fabric does not become isotropic as in the initial state, but some anisotropy remains. Some constitutive models, that include fabric as a state variable (*e.g.*, [DPL04, DM04]), use the direction of the contact normal fabric tensor with respect to the applied loading direction, *i.e.*, the major stress. In these simulations, both are found to (almost) always be coaxial, as the contact fabric tensor picks up the loading direction immediately. The entity that changes with ongoing loading is rather the anisotropy and the coordination number.

All works described here, found that the macroscopic behaviour is dictated mainly by the inter-particle forces and the contact fabric. The forces pro-

[8] See for example Figure 14 in [OC09]. The 50 % are estimated regarding the evolution starting from the initial state.

[9] The cyclic behvaiour is generally distinguished into three modes: Progressive failure, Stabilisation, Shakedown.

vide the main contribution at small strains (or small stress ratios) whereas the contact fabric becomes more important at large strains (or large stress ratios). Furthermore, these simulations validated the correlations between the mobilised stress ratio and the contact fabric anisotropy identified in the experiments. Note that only the geometric fabric will be accessed in this work as the inter-particle forces are still inaccessible from experiments. The studies on the behaviour upon load reversals show somehow conflicting results: on the one hand, the observed response to cyclic loading is called elastic [OC09] whereas on the other hand deformations and also fabric changes are shown to be accumulated [AMH04, JZL19]. This might be caused by only simulating one cycle in [OC09] and possibly understating the evolution of the contact fabric in the unloading regime.

3 X-ray micro tomography for measuring the fabric of granular materials

X-rays were discovered by Wilhelm Conrad Röntgen on the 8th November 1895 while he was experimenting with vacuum tubes [R95]. Their ability to penetrate matter based on its atomic number made them incredibly useful to image objects with an inner structure and thus, a variable density. They are used extensively in medical imaging to such a degree that even many small doctor's offices possess an imaging system nowadays. The interaction of x-rays with matter can be distinguished into three ways: photoelectric absorption, Compton scattering and Rayleigh scattering. In this work as well as in medical imaging of bone-line structures, x-rays are emitted at energies at which the first effect dominates. X-rays can be produced in different ways. In lab conditions they are created by an x-ray tube: electrons are released from a hot cathode and accelerated to hit an anode at high velocity. The x-rays are then created upon the collision of the free electrons with the anode. The object to be imaged is placed between the x-ray tube and a detector which records the photons that penetrate the object. These acquired 2D images are called radiographs and show the accumulated x-ray attenuation through an object at a chosen pixel size. Smaller features can be revealed by choosing small pixel sizes.

The first application in geomechanics goes back to Roscoe [Ros70][1]. He intended to follow the deformation of soil in an experiment on earth pressure behind a retaining wall in plane strain conditions by installing lead markers into the soil. Fortunately, he observed grey-scale changes in the radiographs in the zones of high shear deformation. As visible in Figure 3.1, these zones

[1] To the knowledge of the author.

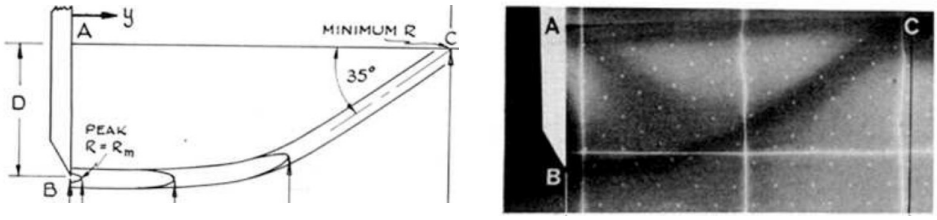

(a) setup

(b) x-ray image

Figure 3.1: Experiment on soil deformation during an earth pressure loading with a retaining wall. Left: Setup of the experiment. Right: X-ray radiograph. From [Ros70].

appear darker than the rest of the sand which means that they have a lower density and thus, have dilated during the deformation. These works on radiographs were followed up by Arthur [ADAAA77] and co-workers. Although the radiographies were able to reveal certain aspects of deformational behaviour, they are inherently restricted to be two dimensional and give only information on the accumulated density along the imaging path.

The development of x-ray tomography enabled the (non-destructive) imaging of objects in 3D. The version of tomography that mostly comes to our mind nowadays, is x-ray computed tomography (x-ray CT)[2]. Sir Godfrey Hounsfield started to develop the first apparatus in the late 1960's which was then used to acquire the first image of an actual brain in 1971 [Old78]. The principal of x-ray CT is the reconstruction of a 3D image from many x-ray radiographies. Therefore, a certain amount of radiographies of the object of interest are acquired at systematically varying angular positions, *e.g.*, every 2°. Many different methods of reconstructing the 3D image from these radiographies exist [BBM00]. The filtered back projection is used [FDK84] in this work.

Starting in the 1990's, x-ray CT has found more and more application in geomechanics, see [MSGJ03, OO04, DVB06] for selected applications. Most images were acquired on specifically prepared or natural specimen in the beginning or on post-mortem specimen after loading them in different experiments [DCMM96, OTT04]. *In situ* experiments, which will be described later in this section, were first introduced in rock mechan-

[2]Another version of x-ray tomography is focal plane tomography [PPP+80] which is mostly used for the imaging of the jaw for dental purposes. It was replaced for most other purposes by x-ray CT and Magnetic Resonance Imaging (MRI).

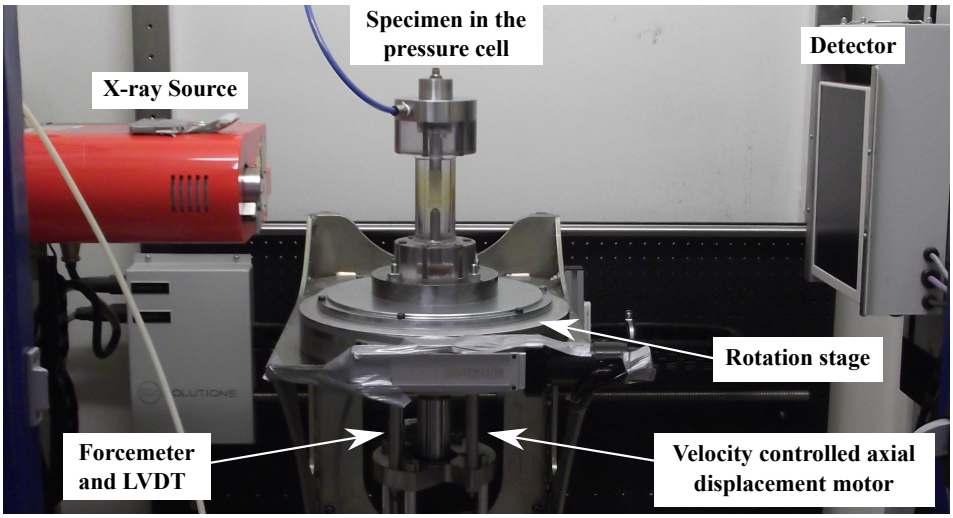

Figure 3.2: X-ray chamber in Laboratoire 3SR. A specimen of Hostun sand is installed in the triaxial cell on top of the rotation stage. The loading is applied from the bottom by the motor that hangs below the rotation stage. Forces and Displacements are measured outside of the cell.

ics [RFM+89, VDW91, KCK+99, LBD+07] and later in soil mechanics by *e.g.*, [OMO00, ASC+00, OMO02, MKU+06, AH08]. The reconstruction, treatment and several image properties and their application to geosciences are reviewed in [KC01]. In the beginning the pixel size that image could be acquired at was not sufficient to resolve and identify individual grains [DCMM96, OMO00, ASC+00, OMO02], which is important for the characterisation of the structure of granular materials. This was overcome by the introduction of micro-focus computed tomography (μCT) which enabled much smaller pixel sizes and the identification of individual particles for *e.g.*, natural sands. After a first test application of x-ray μCT on his post-mortem analysis of sheared sands, Oda concluded [OTT04]: *We can now say with much confidence that microstructure-based soil mechanics will advance greatly if microfocus X-ray CT can be used along with a data-processing method based on stereology.*

The acquisition of x-ray μCT images is possible either in specific facilities such as synchrotrons [LBD+07, HBD+10] or in industrial scanners in the laboratory [ASC+00]. All images in this work, either on experiments run in this campaign or taken from the dissertation of Edward Andò [And13], were acquired using the x-ray μCT imaging system in Laboratoire 3SR in

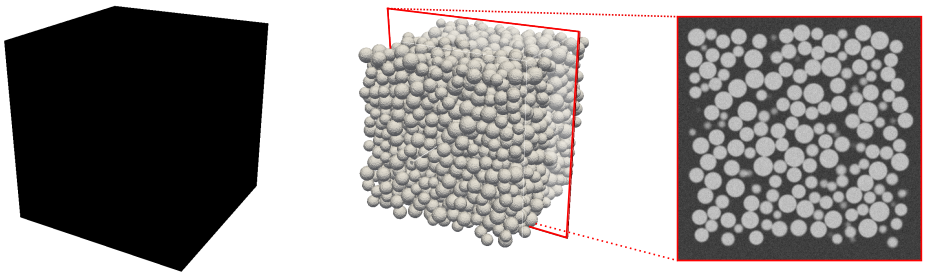

Figure 3.3: Sketch of a three dimensional image and interpreting it. Left: The complete 3D image is full of information and thus, appears as a 3D cube. Centre: 3D rendering of an iso-surface in the 3D image. The red rectangle indicates the plane at which a slice is extracted from the image. Right: Visualisation of the extracted 2D slice with the full information from the 3D image (not the iso-surface).

Grenoble, France. The only exceptions are two very specific images for a metrological analysis on contact and particle orientations, which are taken using the nano-focus tomograph of Laboratoire SiMaP in Grenoble and discussed in section 8.2. The imaging system in Laboratoire 3SR is built in cooperation with RX-Solutions[3]. The loading system to be placed into the tomography chamber was developed in [Len06, LBD+07] and with some modifications is still used to run most experiments. Figure 3.2 shows the imaging system in the tomography chamber with the loading system for a triaxial test in place. The system is described in detail in [VATS14] and [And13]. The commercial software X-Act that is tweaked to the imaging system is employed here to reconstruct the tomographies. Therefore, problems that arise during the reconstruction of the 3D image are not discussed in this work. The focus lies purely on the processing that starts from the tomography and thus, after the reconstruction process.

As a tomography contains a scalar information, *i.e.*, the x-ray attenuation[4], in a 3D field, it is rather difficult to visualise. Figure 3.3 shows how tomographies are presented in this work and most commonly in the literature. The full field itself on the left side cannot be used to observe anything by an

[3] https://www.rxsolutions.fr/

[4] Note that the recorded attenuation differs from the actual value of the material as the x-ray also interacts via Compton and Rayleigh scattering, although the absorption dominates. The x-rays emitted from the source used in this work are polychromatic and thus, give rise to beam hardening as mentioned later and visualised in Figure 3.4.

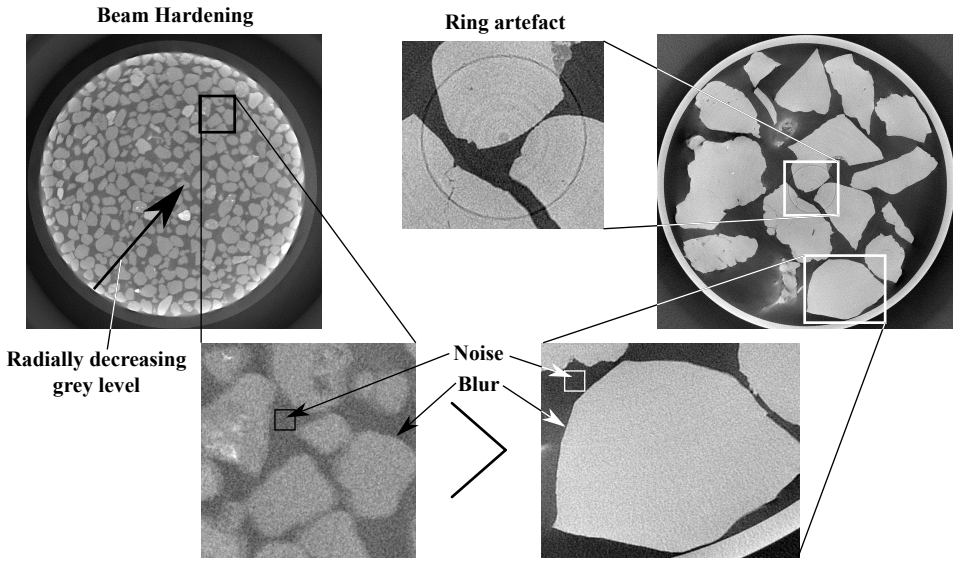

Figure 3.4: Example of the image defects – beam hardening, ring artefact, noise and blur – in tomographies. The zoom ins are supposed to clarify the different level of blur and noise of both images, which are substantially higher in the left image. The left image is courtesy of Bozana Bacic.

image. It can be seen as a 3D matrix that contains the scalar information at its elements. Note that the elements of a 3D image are called voxels, *i.e.*, the 3D equivalent of pixels in conventional (pixelated) images. In the visualised example, an assembly of spheres is imaged. The easiest way to obtain a 3D information is to plot a surface which can be achieved by interpolating and rendering an iso-surface as done in the centre of the figure. The value for the iso-surface is chosen as the threshold that distinguishes between the two phases: solid and void in order to visualise the spheres. This is convenient for the presentation of such packings, but no further quantitative information is available from such renderings. In order to fully observe the acquired information, we are restricted to 2D slices. Such a slice is extracted from the image and displayed on the right side of Figure 3.3. The values of every pixel are imaged using a grey-scale: no attenuation, *i.e.*, total void, is imaged with black and full attenuation, no penetration of x-rays through the matter, with white. In this way, the spheres are clearly visible.

Tomographies, just as any other image as well, come with inherent properties and defects. Some of the most important defects are visualised in Figure 3.4: beam hardening, ring artefact, blur and noise. The beam hard-

ening occurs as a radial decrease of grey-level progressing towards the centre of the imaged object, which is clearly visible by the lighter colors on the boundary of the pictured specimen. Its caused by the higher attenuation of lower energy x-rays as they pass the object and as such occurs for polychromatic beams, *i.e.*, beams of differing x-ray energies, which are typical in lab scanners. Ring artefacts appear as disturbances around the centre of rotation of the image and are caused by the detector. Tomographies can be corrected to some extent regarding these artefacts by various algorithms. In this work, the software X-Act is used for the reconstruction of the tomographies and is able to minimise these artefacts. Blur and noise are also important properties, that play a crucial role for identifying objects and phases in the tomography. Blur can be described by the distinctness of edges and surfaces of objects: the edges are either well-defined or span over many pixels, which can cause problems for the their proper identification [OYJB13]. Noise is generally described as the amount of the original signal that is received (Signal to noise ratio). In the left image in Figure 3.4 the amount of noise is rather high compared to the right example, which is visible from the high variation in the void or solid phase that are much flatter in the right image. See the concise contribution of Ketcham and Carlson [KC01] for further details on the artefacts and properties of x-ray tomographies and ways to process them. Especially the influence of blur and noise on the determination of fabric from the tomographies is investigated thoroughly later in this work.

Another not less important, but inherent image property is the partial volume effect (PVE). The reason for its existence is the pixelisation of the images, *i.e.*, an average signal is given for the occupied area of the pixel, *i.e.*, the pixel size. As the information is acquired per pixel, surfaces that pass through the image grid, cannot be clearly resolved. The PVE is visualised using a one dimensional (1D) example in Figure 3.5: An object of defined length is imaged on two different grids. Its edges fall exactly on the pixel boundaries in Grid A whereas they pass through the pixels in Grid B. This leads to different images, as the solid phase of the object is imaged accurately by Grid A, but smeared in Grid B. All pixels in the image have values that correspond to the ratio of solid to total volume in this two phase material, *i.e.*, 50 % on the boundary of Grid B. Thus, the PVE is responsible for many problems in detecting edges and defining objects in the images, which becomes impactful in the image processing when determining the fabric properties. As the PVE will be of great importance throughout

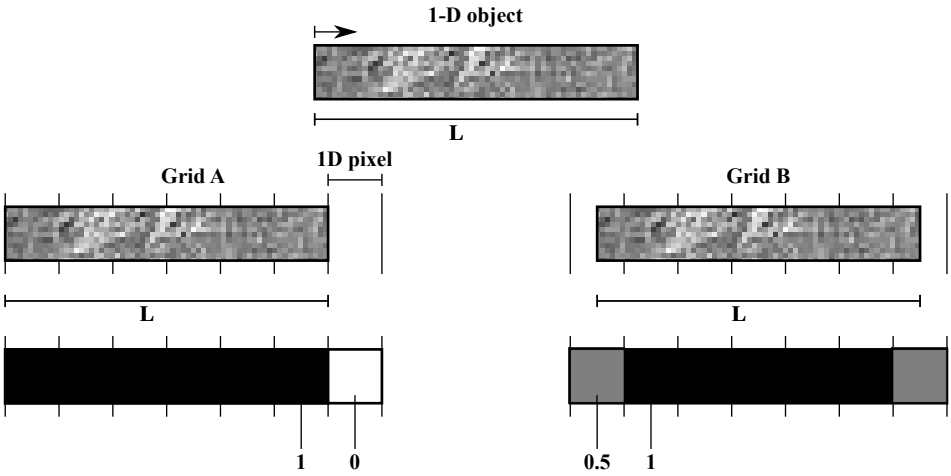

Figure 3.5: Visualisation of the partial volume effect on a 1D example. The object is imaged on two different grids which leads to different resulting images. The pixel value in the resulting image corresponds to the ratio of solid to total length inside each pixel. This example is inspired by Figure 4.9 from the dissertation of Edward Andò [And13].

this work, it is explained for more complex shapes and interfaces later[5].

Nowadays, tomographies are evaluated mostly numerically and not by eye any more. The tomographies are therefore processed as 3D matrices using operations, such as from mathematical morphology. Throughout this work, tomographies are presented mostly by 2D slices through the centre of the specimens for easier visualisation.

3.1 Image processing of tomographies

In order to obtain information from tomographies, they have to be processed in a certain way. Here, the most common way of dealing with 3D images of granular assemblies is described in a simplified manner. The example that serves as the basis of this showcase is part of the metrological study on contact fabric of large sphere packings, which is described in 4.2. The processing of this image is carried out using the open source software *spam* [ACR+]. In section 9, the complete processing of this example is described

[5]See *e.g.*, Figures 4.2, 7.2.

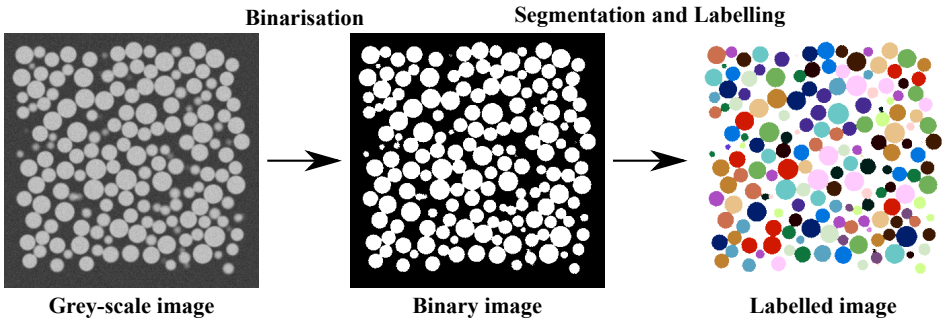

Figure 3.6: Classic image processing steps for granular materials visualised on 2D slices. Left: Grey-scale image, identical to the slice extracted in Figure 3.3. Centre: Binary image after applying a threshold to distinguish between the solid and the void phase. Solid phase and void phase are displayed in white and black, respectively. Right: Labelled image after segmenting the binary image and assigning a unique label to each separate object.

in detail and small codes for the execution of the specific steps are given. As *spam* is open source and can easily be installed on a linux machine[6] and the information for creating the image is available in an open access repository [Wie19], the processing can be repeated by following the step-by-step instructions. This section, however, is meant to be a short introduction to the most common steps of the processing and thus, does not go into detail.

The starting point of every analysis is the raw tomography in which a scalar value is assigned to every voxel. This value, *i.e.*, the x-ray attenuation, corresponds indirectly to the density. In the 2D slice of the example in Figure 3.3, individual particles can clearly be identified by eye. To also identify them numerically is the main goal of processing the image in order to determine the granular fabric later. The necessary processing steps for obtaining a segmented image are explained on slices through the same image and are visualised in Figure 3.6.

The raw images with the scalar information at every voxel will be called grey-scale images and the values grey-values, henceforth. There is no objective reason for this naming, it is simply the color range for these images. Since purely dry granular materials are investigated in this work, there are only two distinct phases in the image: solid and void. The first major step

[6]It does work on MAC machines as well, but possibly needs some further adjustment.

is to distinguish between these phases. Every voxel is assigned to either phase based on whether its grey-value is above or below a threshold. In this work, the same threshold is applied to every voxel and is, thus, called global threshold. This threshold can be calibrated either on image statistics, such as the frequency of grey-values [Ots79], or on physical quantities, such as the volume of the actual grains that are located in the imaged specimen (as in [And13]). Voxels that are above or below the threshold are assigned values of 1 or 0 and allocated to the solid or void phase, respectively.

The resulting binary image only contains information on the phases in the specimen, but still not on particles and contacts. To identify individual particles, the image has to be segmented. In the geomechanics community, this is most commonly achieved by applying a morphological watershed algorithm to the binary image and assigning a unique label to each separate object. To be precise, there are more steps involved than simply applying a watershed, but these are not detailed in this section. The complete process with all the steps is explained in section 9.1. The result is a labelled image as displayed on the right side of Figure 3.6.

These are the general steps to process images of granular materials and the resulting images form the basis for determining the contact and particle fabric. Two major steps are distinguished to extract information on the contact fabric: the identification of contacts and the calculation of their orientations. The labelled image serves as the basis to built a topology of contacts and their corresponding particles. One possible way of determining such a topology is detailed in section 9.2: it basically consists of checking whether voxels of one distinct label have neighbours with a different label (other then 0 for void). The corresponding labels are then collected in a topological structure or a simple list. The orientation is determined on each pair of contacting particles separately: the voxels of both labels that share a face with the other label are identified and a plane is fitted based on their positions. This can be done by applying a principal component analysis (PCA) on the point cloud and determining the minimum eigenvector of the resulting covariance matrix. This vector is considered to be the contact normal orientation.

The particle fabric, on the other side, can be determined in a much simpler and faster way. The principal axis of each particle are calculated as the eigenvectors from its moment of inertia tensor. The details on this procedure are described in section 4.3. As there is no unique solution for spheres, the commands using *spam* [ACR$^+$] are not detailed in the same section as the

tools for the contact fabric (9), but on an image of angular sand particles in section 12.4.8.

3.2 Literature study on the metrology of granular fabric

The image processing outlined above and detailed in 9.1 is the most common approach to extract information on the fabric of geomaterials. With slight variations, this was already employed in various studies mostly to gain information on contact fabric and its evolution during a specific macroscopic loading. These works comprise post-mortem analyses [Fon11, FOCL12, FOCL13] as well as *in situ* experiments [DAAR16, IDA18] and will be discussed in the next section.

In most contributions, commercial software such as Avizo or Visilog is employed for the first image processing steps: binarisation and segmentation. A global threshold is used in the works of Fonseca [Fon11] and an interactive one[7] by the group of Alshibli [DAAR16]. Two different approaches to detect contacts from a labelled image are found in these works. A neighbourhood search with a 6-connectivity structure is employed in [FOCL13]: the direct neighbours of every voxel of a selected label are searched for different labels. This is also described in the previous section and detailed in 9.2. In [FNRA+16], the same authors surprisingly propose to take an enlarged 16-connectivity neighbourhood for contact detection without proving its necessity and accuracy. Another technique is to dilate each label and look for overlaps [DAAR16]: if any other labels are found in the dilated volume of a selected label, a contact is considered between the labels. This technique is considerably faster, but not proven to be more accurate than the aforementioned one. Orientation of contacts are computed by similar approaches: a least squares regression is used to fit a plane on the contact area in [FOCL13] whereas a PCA is employed in [DAAR16, IDA18].

Particle orientations are determined in both groups by a PCA on the point cloud defining each particle (label) [FOCL12, DAAR16]. Druckrey et al [DAAR16] state that this technique is accurate, but lack any proof or study on the accuracy. The common problem of all of these contributions, however, is a missing characterisation of the accuracy of their approaches and

[7] But no explanation of what this interactive thresholding might be was given.

tools. If any comment on the metrology is given, it is at most of qualitative nature.

In contrast to these contributions which observed fabric changes for monotonic loading, the main goal of this work is to investigate the fabric evolution in experiments with load reversals. The changes to both, the contact as well as the particle fabric, might be rather small during an un- and reloading cycle as found in numerical simulations [OC09]. Thus, it is of utmost importance to gain information on the accuracy of the image analysis tools in order to check whether such changes can be measured and if so, to which extent the measurements can be trusted. Such an investigation is one of the key points of this work and is presented later. Here, some approaches and metrological insights on the processing of tomographies are presented in a general manner. Note that many more tools for dealing with tomographies and 3D images exist, which are not presented here. That might be due to the sheer amount of tools or to their inapplicability to images of granular materials.

One of the first studies on the accuracy of x-ray μCT was carried out by Kerckhofs et al [KSV+08] with the aim to assess the binarisation process. Their method was to match the tomographies with microscopic images of sliced sections of the same object, *i.e.*, a porous titanium cylinder. The microscopic images were taken as the *golden standard*, *i.e.*, the reference, and matched to the corresponding sections in the tomography. It was found that using an *optimised* global threshold[8], the micro-CT visualises 89% of the total amount of voxels (solid and pore) correctly.

A very extensive study on the binarisation of tomographies of pourous materials was conducted in [IGT09]. In contrast to [KSV+08], various binarisation techniques were assessed on three different materials: soils, sand-bentonite mixtures and glass beads. Among the techniques are globally applied and locally adaptive thresholds as well as region growing and probabilistic approaches. The global thresholds performed poor and yielded inconsistent results if calibrated by trial and error. When these are calibrated on image statistics, such as Otsu's [Ots79] or Ridler's methods [RC78], the results were better. Note that Otsu's threshold is employed in most applications in this work. Local thresholds performed reasonably well, but are very sensitive to the input, such as the region of interest in which the thresholds are chosen locally, *etc.* This introduces an operator bias, *i.e.*, the results will differ based on the person performing the local threshold. The

[8] This is the same approach as described in the example above and in 9.1

authors concluded that no algorithm is without problems and declared the main problem in the assessment of image analysis tools to be the missing reference [KSV+08]: *One of the main challenges for comparison of segmentation algorithms for X-ray CT images of porous materials is the lack of ground truth, i.e., lack of knowledge of the optimal binarization result.*[9]

According to further metrological studies [CB13, OYJB13], the PVE is strongly responsible for the imperfect binarisation of objects in tomographies. Obviously, features that are smaller then chosen pixel size cannot be captured, but contribute to partial volume. This especially affects interfaces between two touching objects [CB13] and is thus, of special interest to this study on granular materials with the major interest in contacts. The PVE does not only affect the binarisation, but also the segmentation of the solid phase into separate objects [OYJB13]. Futhermore, blur and noise are made responsible for the difficulties of identifying whether two objects are touching by Amon et al [ABD+17].

While Jiménez et al. [JCY15] do not contribute significantly when analysing segmentation and assessing different techniques for the detection of edges, they conclude very importantly on the limitations of x-ray tomography: *Among these limitations the following can be highlighted: its multiple and complex influence factors, the current absence of standard working procedures and the lack of a reliable approximation for the uncertainty calculation.* Special emphasis needs to be pointed again to the fact, that a quantitative assessment of the accuracy of tools to manipulate x-ray CT images is not possible due to a missing reference.

Additionally to the granular materials community in geomechanics, there is also community in physics that deals with x-ray imaging of granular assemblies. Contrary to our work on mostly irregularly shaped particles, most applications in physics are on spherical and ellipsoidal particles. The knowledge of these imposed shapes was then employed to develop specific algorithms to obtain better segmentation results, that were not based on binarisation and watershed transformation. At first, such a technique was developed for mono-sized spheres by Aste et al [ASS05] as two degrees of freedom, the shape and the size, were fixed. This method was later extended for ellipsoidal particles in [SNS+13] and [SNS+15]. Concerning the information that can be extracted from these tomographies, different methods for detecting contacts were compared in [ASS06] for mono-sized assemblies

[9] Note that what the authors call segmentation here is actually the segmentation of phases, which is denominated as binarisation in this work.

of spheres. They compared three different methods, two of which were specifically developed imposing the shape and size and the third being the binarisation and segmentation that was presented as the standard approach in the previous section. The best results were obtained by a contact number scaling function from [ASS05] and the worst with the standard approach, although it was clearly stated that all of the methods have flaws. These results have been validated later in [RVB+17, WS17] which also compared methods that impose the shape to the more general standard approach. Detecting contacts reliably was found to be a major problem that can go completely wrong independent of the algorithms used. Furthermore, it was remarked in [WS17] that a quantification of the error or the accuracy was not possible as the ground truth is unknown and cannot be determined from tomographies.

The only work that engaged in the accuracy of determining contact orientations, that was found in the literature, is [JAVT13][10]. Admittedly, this is only a problem for non-spherical shapes, which is probably why the physics community does not need to engage here. The findings were very crucial: standard topological watershed approaches were found to drastically create a bias towards specific directions. The problem was solved by applying a more advanced watershed: the random walker [Gra06]. Using the information from the segmentation process, it was possible to determine the orientations at a much higher accuracy. These major problems were also discussed and highlighted in [AVHD13, And13]. The other novelty of this investigation is that the error could actually be quantified by creating synthetic images and running the algorithms on these. The shortcoming of this study, however, is that is was applied only binary images of spheres, but this will be discussed later in 4.1.

To sum up, accessible image analysis tools were employed to extract information on the fabric of granular materials, but without considering their accuracy. This renders the obtained results questionable to a point at which they can at least quantitatively not be used. While some research on the metrology was actually carried out, the accuracy of the studied image analysis tools was never truly quantified. The commonly identified problem is the missing of a ground truth for such metrological analyses.

[10] To the knowledge of the author.

3.3 Advances in soil mechanics using x-ray μCT

There are a couple of groups that worked on the description of fabric in granular soil mechanics after x-ray μCT became more popular in the geosciences community. Fonseca [Fon11] investigated the fabric of sand and its evolution due to a macroscopic loading using a post-mortem approach. Different specimens were prepared in the same way (ideally assuming to be identical) and loaded by triaxial compression. The loading was stopped at different stages for each specimen. The specimens were then fixed using an epoxy resin to extract small cores from different positions in the specimen [FOCL12]. The fabric was determined from the tomographies of the small cores and an evolution was drawn by connecting the fabric states from the different specimens. This is only possible by assuming that all the specimens would behave in the same manner, not only macroscopically but also micro-mechanically. In this way, it was found that the contact normals align with the major principal stress direction and thus, increase the contact fabric anisotropy [FOCL13][11]. Furthermore, an initial decrease of the anisotropy of the contact fabric was observed, which is generally contradictory to findings from numerical simulations, such as in [Tho00]. In terms of particle orientations, the fabric becomes less anisotropic with shearing. Different cores from within the evolving shear band and from outside of this band were extracted and compared considering its evolution: contacts outside mainly remain vertical after having aligned with the major stress direction whereas they realign with the normal direction of the shear band inside the band.

Fonseca proposed a contact fabric tensor weighted by the area of its contacts [FOCL13]. The area is measured on the faces of the voxels involved in the contact, which is highly dependent on the chosen pixel size. As it will be shown in section 4.1.2 and visualised in Figure 4.12, the apparent contact size differs strongly with the pixel size. This is due to the fractal features of the surface: the higher the spatial resolution, the more features will be visible in an image. Thus, such a weighting of the fabric tensor would be not only be inconsistent for different sizes but also non-physical.

Contrary to this post-mortem approach, the group of Alshibli performed *in situ* experiments in the synchrotron using x-ray μCT [IDA18]. Here, sand specimens are loaded by monotonic triaxial compression directly in the x-ray imaging set-up. The loading is stopped at chosen stages and tomographies

[11] This is stated in the text [FOCL13], but is not obvious from the figures.

of the specimen are acquired. This enables the direct determination of the evolution of the fabric of one and the same specimen. The experimental campaign comprised two sands and glass beads which were tested at varying initial densities and different confinement pressures. This study focused on the evolution of the contact fabric and it was generally observed, that the anisotropy increases with the shearing of the specimen. The anisotropy increase was delayed when compared to the deviatoric stress: a similar response of the anisotropy is observed, but at a lower rate than the stress and thus, reaching the peak at larger strains. In some experiments, an increase of the anisotropy is measured for a decrease of the deviatoric stress (softening) at larger strains which is counter intuitive and not yet found in numerical simulations. Furthermore, several trends were observed for the varying materials and test conditions: the larger the initial density or the confinement, the higher the isotropy at the initial state. A more isotropic initial contact fabric as well as a stronger evolution of the fabric are found for more angular particles. Making only the shape responsible for this trend is incomplete, because totally different materials have been tested that do not only differ in shape. The surface roughness and mineralogy of the sand and glass beads were not compared and this effects might arise also from these properties.

Another very recent work by Cheng and Wang [CW18] combined the measurement of fabric with a particle tracking approach. As this produces a consistent labelling of the particles through the image series, they were able to observe whether contacts are lost, gained or moved during a load increment. Furthermore, using the particle tracking they determined which particles and contacts are located in the developing shear band in their triaxial tests on glass beads and sand. Although only a small fraction of contacts are newly gained or lost within a load increment, they are found to play a major role in the induced anisotropy. The highest changes were measured in the forming shear band until the peak stress ratio and before the anisotropy tends to a steady value. This technique is promising, especially regarding the findings from numerical simulations by [AMH04, AMLHV05] where sliding contacts are observed to play an important role and might be used to described to macroscopic stiffness. The major short-coming of this study is the use of branch vectors instead of contact normals to describe the contact fabric[12].

[12]The authors chose this simplification because of known problems in the determination contact orientations, *e.g.*, [WAHV17]

Building further upon this work, Cheng and Wang [CW19] tried to identify force chains, *i.e.*, sub-structures of more than two particles that are transmitting more than the average force, based on two stress transmission criteria defined by Fonseca et al [FNRA+16]: (1) a stability criterion that considers only particles that are in mutual contact with at least two other particles to consider lateral support; (2) a load transmission criterion that considers only contacts whose orientation is close to the major principal stress. The authors observed, that the fraction of particles carrying a substantial force decreases with increasing shear in monotonic triaxial shearing. This load carrying fraction of particles consists mainly of particles that are larger than the average of the sample. Furthermore, they split their observation into what happens in the shear band, where the force chains buckle continuously and outside the shear band, where there is a gradual decrease of buckling. Although the criteria are inspired by numerical simulations and partly 2D experiments on photoelastic discs, they are strong assumptions based purely on the geometry that might imply some of the observation. For example larger particles are statistically more likely to have more contacts and thus fulfil the stability criterion. Hence, they are also more likely to belong to the load carrying fraction assuming an equal distribution of contact orientation in the network of contacts complying with (1). This would mean that the numerical observations, that are the basis for these considerations, could be imposed on the experimental observations by applying these criteria. The goal of the experiments should be to verify these findings independently rather than to impose them.

Part II

Contact fabric evolution in monotonic and cyclic experiments

4 Metrology of contact and particle fabric

The aim of this thesis is to investigate the structural changes in a granular assembly upon reversing the imposed macroscopic load. Therefore, different experiments are carried out inside a tomography chamber to acquire images of the specimen during the loading. These will be described in chapter 5. A variety of tools to determine the fabric from tomographies already exists, as described in 3.2, and is applied to soils [FOCL13, IDA18], but they lack any thorough metrological study on their accuracy. Contrary to the experiments targeted here, previous works purely dealt with monotonic loading, for which substantial changes of the fabric are known to occur (see chapter 2). Load reversals, however, might be accompanied by only small to negligible changes [AMH04, OC09, JZL19] which requires a detailed knowledge on the metrology of the tools that are used to extract the fabric from tomographies. If their accuracy is not known, or at best only assumed, a quantitative analysis is impossible and even measuring trends qualitatively might become meaningless. Furthermore, it is of utmost importance to know what can actually be measured. Any conventional experimental apparatus, such as a simple oedometer, is equipped with calibrated sensors to measure displacements, forces and many more quantities. If these sensors would not be calibrated, no experimentalist would ever trust the measurements recorded during a test. The calibration of sensors is a standard procedure that must also be applied to image analysis. The main problem is that there is no standard working procedure [JCY15] because an actual measurement of the accuracy is thought of as impossible as the ground truth of a structure that is imaged is inherently unknown [KSV+08].

A horizontal slice through a representative tomography of a sand sample is shown in the two images on the left part of Figure 4.1. The tomogra-

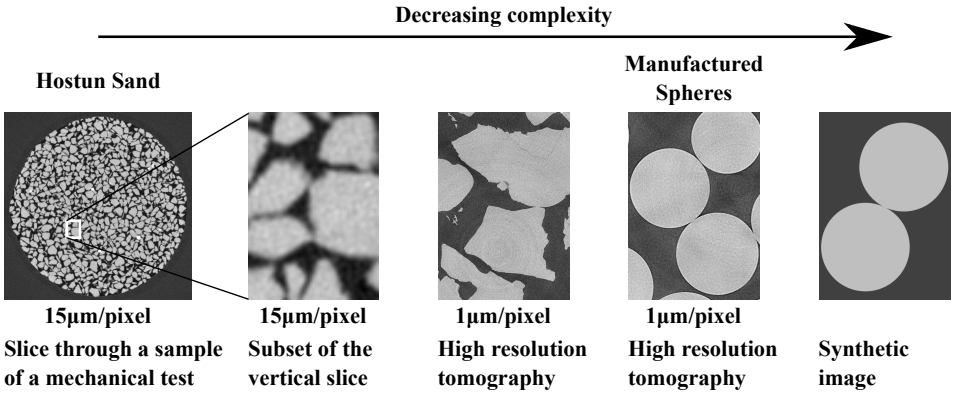

Figure 4.1: Reducing the complexity of the image to study the metrology of inter-particle contacts. Image slightly changed from [WAHV17].

phy was acquired at a pixel size of 15 µm in order to image the complete specimen that consisted of approximately 50,000 grains. It seems obvious that no conclusions on the accuracy of the tools can be determined on such images mainly due to two factors: the missing ground truth of the imaged geometry as well as the complexity of the particle shape. Even if the shape of an irregular particle is perfectly known, a closed analytical solution does generally not exist. In order to avoid these problems, a completely different approach to the metrology is developed and followed here.

The complexity of the particle shape is reduced to a minimum by starting with an analysis on spheres[1]. The main advantage is that the contact normal orientation for spheres is identical to the orientations of the corresponding branch vector. The problem of the missing ground truth inherent to tomographies is addressed by using synthetic images. These are created considering the main properties of real tomographies, *i.e.*, the partial volume effect (PVE), blur and noise. As these images are synthetic, the complete information on the fabric is perfectly known. Kalisphera [TA15] is a tool for the creation of synthetic images of spheres that solves the PVE analytically and is therefore used throughout the metrological analysis.

The necessary study on the metrology of inter-particle contacts starts with artificial images of two touching spheres as depicted in Figure 4.1 on the right-most image. The complexity is then increased by studying the same

[1]Note that the correct geometric denomination is ball (or bead) and that sphere just stands for their surface, but that the word sphere is adopted throughout this work.

problems, *i.e.*, the detection of contacts and the determination of their orientations, on real tomographies of high precision manufactured spheres. These were acquired at very high resolution (*i.e.*, with a very small pixel size of 1 µm) and serve as the ground truth for the analysis at lower resolutions[2]. In the next step of increasing the complexity, a high resolution tomography of contacting Hostun sand grains, the material used in the experiments in this work, is considered. The definition of a ground truth is more complex in this case. These images are also used to infer the accuracy of the determination of particle orientations.

In order to relate the findings on individual contacts to assemblies and assess the impact of errors of individual orientations to statistical fabric measures, artificial images of mechanically meaningful sphere packings are created and studied. This is achieved by coupling a discrete element simulation with Kalisphera and the image processing tools, which also allows to apply a loading to the assembly and follow the evolution of the fabric. As all fabric entities are perfectly known and extracted from the DEM simulation, the errors can be determined individually on each contact and statistically on the fabric tensor. The last step of assessing the accuracy is a triaxial compression test on spherical glass particles. As the centre of mass (COM) of each particle is a very accurate measurement from an image [And13], the branch vectors can be computed accurately and allow a determination of the accuracy of the contact orientations.

This complete chapter is concerned with the determination of the accuracy, which is a measure of how close a measurement is to the ground truth. A complete description of the metrology, however, would also involve a discussion on the precision of the tools. The precision of a measurement describes its repeatability and is therefore not necessarily connected to the accuracy. It is only investigated considering the statistics in terms of the overall fabric measures of a sand specimen that was imaged twice in 12.4.4.

4.1 Metrology of individual contacts

The starting point of this metrological study on contact orientations is the individual contact between two particles. In order to start from a perfectly known ground truth (or reference), synthetic images are the object of the

[2]Note that the pixel size of the tomographies of the specimens in this work is an order of magnitude higher.

first part of this analysis. The particles are chosen to be spheres as this simplifies the creation of synthetic, but realistic images as well the determination of the reference. Contact orientations between touching spheres are similar to the orientation of their branch vectors, *i.e.*, the vector connecting the centres of mass of the spheres in contact.

A similar study on the accuracy of determining contact orientations between touching spheres was already carried out in [JAVT13]. The spheres were created as binary images and thus, lack the inherent properties of real tomographies, such as the PVE, blur and noise. As found in previous studies, especially the PVE is causing problems when identifying the surface of objects, especially if they are close or in contact [CB13, OYJB13, ABD+17]. The goal of this work, however, is to relate the accuracy that is assessed on synthetic images to real tomographies and thus, it is necessary to consider these properties when creating the synthetic images.

The synthetic images are created with Kalisphera [TA15].This tool is briefly presented in section 7.3 with a visualisation of the creation process of a single sphere in Figure 7.2. The creation of two spheres in contact is depicted in Figure 4.2. Geometrically, the contact between the two spheres is chosen to be a single point in this configuration. The centre image in the figure explains the synthetic image that is produced using Kalisphera: voxels that are filled completely by either solid or void are depicted as white or black and have a value of 1 or 0 in this case, respectively. The PVE is captured and visualised for the blue voxel: as the solid phase takes 57 % of the total volume of the voxel, a value of 0.57 is assigned to the voxel.

The 3D rendering depicted in Figure 4.2 is the isosurface at the value of 0.5, *i.e.*, the surface of all voxels that are filled by equal or more than 50 % solid. The contact appears enlarged in this rendering although the spheres should geometrically meet at a single point. This artificial enlargement of the contact is due to the PVE and as such affects contacts in any pixelated image independent of whether they are synthetic or real tomographic images. The voxels that are close to both spheres with a higher value than 0.5 are identified as solid and as such enlarge the actual contact.

With the PVE leading to contacts that appear larger than they geometrically are, the following questions arise: What effect does the PVE have on particles that are close, but not touching? If the effect on the contact fabric turns out to be not negligible, how can it be mitigated?

A metrological approach is developed throughout the following sections that

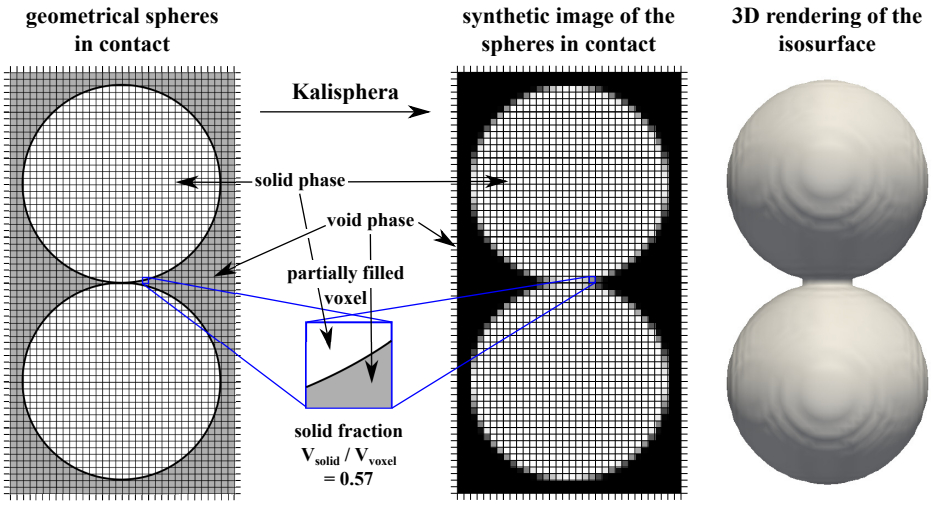

Figure 4.2: Creation of an image of two touching spheres using Kalisphera – left: geometrical spheres in contact at exactly one point. centre: slice through the synthetic image of these spheres. right: 3D rendering of the iso surface in the synthetic image.

tries to answer these questions and to quantify the accuracy of the detection and orientation of contacts. The base line of this study are synthetic images of two spheres. To cover the effects that the pixelation of images can have on the metrology, a systematic set of reference configurations is studied. These configurations are defined by the orientation and the distance of the spheres to each other. 5,000 different orientations that are equally distributed on the surface of a semi-sphere are imposed in the analysis on the synthetic images as described in detail in 8.1.1.

As visible in Figure 4.2, the synthetic images produced with Kalisphera are too perfect and not fully representative of real experimental measurements. In order to create more realistic images, blur and noise are additionally added to the synthetic images. This process is depicted in Figure 4.3. The first step is to re-scale the image, such that the solid and void phases are centred at 0.75 and 0.25 instead of 1 and 0, respectively. Blur and noise are then added subsequently to the rescaled image. The re-scaling is necessary when applying noise, which could otherwise lead to values outside of the range of $[0.; 1.]$. The values of blur and noise that are added to the images are carefully calibrated on x-ray tomographies of real granular materials in the lab scanner of Laboratoire 3SR. The whole process of deforming the

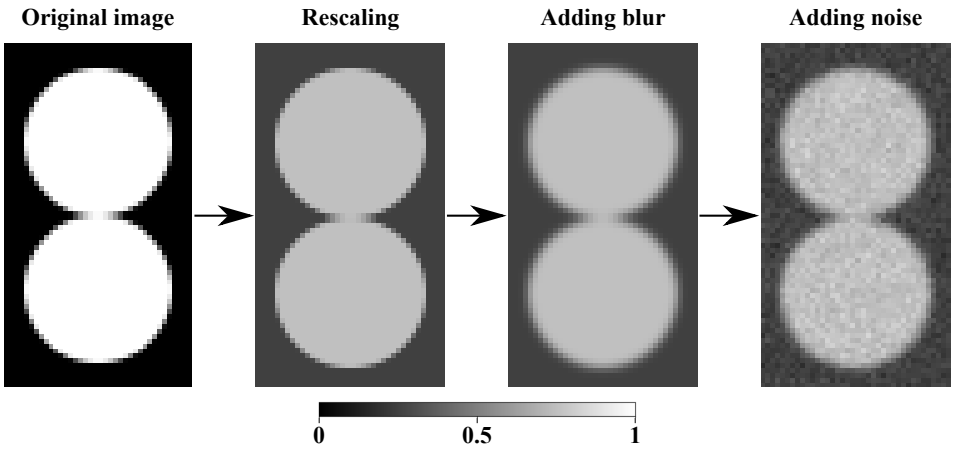

Figure 4.3: Incorporating image defects in synthetic images of spheres.

otherwise perfect synthetic images to realistic images and the calibration of the blur and noise levels is explained in detail in 7.4.

Even though these images are close to real tomographies and have similar properties, they remain artificial and the results obtained using them need to be validated. Therefore, x-ray tomographies of real granular materials are acquired at the (very low) pixel size of 1 µm in the nano-focus tomograph at the Laboratoire SIMaP in Grenoble. A few particles of either high precision spheres or the natural Hostun sand are filled in a capillary and scanned. The images of these small assemblies serve as the basis of a similar analysis as performed on the synthetic images. The manufactured spheres are chosen to validate or disprove the findings on the metrology and the Hostun sand grains to extend them to real natural particle shapes. Figure 4.4 shows slices through the small specimen of the spheres and Hostun sand as well as a 3D rendering of two contacting particles in the Hostun sand specimen.

The analysis of these images has to be carried out differently as the ground truth is not clearly defined. Therefore, the reference is determined at the highest resolution and declared a *golden standard*. In the case of the manufactured spheres, the orientation can be determined from the branch vectors, as both of them coincide. This measurement can be acquired very accurately at the chosen pixel size as the centres of mass are simple and accurate to identify [And13] and the spheres were manufactured with a very high precision as specified in 8.2.1 The golden standard of the contacts in the Hostun sand assembly are determined at the pixel size of the acquired

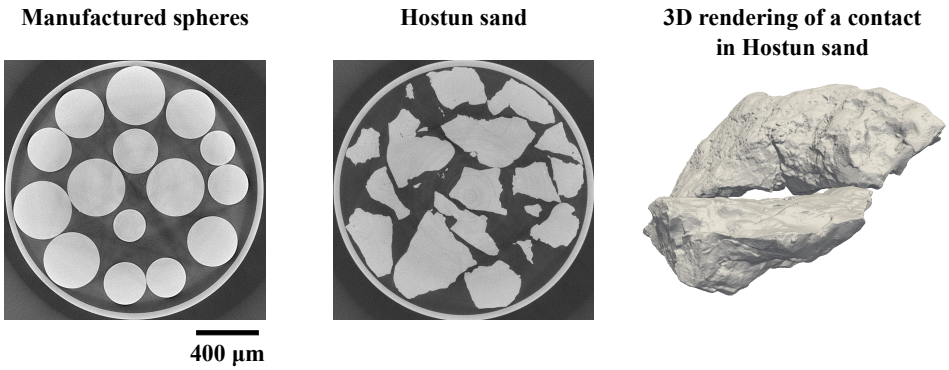

Figure 4.4: X-ray tomographies of manufactured spheres and Hostun sand at a pixel size of 1 µm. Left and centre: horizontal slices through the tomographies. Right: 3D rendering of two contacting particles in the Hostun sand specimen.asds

tomography directly as there is no analytical solution for contact properties of irregularly shaped particles.

4.1.1 Contact detection

The first major step of determining the contact fabric after the binarisation and the labelling of the grey-scale image is the detection of contacts. It is obvious from Figure 4.2, that the PVE leads to an enlargement of the contact of two touching spheres. As it happens at voxels close to the actual contact, where the two solid surfaces are proximal and thus, both contribute to the grey level of the voxel, this effect might bias the detection of contacts: if two particles are very close but not touching, they could appear as being in contact.

Figure 4.5 shows such a configuration. Two spheres are created such that they are at a distance of 0.4 pixel. A perfect detection technique would not detect a contact. But due to the PVE of both spheres, they appear to be in contact in the image. Since the spheres are close to each other around the apparent contact, the adjacent voxels that inherit parts of both spheres will have a higher grey value, representing the sum of the solid fractions of both spheres. Every sphere only has a solid fraction of 0.286 in the highlighted voxel, but as both contribute the total volume fraction becomes 0.57. As long as only spheres are imaged, this effect can very well be covered by

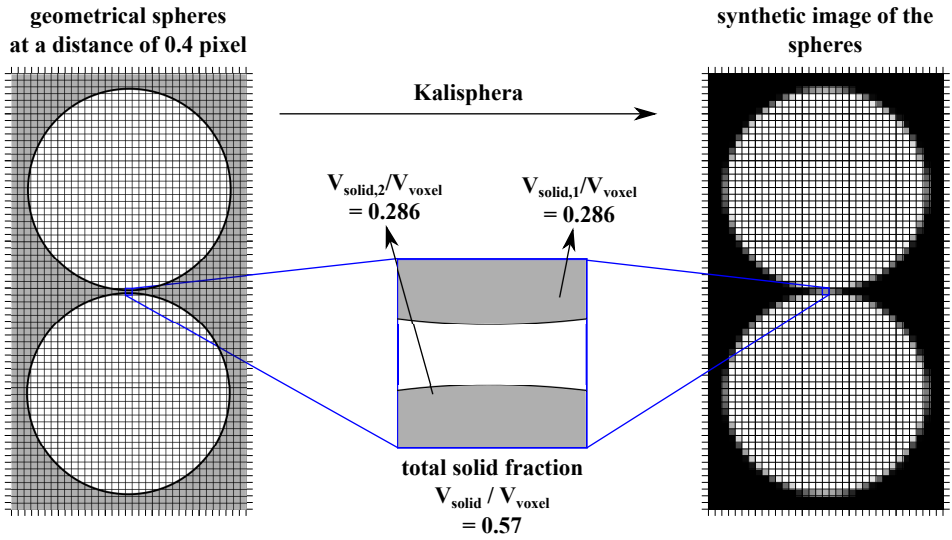

Figure 4.5: Visualisation of two spheres that are at a distance of 0.4 pixel geometrically. Left: Image of the geometrical configuration with the overlay of the image grid. Right: synthetic image of the two spheres. Due to the partial volume effect, the spheres appear to be in contact although they are at a distance. The PVE is explained in the centre by giving the exact solid fractions in a chosen voxel.

different approaches that use the restrictive information on the geometry, as discussed in 3.2. The aim of this work, however, is contact detection in more general and irregular shapes.

This over-detection is a serious problem for the image analysis as contacts will be detected although they do not exist. These apparent, but not existing contacts can artificially increase the coordination number and impact the fabric tensor. Furthermore, averaging over many particles will still yield wrong contact densities, since this is a one-sided standard error. In order to quantify the over-detection, a systematic analysis is carried out on the reference set of configurations in the following way. A synthetic image of two spheres in perfect contact is produced for one orientation as described in 8.1.2. The common way of detecting contacts is described in 3.1. The grey-scale image is first binarised and then segmented and labelled. Contacts are detected in the labelled image by checking whether voxels with a specific label have neighboring voxels of another label.

As the images in this analysis contain only two particles, it is sufficient

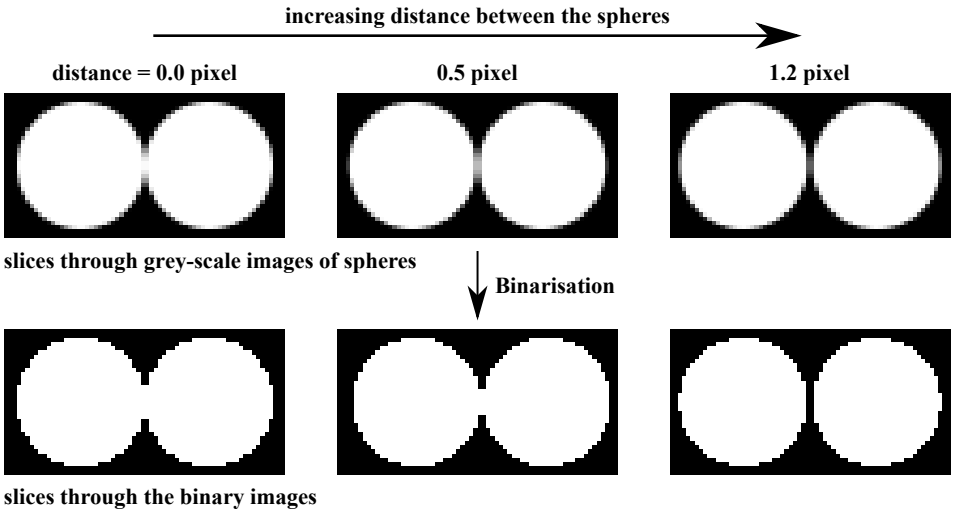

Figure 4.6: Workflow of the analysis on contact detection. 3 steps – from contact to non existing but apparent contact, to no contact at all!

to work on the binary image without segmenting and labelling it. If the binary phase in the image is connected, the two particles are detected to be in contact. If it is split in distinct regions, the two particles are not in contact. The connectivity in the image is determined by applying a structuring element on the binary image as explained in 8.1.3[3]. Obviously, a contact is detected in the image of the two particles that are geometrically in perfect contact. The problem is that contacts might be detected although the particles are not in contact. To test when this over-detection happens, an image of two spheres with the same orientation, but a distance between both spheres is created as shown in Figure 4.5. The same analysis is run on this image to check whether a contact is detected. The distance is increased subsequently until no contact can be detected any more. This maximum distance at which an apparent contact is still detected is called *over-detection distance*.

Figure 4.6 visualises the approach of this metrological study: An image of two spheres in contact is created and then binarised in order to check whether both binary phases are connected or not. A contact is still detected for a distance of 0.5 pixel between the spheres, whereas no contact can be

[3] An element with a squared connectivity of one is employed throughout this work. A comparison between two different elements and their effect on the detection of contacts is shown in Figure 8.2b.

found at 1.2 pixel. The analysis is repeated with a set of spheres for each branch vector in the reference set. The approach is described in more detail including specifics on the implementation in 8.1.3.

The over-detection distance is determined for each of the 5,000 reference orientations and statistically expressed as the probability of finding a contact at a given distance. The results of this analysis are plotted in Figure 4.7a. A perfect detection would give a probability of 1 (or 100 %) at a distance of zero and 0 for increasing distances. Unfortunately, the analysis shows that this is not the case. Even for a perfect (and rescaled) image that only considers the PVE as an image property, the over-detection on average, *i.e.*, for 50 % of the studied configurations, amounts to 0.6 pixel. The over-detection line for the perfect images are plotted in green. It is influenced strongly by the level of blur of the image. If blur as calibrated for the imaging system of Laboratoire 3SR is applied to the images, the average over-detection roughly doubles as plotted with the blue line. Blur directly impacts the edges and thus, increases the range of the PVE. The addition of noise to the blurred images (plotted with the red line) does increase the over-detection slightly, but its effect is not as significant as the consideration of blur. All the results presented here are obtained on spheres with a diameter of 30 pixel. The impact of the diameter is, however, almost insignificant in the range of the ratio of average particle sizes to corresponding pixel sizes in this work. See 8.1.3 for a more detailed analysis of the effect of blur and noise as well as different diameters of spheres.

These results show that for realistic images of spheres, a contact between two not touching spheres is always detected until the distance is higher than 1 pixel. For spheres with a diameter of 30 pixel, this gives a relative over-detection distance of 1/30. This is unacceptably high for a reliable, quantitative analysis of the contact fabric. The main reason for the over-detection to happen is the PVE in the zone where both particles are close. The image defects, blur and noise, only deteriorate this error further. In order to mitigate this error, a strategy based on local refinement is developed.

To reduce the systematic over-detection, the region in the image where both particles appear in contact is binarised with a higher threshold. This second threshold will be called *local threshold*. In order to assess this approach, subsequently increasing local thresholds are applied to the same images as before. Figure 4.7b shows the probability of finding a contact for spheres of a diameter of 30 pixel and the reference values for blur and noise of 0.8 and

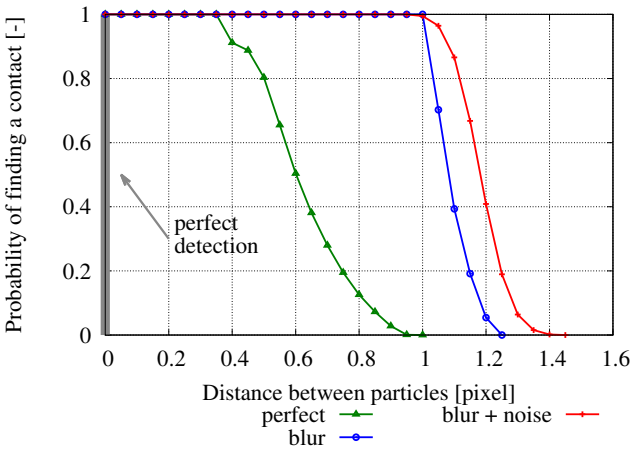

(a) Results of the global contact detection.

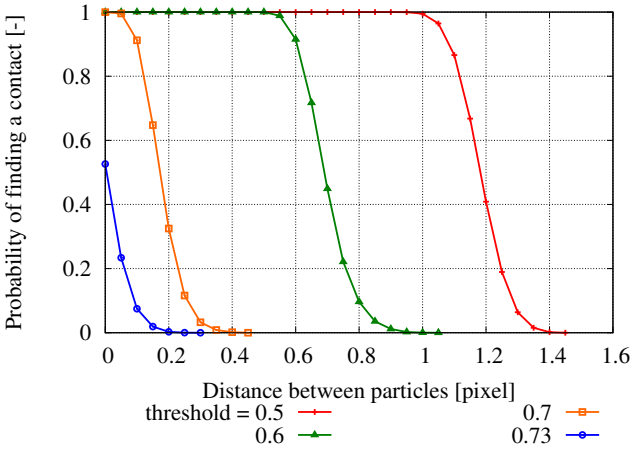

(b) Results of the local contact detection.

Figure 4.7: Results of the analysis on contact detection including image defects. The virtual diameter of the spheres is 30 pixel. The perfect detection is indicated in the left plot. Top: Contacts are detected at a physically correct threshold of 0.5. The results are plotted for different image defects – from perfect to blurry and noisy images. Bottom: Results for different locally applied thresholds to detect contacts. The images have the reference values of blur and noise. The threshold of 0.5 is the global threshold and thus, the red lines in both plots are the same.

0.03, respectively. The red line from Figure 4.7a is replotted as the reference for the application of the global threshold. Applying higher thresholds to the image reduces the over-detection distance significantly. The best results are achieved with a threshold of 0.7 for the thresholds studied. In the case of the even higher threshold of 0.73, some contacts that do in fact exist (distance of 0 pixel) are lost. Thus, care must be taken when calibrating a local threshold for the application.

The presented results are obtained on a fixed position of the spheres on the imaging grid. The position in the grid, however, is important as the partial volume of the voxels on the boundary of the particles will be affected. This impacts the detection on specific contacts, but statistically has no effect on the overall results as shown in 8.1.4. Furthermore, a locally adaptive threshold as defined in scikit-image [vdWSN+14] is tested in 8.1.5. It does yield comparable improvements to the local re-thresholding of every contact developed here, but requires a calibration that is more sensitive to the size of the particles and the image properties.

The results so far have been obtained purely on synthetic images of spheres, which limits the ability to draw conclusions for the treatment of real x-ray tomographies. In order to validate these findings on and relate them to real tomographies, high resolution images of two different granular materials were acquired and serve as the basis for a similar analysis on the detection of contacts. The notation *high resolution* is somewhat vague as resolution is not only related to the pixel size but also to numerous other factors of an image. The important parameter for this study, however, is the low pixel size of 1 µm at which the images are acquired. As shown in Figure 4.4, the two materials are manufactured spheres and Hostun sand.

The main problem of a metrological analysis on real images is the missing ground truth – it simply does not exist. This is especially true for the existence of a contact, which is image-wise a fundamentally ill-posed question [ASS05]. For the sake of this analysis, a *golden standard* is defined on the manipulated tomographies at the pixel size of 1 µm. This pixel size is an order of magnitude lower compared to the one of the real tomographies that are analysed later in this work. If two spheres or Hostun sand grains appear to be in contact at this scale, they are supposed to be in contact. Due to the low pixel size in relation to the particle size the treatment of these tomographies requires more than the standard steps and is described in 8.2.2.

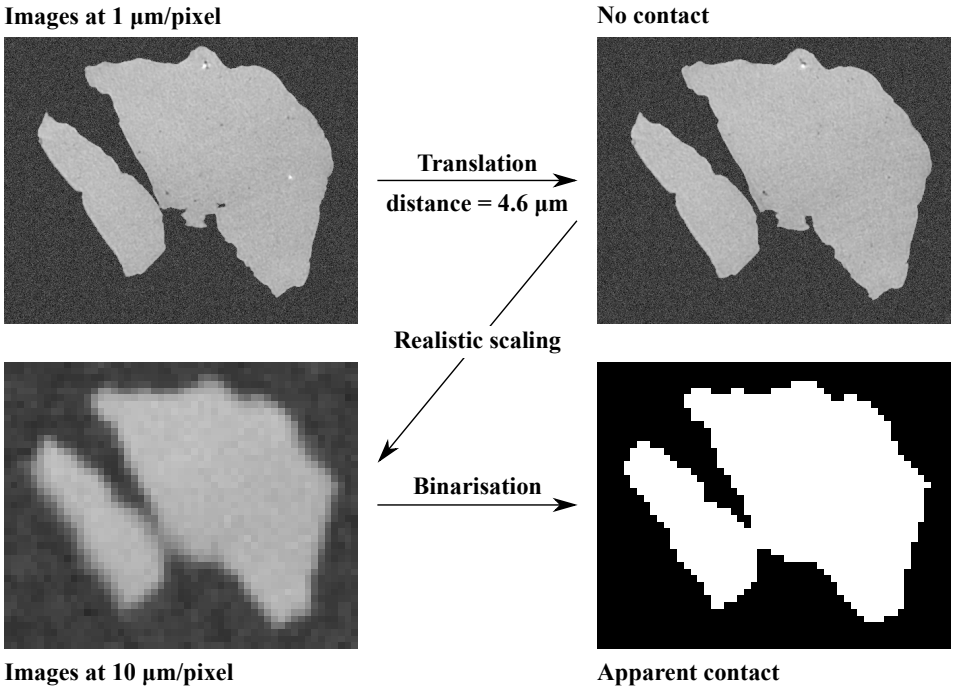

Figure 4.8: Procedure of assessing the detection of contacts for the high resolution tomographies. The original images are translated, then scaled down considering realistic image properties and binarised to check whether the particles are contacting. The contact is indeed appearing in this example although the particles are at a defined distance.

The approach to determine the over-detection of contacts is generally the same as before and is illustrated in Figure 4.8 on the example of two supposedly contacting Hostun sand grains. A sub-image of a pair of two contacting particles is fetched from the tomography. The two particles in this image are then translated from each other by a specific increment in the direction of their branch vector. As the Hostun sand is irreguarly shaped, the distance between the two surfaces does not necessarily equal the amount of translation and is not trivial to determine. The calculation of the distance is described in 8.2.3 along with the other specifics of this approach. The image of the translated particles is scaled down to different typical pixel sizes for lab scanners, *e.g.*, 10 µm as in the visualisation. Special care must be taken when scaling down these images in order to consider the typical image defects, *i.e.*, noise and blur. The image is then binarised in order

to check whether the two particles, that are by definition not in contact, appear to be in contact. In the case of the example this is true, although the particles are at a distance of 4.6 µm. The two particles are translated from each other until they do not appear in contact at the lower scales anymore. This process is repeated for each set of contacting particles in the images of the spheres and Hostun sand.

The results of the contact detection analysis on both materials are displayed in Figure 4.9. The over-detection distances for the global approach are plotted as the red lines similar to Figure 4.7b. In order to simplify the presentation only results for the pixel size of 10 µm are presented here. The other pixel sizes yielded similar results as shown in 8.2.3.

The results on the spheres shown in Figure 4.9a are qualitatively similar to the results of the synthetic images, see Figure 4.7b. The slope and the actual over-detection distance are slightly lower than for the synthetic images. This over-detection is reduced tremendously by the application of a local threshold. The optimal local threshold from the values tested is 0.65 as existing contacts start to not get detected with the higher 0.7. This is lower than the optimal threshold of 0.7 found for the synthetic images, although the images are prepared having similar but partly random defects.

The observation of the systematic over-detection also holds for Hostun sand, see Figure 4.9b. The over-detection distance is, however, lower. The local thresholding does not work as expected from the experience gained on spheres. Existing contacts are already lost when slightly increasing the local threshold to 0.55, meaning that under-detecting contacts is a possibility for these shapes. The reason must be the angular shape. In general, the impact of the PVE on the contact detection is not as strong as for round shapes as there are contacts that tend to singular contact zones (called 'sharp' point-like contacts in [WAHV17]). Scaling these 'sharp' contact topologies leads to a loss of grey value in the area of the apparent contact due to the large amount of void adjacent to this contact in the original image at 1 µm/pixel.

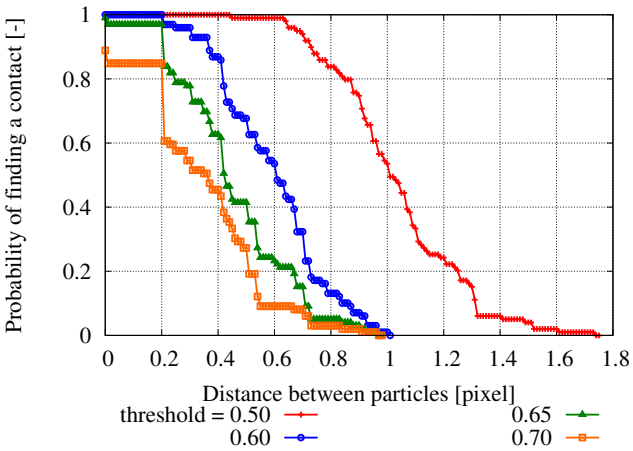

(a) Manufactured spheres.

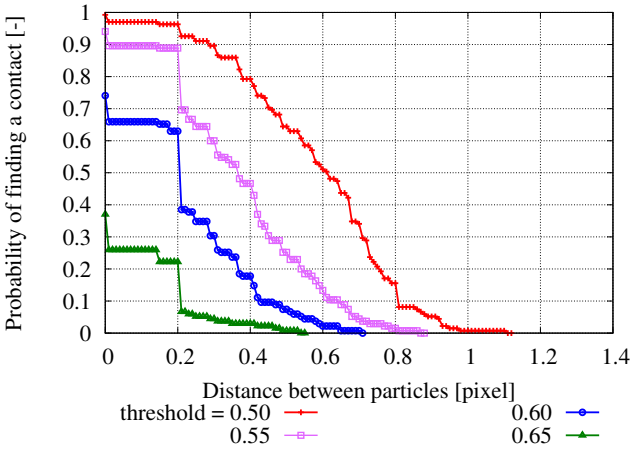

(b) Hostun sand.

Figure 4.9: Results of the study on contact detection on the high resolution tomographies at a pixel size of 10 µm. Application of higher local thresholds to reduce the over-detection distance.

4.1.2 Contact orientations

The challenge after the detection of contacts is the determination of their orientation. This is commonly done directly on the basis of a topological watershed, as *e.g.*, in [Fon11, FOCL13, DAAR16, IDA18]. It has been shown that this method of estimating contact normal orientations introduces a strong bias and results in inaccurate measurements [JAVT13]. To increase the accuracy of these measurements, the random walker, a power watershed, has been proposed as an alternative way[4].

Both methods, the standard watershed and the random walker, are investigated here regarding their accuracy. These two methods allow for different approaches to determine the contact orientations, which are visualised in Figure 4.10. Similar to the previous study, the starting point of this analysis are synthetic images of two contacting particles. A slice through one exemplary image is depicted on the left side in of Figure 4.10. This image is created by imposing an orientation of [0.707,0.707,0] (x,y,z), *i.e.*, purely in the plane of observation, and already incorporating the image defects typical for a tomography in the lab scanner of Laboratoire 3SR as calibrated in 7.4. The labelled image in the centre of the figure is obtained after applying a standard topological watershed [MB90], as described in 9.1. In order to determine the orientation of the contact between these two objects, the voxels that form the contact, *i.e.*, the voxels of one label that are touching the other label and vice-versa, are identified. The contact normal is then determined by performing a principal component analysis (PCA) on this set of positions. The direction of the eigenvector corresponding to the minimal eigenvalue is considered to be the contact normal orientation.

The random walker offers an additional way of identifying the contact plane than on the purely voxelised labelled image. When applied, it produces probability maps that assign each voxel a probability of belonging to one or another label. The probability of belonging to label 1 (the blue label in the centre image) is shown on the right side of Figure 4.10 with values for chosen voxels. If the probability is higher than 50 % in this image, the voxel is considered to be part of label 1. This map provides the possibility of determining the contact plane on a sub-pixel level by interpolating a 50 % probability surface. Similar to the approach above, a PCA is performed on the set of positions defining this surface to determine the contact normal

[4]The analysis on the proposed usage of the random walker in [JAVT13] has been carried out, however, on simplified synthetic images of spheres as discussed in 3.2.

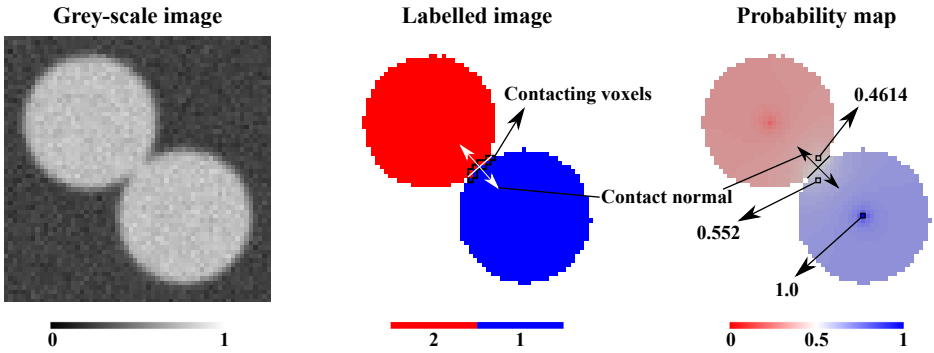

Figure 4.10: Determination of contact orientations from two different watersheds: a topological watershed and the random walker. Left: synthetic grey-scale image of two contacting particles considering inherent image properties. Centre: Labelled image. The contacting voxels from both objects are marked. Right: Probability map of marker 1 of the random walker. Displays the probability of each voxel of belonging to label 1. Some values are given. The contact normal is visualised for both methods.

orientation.

The contact orientation determined on the labelled image in the small example is [0.0640, 0.7152, 0.6960] whereas the evaluation of the probability map yields [0.0067, 0.7035, 0.7107]. The angle between the imposed orientation and the determined contact orientation serves as a scalar quantification of the error of each approach. The errors amount to 3.753° and 0.483° for the topological watershed and the random walker, respectively. The random walker, thus, yields a more accurate measurement for the chosen configuration.

To generalise the analysis, these steps are repeated for all 5,000 reference orientations, described in 8.1.1. Furthermore, the diameter as well as the image defects, blur and noise are systematically varied to investigate the effect of each parameter on the accuracy of the contact orientations. More details on both approaches and the complete analysis on the synthetic images are given in 8.1.6.

The results of the analysis on the synthetic images are plotted in Figure 4.11a as the mean error versus the virtual diameter of the spheres in contact. The analysis on perfect images, *i.e.*, images that only consider the PVE without any blur or noise, is again plotted with the green lines. In the

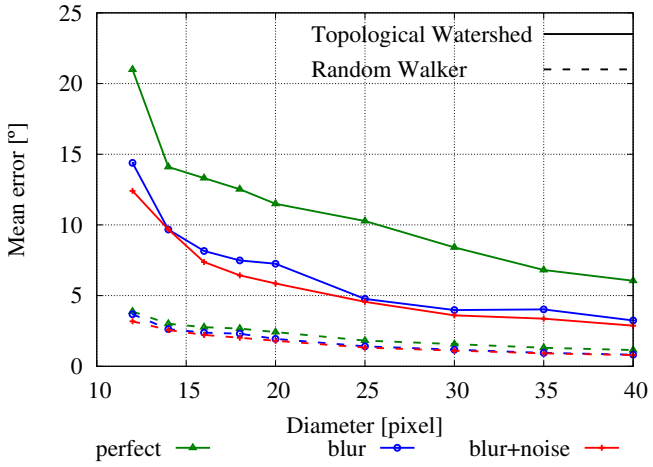

(a) Synthetic images.

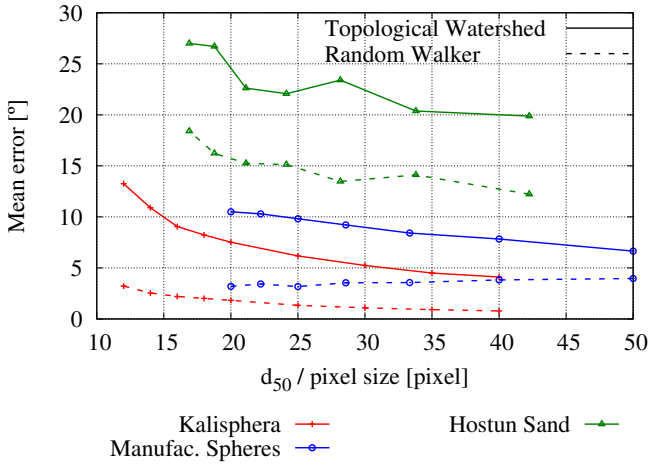

(b) Results of the complete analysis.

Figure 4.11: Results of the metrological study on contact orientations of individual contacts. Top: Accuracy of contact orientation in the synthetic images of spheres with varying degree of complexity – from perfect to blurry and noisy images. Bottom: Comparative plot of the accuracy of contact orientation in all the materials from synthetic images to real tomographies of manufactured spheres and Hostun sand. d_{50} is the average particle diameter.

range of diameters plotted, the mean error decreases from 21° to 6° with increasing size of the particles for the standard watershed. This is due to the PVE as more voxels are included in the contact with increasing diameter of the spheres. The PCA is thus performed on more positions which increases the accuracy of the result. The observation from the example in Figure 4.10 also holds statistically with the mean error between 4° and 2°.

The first step of increasing the complexity is again the incorporation of blur. This leads to a strong decrease of the mean error by approximately 5°. Both, blur and the PVE, lead to an artificial increase of the contact surface and consequently to a more accurate determination of the contact orientation. Note that the actual contact consists of only one point geometrically and only the image properties and defects lead to the detection of a surface. In the case of contacting spheres with round and smooth surfaces, this apparent surface helps tremendously in determining orientations, but that is less true for irregular shapes. The effect of adding blur on the approach by the probability map of the random walker is insignificant. A further deterioration of the image quality by adding noise has no significant statistical effect on any of the approaches. It does, however, impact individual configurations as the noise is added randomly. Unlike for the detection of contacts, the error of an orientation is random. Thus, the mean error can be reduced by averaging over many contacts. More details on the results of this analysis including the frequency distribution of the errors and the spatial distribution of the obtained orientations compared to the reference set are given in 8.1.6.

Another method that can be used to extract fabric properties from tomographies are level sets [VAVA13]. The accuracy of level sets is assessed in the same way as the two watershed approach on the synthetic images of spheres and described in 8.1.7. The levels sets yield even lower errors that the random walker, but needs far longer for the computation. In sight of the computations required for the big assemblies tested later in this work, the substantially higher computational cost of level set appears to be too high. Thus, the orientations are determined using the random walker to analyse the tomographies in reasonable time. This still required the parallelisation of the code and the use of the high performance centre of computation in Dresden as described later.

Similar to the study on the detection, the methodology of this analysis needs to be adapted to be applicable to the high resolution tomographies of spheres and Hostun sand. As the ground truth of the contact orientation is

unknown, a golden standard for each contact is determined on the images at the original low pixel size of 1 µm. For the manufactured spheres, it can be estimated rather accurately due to their shape and the high precision manufacturing process. The branch vector is determined by calculating the centres of mass of two touching spheres at the pixel size of 1 µm and considered to be the reference orientation. As Hostun sand grains are irregularly shaped, the reference cannot be estimated based on the particle shape. It is determined by carrying out a PCA on the contact surfaces in the original image.

Sub-images of two particles in contact are then scaled down to pixel sizes that are representative for x-ray tomographies of samples in the lab scanner of Laboratoire 3SR in Grenoble[5], *i.e.*, the imaging system that is used in this work. Blur and noise are added to the images after fetching and scaling them in order to incorporate realistic image properties. This is necessary as the acquired and reconstructed tomographies have a very low level of noise which is reduced even further after scaling them to lower pixel sizes. The orientation at each scale is then determined in the same way as for the synthetic images, *i.e.*, by either segmenting and labelling the image and running a PCA directly on the positions of the contact surface or by segmenting with the random walker and using its probablity map to determine the contact surface. This whole process is specifically described in 8.2.4.

In order to express the spatial resolution of the grains in pixel, *i.e.*, the base unit for working on images, the average grain diameter d_{50} [µm] is divided by the pixel size [µm/pixel]. The results of the complete study on individual contact orientations are summarised in Figure 4.11b. The mean errors determined on the synthetic images are plotted with red lines similar to their corresponding curve in Figure 4.11a. The trends are similar for all three materials: the mean error mostly decreases with increasing spatial resolution. The error obtained on the tomographies of the manufactured spheres is higher than the one found on the synthetic images of spheres. Using the random walker, the error does seem to stay constant with increasing spatial resolution although it is slightly decreasing for the synthetic images. There are two reasons for that: (1) as these images come from a real tomography, they do have more artefacts, such as the phase contrast[6] or a ring artefact;

[5]The pixel size of these images is an order of magnitude higher than for the high resolution tomographies.

[6] Phase contrast is an effect that causes the edges of objects to be non-physically enhanced, *i.e.*, to be more clearly defined by *e.g.*, a higher grey value. It is caused by

(2) there is in fact only a limited set of orientations. Due to the low pixel size at which the tomography is acquired, there is only a limited number of contacts in the images, as explained in 8.2.2.

The mean error of the investigated contact orientations in Hostun sand is substantially higher compared to spheres as plotted in Figure 4.11b. In the range of interest for the experiments that are conducted within this work, the mean error lies between 15° and 14° for the random walker and ranges from 20° to 24° for the topological watershed. The high errors can be explained by three factors: the definition of the golden standard as described above, the 'sharp' contact topologies and the change of surface topology when scaling down. Point-like contacts in both the reference as well as the scaled images are defined by few contacting voxels which impact the quality of the fit with the PCA: the fewer voxels are part of the contacting zone, the fewer data can be used for the PCA, which might result in bad fits.

The main problem, however, is relating the orientations on the lower scales to the reference orientations at 1 µm. Due to the angular shape, areas that are in the vicinity of both particles can undergo changes in their topology when scaling down the images. Three effects are observed from scaling the images of the selected contacts: (1) the creation of artificial contacts, (2) the enlargement of existing or artificial contacts and (3) the merging of originally distinct contacts. Figure 4.12 shows these three scaling effects on slices of two selected contacts. Note that these scaling effects are also present in the complete 3D images, but their presentation is facilitated using the slices. The contact in the upper image consists only of a few voxels in the original resolution, which lowers the quality of the fit and thus, makes the determination of the reference orientation error prone. After scaling to a pixel size of 8 µm another contact appears artificially (1), which is basically the problem that is investigated in the study on contact detection, see 8.1.3 and 8.2.3. As the orientation is determined by running the PCA on all contacting voxels here, both contacting regions are taken into account which results in an error of 23° when comparing it to the golden standard. When reducing the spatial resolution further to 16 µm/pixel the same contact shows scaling effect (2) as well: the size of the artificially created contact, *i.e.*, the number of voxels defining this contact, is increasing. Due to the larger contact size as visible in the 2D slice, the artificial contact gains more weight in the fit which increases the deviation from the

the coherence of the x-ray beam and the refraction of the x-rays. Using laboratory x-ray scanners, it is mostly occurring at high resolution and low attenuation [CB13].

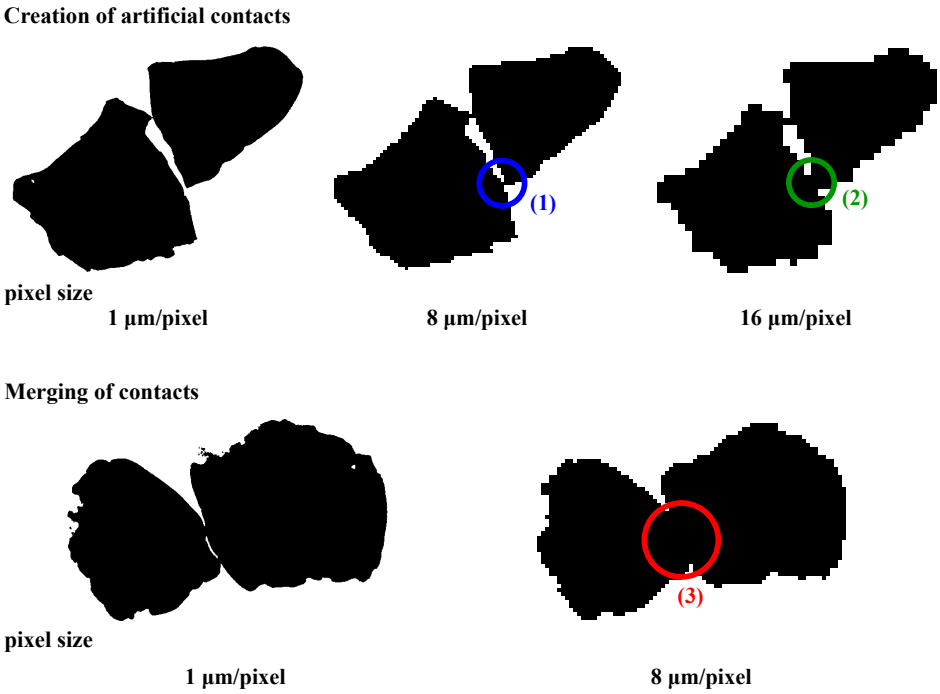

Figure 4.12: Two chosen contacts for displaying the change of contact topology after scaling the images. Only 2D slices of the binary 3D images are shown. They are chosen to go through the contacts displaying these features.

orientation at this scale to the reference orientation to 27°. The 2D slices of the other contact displayed in the lower part of Figure 4.12 displays scaling effect (3): the contact consists of multiple distinct contacts between the two particles at the initial pixel size, which become a flat surfaces after scaling to 8 µm/pixel. The merging of these distinct contacts, however, yields only an error of 5°. In this particular case, the low error is due to the alignment of both contact normals in the original image which is almost similar to the flat contact at the lower scale. Level sets might be a way out of this problem of contact topology, but require more computational cost and are therefore not assessed here.

4.2 Metrology of contact orientations in assemblies

So far, the accuracy of measuring contact properties is only investigated on the individual contacts. One open question is how these uncertainties impact measurements on assemblies of particles. The contact fabric on these scales is usually expressed in terms of global, bulk properties as described in 1.2.2. In order to relate these two scales, the particle and the assembly scale, a similar approach is developed. At first, a synthetic assembly of spheres is created for which the ground truth is perfectly known. In a second step, a real assembly of glass spheres is experimentally tested and tomographies are acquired at different stages of the loading. The latter is described in 10.2 and only briefly mentioned in the summary of this section.

Using the same methodology as before, *i.e.*, creating a synthetic image incorporating realistic image defects, enables a simple determination of the accuracy of various image analysis tools. The accuracy could be determined on a simple, artificial packing of spheres as there are many algorithms to create such assemblies. But the aim of this analysis is to also check whether and how accurate the evolution of contact fabric due to an external loading can be captured by the different image analysis approaches. Using the discrete element method makes it possible to combine these two topics and answer both questions from the same data set: (1) how accurate are the image analysis tools in terms of global measurements with the known uncertainties from the previous analysis. (2) how well can we track changes in fabric, *i.e.*, the evolution of contact density and the fabric distribution, for reasonable displacements in a granular assembly. The second question can be related to monotonic loading as well as changes due to small strain increments, such as during load-unload cycles. In order to answer these, a benchmark strategy is developed here.

The open-source code *WooDEM* [Š16] is used in this work to carry out two simulations on the particle scale: a monotonic and a cyclic one. Both are created and run using the same parameters and conditions, but only the cyclic test is presented here because it is sufficient to answer all the questions raised. In this case, the interest is not on the actual behaviour of the packing, but on the image analysis that follows. Thus, a simple contact model is used with a linear spring in the normal direction and a linear spring and a frictional slider in the tangential direction. The size of the particles is chosen to lie in the range of the materials that are used for the experiments in this work and ranges linearly from 320 µm to 480 µm.

After creating a set of 5522 spheres[7], the initial packing is isotropically compressed. It is then loaded in triaxial compression, *i.e.*, the stress at the four radial sides of the cube (x and y) is kept constant and the axial dimension (z) is compressed by controlling the deformation. At different strain levels, the specimen is unloaded to the initial isotropic stress state and reloaded. The deviatoric stress-strain response of the specimen is plotted in Figure 4.13. At chosen stages of the loading, the fabric of the specimen, *i.e.*, the positions and radii of the particles as well as the contact network, is exported from the numerical simulation. These states are indicated by the grey squares in the plot of the macroscopic answer. Details on the simulation as well as the complete behaviour of the specimen are given in 10.1.1.

A synthetic image is created for each of the states at which the fabric is exported. This is done in a similar way as before in the study on synthetic images. A pixel size of 15 µm is employed to translate the metric for the radii and positions of the fabric, that is expressed in meters in the DEM simulation, to pixel. This is the pixel size at which the tomographies of triaxial samples are acquired in the imaging system of Laboratoire 3SR. An image of each sphere is created separately in a box of the final dimensions of the complete specimen using Kalisphera [TA15]. These images are superimposed to form the complete assembly. The image defects, blur and noise, are added after assembling the complete image as calibrated from real tomographies in 7.4. Figure 4.14 visualises the transformation of a DEM sample to a synthetic image with real properties on the initial state of the simulation. This process requires several considerations, *e.g.*, regarding the periodic boundary conditions or the inherent overlap of particles at contacts[8]. It is therefore described in detail in 10.1.2. A small illustrative code using *spam* is given there as well.

The images are analysed using the open source software *spam* [ACR$^+$]. The approaches described and developed in the study on the metrology of individual contacts are implemented in *spam*. At first, the grey-scale image is binarised using a global threshold. It is then segmented and labelled with an ITK watershed [YAL$^+$02, BL06] as implemented in *spam*. The real work

[7] Note that these ≈ 5000 sphere are not at all related to the 5000 reference orientations from 8.1.1

[8] The overlap of particles at contacts in the numerical simulations is non-physical, as particle do not interpenetrate one another. The surfaces instead experience wear and abrasion at the contacts. The amount of overlap is used by DEM approaches to determine the contact force. Its consideration for creating the synthetic image is described in 10.1.2.

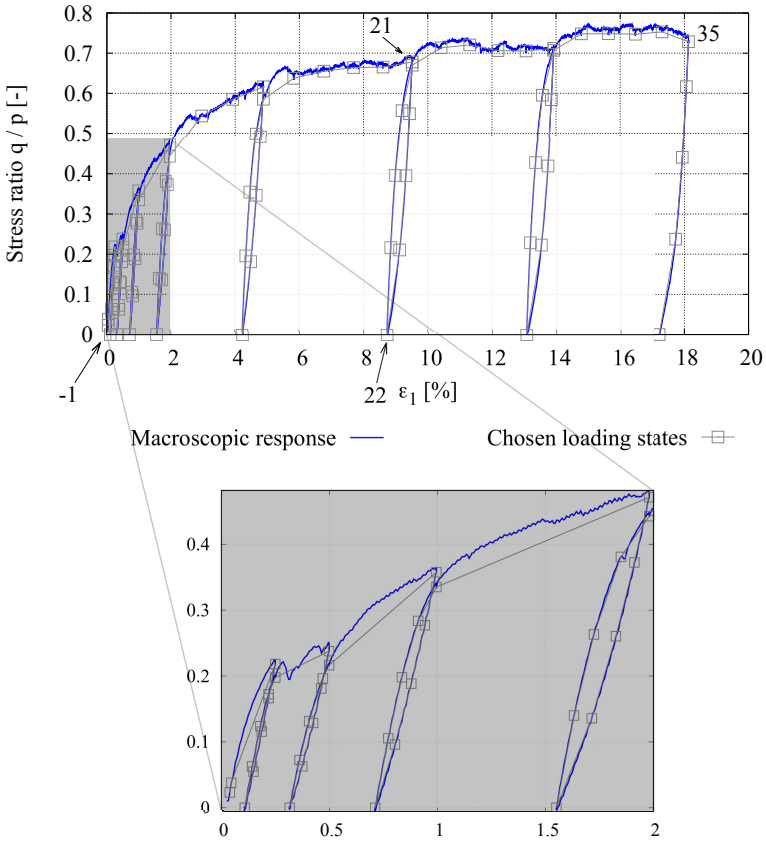

Figure 4.13: Macroscopic deviatoric stress-strain response of the sphere packing in the cyclic benchmark test. A zoom-in on the bottom of the figure is given to show the anisotropy at the small strain cycles. See Figure 10.2 for the complete macroscopic response.

of this study starts thereafter: at the determination of the contact fabric. To assess the accuracy of the standard as well as the proposed approaches for the detection and orientation of contacts, both ways are carried out here. The contacts are detected directly on the labelled image as done commonly. As this is found to lead to a systematic over-detection of contacts on individual contacts, the identified contacts are locally refined using the approach described in 4.1.1. The optimal value of the local threshold for the refinement as calibrated on synthetic images is applied here. See Figure 4.7b for reference. The orientations are determined either directly on the labelled image or as proposed with the random walker [Gra06]. In the

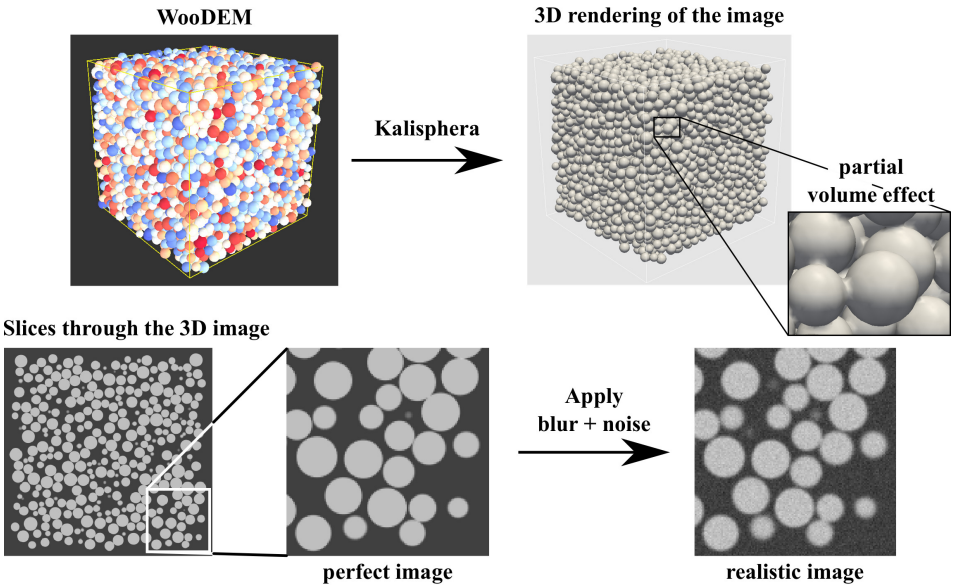

Figure 4.14: Sketch showing the transformation of a numerical assembly created by the discrete element method into a synthetic image. Kalisphera is used to create images of spheres considering the partial volume effect. Blur and noise are added to degrade the image to a realistic level of tomographies. 2D slices of the 3D images are presented at the lower part to show the transition to synthetic, but realistic images. As published in [WAŠ+19]

following, the orientations determined on the labelled image are named by the initial watershed, the ITK watershed. They are denominated by topological watershed in 4.1. A description of the implementation of these tools along with an example is given in 9. The example given there is an image from the monotonic benchmark.

The contact density is usually expressed globally using the coordination number as defined in Equation (7.9) if only a scalar value is sought for the description. The evolution of all three coordination numbers is plotted in Figure 4.15. The ground truth, *i.e.*, measured from the numerical simulation, is shown in green. The density does not change significantly throughout the monotonic part of the loading, but small loops are observable at the load-unload cycles: the coordination number decreases at unloading and increases again at reloading. It is interesting to note that the actual value

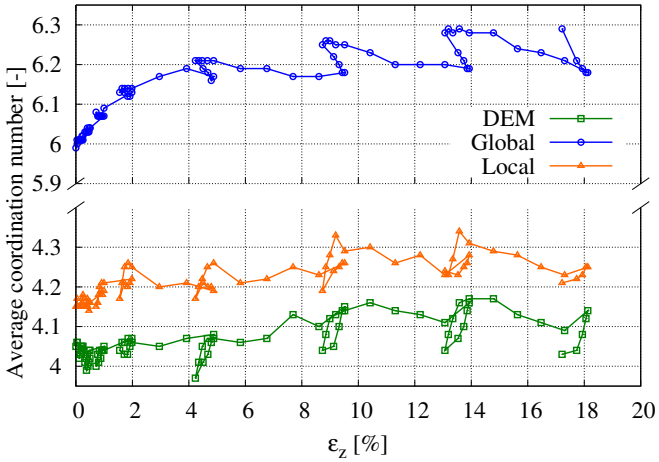

Figure 4.15: Evolution of the average coordination number in the cyclic test given by the numerical reference values (green) and determined by the global (blue) and local (orange) image analysis approaches. Note the broken vertical axis that separates the actual values due to the big differences.

is close to four, which is the coordination number at the isotatic state[9] for monodisperse packings of hard, cohesionless spheres [Edw98]. Note that rattlers[10] are not excluded in this case, as the only purpose of the simulation is the study of the accuracy of contact fabric measurements. The coordination number is also calculated by excluding contacts at the periodic boundaries, as these cannot be taken into account in the image analysis. Excluding rattlers would lead to a slightly lower actual coordination number, whereas the inclusion of the contacts to the periodic boundaries would lead to a substantially higher value. The assembly is thus, at a relatively loose state close to the onset of jamming.

The global, most common, approach is plotted in blue and shows significantly higher values. Note the broken vertical axis. In addition to the actual values that are ≈50% higher than the reference, the measured evolution is showing a different trend. That is especially true for the cycles: the coordination number does stay relatively constant during the first cycles

[9]The isotatic state remarks the onset of jamming in granular materials. This is commonly also noted as the Random Loose Packing.

[10]In order to calculate a mechanically meaningful coordination number, rattlers are usually excluded. They are commonly particles that have less than 4 contacts (isostatic limit) [GDL10].

at low strains. For the cycles at higher strains, it changes in the opposite direction: it increases at unloading and decreases very slowly at reloading. The local refinement of the contact network is plotted in orange. The refined coordination number is only 2.5 % higher than the reference one, which is a huge improvement from the 50 % before. Using an optimal local threshold as defined in 4.1.1 will always lead to a slight over-detection as we chose it in order not to loose any contacts. And if no contacts are lost, some must be gained compared to the ground truth as the detection cannot be perfect with this approach. Furthermore, the evolution of the reference is mostly captured. The only slight differences are in the cycles at higher strains where the measured coordination number overshoots at reloading compared to the reference. The cycles, however, are also visible in these refined measurements. These results show that at least for particles with round surfaces, a local refinement is necessary to make a good estimate of the contact density from tomographies. Not only the actual values, but also the evolution is captured completely wrong with the common approach. The evolution as such might be even more important for an incorporation of such fabric quantities into constitutive models.

The orientations are compared visually at first in order to get a feeling for a possible bias that is introduced using the different watersheds. These biases are for example visualised in 8.1.6. The orientations are plotted using a Lambert azimuthal equal area projection. As there are more than 10,000 orientations, they are binned to facilitate the understanding of the plots. The projection is explained in 7.2.1 and sketched in Figure 7.1. To use the same scale for all plots, the bins are normalised by the average count of orientations per bin.

Figure 4.16 shows the projections from four chosen states for the numerical simulation as well as both image processing approaches. These states are indicated in the plot of the macroscopic answer of the specimen in Figure 4.13. The contact fabric is rather isotopic in the initial state (-1) with only slight random variations. It does align with the vertical direction (z), *i.e.*, the centre of the plot, with increasing loading (21). This is also the direction of the principal stress and thus, agrees with the huge body of research done using DEM and experiments as described in 2. (22) is a state after the sample is completely unloaded to the initial isotropic stress state. The contact fabric does change visibly due to this unloading: it seems to be reverted to a more isotropic state as the contact density is decreasing in the centre of the plot, *i.e.*, the loading direction, and is increasing in the

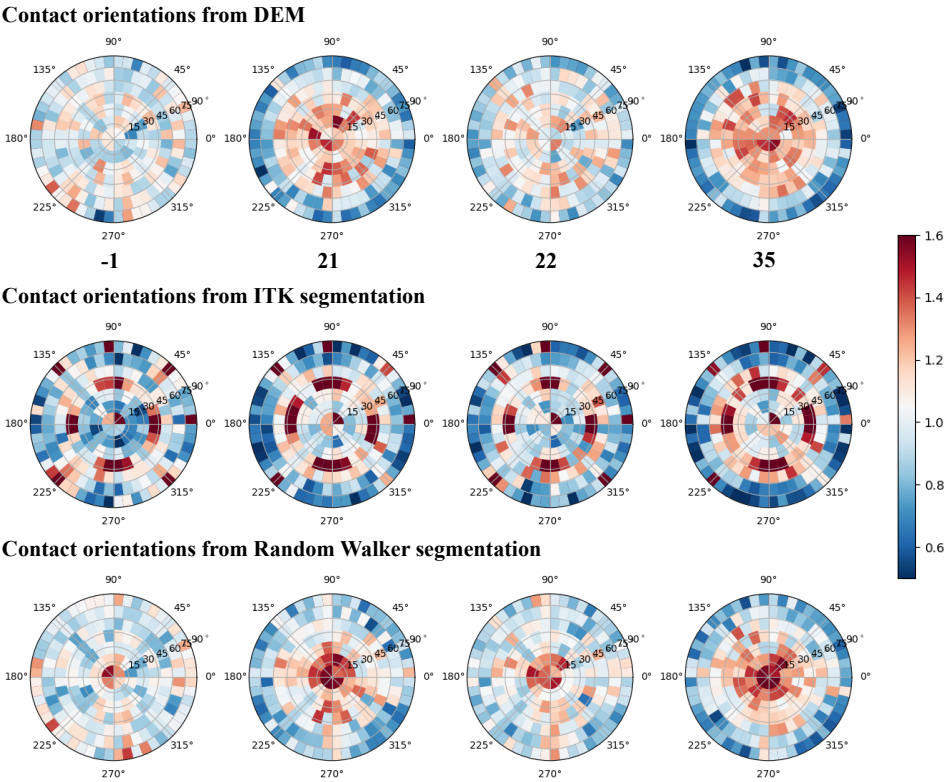

Figure 4.16: Plots of the orientations from the cyclic benchmark test using Lambert azimuthal equal area projection. The chosen loading stages are indicated and referred to in the plot of the macroscopic response, Figure 4.13. The orientations from the reference DEM simulation and the image processing by the ITK segmentation and the random walker are plotted along the respective rows. The bins are normalised by the average count of orientations per bin.

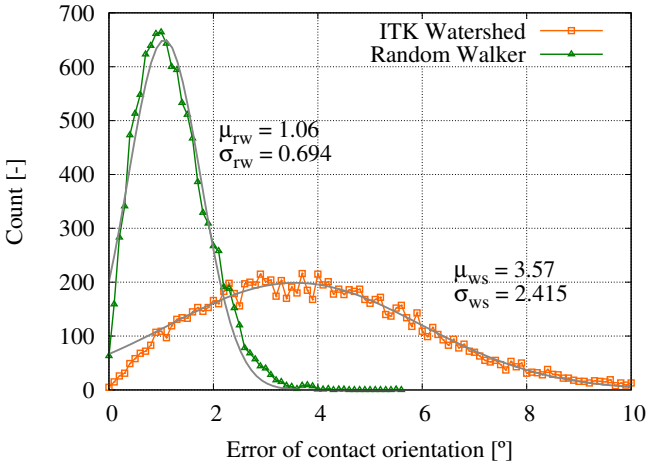

Figure 4.17: Histogram of the error of contact orientations determined with the random walker and the ITK watershed for state 35 of the cyclic simulation. The grey lines and the μ and σ values represent a fit of a Gaussian on the data.

outer rings of the plot, *i.e.*, the radial direction. With further loading (35), the orientation align even more with the principal stress direction.

The topological watershed (ITK) does show a strong bias which confirms the findings of the study on individual contacts in all plotted states. The bias is directed towards the diagonal axes in the euclidean coordinate system, which also applies for pixelated images. This can be observed from the red bins that are oriented at a multiple of 45° inclination and/or azimuth. A similar evolution as in the simulation, which is a concentration of the orientations in the centre of the plot, might be observed, but is not clearly visible. The random walker segmentation, on the other hand, yields rather similar plots compared to the reference. Most importantly, it even shows a similar evolution towards a more isotropic state upon unloading.

To assess the accuracy not only based on visual inspection, the orientations from the image processing are directly related to the orientations from the numerical simulation. This is necessary as the labelling in the image and the simulation is not identical. The steps needed to do that are described in 10.1.4. A histogram of the errors is plotted in Figure 4.17 for state 35 of the cyclic simulation. The projections of orientations for this state are highlighted in Figure 4.16 on the far right. Surprisingly, the actual errors of

the orientations directly determined from the ITK watershed are low with a mean value of 3.5°. That means, that even though the actual error is low, the orientations can still be strongly biased. The random walker yields a mean error of 1.1°. Both errors are slightly lower than the ones determined on the synthetic images of individual spheres[11]. The main reason for the lower errors, is the elasticity of the contacts in DEM: the overlap of particles causes larger contacting zones than in the analysis on individual contacts. This results in a larger data base for the PCA and thus, yields more accurate results for round surfaces in contact as discussed in 4.1.2.

It is difficult, however, to work with these individual orientations and to describe an evolution clearly. Therefore, different fabric tensors are commonly used to statistically describe such distributions. Some chosen formulations of these tensors are described in 7.1. Throughout this work, the most commonly employed and probably simplest formulation is used: a second order fabric tensor as given in Equation (1.2) and defined thoroughly in [KI84]. In this benchmark, only the anisotropy of this fabric tensor is employed to describe the evolution of the contact fabric and test the image analysis results of the different approaches. The anisotropy is expressed by a scalar anisotropy factor that is calculated from the deviatoric part of the fabric tensor as described in Equations (7.7) and (7.8).

Figure 4.18 displays the evolution of the scalar anisotropy factor with the macroscopic loading. The reference from the numerical simulation is again plotted in green. As observed from the projections of the orientations in Figure 4.16, the contact fabric of the sample is initially very isotropic. The anisotropy then increases with increasing shear: the rate of change is higher at the beginning of the loading at smaller strains and decreases with increasing strain. During the cycles, the anisotropy generally decreases at unloading and increases again at reloading. The former value from before the unloading is, however, not reached at the end of the reloading.

The behaviour of the contact fabric observed in the simulation agrees partly with the numerical studies dealing with load cycles described in 2.2. The fabric anisotropy is changing substantially during the load cycles as observed in [OC09, JZL19]. It does, however, not completely revert back to its state before the load cycles as found by Alonso-Marroquin [AMH04], which means

[11] See the red line in Figure 4.11b for a comparison with the results of the analysis of individual orientations. As the d_{50} is about 27 pixel for this simulation, based on the chosen pixel size and the particle size distribution, the mean errors are 4.1° and 1.2° for the topological watershed and the random walker, respectively.

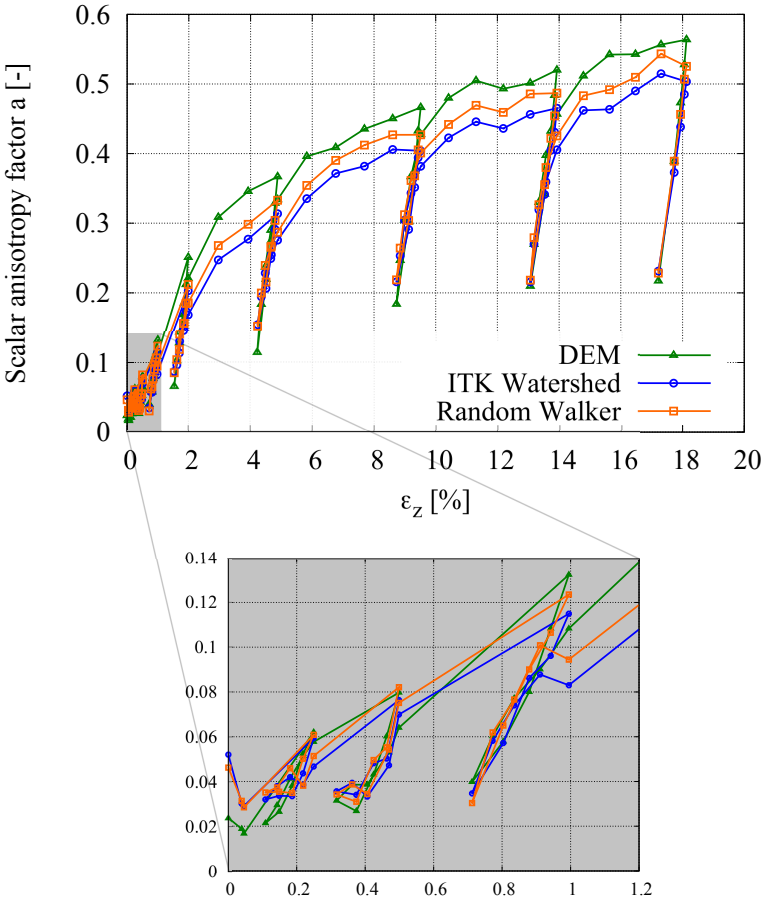

Figure 4.18: Evolution of the anisotropy of the fabric tensor in the cyclic benchmark test. See Figure 4.13 for the macroscopic response. A zoom-in on the bottom of the figure is given to show the anisotropy at the small strain cycles.

that the fabric does not behave elastic. This might be related to the small amount of plastic strain that occurs at every cycle; even the smallest cycles at low axial strain, which can be observed on the macroscopic behaviour of the numerical specimen. Figure 4.13 shows that a further loading is necessary to reach the same stress level after the load reversal is completed. Hence, the simulation captures the general behaviour observed in more sophisticated models even though the simulation is strongly simplified.

Surprisingly, both image analysis approaches agree with the numerical reference. This is in accordance with the benchmark on the monotonic test in 10.1.4. The zoom-in on the right side of the figure shows that the approaches are able to pick up the small changes recorded by the DEM simulation. Intuitively, this is not to be expected from the bias and error of the individual orientations that is very different for both approaches, the ITK watershed and the random walker. The anisotropy itself, however, only describes the spread of the distribution: if the orientations are evenly spread it is close to zero and if the orientations are concentrated along a single orientation it can reach a value of up to 7.5 due to its formulation. For both approaches, the orientations concentrate along the vertical direction with increasing axial loading. Thus, the anisotropy may increase in the same way. Furthermore, only a second order approximation of the fabric is used. As the bias of the ITK watershed is spread along 4 axes symmetrically, it cannot be captured in the fabric tensor and consequently not in the anisotropy. This is also in agreement with another statistical description of the fabric distribution, the mean inclination of all orientations, as discussed in 10.1.4. Another reason is the alignment of the principal stress direction with the vertical axis. The alignment of contact orientations with the principal stress can thus be captured without making a larger error by the ITK watershed as this axis is also one of the axis towards which this approach is biased.

Overall, the contact fabric due to the unloading in this simple DEM simulation is not only changing, but the changes are also measurable using the more advanced random walker segmentation. Note that the base for this benchmark is perfect by definition. These small changes might not be picked up in real experiments as there are more influences and uncertainties than only the image properties and defects that are considered here. Furthermore, the contacts between the spheres are geometrically larger than just contact points (excluding the partial volume effect), as the underlying numerical method is based on the elasticity of particles and the interpenetration of the spheres to calculate contact forces. This leads to better fits

using the PCA with more data points being supplied to the fit, which might explain the good agreement between the results from the ITK watershed and the reference for the statistic measures.

All data and scripts to re-run and reproduce this analysis and the results are available in an open access repository [Wie19]. This work initially started with a simulation of monotonic loading. The results of this analysis are given in see 10.1.3 and 10.1.4.

The main difference to tomographies of natural materials is the particle shape, as pixel size and particle size of this benchmark are set to be similar. The problem for more complex shapes is that the ground truth of contact fabric cannot be known as there are no closed solutions for the surface orientation of irregular shapes.

4.3 Metrology of particle orientations

Particle fabric is generally described in terms of the orientation of the particles. These orientations are determined from the shape of each particle. Most commonly, either the longest or the shortest extent/axis are assigned as the principal particle orientation. In this work, the particle orientations are determined based on the moment of inertia (MOI) tensor $\mathbf{M}$ which is defined by:

$$\mathbf{M} = \int_V \rho\,(\mathbf{r})\,((\mathbf{r}\cdot\mathbf{r})\,\mathbf{I} - \mathbf{r}\otimes\mathbf{r})\,dV \tag{4.1}$$

with $\mathbf{r}$ being the position with respect to the centre of mass of the particle, ρ the density at this position, V the volume of the particle and $\mathbf{I}$ the second-order identity tensor. To determine $\mathbf{M}$ of a particle, a binary sub-image of this particle is fetched from the labelled image. The centre of mass of the particle is calculated on its binary image and $\mathbf{M}$ is determined by replacing the integral by the sum over all voxels defining the particle. Note that the position $\mathbf{r}$ of every solid voxel has to be given with respect to the centre of mass of the particle.

The principal particle orientations are then defined as the eigenvectors of the MOI tensor. These can be considered as the particle fabric based on their corresponding eigenvalue. As the MOI represents the resistance to angular acceleration, the eigenvector corresponding to the smallest eigenvalue points in the direction of the longest particle axis, *i.e.*, the axis along which the resistance is smallest. Depending on the shape of the particle, the characteristic particle orientation can differ. A good example is the general ellipsoid with the principal axes $a > b > c$: the extreme situation of this ellipsoid can either be $a = b > c$ or $a > b = c$. In the first case, the smallest axis (which corresponds to the largest eigenvalue) is the most representative as the other two are identical and thus, not uniquely distinguishable from images. The longest axis would be the representative axis in the latter case. If arbitrarily shaped particles are imaged, a suitable orientation has to be chosen based on the shape characteristics.

The accuracy of this approach to determine principal particle orientations is studied in the same light as the contact orientations of natural grains. Initially, an image of an individual Hostun sand grain is acquired with the very low pixel size of 0.35 µm with the nano-focus tomograph at SiMAP in Grenoble. A very distinct shape with well defined principal axes is chosen

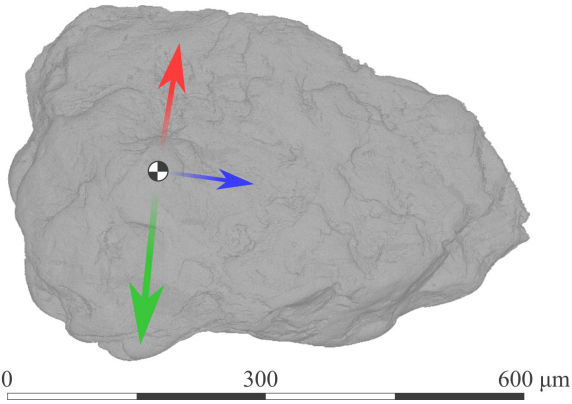

Figure 4.19: 3D rendering of an individual Hostun sand grain. The tomography is acquired at0.35 µm. The eigenvectors (EV) are plotted starting at the centre of mass: blue – third EV; red – second EV; green – first EV.

for this analysis as shown in the 3D rendering in Figure 4.19. The principal particle orientations are also indicated in the image.

To study the accuracy, a reference particle orientation, the golden standard, has to be defined as the ground truth is unknown. Similar to 4.1.2, the golden standard is determined on the image at the original pixel size. The grey-scale image is rotated around a given rotation axis by an predetermined angle. The main difference to the analysis of contact orientations is that no systematic set of orientations is studied here and both, the rotation axis and the angle are chosen randomly. After applying this rotation, the grey-scale image is scaled to various pixel sizes. At each scale, the image is binarised and the principal particle orientations are determined from the MOI tensor. In order to assess the error, the reference orientations are rotated by the same amount and in the same direction and compared to the determined orientations. The angle between both orientations is referred to as the error. This process is repeated for 4000 times to acquire a statistical measure. The implementation of this analysis and the details on scaling and rotating the images along with the results are explained in 11.1.1.

The outcome of this specific analysis is not shown here, as it applies only to the very specific shape of the imaged Hostun sand grain. To extend this analysis to more and especially different shapes, the image of the small assembly of Hostun sand grains used to study contact orientations is taken as a new basis. The golden standard can only be determined at a pixel size

of 1 µm, as the image is acquired to host more then one individual grain. This, however, does not impact the accuracy, as the mean error at this scale is found to be lower than 0.02° on the individual Hostun sand grain. The same procedure as described above is applied to every single grain that is located in the image, *i.e.*, 53 grains.

The mean error of all three eigenvectors is plotted in Figure 4.20a. The error of all three eigenvectors increases with increasing pixel size, *i.e.*, decreasing spatial resolution. The 2nd eigenvector, *i.e.*, the one corresponding to the intermediate eigenvalue, shows the lowest accuracy, because it is the least well defined in any possible configuration. Although it seems clear-cut from the plot, that the first eigenvector is the best defined orientation, this is highly dependent on the individual shape of each particle.

In order to investigate the dependence of the error on the shape of the grains, the mean error of each grain is related to the ratio of first to the third eigenvector for a given resolution. A high ratio means that the longest and the shortest axes are very different in extent whereas a small ratio would indicate very similar length of the principal orientations. The limits would be a ratio of infinity for an infinitely long line and a ratio of 1 for a sphere that has no distinct orientation. Figure 4.20b shows this relation for a pixel size of 12 µm. Although there is no unique relation, a trend can be observed: the error is lower for a higher ratio of the eigenvalues, and thus, more well-defined particle axes. This applies for all particle orientations. A more detailed analysis of these results is given in 11.2. Three very distinct particle shapes are analysed in addition to the more general relation in Figure 4.20b.

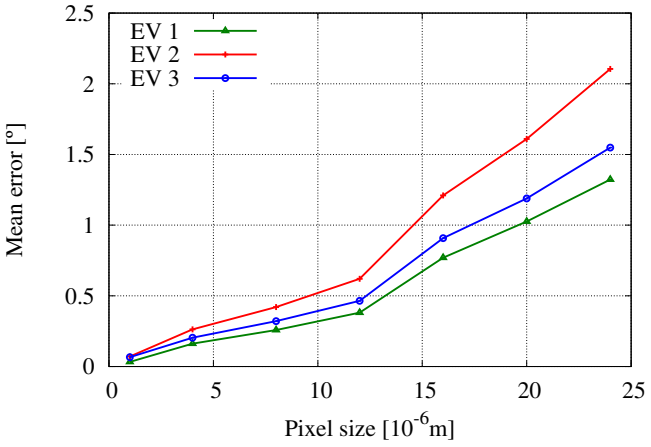

(a) Mean error of particle orientations.

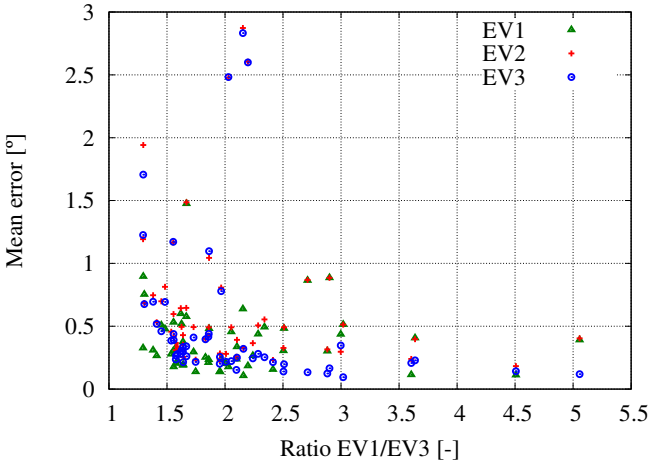

(b) Relation of the error of particle orientations and the shape of the particle.

Figure 4.20: Accuracy of determining particle orientations with the moment of inertia tensor. The analysis is carried out on Hostun sand grains. Top: Mean error versus the pixel size from the analysis on all grains. Bottom: Relation of the mean error and the ratio of the largest and smallest eigenvectors for the pixel size of 12 µm.

4.4 Summary of the metrological analysis

A thorough metrological analysis was carried out in order to determine the uncertainty of different image analysis tools. The focus lay on the determination of contact and particle orientations from x-ray tomographies as well as their statistical treatment in terms of continuum fabric variables. This analysis was carried out in different steps with increasing complexity. The most crucial steps in extracting the contact fabric were found to be the detection of contacts and the determination of their orientation.

Controlled synthetic images of individual contacts consisting of two spheres were the starting point of this analysis. It was found that using a global threshold, which is the most common method, to distinguish between the two phases of a dry granular material leads to a systematic *over-detection* of contacts. That means that if two spheres are close to each other, but not in contact, they can still be detected as such up to a specific distance. The main reason is the partial volume effect, which can lead to elevated grey-values in voxels that are shared by both particles. This is further worsened by introducing blur (and also noise) to an image. A strategy was developed and successfully validated to decrease the amount of over-detection – local thresholding – which basically applies a higher threshold locally to the sub-image of two particles that are apparently in contact.

In terms of the determination of contact orientations, two different watershed methods were assessed: a standard topological watershed [MB90], which is commonly employed in the geomechanics community, and a more advanced watershed, the random walker [Gra06]. The random walker yields substantially lower errors than the standard watershed, which is due to the probability map, which is calculated in the process, that can be used to interpolate the contact area at a sub-pixel level in contrast to the pixel-level of the standard watershed. Contrary to the detection, the results are improved by increasing the level of blur. The reason is the artificial growing of the contact (in the image) which results in more contact positions that can be used in the PCA. This is, however, specific to spheres as the contacts grow symmetrically around these round and regular surfaces.

These findings were then extended to more complex images: nano focus x-ray tomographies of manufactured (high precision) spheres and (natural) Hostun sand grains. The spheres basically validated the findings coming from the synthetic images with small changes on the accuracy of the orientations and the *optimal* local threshold. The natural sand, on the other

hand, showed different results: the *over-detection distance* is substantially lower than for spheres and does not necessarily improve upon local thresholding as some small contacts (consisting of few points) can be lost. The inaccuracies of the orientations are substantially higher than for spheres due to the more complex contact topologies, which lead to fewer positions that can be used for the PCA. Nevertheless, the random walker yielded substantially lower errors than the standard watershed.

As thousands of contacts exist in granular assemblies, the fabric is usually expressed statistically. In order to relate the uncertainties found in the study on individual contacts to common statistical measures and investigate whether they have an impact on the bigger scale, a benchmark was developed. To control this benchmark, a numerical packing of spheres was created and loaded using DEM. Snapshots of this sample during the loading were converted into synthetic, but realistic images incorporating the major image properties and defects. The shortcomings of the standard techniques, *i.e.*, systematic *over-detection* of contacts and a strong bias of orientations, are validated and the suggested improvements are found to greatly improve the results.

In order to close the last gap in this metrological study between the synthetic and high resolution images and real tomographies at reasonable spatial resolution, a specimen consisting of glass spheres was created and loaded in cyclic triaxial compression similar to the conditions of the experiments on Hostun sand in this work. Unfortunately, several problems of the image analysis were encountered, so that the preceding analysis from the benchmark could not be directly related to real tomographies, which is why this experiment was not mentioned here, but only in the technical part in section 10.2. Nevertheless, two factors were identified that mainly caused these problems. The main fraction of the spheres was imaged at a low spatial resolution that introduces a bias in the orientations when determined with watershed approaches although the particle size range was well within the sizes studied in this work. Furthermore, the local refinement of contacts tends to exclude specific orientations for a low spatial resolution which leads to strongly biased results even for a simple measurement such as branch vectors. This must be taken into account before imaging a granular material when the contact fabric is to be taken into account. The major fraction of particles should have an equivalent diameter that is resolved by more than 16 pixel.

All tools that are developed in this work are implemented in the open source

software *spam* [ACR+]. *Spam* is the acronym for Software for the Practical Analysis of Materials. The software is mostly devoted to extract information from images and especially image series of deforming materials. A general example of how to process a 3D tomographic image in order to obtain information on the fabric using *spam* is given in 9. This example can also be repeated on your personal computer[12] as all the necessary information are given in an open access archive [Wie19]. The usage of the improvements developed and suggested based on this metrological study are also shown there. The code snippets given throughout this work, are mostly using algorithms implemented in *spam*.

[12] As of October 2019 it was only installed on various Linux OS and macOS.

5 Experimental work

Before starting the experimental campaign on fabric changes upon load reversals, the image analysis tools are applied to monotonic triaxial compression tests with strong shear banding that were carried out by Edward Andò during his PhD research [And13]. Before the application to real tomographies with limited spatial resolution, the toolbox was developed purely on synthetic or ideal images and validated for these. Thus, these experiments mainly serve as a first application on experiments with presumably strong fabric changes but a pixel size similar to the one used for the experiments in this work. Using these images, the toolbox is developed further, especially in the case of bad segmentations that raise errors if not dealt with accordingly in the code or error-prone orientations. At the same time, they allow the characterisation of strain localisation from a fabric point of view.

The experimental campaign of this work comprises two tests on the compressional behaviour, *i.e.*, an isotropic and an oedometric experiment, and five on shearing, *i.e.*, triaxial compression tests. All of these include several unloading and reloading cycles at different strain or stress levels. Only the oedometric compression test is presented here, because the isotropic test showed an even smaller evolution of the fabric which is within the uncertainty of the measurements. Five triaxial compression tests on Hostun sand specimens are carried out in this work with varying initial conditions. Due to problems with the creation of the specimen and a slightly different experimental set-up, the first test is completely avoided. The remaining four are conducted at either 100 kPa (TC02, TC03) or 400 kPa (TC04, TC05) cell pressure. Each pair is prepared either by pluviation (TC02, TC05) or piling (TC03, TC04) to have a different initial density, *i.e.*, dense and medium-dense, respectively. Additionally, a triaxial compression test on lentils is conducted as part of a different research project on the effect of inherent anisotropy on the macroscopic and fabric response. It is also described in

this work in section 12.5 since it includes load reversals, but only briefly mentioned here. Only the two experiments that experience the largest differences at both the macroscopic and the grain scale are discussed in this chapter: TC02 the dense specimen at the lower cell pressure and TC 04 with a medium dense initial packing at the higher cell pressure. The others are explained and investigated in section 12.4, which also includes a comparison of all tests.

Two specific conditions apply for these experiments compared to standard laboratory tests: (1) all specimens are dry; (2) the specimens are substantially smaller. The first is chosen to facilitate distinguishing the phases in the tomographies as water has an x-ray attenuation that lies somewhere between the solid grains and air. To deal with three phases affords a trinarisation of the image (instead of a binarisation) and increases the complexity of the analysis. It also facilitates the preparation of these small samples. The latter difference (02) is due to the limited spatial resolution of tomographies and the aim to access the grain scale: the larger the specimen, the higher the pixel size which at a certain point makes an identification of individual grains impossible. Smaller specimens with a small pixel size can be resolved very accurately, but might not represent the granular assembly as a continuum any more. The specimen and the pixel size are thus chosen as a trade-off between spatial resolution and mechanical representativeness [AVHD13]. The macroscopic responses of specimens with a standard size and the small size used in this work are discussed in [And13].

5.1 Monotonic triaxial compression tests

In order to apply the developed tools on real x-ray tomographies of natural materials, two experiments are chosen from the PhD thesis of Edward Andò [And13]. These have already been thoroughly analysed regarding the kinematics using either digital image correlation [AHV12a] or a particle tracking approach [AHV$^+$12b]. The focus of these analyses was the identification of a shear band from tomographic images and to describe the characteristics of these. To study these shear bands, triaxial compression tests were carried out using the miniaturised loading system developed for the x-ray tomograph in Laboratoire 3SR, Grenoble. The experiments were conducted on two very different materials, Hostun sand (HNEA01), which is an angular silica sand, and Caicos ooids (COEA01), a calcareous round sand. Section 12.1 briefly describes these materials.

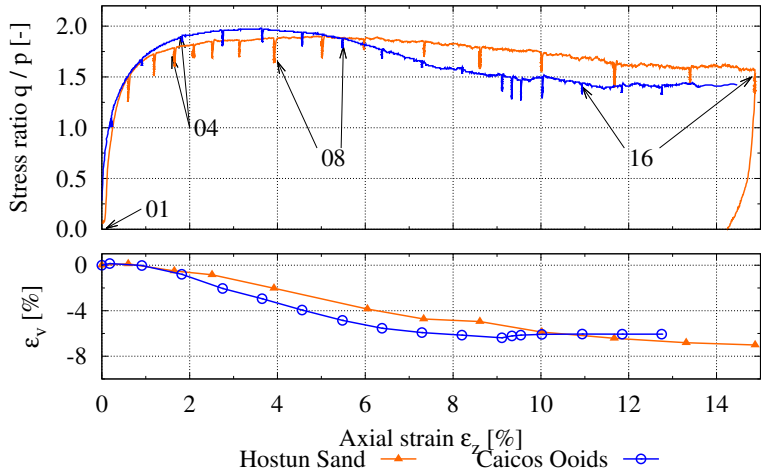

Figure 5.1: Macroscopic response of Hostun sand and Caicos ooids samples in the triaxial compression tests HNEA01, COEA01, respectively. The macroscopic states of four chosen scans are marked in the stress-strain plot.

Using these older experiments allows measurement development and validation on a well studied data set: (1) Checking and developing the image analysis tools. Until now, the tools presented consider only synthetic images of well defined quality and particle shapes. Natural materials do create situations that have to be treated differently, *e.g.*, over-segmentation of particles or judging the quality (in terms of accuracy) of a determined orientation. These adaptations are integrated in the image analysis toolbox and are described in sections 9 and 9.4. (2) Getting an idea about the fabric evolution in monotonic loading conditions regarding the forming of a shear band and its measurability. There are works on redefining the critical state by adding a condition about the fabric anisotropy [LD11, TVDP16], as explained in section 2.2. Some constitutive models are already developed that take fabric anisotropy into account [GZLD13], but so far lack detailed experimental information. Thus, this analysis is also carried out to get a first idea of the fabric evolution in experiments with strain localisation and complement numerical simulations, such as *e.g.*, in [FD11].

Both specimens were prepared by dry pluviation resulting in a dense initial state. The initial porosity of the experiment on Hostun sand, HNEA01, is 39.7 % which corresponds to a relative density of 83.2 %. For the Caicos ooids specimen, the relative density could not be calculated, because a deter-

mination of the minimum and maximum density was not carried out. With an initial porosity of 35.2 % and by observing the volumetric behaviour due to the loading, which is dilative, the initial state can be regarded as dense. The macroscopic response of the two specimens to the triaxial compression test is plotted in Figure 5.1. The cell pressure is 100 kPa in both experiments.

The images are only analysed within two chosen observation windows in space. This is done in the same light as the analysis of a subset located inside the forming shear band in [AHV12a]. The difference, and thus the change in the denomination, is that the windows are fixed in space, whereas the subset is tracked to cover the same set of grains throughout the analysis. Similar to the kinematics [AHV+12b], the major changes are expected to happen in the shear band with a rigid body like behaviour outside. Thus, the two observation windows are placed in order to account for the strong localisation identified in these tests: one is located inside the shear band, another one outside, close to the top cap of the specimen, *i.e.*, the one that does not move in this setup. Their position is chosen from the image of the last state (highest shear strain) and visualised in Figure 5.2. The subsets are cubic with a side length of 300 pixel, *i.e.*, equivalent to 4500 µm. It has to be noted that because of the chosen size, the window inside the shear band covers slightly more than just the shear band, *i.e.*, some particles that are part of the image are not inside the forming shear band.

The image analysis follows the workflow explained in section 9: the two observation windows are extracted from the original grey-scale image of the two tests. They are binarised using a global threshold taking into account the changing grey-value distributions: a global threshold is determined on the first image and then translated to the other images of the series depending on the mean value of the solid and void phases. This is described in detail in section 12.2.1. The binary image is then segmented and labelled using a topological watershed. The contacts are detected based on the labelled image. At this stage, the image processing diverges for both experiments: in the case of the Caicos ooids specimen, these globally detected contacts are refined by applying a local threshold on each contact pair. As the analysis on the high resolution images of Hostun sand has shown, the angular shaped particles suffer less from the over-detection of contacts. Furthermore, the local refinement might lead to a loss of contacts as discussed in sections 4.1.1 and 8.2.3. Thus, the contacts in the images of the Hostun sand specimen are not locally refined directly after the detection. As pro-

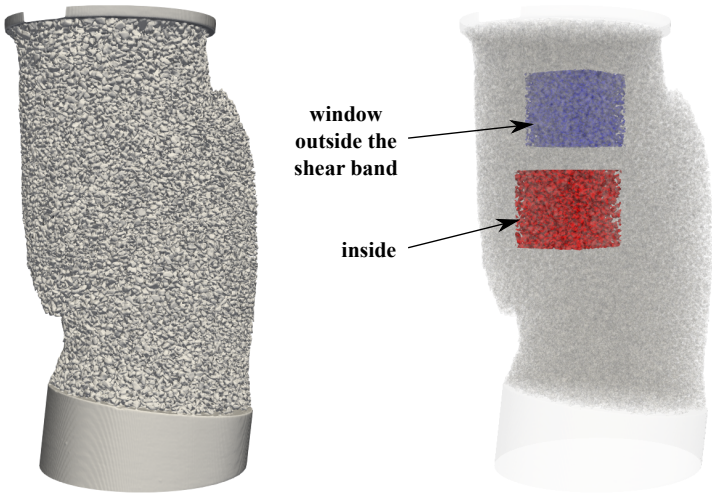

Figure 5.2: Visualisation of the observation windows in the experiment on Hostun sand. State 16 at large axial strain is imaged here to illustrate the developed shear band. The windows inside and outside the shear band are coloured red and blue, respectively.

posed in the metrological study, every contacting pair is segmented again using the random walker in order to determine its orientation.

The contact density is expressed globally using the coordination number, as defined in Equation (7.9). Its evolution for the two experiments in both observation windows is plotted in Figure 5.3. It is considered as an estimation to get a qualitative response as explained in section 12.2. The windows inside and outside the forming shear band are represented by the red and blue lines, respectively. In the case of the Caicos ooids specimen, the evolution of the coordination numbers inside and outside the shear band are qualitatively similar until $\approx 2\,\%$ axial strain. As the specimen is not perfectly homogeneous, the actual values show slight differences. This can also be observed for the Hostun sand specimen until reaching an axial strain of $1\,\%$. After these strain levels, the behaviour is qualitatively similar for both experiments. The contact density decreases further inside the shear band with ongoing macroscopic loading whereas it does stay relatively constant in the observation window outside. It even jumps back to its initial value for the Hostun sand specimen. The range of the actual values is, however, very different: it changes by 1.71 and 1.26 in the Caicos ooids and the Hostun sand sample, respectively. Note that the measured values might not

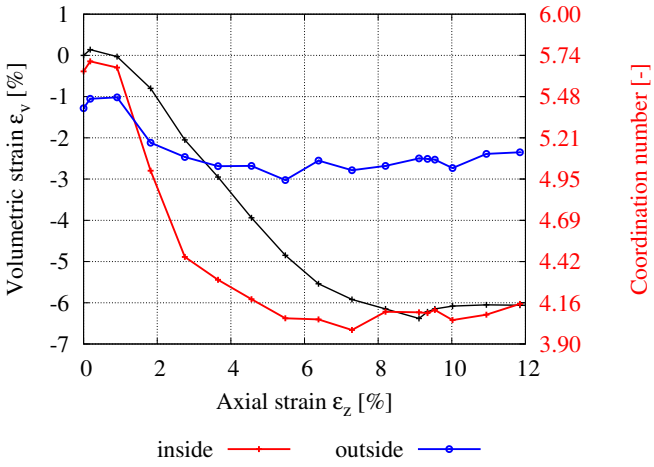

(a) Caicos Ooids (COEA01)

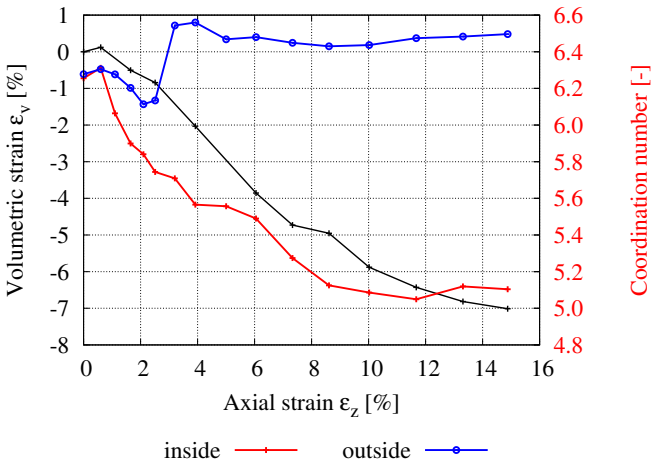

(b) Hostun sand (HNEA01)

Figure 5.3: Evolution of the coordination number in triaxial compression tests on Caicos ooids (COEA01) and Hostun sand (HNEA01) in two windows of the specimen: inside and outside of the forming shear band.

be close to the actual existing coordination number due to the approach of evaluating the windows and the systematic over-detection of contacts. The coordination number inside the shear band converges to four for the Caicos specimen and to five for the Hostun sand specimen. This indicates that the rather round Caicos ooids tend to the isostatic coordination number for rough spheres whereas the Hostun sand tends to a higher value. The higher value of Hostun sand is not due to multiple contacts that are more apparent for the more angular particles as only one contact per contacting pair is counted. It can also be guessed from both, the macroscopic response[1] and the surface characteristics[2], that Caicos ooids have a higher interparticle friction than Hostun sand. This could be the reason for the difference in the final coordination number as the isostatic coordination number was found to vary depending on the amount of friction for monodisperse sphere packings [SEG+02].

The coordination numbers are plotted on top of the volumetric strain in order to compare these measurements. The evolution of the coordination number inside the shear band agrees qualitatively to the volumetric strain. The dilation of the grains is picked up slightly earlier by the coordination number, which seems natural as the coordination number requires only very slight motion between the contacting grains whereas the void ratio requires a larger volumetric change. This difference depends on the contact stiffness and the topology: if two grains are in contact at multiple places, the contacts are less likely to be lost upon small volumetric changes. Therefore, it seems reasonable that the coordination number evolves faster for the Caicos ooids.

The contact orientations are plotted using the Lambert azimuthal equal area projections[3]. In this section, only the experiment on the Caicos ooids specimen is analysed in terms of individual orientations as well as the full fabric tensor plots as most of the discussion is similar for the experiment on Hostun sand. The analysis of the Hostun sand specimen is given in sections 12.2.2 and 12.2.3 and referred to when necessary to draw conclusions in this section.

Figure 5.4 shows the projections of the orientations for four chosen stages of the loading in the Caicos ooids specimen: (01) is the initial state, (04) and (08) are pre- and post- stress peak states and (16) is a state at large

[1] The mobilised friction angle is much higher for the Caicos ooids specimen.

[2] X-ray nano focus tomographies revealed that the ooids are highly porous on the outer layer and very compact at the centre.

[3] See section 7.2.1 for an explanation of the chosen projection and plotting.

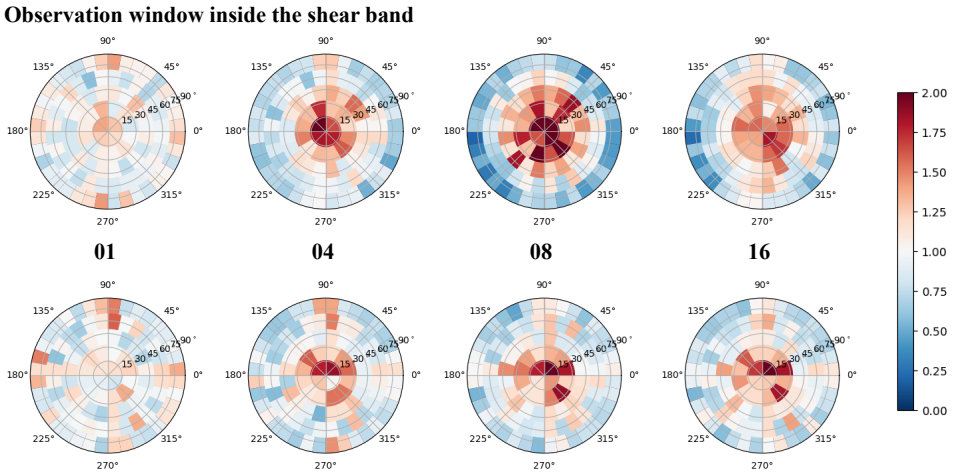

Figure 5.4: Lambert azimuthal equal area projections of the contact orientations for the triaxial compression test on Caicois ooids (COEA01) in two observation windows of the specimen: inside and outside the forming shear band. The orientations are plotted for four chosen states of the macroscopic loading. For a reference of these states see Figure 5.1. The bins are normalised by the average number of orientations per bin.

axial strain. See Figure 5.1 for a reference of the states in the macroscopic answer of the specimen. Initially, the orientations in both subsets in the experiment on Caicos ooids are distributed rather isotropically. A slight preference towards the vertical axis (*i.e.*, the center of the spherical plots) is observed. This can be explained by the preparation of the specimen: due to the vertical pluvation of the ooids, a slight majority of contacts form in the vertical direction. Up to the 4th imaged state, the orientations in both subsets show a similar tendency and align with the vertical direction, *i.e.*, the direction of the major principal stress. After this state, the orientations of the subset outside of the shear band experience almost no change. This agrees with the observation on the kinematics in [AHV+12b] that showed a rigid behaviour of the granular assembly outside of the shear band, either regarding strains or particle rotations. The orientations of the subset inside the forming shear band continue the align in the vertical direction. Orientations pointing in the planar direction are lost, which is observed from the outer ring of the projection of state 08. In the last state, in which the shear band has clearly formed, the orientations have slightly realigned from the

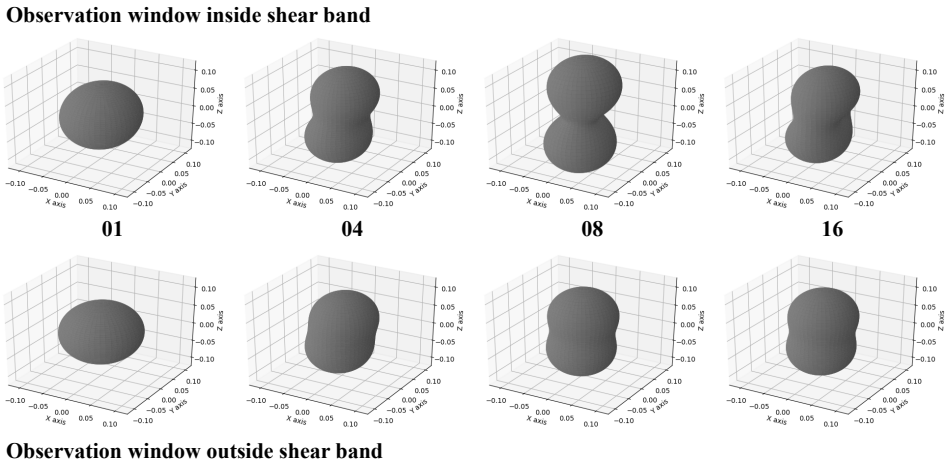

Figure 5.5: Surface plots of the fabric tensor for the triaxial compression test on Caicos ooids in two observation windows of the specimen: inside and outside the forming shear band. The tensor is plotted for four chosen states of the macroscopic loading. For a reference of these states see Figure 5.1.

preferential vertical direction to a band that follows the y-z plane, *i.e.*, a vertical line passing through the centre of the projection. This corresponds well with the shear band in the specimen, that forms in the y-z plane. The shear band is captured in the vertical slices plotted in Figure 12.1.

The statistical distribution of all contact orientations is expressed with a second order fabric tensor, as defined in Equation (1.2). The main interest of this work is to characterise the evolution of the fabric tensor. The shape of this tensor can be visualised by plotting its surface as described in section 7.2.2. It is shown in Figure 5.5 for the experiment on Caicos ooids.

As observed on the individual orientations, the initial fabric of the Caicos ooids specimen is rather isotropic in both windows. The fabric surface evolves into a peanut shape with the longest axis being directed in the vertical direction. This resembles the projections of the individual orientations, although the extent of the anisotropic distribution is more pronounced in these plots. The fabric inside the forming shear band is more anisotropic than outside the shear band in state 04, although the shear band has not yet clearly formed. The contact fabric in the window outside of the shear band is getting slightly more anisotropic with ongoing loading but stays relatively similar to state 04. The distribution inside the shear band is very

anisotropic in the post stress state (08) with the preferential and the major principal stress axis being identical. With further loading, this strong anisotropy is released and the fabric seems to align in the plane of the now strongly formed shear band. The major fabric direction is still aligned with the major principal stress direction.

The anisotropy of the fabric tensor is discussed only in terms of the scalar anisotropy factor as defined in Equation (7.8). It is plotted in Figure 5.6 – again using the same colouring conventions for the observation windows. The respective error for both particle shapes, that was estimated in section 4.1.2, is propagated through the fabric tensor to the scalar anisotropy factor as described in sections 10.3 and 12.2.3.

The anisotropy of the fabric tensor basically coincides with the observations on the surface plots and the individual orientations. The contact fabric is initially almost perfectly isotropic in both subsets of the Caicos ooids specimen, whereas it is already far more anisotropic in the Hostun sand specimen. Both subsets in both experiments evolve qualitatively rather similar until the 3rd or 4th imaged state. This coincides with the onset of the localisation as observed from the kinematics in [AHV+12b]. Both subsets then diverge with the fabric outside of the forming shear band either staying rather constant in the case of the ooids or reverting back to the initial state for the sand assembly. The fabric inside the shear band evolves differently in both specimen: the anisotropy builds up to a pronounced peak and then decreases to a constant value at high shear strain for COEA01. In the Hostun sand the anisotropy reaches its peak faster than the ooids specimen and stays at this peak for longer until decreasing at higher shear strains. This, however, coincides qualitatively with the stress strain behaviour plotted in the same figures: the Caicos ooids has a pronounced stress peak whereas the Hostun sand has a rather flat one.

The mean inclination of all orientations is also investigated as another statistical measure in section 12.2.2. The evolution and the conclusions, however, are similar to the ones drawn from the anisotropy, which is why it does not add substantial insight here. None of these measures, however, is superfluous as explained in section 12.2.3.

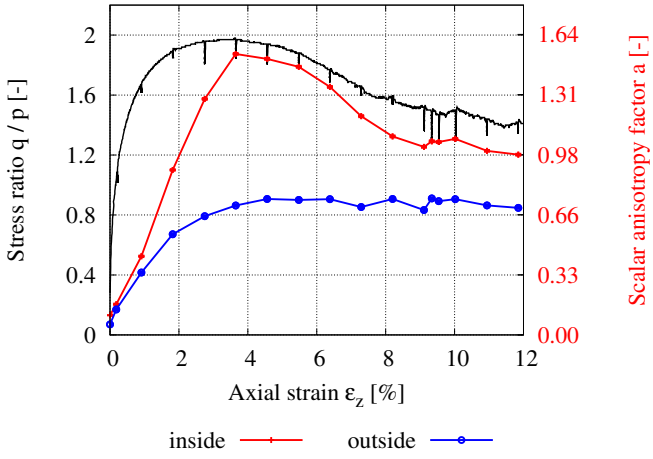

(a) Caicos Ooids (COEA01)

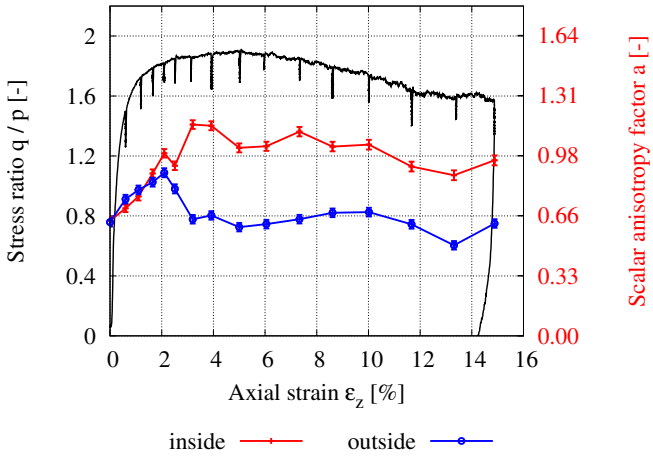

(b) Hostun sand (HNEA01)

Figure 5.6: Evolution of the scalar anisotropy factor in triaxial compression tests on Caicos ooids (COEA01) and Hostun sand (HNEA01) in two observation windows of the specimen: inside and outside of the forming shear band.

5.2 Cyclic experiments in compression

The image analysis of the already conducted experiments in the last section served two purposes: (1) the characterisation of the contact fabric evolution in experiments with strong localisation of deformation and (2) the testing and further development of the image analysis tools for the application to tomographies of irregularly shaped particles. Especially the latter made it possible to proceed to the initial main goal of this work: the analysis of fabric in experiments with load reversals.

The experimental campaign comprises one oedometric and several triaxial compression tests. All of these include unloading and reloading cycles at several stages of the loading. Only the oedometric and two chosen triaxial compression tests are presented in the following. The complete campaign is described in section 12.

5.2.1 Oedometric compression test

The first experiment that is conducted in this work is an oedometric compression test with unloading-reloading cycles. The sand grains are placed in the oedometer cell with a funnel in order to achieve a rather loose initial density. This dry preparation, however, failed and the initial density is in fact medium dense. Contrary to classic oedometer tests, the loading is displacement driven since the loading system in the tomograph of Laboratoire 3SR is employed. The maximum load is chosen to 1500 MPa in order to avoid substantial grain breakage. The macroscopic response of the specimen is plotted in Figure 5.7. The preparation, the calibration and details on the oedometer cell are explained in section 12.3.1.

The images are processed as described in section 9: they are binarised with a global threshold and segmented with the ITK watershed [BL06] as implemented in *spam* [ACR$^+$]. Contacts are then characterised on the labelled images. Similar to the previous analysis, the contacts are not locally refined as Hostun sand is rather angular and refining might cause the loss of some existing contacts. The image processing of these images is explained more detailed in section 12.3.2

The response of the contact fabric to the macroscopic loading is analysed in terms of the coordination number and a second order fabric tensor. As thoroughly studied in section 8.2.3 contacts are systematically over-detected

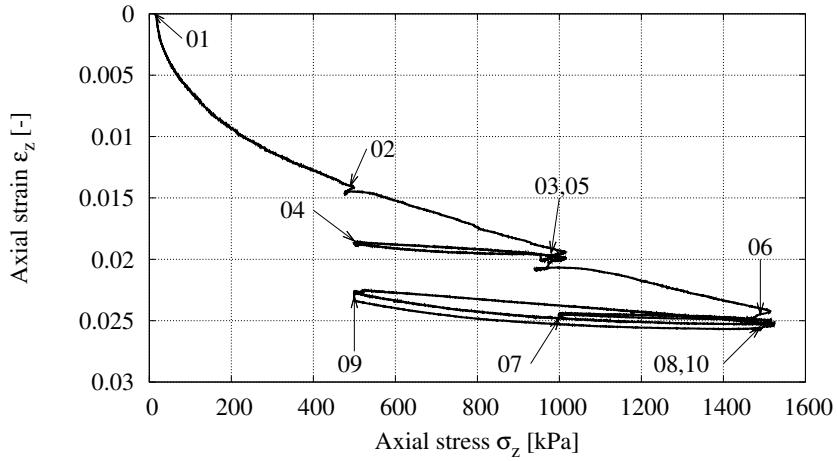

Figure 5.7: Macroscopic response of the Hostun sand specimen to oedometric loading with load reverals. The labels indicate the ID of the tomographies acquired during the experiment.

which leads to a higher apparent coordination number than truly present in the specimen. The apparent coordination number might, however, be slightly lowered as contacts between the wall of the cell and the specimen cannot be detected from the image. Figure 5.8 shows the evolution of the coordination number plotted on top of the axial strain. Note that the axial strain corresponds to the volumetric strain and might, thus, be related to the coordination number in these test conditions. Although the determination of the actual coordination number is error-prone, its evolution corresponds almost perfectly to the volumetric strain and thus, also the void ratio. Both vertical axes in the plot are chosen to capture the same range from the lowest to the highest value. In this way it can be observed, that the coordination number is reacting stronger in the initial compression until the end of the first cycle and slows down to the same rate afterwards.

The distribution of contact orientations is statistically described again using a second order fabric tensor as defined in Equation (1.2). Only orientations that are sufficiently accurate are used to determine the fabric tensor based on criteria that are detailed in sections 12.3.2 and 9.3. The anisotropy of this distribution is then calculated from the deviator of the fabric tensors, as defined in Equations (7.7) and (7.8). Its evolution is plotted in Figure 5.9 with error bars, again on top of the macroscopic response of the specimen.

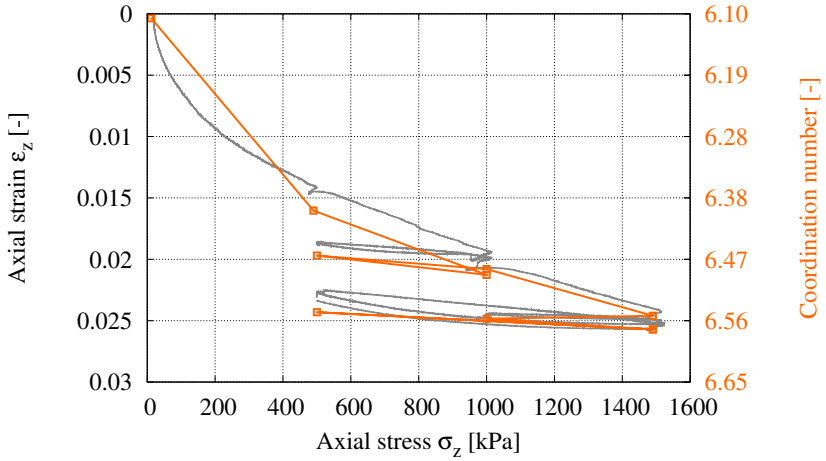

Figure 5.8: Evolution of the coordination number in the oedometric compression test.

Note that the anisotropy has a reverted range similar to the axial strain, *i.e.*, increasing from top to bottom. The error bars that are included for every state are determined by propagating the mean error of contact orientations in Hostun sand determined in 4.1.2 for the pixel size of 10 µm[4].

The anisotropy increases during the first loading increment. Surprisingly it decreases slightly upon further loading, which is not to be expected as the deviatoric load increases. This increase is well within the error bar, which means that the change is too small to be accurately tracked by our image analysis tools. It could as well stay constant or increase slightly upon further loading. The anisotropy stays constant during the first unloading and increases drastically upon reloading, in the range of values that is observed here. A similar behaviour is observed for the second cycle. The anisotropy decreases strongly during last unloading, which is in contrast to the first two cycles where the it stays constant. The main point to highlight here is the high uncertainty as simply observable from the plot. This renders the results quantitatively inconclusive and only partly qualitatively useful.

But why is that? Is the range of deformation too low in order to achieve a

[4]The error propagation from the individual orientations to the fabric tensor and finally the anisotropy is described in section 10.3. The individual error is determined in the metrological study on Hostun sand grains and plotted in Figure 8.14b.

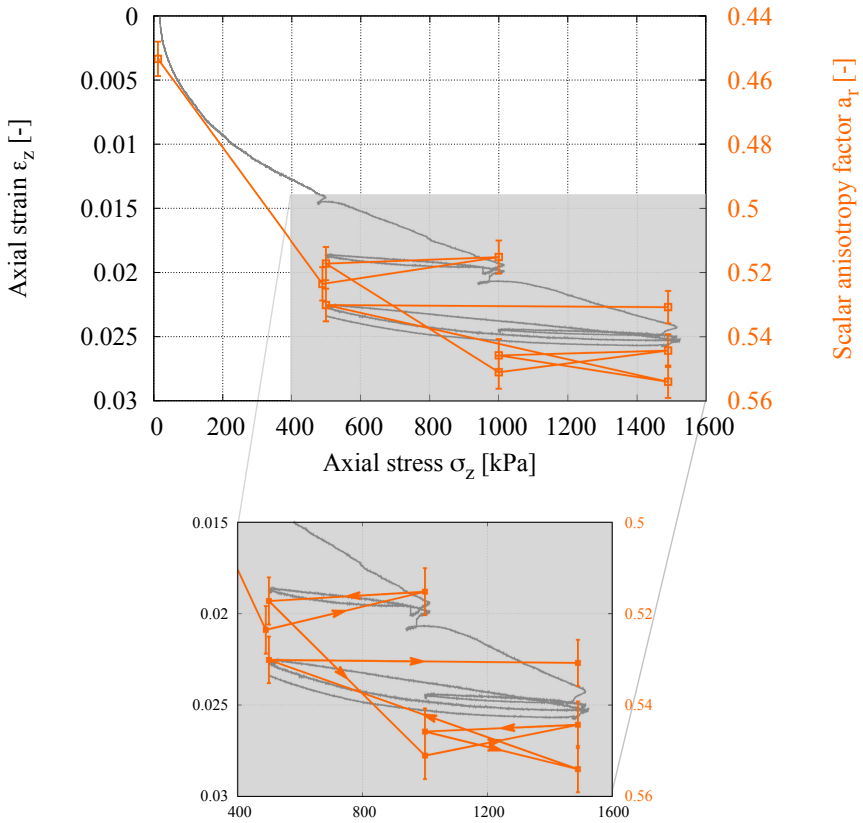

Figure 5.9: Evolution of the scalar anisotropy factor in the oedometric compression test HNMWOD01.

measurable change in fabric? Or is this a problem that stems purely from the image analysis and the change of contact fabric should be higher?

Two different paths are investigated further in order to clarify these questions: (1) a smaller observation window located close to the moving load platen is analysed similarly to the previous analysis; (2) a simplified DEM simulation of an oedometric compression test is conducted in order to assess the magnitude of fabric changes;

(1) The analysis on the observation window showed that the fabric is evolving stronger in specific zones of the specimen. Following this experience, an observation window close to the moving platen is chosen, expecting more fabric changes in this area of the specimen compared to the overall fabric. The latter should be smeared by areas close to the non-moving boundaries

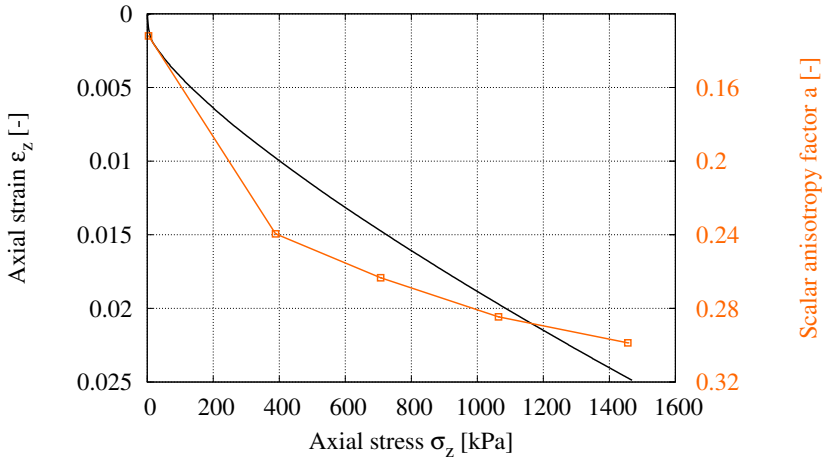

Figure 5.10: DEM simulation of an oedometric compression test. The evolution of the contact fabric anisotropy is plotted on top of the macroscopic response of the specimen.

where the fabric is not expected to evolve significantly. This, however, did not show a more pronounced evolution. The procedure and the results of this analysis are explained in section 12.3.3.

(2) To investigate the range of change of contact fabric further, a simple DEM simulation of an oedometric compression test is carried out. The simulation is basically similar to one used for the benchmarking of the image analysis tools in section 4.2. The main difference, however, is that the loading is applied differently to the specimen by keeping the lateral boundaries at constant position and compress the vertical extent of the specimen at constant velocity. The simulation itself along with the parameters and the creation of the initial state is described in section 12.3.4. In contrast to the real experiment, no unloading is simulated as a DEM simulation of this simplicity is not capable of realistically predicting the behaviour in oedometric compression upon unloading. This is either bypassed by using different parameters for loading and unloading in the simulations [SV09], which is, however, a completely non-physical approach or by using more complex and realistic models. These for example incorporate particle breakage and successfully model loading and unloading in oedometric compression [RB01].

The evolution of the contact fabric anisotropy is plotted on top the macroscopic response in Figure 5.10 for the DEM simulation. The anisotropy con-

tinually increases throughout the loading as the contact orientations align further with the principal stress direction. This is qualitatively similar to the evolution of the loading parts in the experiment. The range of change of the anisotropy is $\Delta a = 0.17$ in the simulation and thus, in the same order as the change in the experiment $\Delta a = 0.1$. A stronger evolution is expected in these simulations as the particles are spheres which tend to rearrange easier and the boundaries are periodic. The at least partial responsibility of particle shape to the more pronounced change of anisotropy is also validated by the monotonic experiments on the rather round Caicos ooids and the angular Hostun sand in section 5.1. Thus, the overall fabric changes measured in the experiment seem reasonable and the problem truly is that accuracy of the employed image analysis tools is not sufficient to capture such small changes.

5.2.2 Triaxial compression tests

Five triaxial compression tests are conducted in the x-ray scanner in Laboratoire 3SR, Grenoble. The well documented loading system that is designed for running such experiments in the tomography chamber is used for these tests [Len06, And13]. All specimens consist of dry Hostun sand. In order to study the effects of density and overall stress state, *i.e.*, pycnotropy and barotropy, the initial state is systematically varied. Two experiments are run at a cell pressure of 100 kPa and two at 400 kPa. The specimen are prepared differently, either by pluviation from a specified drop height to achieve a dense initial state or by what is called piling here. In the latter method, sand grains are put into a funnel that already rests on the bottom plate of the cell and the funnel is slowly pulled upwards. The initial goal was to achieve a loose initial packing, but as the sand was only processed in a dry state, that did not succeed. The specimens prepared by piling have, however, a slightly looser initial packing (*i.e.*, medium-dense) than the ones prepared by pluviation. The set-up of the experiments along with the initial states of all specimens is detailed in section 12.4.1. An image of the set-up is given in Figure 3.2. Similar to the tomographies of the monotonic experiments in section 5.1, the distribution of grey-levels shifts within most of the image series apart from the experiment TC02. This is considered in the same way as described in 12.2.1 by calibrating the thresholds for binarisation and contact detection accordingly. Only two experiments are discussed in this part. The data and the microscopical analysis of the other experiments along with a comparison of all in terms of their initial state is given in section 12.4.

The experiments presented here are the pluviated specimen tested at 100 kPa (TC02) and the specimen prepared by piling and tested at 400 kPa cell pressure (TC04). Figure 5.11 shows the macroscopic response of the specimens. The volumetric behaviour of the specimens cannot be directly measured because the sand is tested in dry conditions. It is obtained from the processed images by a combination of dilation and erosion operations on the binary images. This operation along with a calibration is explained in section 9.6. Specimen TC02 has an initial relative density of 83 % which is consistent with the observed volumetric behaviour. It is dilating throughout the shearing after staying constant in the first load increment. Specimen TC04 on the other hand is slightly contracting overall as it starts from an initial relative density of 64 %. The stress ratio does confirm the effect of the initial state: it is higher for the denser test at lower overall stress (TC02) through-

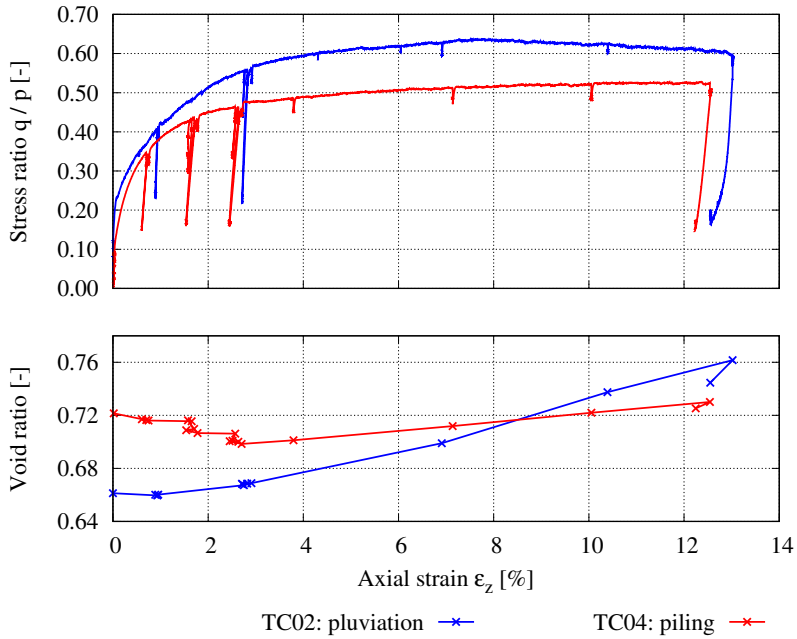

Figure 5.11: Macroscopic response of two triaxial compression tests. The experiment TC02 is conducted at 100 kPa cell pressure and is pluviated to achieve a dense initial state. Specimen TC04 is prepared by piling to achieve a looser initial packing and tested at 400 kPa cell pressure.

out the loading. It slightly builds up to a peak and decreases again at around 8 % axial strain for the dense specimen (TC02) whereas it increases monotonically for the medium-dense specimen (TC04).

At different strain levels, the specimens undergo an unloading-reloading cycle. It is not unloaded to an isotropic stress state in order not to risk a contact loss between the loading plate and the specimen. Furthermore, the residual axial stress after unloading is considered to account for friction between the loading ram and the triaxial compression cell because the force is measured outside of the cell. Volumetrically, specimen TC02 does not react to the load cycles. It appears locked and only resumes to change after the reloading. This is different for the looser specimen 04. Its volume undergoes a small compaction, especially during the reloading in cycles 2 and 3 and the unloading in cycle 4. The volume dilates after the last cycle and before compacting at the final unloading step.

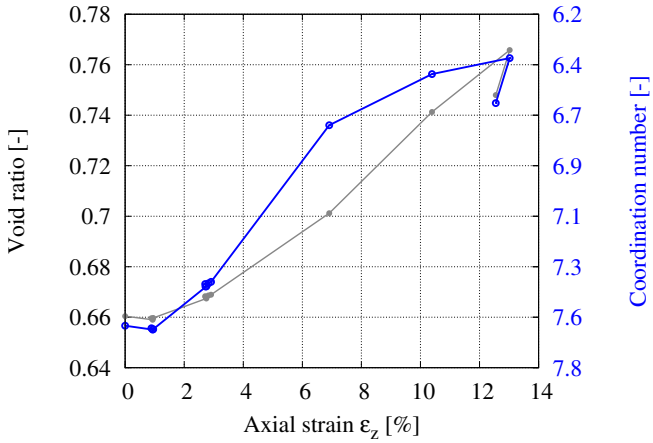

(a) TC02

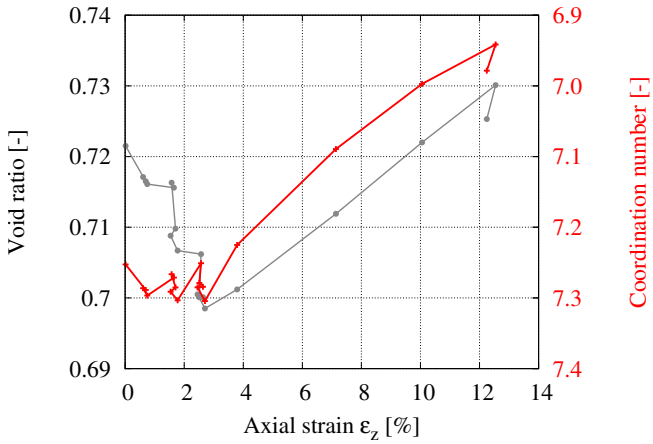

(b) TC04

Figure 5.12: Evolution of the coordination number in the triaxial compression tests TC02 and TC04.

The first measure of the contact fabric is again the coordination number. It is plotted in Figures 5.12a and 5.12b for specimens TC02 and TC04, respectively. The void ratio is provided in these plots with the grey lines as both measures are bulk measures describing the density of the assembly. Consistently to the macroscopic behaviour, the contact density of specimen 02 decreases continuously throughout the loading. It picks up the dilation at a faster rate than the void ratio and is already at decreasing rate at the end of the loading when the void ratio is still increasing. This is very consistent with the observations on the monotonic loading tests in section 5.1. The most interesting part for this analysis, however, is that the contact density does not change during the load cycles. It stays locked upon unloading and reloading. Only at the final unloading it increases measurably.

The coordination number of the specimen TC04 reacts rather differently and does not follow a similar trend to the void ratio. It must be noted that although both measures are computed from the images, the way of determining them is completely different. Initially the coordination number stays rather constant while reacting to the load cycles whereas the void ratio decreases throughout the cycles. Note the smaller scale of the plot compared to the experiment on specimen TC02. The coordination number decreases substantially in the monotonic loading after the load reversals until the final unloading where it increases again.

The distribution of the contact orientation is measured using the scalar anisotropy factor and plotted in Figure 5.13, as the other possibilities have already been shown on the monotonic experiments in section 5.1. The anisotropy of specimen TC02 increases almost monotonically until the final unloading. There is, however, a small peak 10.5 % axial strain. Similar to the contact density, the anisotropy does not change measurably during the load cycles. That means that in these conditions, the contacts not only stay locked in terms of the density, but they also do not change their distribution of orientations significantly. This is an important finding, as DEM simulations on granular materials suggest small to medium changes in the contact fabric [AMH04, OC09, JZL19].

The anisotropy of specimen TC04 increases mostly monotonically. The stronger reaction of the coordination number is also reflected in the anisotropy. It reacts almost similarly to every load cycle by decreasing during unloading and increasing or at least staying constant during reloading. This reaction is stronger than for specimen TC02, which reacts also by staying on the same path for loading and unloading. Overall, it is consistent with the

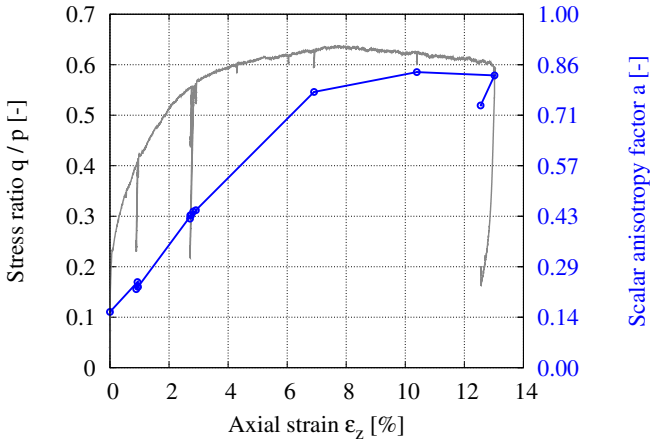

(a) Scalar anisotropy factor in TC02.

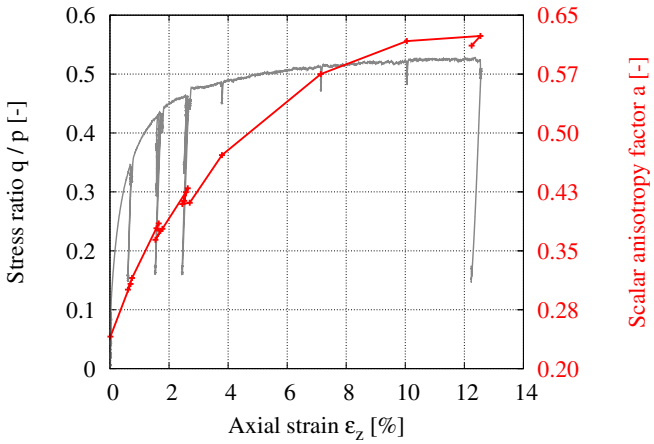

(b) Scalar anisotropy factor in TC04.

Figure 5.13: Evolution of the contact fabric anisotropy in the triaxial compression tests TC02 and TC04.

observations from the monotonic experiments as it increases at a faster rate in the beginning and slows down well after the stress rate increase slowed.

When comparing all experiments, two preliminary conclusions on the overall evolution of the contact fabric can be drawn: (1) the initial density plays the major role in determining the range of the change in contact density and anisotropy. For the dense specimen (TC02 and TC05) the range is substantially larger than for the medium dense specimen (03 and 04). (2) the overall stress state seems to play, if at all, a minor or even an insignificant role. The dense specimens at different initial stress states (TC02 at 100 kPa and TC05 at 400 kPa) experience a very similar change in coordination number whereas the anisotropy changes even more for the experiment at higher cell pressure (TC05). This is not the case for the looser specimen at different cell pressures: here, the contact fabric of the specimen at lower average stress (TC03) changes more than the one at higher average stress (TC04). That seems more consistent with the macroscopic behaviour of specimen at different stress levels where more changes are expected at lesser confinement, *i.e.*, barotropy. These observations are detailed and visualised in sections 12.4.6 and 12.4.7. They, however, obviously suffer from being based on one experiment per specific initial state, which is why they should not be generalised.

In the analysis on the monotonic experiments in section 5.1, the main changes of the contact fabric are observed to happen inside the shear band. Therefore expecting that more changes during the load-unload cycles appear in such smaller zones, one observation window is placed in the image series of each specimen of the cyclic triaxial compression tests. It is chosen at the last imaged state in order to locate it in the zone with the most apparent localisation happening. The results are displayed in Figure 5.14 for the observation windows as well as the complete specimen. In difference to the processing of the observation windows in the monotonic experiments, the fabric of the window is extracted from the already determined fabric of the complete sample. This allows to take contacts to the outside of the observation window into account, which inherently leads to higher coordination numbers than plotted in Figures 5.12a and 5.12b for the complete sample[5]. Contacts to the outside, *i.e.*, the membrane, could not be taken into account for the complete specimen.

The coordination number inside the shear band does qualitatively evolve in

[5]The slightly different processing of the observation window is described in detail in section 12.4.7.

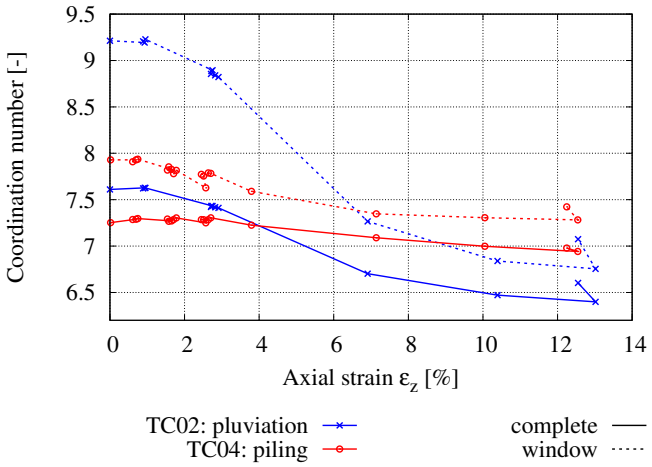

(a) Coordination number in TC02 and TC04.

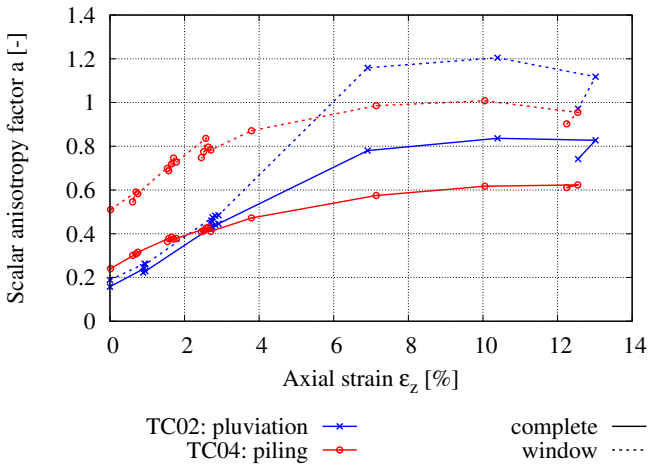

(b) Scalar anisotropy factor in TC02 and TC04.

Figure 5.14: Evolution of the contact fabric in the triaxial compression test TC02 (blue) and TC04 (red). The results are displayed for the complete specimen (solid lines) and an observation window (dotted lines) that is placed in the zone of localisation.

the same way as for the complete specimen with the major difference being its total change. As expected, the change in the observation window is higher as most changes happen in the zone of localisation. The same cannot be observed for the medium-dense specimen (TC04) where the coordination number evolves basically in the same way by the same amount. The actual value is only slightly increased, but that stems from the different ways of obtaining the coordination number. A clear localisation cannot be detected visually from the image series of that specimen. It is thus, not surprising that both, the fabric inside the observation window and in the complete specimen evolve similarly. In terms of the contact density, the fabric does not react stronger to the load cycles inside the observation window than in the complete specimen in both tests.

As expected from the analysis in section 5.1 the anisotropy for specimen TC02 is building up similarly in the observation window and the complete specimen at lower axial strains. After 2.6 % axial strain the anisotropy in the observation window increases at a higher rate and to a higher peak state than overall. This happens due to the localisation of deformation in the specimen. As all the cycles are carried out before or exactly when the localisation initiates, the reaction to the cycles is almost similar in the observation window. The anisotropy only slightly decreases upon unloading and increases at reloading in the second and third cycle. These observations, however, do not apply to specimen TC04: the initial anisotropy is substantially higher inside the observation window which means that in terms of the contact fabric the preparation caused a very inhomogeneous initial state in contrast to specimen TC02. The overall evolution of the fabric is very similar to the complete specimen, just offset by a higher base anisotropy. A similar, but much stronger, reaction to the cycles can be observed inside the observation window. The anisotropy decreases for every unloading and increases or stays constant at every reloading step. The full analysis on all experiments is given in section 12.4.7.

So far, the fabric is only analysed in terms of contacts, but particles might also play an important role, as highlighted in [Oda72b]. In order to determine a particle fabric tensor, one particular orientation has to be chosen. Particle orientations in this work are calculated based on the moment of inertia tensor and its eigenvectors as explained in section 4.3. The characteristic particle axis depend on the overall shape of each particle. For the shapes investigated in the analysis on the metrology, either the eigenvectors corresponding to the maximum or the minimum eigenvalue are the most

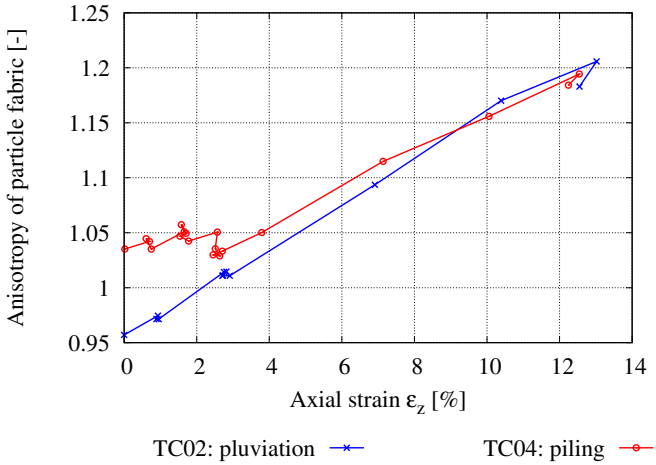

Figure 5.15: Evolution of the anisotropy of the particle fabric in the triaxial compression test TC02 (blue) and TC04 (red). The particle fabric is calculated on the eigenvector corresponding to the minimum eigenvector.

characteristic for the studied Hostun sand grains. Here, the particle fabric is defined on the eigenvector of the minimum eigenvalue, *i.e.*, the longest axis of the grain. All orientations are described using the same formulation of the fabric tensor as for contacts and defined in Equation (1.2).

It is again analysed in terms of its anisotropy which is plotted in Figure 5.15 for the specimen TC02 and TC04. The anisotropy of the particle fabric increases steadily and almost linearly for the complete experiment. Similar to the contact fabric, it does not react to the load cycles. The medium-dense specimen TC04 oscillates around its initial value in the beginning of the experiment before increasing similarly to specimen TC02. The particle fabric anisotropy does not seem to add any value to the microscopic analysis as it does only increase linearly during the complete loading. This also applies to the other experiments carried out in this work. All of them, disregarding specimen 01, appear to have a similar, linear increase in anisotropy upon shear.

This is in contrast to assemblies of more distinct shape, such as lentils. One experiment on lentils with a specific initial anisotropy is carried out within this thesis and described in section 12.5. For this experiment, the particle fabric did show a distinct evolution and followed the evolution of the contact fabric. Both appear to be linked as already postulated from

DEM simulations, such as the ones in [FD11]. The fabric does seem to be locked upon un- and reloading, which might be further enforced by the strong initial anisotropy.

5.3 Summary of the experimental work

The first experiments analysed in this work were monotonic triaxial compression tests on two different materials with strong strain localisation. To study this localisation from a fabric point of view, the fabric was evaluated in two different observation windows: one inside and one outside the developing shear band. It is generally evaluated in terms of the coordination number and the contact fabric anisotropy. Up to a certain point, well before the peak stress, the contact fabric evolves similarly in both windows. It then diverges with the major changes occurring inside the shear band and almost no changes outside the band. The contact fabric anisotropy evolves similarly, but with a delay compared to the stress ratio, building up to a peak and then decreasing to an apparent steady state.

These findings are generally in accordance to previous experimental work and numerical simulations. Fonseca et al. [FOCL13] made similar observations for the fabric evolution inside and outside shear bands. Contrary to the *in situ* measurements in this work, they carried out a post-mortem study. To characterise the evolution of the fabric from post-mortem specimens, multiple specimens were prepared and sheared to different strain levels at which they were imaged. It can only be assumed that the specimen started from a similar initial fabric as it is impossible to verify using this technique. Note that in this work, the initial fabric of the specimens differed although they were prepared using the same protocol, see section 12.4.5. Fonseca et al. [FOCL13] observed an initial decrease of the contact fabric anisotropy, which was neither apparent in any of the experiments in this study nor in numerical simulations. This observation can be caused either by the nature of the post-mortem analysis as different initial anisotropies could have been present or by the uncertainty of the image analysis. Another finding that is contrary to this work was a decrease of the particle fabric anisotropy with ongoing shear. The particle fabric in this work does only increase slightly and linearly with ongoing shear. This difference can only be explained by the post-mortem analysis, as the accuracy of particle orientations is rather high compared to the range of its evolution.

The evolution for the monotonic parts of the loading are also in accordance to the work of Imseeh et al. [IDA18] which included materials of different shape. For some experiments, an increase of the anisotropy is found in the softening regime, *i.e.*, for a decrease of the deviatoric stress after reaching a peak. This is not found for any of the experiments carried out in this

work. Only a decrease of the fabric anisotropy for softening is observed here. The conclusions on the effect of the particle shape, however, do not agree with the findings in this work. A more isotropic initial state and a larger range of change of the fabric were observed for a higher angularity of the particles in [IDA18]. On the contrary, exactly the opposite is found in this work comparing Hostun sand and Caicos ooids in section 5.1. It must be noted, that this could also be attributed to the high friction apparent in Caicos oods.

Zhao and Guo [ZG15] investigated the fabric evolution inside and outside of evolving shear bands using a coupled FEM-DEM approach. The constitutive model is replaced by a discrete element model in such approaches and allows accessing the particle scale. They observed a stronger contact fabric evolution inside the shear band and a rather insignificant particle fabric evolution. These findings are in very good accordance with the experimental results in section 5.1.

A similar, but less pronounced evolution of the contact fabric anisotropy is observed for the monotonic loading in the cyclic triaxial compression tests. It is less pronounced because the complete specimens are analysed. The contact fabric of the dense specimens prepared by pluviation changes stronger than for the medium-dense specimens prepared by piling. This is also confirmed by the contact density: the higher the initial coordination number, the stronger the change of the contact fabric upon shear. An influence of the cell pressure is not clearly evident as the fabric of the dense specimen at high pressure changes most strongly although the dense specimen at low pressure was expected to.

Upon reversing the loading, the fabric did not change significantly. Both, the coordination number as well as the anisotropy, change only very slightly, but generally agree in the direction of the change with the numerical simulations. Such simulations resulted in substantial changes of the fabric upon load reversal as evident from [OC09, JZL19] and also from the benchmark test in section 4.2. These were, however, conducted on assemblies of spherical particles. With the initial goal of concluding the metrological study, a triaxial compression test with load reversals was carried out on an assembly of glass beads. Other than the material, there is practically no difference in the conditions of the experiment compared to the ones on Hostun sand presented here. Contrary to the numerical simulations, the contact fabric changed only slightly during the load cycles as visible in Figure 10.12b. This response is very similar to the Hostun sand specimen which means

that the different microscopic behaviour between the experiments and the simulations is not caused by the shape of the particles. Either the image analysis tools cannot measure what the simulations correctly predict or the simulations over-predict the response upon load reversal. The benchmark study in section 4.2 showed, that at least in the case of spheres the employed tools are able to capture this evolution correctly, even if a strong change of fabric is predicted by the simulations. Thus, the latter appears to be responsible for this discrepancy.

In addition to the triaxial compression tests, an oedometric as well as an isotropic compression test were conducted on Hostun sand specimen. Both are carried out in range of stresses where substantial particle breakage should not occur, according to the experimental study of Hostun sand in [CD86]. Due to these low stresses, the specimen did not deform strongly which is also manifested in the fabric evolution. The changes of the orientational contact fabric are too small for a quantitative determination. This is especially apparent for the load cycles where the uncertainty of the anisotropy is larger than its change. A general evolution can, however, still be qualitatively guessed: it increases upon loading and decreases upon unloading. The coordination number changes more substantially and seems to be directly related to the volumetric strain (or the void ratio). The isotropic test is not described in this work, but it showed a comparable micromechanical behaviour. The coordination number does show a similar evolution to the volumetric strain, but the fabric anisotropy evolves even lesser than for the oedometric test. It can be estimated that the fabric anisotropy does not evolve at all for this initial isotropic fabric in isotropic test conditions.

6 Final thoughts

This thesis aims at improving the understanding of the behaviour of granular materials upon load reversals. Macroscopically, different phenomena occur during load reversals and if repeated often, cyclic loading, *e.g.*, an abrupt change of stiffness or the accumulation of permanent deformation. The underlying causes for such macroscopic behaviour are often sought at the particle scale. In this specific case, there have been several attempts to explore the micro-mechanics using numerical simulations, but a satisfactory explanation with physical evidence is still missing.

Therefore, several experiments with load reversals at chosen stages of the loading have been conducted on either glass beads or natural Hostun sand. These tests have been carried out in an x-ray μCT chamber to acquire tomographies of the specimen throughout the loading process. The only part of the fabric that can be currently accessed from such images is the geometrical structure of the specimen, *i.e.*, the particles, the inter-particle contacts and the void space. Throughout the body of published research on the determination of fabric from tomographies, one crucial part was still missing: a metrological characterisation of the approaches to access this information, *i.e.*, the image analysis tools. To repeat a simple analogy from the introduction: An experimentalist would never run a test using sensors that are not calibrated or in the worst case that never have been calibrated. It is of utmost importance to understand the uncertainties of these measurements in order to classify the results and eventually build models based on them. This seemed especially true for the experiments with load reversals, as there might be rather small changes to the geometrical fabric of the specimen during them. In order to remedy this lack, a thorough metrological analysis of certain image analysis tools was carried out in this work before running and analysing the experiments.

6.1 Image analysis

The focus of the metrological study was the determination of inter-particle contact orientations. The most crucial steps turned out to be the detection of contacts and the measurement of their orientation. To study both, the problem was initially simplified to synthetic images of spheres. Already the least complex images showed that contacts are systematically over-detected using the most common, standard approaches. That means that particles that are very close to each other, but not in contact, appear as such, which necessarily leads to high coordination numbers, *i.e.*, one of the key parameters of the contact fabric describing the contact density. This systematic error introduces orientations of contacts, that do not exist, into the spatial distribution. A local refinement of the detected contacts was proposed and shown to substantially reduce the amount of over-detection.

Once the contacts are detected satisfactorily, the orientations have to be determined. Two different watershed approaches were assessed in this work: a basic, topological watershed and the random walker, a more advanced power watershed. The latter yields orientations that are considerably more accurate than the basic watershed. Furthermore, the error of the topological watershed is not purely random, but introduces a strong bias towards specific axes. Thus, the random walker watershed is recommended and is employed for the image analysis of the experiments in this work.

These findings on the detection and orientation of contacts were reviewed and validated by subsequently increasing the complexity of the images of individual contacts. On the one hand, blur and noise were applied to the synthetic images of spheres up to a realistic level of image defects, which changed only the actual values of the uncertainties, but not the observations themselves. On the other hand, real tomographies of spheres and Hostun sand grains were acquired at a very small pixel size. These tomographies allowed the detection and orientations to be studied starting from this high spatial resolution by downgrading it to a realistic level. The irregularly shaped Hostun sand grains are not as susceptible to an over-detection of contacts which might lead to a loss of contacts if the strategy proposed here is employed to locally refine the contacts. Furthermore, the uncertainty of determining orientations is higher for such angular contact topologies, as various scale effects come into play.

The next step for increasing the complexity of the problem was to increase the number of particles and consider assemblies. So far, the main problem,

due to which no thorough metrological study has been carried out so far, was the non-existence of a ground truth in tomographies as cited in the introduction. This was solved by creating a synthetic image that resembles a tomography of an assembly of particles incorporating the most important image properties and defects. To consider a mechanically meaningful packing, a numerical sample was created and loaded using the discrete element method which serves as the ground truth since the complete information of the sample is perfectly known. Applying the standard techniques for either the detection or the orientations of contacts resulted in substantial errors, *e.g.*, a 50 % error on the coordination number. Both proposed improvements, however, were able to minimise the error and produce satisfying results. All the data of this benchmark along with the codes necessary for the image creation and analysis were published as a benchmark in an open access archive [Wie19]. This should enable others working on similar problems to test their approaches or to simply repeat this analysis.

6.2 Experimental insight

Two different sets of experiments are investigated in this work: monotonic triaxial compression tests on two different sands with strong shear banding and experiments with load reversals on a sand and a packing of glass beads. The first were already conducted and analysed regarding their kinematics in [AHV12a, AHV+12b] and should initially serve to test and adapt the image analysis tools. Additionally, they offered the possibility to track the contact fabric inside and outside of a developing shear band. It must be noted, that such a localisation analysis has been already performed in the past [FOCL13], but only on post-mortem specimens and without drawing reliable and conclusive results. However, in this work, tomographies are acquired *in situ*, *i.e.*, using the same specimen and imaging different states of the loading. The fabric did evolve very clearly in these experiments with the two regions experiencing a distinct difference after the onset of localisation. The contacts inside the evolving shear band aligned geometrically with the direction of the shear band and also with the major principal stress, *i.e.*, a coaxiality with the stress in shear. The anisotropy of the contact fabric was found to be a valuable scalar descriptor capturing both its evolution and alignment. It generally follows the stress ratio with a delay that is dependent on the initial state and the particle characteristics, *i.e.*, shape, roughness and composition. That includes the mobilisation as well as the

shape of the stress response: if a stress peak exists and is well pronounced, there is also a clear peak in the evolution of the anisotropy. It seems that the more isotropic the initial state, the more shear is needed to mobilise the anisotropy, as the particles and contacts first need to rearrange to carry the loading. The cause of this evolution cannot be attributed to a specific characteristic since the chosen spatial resolution does not allow a distinction of shape and roughness, and the number of experiments is too small (in terms of the influence of the initial state).

A substantial disagreement between numerical simulations and experimental tests was observed regarding the response of the contact fabric to load reversals. The simulations conducted in this work, which were strongly simplified, as well as more sophisticated ones in the literature [OC09, JZL19] showed a contact fabric that follows the stress ratio almost perfectly regarding the rate of change and the amount. It must be noted though that the anisotropy does not return to its initial value for an unloading from shearing to an isotropic stress state, which leaves the specimen with a residual amount of anisotropy. Experimentally, only slight changes of the contact fabric upon unloading and reloading were observed. The fabric almost seems locked upon unloading. The small changes, however, mostly evolve in the same direction as numerically observed and as expected from the monotonic experiments, where the stress was related to the anisotropy: a decrease of the anisotropy follows a decrease in deviatoric stress and vice-versa for the reloading. This happens for both: specimens with a strong inherent anisotropy (the experiment on lentils) as well as initially almost isotropic specimens.

One possible reason, and maybe the most plausible one, might be the particle shape, that is spherical in the simulation and thus, vastly different from the irregular Hostun sand as well as the lentils. Following that line of reasoning, as well as some metrological investigations, an experiment on glass beads was conducted to explore the impact of the particle shape. Unfortunately, some image analysis problems occurred that are mostly caused by the low spatial resolution of the smallest particles in the specimen. The evolution of the contact fabric could, fortunately, still be measured using simpler tools and showed a similar behaviour upon unloading as the Hostun sand and lentils specimens: a slight response of the fabric. As the glass beads are mostly composed of silica similar to the Hostun sand grains, the only major difference of the materials is the particle shape[1]. Thus, it might

[1]The particle shape also includes the roughness in this case, as shape and roughness

be concluded that the discrete element method, in the state of the employed complexity, is unable to recreate the geometrical interactions upon reversing the loading in real materials.

This conclusion is, however, not without a doubt. Another possible reason could be that the unloading was not sufficient to cause a rearrangement of particles and especially the contact network. An analogy drawn from the observations of the monotonic experiment might help to explain this: the higher the initial anisotropy of the specimen, the more shear is needed for the mobilisation of the contact fabric. Thus, the fabric might need more unloading especially in terms of axial strain, to rearrange and react to the load reversal. As long as this does not happen, there will not be a lower macroscopic stiffness and rearrangements. Note that the disagreement between experiment and simulation could also be due to boundary effects such as the flexible membrane or physical interactions between particles that are not taken into account in the friction model, that are not taken into account in the simulations.

6.2.1 Incremental response upon load reversal

In the section explaining the motivation for this doctoral work (1.1), the inter-granular strain tensor was introduced as one possible strategy to model the macroscopic behaviour upon load reversal. Its evolution was showcased for several unloading-reloading cycles in a simplified and idealised triaxial compression test. This additional, phenomenological state variable was originally considered to describe the deformation of an inter-granular interface layer [NH97]. Following this line of thought, the inter-granular strain should be related to the contact fabric or rather its change during a loading. Therefore, the anisotropy is considered as a scalar descriptor for the contact fabric and its incremental response to the load cycles is examined in the following.

Similar to the analysis of the inter-granular strain, the change of the anisotropy Δa is determined for each unloading $\Delta\epsilon_{zz} < 0$ and reloading step $\Delta\epsilon_{zz} > 0$ in the discrete element simulation from the benchmark analysis in section 4.2 and the triaxial compression tests TC02-TC05 on Hostun sand. The change of anisotropy for the load reversals in the DEM simulation is determined as a continuous evolution and plotted in Figure 6.1a with each

cannot be distinguished from one another due to the employed spatial resolution of the images.

colour corresponding to one load cycle. The evolution is almost linear with only the reloading part possibly tending to a steady value. Such a value is, however, not reached during the cycles since the anisotropy keeps evolving after reloading to the stress state previous to the cycle. An evolution of the change of anisotropy cannot be determined for the experiments since only two scans of the specimen are acquired that cover the state before and after the unloading or reloading. Therefore, only one point of the change of the anisotropy for every load reversal is plotted in Figure 6.1b[2]. The general trend is similar to the changes in the DEM simulation: the anisotropy decreases upon unloading and increases upon reloading. There are several outliers that do not follow this trend and can be explained by the uncertainty of the measurement. The trend is also almost linear.

The magnitudes are, however, substantially different in the simulations and the experiments. There are different causes that could be responsible for this discrepancy. As mentioned before, the particle shape was excluded from the list of causes, because the experiment on glass beads showed a similar response of the contact fabric to the Hostun sand specimens. Another possible reason could be the contact model and the employed parameters, which were chosen rather arbitrary to make qualitative observations. As other less simplified DEM simulations [OC09, JZL19] showed similar changes in magnitude, this cause can probably also be excluded. This leaves either the method itself as not able to capture this behaviour or the experiment with possibly not sufficient unloading during the reversals as explained before.

The simulation as well as the experiments show an almost linear relation between the change of anisotropy and the strain increment. The inter-granular strain tensor does not follow the trend in the simulation presented in section 1.1. It increases rapidly before approaching a steady value during each load reversal as plotted in Figure 1.2b, whereas the contact fabric anisotropy evolves at a substantially lower rate than $\boldsymbol{\delta}$ during the cycles and transitions smoother, if at all, towards further loading. Furthermore, the contact fabric does not stop evolving after being realigned with the strain, but keeps changing until a steady state is reached. This range is restricted by the parameter R in the inter-granular strain model. Once R is reached, $\boldsymbol{\delta}$ does not evolve further if the direction of the loading stays constant. One problem of the inter-granular strain concept is, that the

[2] The uncertainty of Δa is determined by the propagation of δa for $\Delta a = a_i - a_{i-1}$. With $\delta a_i \approx \delta a_{i-1}$ known from the numerical propagation in section 10.3 the uncertainty is given by $\delta \Delta a = \sqrt{(\delta a_i)^2 + (\delta a_{i-1})^2} = \sqrt{2}\delta a$.

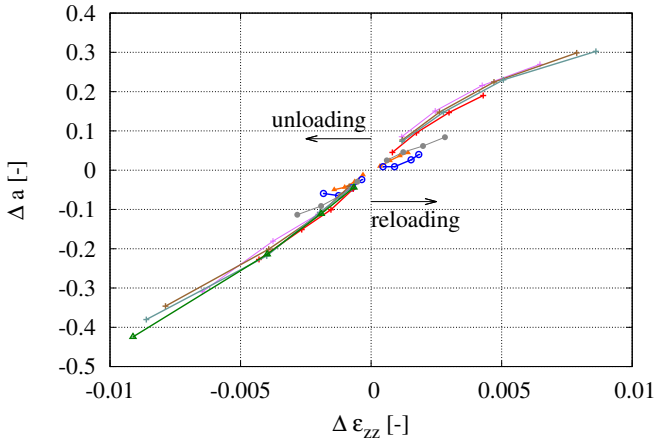

(a) DEM simulation.

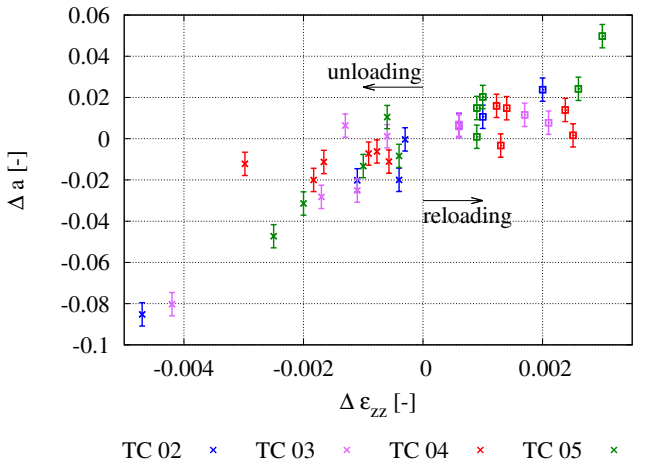

(b) Experiments.

Figure 6.1: Change of the anisotropy in each cycle for the unloading and reloading step. Top: DEM simulation from the benchmark study in section 4.2. Bottom: Changes from all triaxial compression tests from sections 5.2.2 and 12.4.6.

parameters have to be calibrated specifically for the load situation [Wic19], *e.g.*, for the size of the load cycles. In this specific case, the disagreement of the fabric and the inter-granular strain might be connected to the defined range of evolution. Obviously, the physical meaning of the inter-granular strain concept cannot be related to the contact fabric.

6.3 Further work and outlook

The metrological study on the Hostun sand grains in section 4.1 showed that no matter which watershed is employed, there are still substantial errors when determining the contact orientations. This especially applies to contacts that involve very 'sharp' contact topologies as the watershed approaches rely on a fitting such as a principal component analysis. Their results in turn depend strongly on the size of the data set which is small in terms of a sharp topology. To avoid errors that are too high, orientations determined on too few data points were excluded in this work[3]. A possible alternative to determine the orientations are level sets [VAVA13]. These smooth functions are fitted on each grain, based on an optimisation. Applying them on the synthetic images of spheres in section 8.1.7 resulted in an even lower error than the random walker. Since the iterative matching of the level set function to the image still lacked a convergence criterion and was computationally substantially more expensive than the random walker in the beginning of this work, the image analyses were carried out using the latter. These should, however, be revisited especially concerning the orientations between angular particles.

One possible further development is the combination of the fabric analysis with a discrete Digital Image Correlation (DIC). This would enable the tracking of individual grains throughout the loading and relate their movement with their constrictions, such as *e.g.*, their local coordination number. For x-ray μCT this has already been attempted by [CW18], but it was restricted to the analysis of branch vectors due to the difficulty in determining the contact fabric accurately[4]. A very specific group of contacts was observed to be responsible for certain macroscopic phenomena in the numerical simulations by Alonso-Marroquin et al. [AMH04, AMLHV05]: sliding contacts. The amount of contacts that are sliding increases during monotonic shear and can be related to a decrease in stiffness. The abrupt change of the stiffness upon load reversal was linked with a sudden reduction of sliding contacts. And also the accumulation of permanent strain was related to the amount of sliding contacts, even for very small stress cycles. All this information is vital for better understanding the link between the micro-mechanics and the macroscopic behaviour. Especially as,

[3] This was described *e.g.*, in sections 12.3.2 and 12.4.2 for the processing of the oedometric and triaxial tests.

[4] Their reason for this decision was the metrological study presented in this work and [WAHV17].

so far, the purely kinetic constraint of distinguishing between the weak and strong contact network depending on their corresponding force (as introduced in [RJMR96]) cannot be made. A very sophisticated discrete DIC is implemented in the *spam* project and could be coupled with the contact fabric measurements. If these relations are validated by experimental measurements, the traditional fabric tensor as employed in this work has to be expanded to distinguish between these different characteristics of contacts.

Only a very simple fabric tensor was used in this study. As described in section 1.2.2, there are very different formulations which enable such tensors to *e.g.*, carry more information or evolve more freely. In numerical simulations it is simple to choose fractions of the contact network that contribute more to the macroscopic behaviour than others, *e.g.*, due to the duality of the contact force network. As measurements from x-ray tomography are still restricted to purely geometrical measurements, such a distinction is not obvious, but there have already been some attempts to weigh the contact fabric tensor[5]. A possible way to respect the contribution of each contact to the bulk is to associate a volume to each one as proposed by [MTLL04]. Especially if such a measure is to be implemented in a thermodynamic framework, the whole space should be accounted for rather than only the volumes of the contacting particles. This could be accomplished by a tessellation. In that manner, it would be considered that a contact between two large particles is likely to transfer a higher force than between two small ones or other configurations.

Another interesting field where fabric might come into play is the liquefaction potential of coarse grained soils. In her PhD work, Bozana Bacic developed an index test to assess the sensitivity to liquefaction in dependence of relative density [BH19b]. She observed a similar potential for different sands at different relative densities [BH19a]. One possible reason could be the employed preparation procedure which was identical for all her experiments and thus, could have created a similar initial fabric. If the initial fabric is an additional and important factor, the models for the prediction have to be adapted. In order to check that, similar specimen will be created and imaged using x-ray μCT and the contact fabric will be assessed using the toolbox developed here. Such information could then be crucial for the next step: the identification of zones that are susceptible to liquefaction. Prof. Nicholas Sitar[6] works on the latter by taking undisturbed

[5] This was briefly discussed in section 3.3.
[6] Professor of Civil Engineering at UC Berkeley.

samples from such zones. In a recent collaboration, samples taken from a post-liquefaction zone were brought to Grenoble and we characterised the contact and particle fabric of multiple frozen samples. But in order to reliably predict such tendencies, more information also in the light of the fabric has to be gathered.

A further application that is not yet fully understood is the installation of geotechnical structures into the ground, such as piles. Jeanne Doreau Malioche investigated the micro-mechanics of soil around a model pile during the installation and in cyclic loading in her PhD [DM18]. Using the particle orientation measurements defined and studied in section 4.3, she identified different zones close to the pile tip and shaft and determined the influence around the pile. Depending of these zones the particle long axes either aligned to the direction of pile penetration or remained in their initial configuration. Unfortunately, contact fabric measures were not yet at a reliable state when this thesis was carried out, so this still remains an open topic.

6.4 Conclusions

This work has accessed the contact and particle fabric of a granular soil and followed its evolution during monotonic and cyclic loading using x-ray μCT. To extract reliable data from any kind of image, the tools employed to do so have to be well understood. Therefore, a methodology was developed and presented to study the metrology of contact and particle fabric from individual to bulk measurements. Based on this, a benchmark study was proposed and published in an open access archive that can be used either to retrace this study or to measure the accuracy of different approaches. All the tools and strategies that were proposed and developed here, are implemented in the open source software *spam*.[7]

The fabric evolution was captured for monotonic and cyclic loading in vari-

[7] I strongly believe in the idea of sharing research data in open access archives and software in open source projects. A part of this belief is definitely based on my supervisors, but also on my experiences in research. Instead of everyone developing their own tools, that are then restricted to a specific group of users, we should try to work together more. Working on the same code and idea might make decision making more complex and slower, but it also helps tremendously to spot mistakes and develop better strategies. And if that does not count, it does save human resources in terms of time and therefore, money. I hope that *spam* will thrive and that we can expand our community even further.

ous experiments. Its incremental changes were extracted specifically for the load reversals and compared to the evolution of the inter-granular strain tensor $\boldsymbol{\delta}$ in hypoplasticity, which was proposed to realistically predict the behaviour upon load cycles. There are certain differences in their evolutions, which might explain some of the shortcomings of the phenomenological concept. Two main differences were observed: the rate of change during a load cycle and the range of its change after reloading. These experimental observations could help to either reformulate the evolution equation of $\boldsymbol{\delta}$ or to introduce a different concept.

Comparisons of the experimental results with DEM simulations, both very simplified and more complex ones, showed substantial differences especially for load reversals. These might have different reasons and have to be revisited to truly find the underlying causes. Thus, care must be taken to not trust every detail arising from DEM simulations as they still appear to miss several aspects of the micro-mechanical behaviour. However, these methods remain a great tool for qualitative predictions and mind experiments in the light of such limitations.

It has to be noted, that the experimental findings in this work are of qualitative nature. More general conclusions on *e.g.*, the influence of the initial state or the particle shape cannot be drawn as the experimental database is too small. A larger set of experiments and a systematic variation of these conditions has to be carried out to draw such conclusions.

The last note may seem counter-intuitive, since this thesis almost exclusively dealt with the metrology and the description of contact fabric and its relation to the macroscopic behaviour. Disregarding its uncertainty aspects, the study on the high resolution tomographies of Hostun sand grains revealed different features of the contact topology depending on the scale of observation[8]. This is due to the surfaces being approximately self-similar in the range of imaging[9], *i.e.*, similar features are repeatedly apparent at every scale. A side result of this observation was, that the surface of a contact is not a physically meaningful measurement, as it is frame-dependent. Thus, a geometrical definition of what a contact actually is and how to characterise it is not straightforward. Furthermore, due to being ill-defined from the image processing point of view, *i.e.*, two particles can be infinitely close without being in contact, it is difficult to say whether two particles are

[8] This was studied in section 4.1.2 and is visualised in Figure 4.12

[9] This excludes the macroscopic scale at which a grain cannot be identified as well as the molecular scale.

actually in contact without knowing whether the contact transfers a force. Hence, the existence of a contact can merely be an assumption based on image properties when working purely on imperfect geometrical information. Geometrically, the existence of a contact could be revealed as, according to nano-tribology, loaded surfaces experience wear. This could serve as a geometrical identifier, but the scale of imaging necessary to reveal wear is far below of the scale when imaging a mechanically representative specimen as done in this work. Nevertheless, there is a relation between the contact fabric determined on images and the macroscopic behaviour as found and emphasised in this work. After all, the contact fabric is the most important geometrical fabric entity from a mechanical point of view, since the forces are transferred via contacts.

Part III

Technical details

7 General topics

7.1 Fabric tensors

The goal of describing a distribution of orientations is to relate it to certain macroscopic phenomena and possibly incorporate it into continuum models. Most of such models use tensors, such as stress and strain, which is why it was a straightforward decision by the pioneers of micro-mechanics to define frame indifferent tensor quantities to characterise the distributions. This work follows the mathematical derivation for fabric tensors by Kanatani [KI84], but uses different notations where his original ones got rather confusing. Particle and contact orientations $\mathbf{o}$ do not have a distinct direction, which means that both, $\mathbf{o}$ and $-\mathbf{o}$ are valid orientations. Thus, it is necessary that all tensors are symmetric to the origin of the coordinate system.

The most commonly used fabric tensor is the average tensorial product $\mathbf{N}$ of all orientations $\mathbf{o}^i$ in a distribution $i \in N$ normalised by the number of orientations N:

$$\mathbf{N} = \frac{1}{N} \sum_{i \in N} \mathbf{o}^i \otimes \mathbf{o}^i \otimes \cdots \otimes \mathbf{o}^i \tag{7.1}$$

In Kanatani's work, $\mathbf{N}$ is called fabric tensor of the first kind. The number of times the tensor product is carried out corresponds to the rank of the tensor and hence the order of approximation. For the application on contact and particle orientations, that have no direction, this tensor has to be symmetric, which is only the case for even ranked tensors. The empirical distribution density $f(\mathbf{o})$ is expressed as:

$$f(\mathbf{o}) = \frac{1}{N} \sum_{i \in N} \delta\left(\mathbf{o} - \mathbf{o}^i\right) \tag{7.2}$$

with δ being the Dirac delta. That makes the fabric tensor defined above a valid approximation of the distribution:

$$\int f(\mathbf{o})\,\mathrm{d}\mathbf{o} = 1: \quad \int \mathbf{o} \otimes \cdots \otimes \mathbf{o} f(\mathbf{o})\,\mathrm{d}\mathbf{o} = \mathbf{N} \tag{7.3}$$

The problem with this distribution is the singularity of the Dirac delta function $\delta\left(\mathbf{o} - \mathbf{o}^i\right)$. Thus, it needs to be approximated by a smooth function. This resulted in a so-called fabric tensor of the second kind in Kanatani's work, which will not be discussed here due to its deficiency of interdependent coefficients. To bypass that, he formulated a fabric tensor of the third kind $\mathbf{D}$ with independent coefficients. Using $\mathbf{D}$, the distribution density can be approximated as follows:

$$f(\mathbf{o}) = \frac{1}{4\pi}\left(D + D_{ij}o_i o_j + D_{ijkl}o_i o_j o_k o_l + \dots\right) \tag{7.4}$$

Its coefficients are calculated by:

$$D_{ij\dots} = \frac{2n+1}{2^n}\binom{2n}{n}\mathrm{dev}\left(N_{ij\dots}\right) \tag{7.5}$$

with $\mathrm{dev}\left(N_{ij\dots}\right)$ being the deviatoric part of the fabric tensor and n the order of approximation. Although $\mathrm{dev}\left(N_{ij\dots}\right)$ is actually the deviatoric part of the fabric tensor, $\mathbf{D}$ will be called deviatoric fabric tensor in this work.

Most commonly and in this thesis, a second order approximation of the distribution is employed. Thus, the fabric tensor $\mathbf{N}$ reads as defined in Equation (1.2) in the introduction. The coefficients of $\mathbf{D}$ can be computed from Equation (7.5) with $n = 2$:

$$\frac{2n+1}{2^n}\binom{2n}{n} = \frac{5}{4}\binom{4}{2} = \frac{15}{2} \tag{7.6}$$

$$\mathbf{D} = \frac{15}{2}\left(\mathbf{N} - \frac{1}{3}\mathbf{I}\right) \tag{7.7}$$

A possible scalar description of the spread of the distribution is the scalar anisotropy factor a as defined in [GHH17]:

$$a = \sqrt{\frac{3}{2}\mathbf{D} : \mathbf{D}} \tag{7.8}$$

This invariant scalar measure is based on the second invariant of $\mathbf{D}$ and can be interpreted analogue to the von Mises stress. Due to the formulation of

D, the highest possible value of the anisotropy a is 7.5, whereas it is equal to 0 for an isotropic fabric tensor **N**.

Another scalar measure specifically for the contact fabric is the coordination number:

$$CN = 2 \cdot \frac{N_c}{N_p} \tag{7.9}$$

with N_c and N_p begin the number of contacts and particles, respectively. This is a measure of the contact density: the more contacts in a defined assembly, the higher the coordination number.

7.2 Graphical representations

7.2.1 Plotting of individual orientations

In this work, the fabric of granular materials is mostly described by orientations. The orientations are three-dimensional and as such difficult to represent in a way that facilitates understanding them. There are many different ways to plot orientations among which some frequently used ones are 3D spherical histograms (as in [IDA18]) or rose diagrams of 2D projections (as in [FOCL13]).

The rose diagrams lack information as they can show only chosen projections of the full 3D information, whereas the spherical histograms might be difficult to read. To capture all information and (hopefully) to facilitate the understanding, Lambert azimuthal equal area projections are employed in this work. This projection of the spherical coordinates (θ_s, φ_s being the inclination and the azimuth) into a polar coordinate system (r_p, φ_p being the radius and the azimuth) reads:

$$\varphi_p = \varphi_s \tag{7.10}$$

$$r_p = 2 \cdot \cos\left(\frac{\theta_s}{2}\right) \tag{7.11}$$

The orientations **o** describing the geometric fabric are expressed as vectors but do not have a distinct direction; they are only aligned along the direction of the vector and could be pointing in any direction along the vector, *i.e.*, either $+\mathbf{o}$ or $-\mathbf{o}$. Thus, the orientations are always expressed with a positive

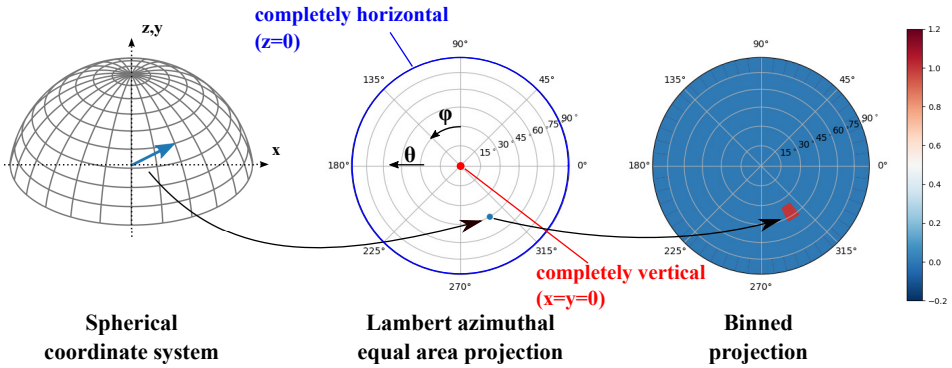

Figure 7.1: Lambert azimuthal equal area projection of a single orientation ($x = 0.35, y = -0.61, z = 0.71$). Left: Orientation plotted in a spherical coordinate system. Centre: Projection of the orientation with an explanation of how to read orientations of this polar diagram. Right: Binned plot of the orientation.

vertical value (z) here: vectors with a negative z-component are flipped. The projection in Equations (7.10) and (7.11) is formulated for orientations that cover a complete sphere with $\theta_s \in [0; \pi]$ and $\varphi_s \in [0; 2\pi)$. As the orientations are always expressed with a positive value along the vertical axis (z-axis) in this work, equation (7.11) is modified to account for $\theta_s \in [0; \pi/2]$:

$$r_p = 2 \cdot \cos\left(\frac{\pi - \theta_s}{2}\right) \tag{7.12}$$

In this way, a purely vertical orientation $\theta_s = 0$ is defined as the center point of the polar diagram with $r_p = 0$, which would otherwise lie on a circle with $r_p = 2$. All orientations that are purely horizontal and have no vertical component lie on a circle with $r_p = \sqrt{2}$ in the polar diagram.

Figure 7.1 shows the plotting of the Lambert projection on the example of a single orientation $\mathbf{o} = [0.35; -0.61; 0.71]$. The orientation given by 3D coordinates in either spherical or kartesian coordinates is projected into polar coordinates using (7.10) and (7.12). The azimuthal coordinate φ is increasing counter-clockwise and the inclination θ is increasing from the centre outwards. Thus, orientations that are purely vertical $\mathbf{o} = [0; 0; z = 1]$ are plotted in the centre whereas purely horizontal orientations $\mathbf{o} = [x; y; 0]$ are located on the outer ring of the polar diagram. When plotting thousands of orientations, as later in this work, the plot of individual orientations gets too crowded with points and a binned presentation of the orientations

becomes necessary. The binning of orientations is shown on the right side of Figure 7.1. In many cases, it is beneficial to plot multiple binned polar diagrams with an equal range of data. In this case, the values of the bins are normalised by the average number of orientations falling into a bin in the specific figure.

7.2.2 Plotting of fabric tensors

In order to plot the surface of a fabric tensor, all that is needed is basically the density distribution $f(\mathbf{o})$ as approximated with the fabric deviator $\mathbf{D}$ in Equation (7.4). This function gives the actual value of the density in each considered direction $\mathbf{o}$. A systematically distributed set of orientations must be set up and the value of f is to be calculated in each of those directions. That can be done for example by using spherical coordinates $0 \leq \varphi \leq 2\pi$ and $0 \leq \theta \leq \pi$ as in the example given below. These coordinates are then transformed to Cartesian coordinates to use the fabric tensor, that is determined in this coordinate system. The surface is plotted from the actual value of f on the discrete set of orientations. An example on how this can be implemented using Python is given below in Listing 7.1 using the Matplotlib Python package [Hun07]. The example in this script is the fabric tensor $\mathbf{N}$ for the 8th imaged state of the experiment on Caicos ooids. For reference, a plot of this surface can be found in Figure 5.5 in the centre right image of the upper row.

Listing 7.1: Python script for plotting the surface of a fabric tensor.

```
import numpy
import matplotlib.pyplot as plt
from mpl_toolkits.mplot3d import Axes3D

#define N or D directly
N = numpy.array([[0.2544, -0.0070, 0.0087],
                 [-0.0070, 0.2839, 0.0057],
                 [0.0087, 0.0057, 0.4614]])

D = (N-((N[0,0]+N[1,1]+N[2,2])*(1./3.))*numpy.eye(3,3)
    )*(15./2.)

# set up the figure
fig = plt.figure()
```

```
ax = fig.add_subplot(111, projection='3d')
ax.set_xlabel('X axis'), ax.set_ylabel('Y axis'), ax.
    set_zlabel('Z axis')

# create directions in spherical coordinates
u = numpy.linspace(0, 2 * numpy.pi, 100)
v = numpy.linspace(0, numpy.pi, 100)
# set up the field of measurement points in Cartesian
    coordinates
x = numpy.outer(numpy.cos(u), numpy.sin(v))
y = numpy.outer(numpy.sin(u), numpy.sin(v))
z = numpy.outer(numpy.ones(numpy.size(u)), numpy.cos(v
    ))

# initiate the field of fabric values
f = numpy.zeros(numpy.shape(x))
for i in range(len(u)):
    for j in range(len(v)):
        o = numpy.array([x[i,j],y[i,j],z[i,j]])

        f[i,j] = 1./(4*numpy.pi) * (1. + numpy.inner(
            numpy.inner(D,o),o))

        # now stretch the direction o by f(o)
        x[i,j] = x[i,j] * f[i,j]
        y[i,j] = y[i,j] * f[i,j]
        z[i,j] = z[i,j] * f[i,j]

# Plot the surface
ax.plot_surface(x, y, z, color='grey')
# set equal axis increments
ax.set_xlim3d([-0.12,0.12]), ax.set_ylim3d
    ([-0.12,0.12]), ax.set_zlim3d([-0.12,0.12])

plt.show()
```

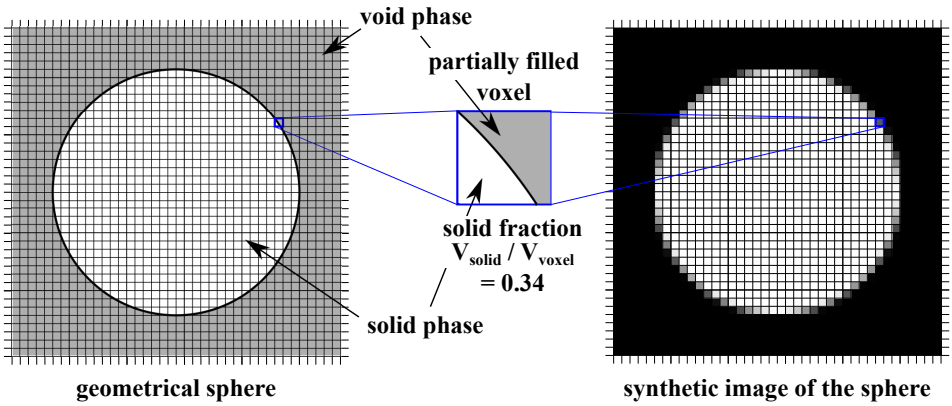

Figure 7.2: Figure showing the creation of an image of a sphere using Kalisphera with a diameter of 30 pixel on slices of the originally 3D image. Left: the geometric sphere on top of the later raster for the pixelated image. Centre: a partially filled voxel. Right: the final 32-bit image of the sphere.

7.3 Kalisphera

Throughout the metrological study of interparticle contacts, Kalisphera [TA15] is used as the tool to create synthetic images of spheres. In order to approximate real tomographic images by synthetic ones, the image properties and defects of tomographies need to be accounted for. Kalisphera considers the PVE – an inherent feature to any pixelated image – analytically.

The program creates a 32-bit image of a sphere with values between zero and one, *i.e.*, [0.;1.], with zero and one being the perfect void and solid part, respectively. Each voxel on the boundary of the sphere is assigned a value taking into account the PVE, *i.e.*, the ratio of solid that lies inside the voxel to the total volume of the voxel. The whole process of creating a single sphere (with a diameter of 30 pixel) is explained in Figure 7.2 on slices through the originally 3D image.

7.4 Towards realistic, synthetic images

Kalisphera [TA15] creates images that do consider the PVE but are otherwise perfect. Real tomographies have a lot of different defects among which

noise and blur are two important ones. In this work, only the PVE, blur and noise are considered in order to create synthetic, but realistic images.

7.4.1 How to incorporate blur and noise in the synthetic images

Kalisphera produces 32-bit images with grey-values in the range of $[0.; 1.]$ representing void and solid parts, respectively. As a result of applying blur and noise on these images, the distribution of grey-values is shifted. In order to allow a shift in grey-values in all directions, the images are first rescaled to $[0.25; 0.75]$.

Incorporating blur in the synthetic images is important to represent the smearing of the edges of the spheres. Its degree is dependent on the point spread function of the x-ray imaging system and the reconstruction of the tomography. To consider blur, a Gaussian filter is applied to the images. The level of blur is given by the standard deviation of the Gaussian. Such a generator is already implemented in Kalisphera. The Gaussian filter from the python package *scipy* [JOP+], however, runs slightly faster and creates almost identical results. Thus, the function `scipy.ndimage.filters.gaussian_filter` is used for the application of blur.

The level of blur was calibrated in [TA15] by matching spheres from Kalisphera in synthetic images with real tomographies of manufactured spheres. The spheres were matched based on an optimisation that started from an initial guess of the position and the radius of the spheres in the real tomography and the blur of the image. The level of blur was found to be ≈ 0.8 for the tomograph in Laboratoire 3SR (Grenoble) – which is the image system that is used throughout this work.

For the study on the metrology, an image of two spheres in contact is produced by creating each individual sphere and merging the two images. It does not make any difference in the final image whether the blur is applied to each individual image before or the complete image after merging. The blur is applied to the merged image as it represents the acquisition of the image better and saves computation time.

Noise is apparent in any acquired image. The noise in tomographies has been classified into random, artifactual and structural noise and related to its origins in [Han81]. As filters and reconstruction algorithms are able to

deal at least in part with the latter two, this study considers only the random noise, which can be interpreted as a combination of Poisson and Gaussian noise. However, it seems sufficient to include Gaussian noise to create synthetic images with similar features to real tomographies [SSBW14]. Therefore, only Gaussian noise is applied to the images using the function `numpy.random.normal` from the python package *numpy* [Oli06]. This operator applies a random variation based on a Gaussian distribution to each voxel individually. The value of each voxel becomes the mean of the distribution and is randomly varied by the standard deviation. The level of noise is specified by the standard deviation of the Gaussian distribution.

Here, the influence of noise on the image properties is described with the histogram of the grey-values of the image. Figure 7.4 depicts the histograms of images with an increasing level of noise. In both, the original and the blurred images without noise, the histogram tends to a narrow distribution at the solid (0.75) and void phase (0.25). The application of noise changes the distribution of grey-values significantly: the higher the level of noise, the wider the distribution of grey-values belonging to the solid and void phases. The resulting standard deviation of the distributions in the histogram is almost equal to the applied level of noise.

The whole process of creating an image of two spheres in contact and incorporating the image properties and defects is depicted in Figure 7.3. As described above, Kalisphera produces 32-bit images of individual spheres in the range of $[0.;1.]$. These individual images are then merged and the range of grey-values is changed to $[0.25;0.75]$ in order to leave room for applying noise in the available range of the image ($[0.;1.]$). Blur is applied to the complete image with the Gaussian filter set to the value of 0.8, a value calibrated for the tomograph in Laboratoire 3SR. At last, random noise is applied to the image with a standard deviation of 0.03 chosen for this graphical representation of the process.

7.4.2 Image properties of real x-ray tomographies

The blur has already been calibrated for the x-ray imaging system in Laboratoire 3SR (Grenoble) in [TA15]. The level of noise is calibrated on tomographies of mechanical experiments that are used later in this work. The evaluation of the distribution of grey-values is explained for the first tomog-

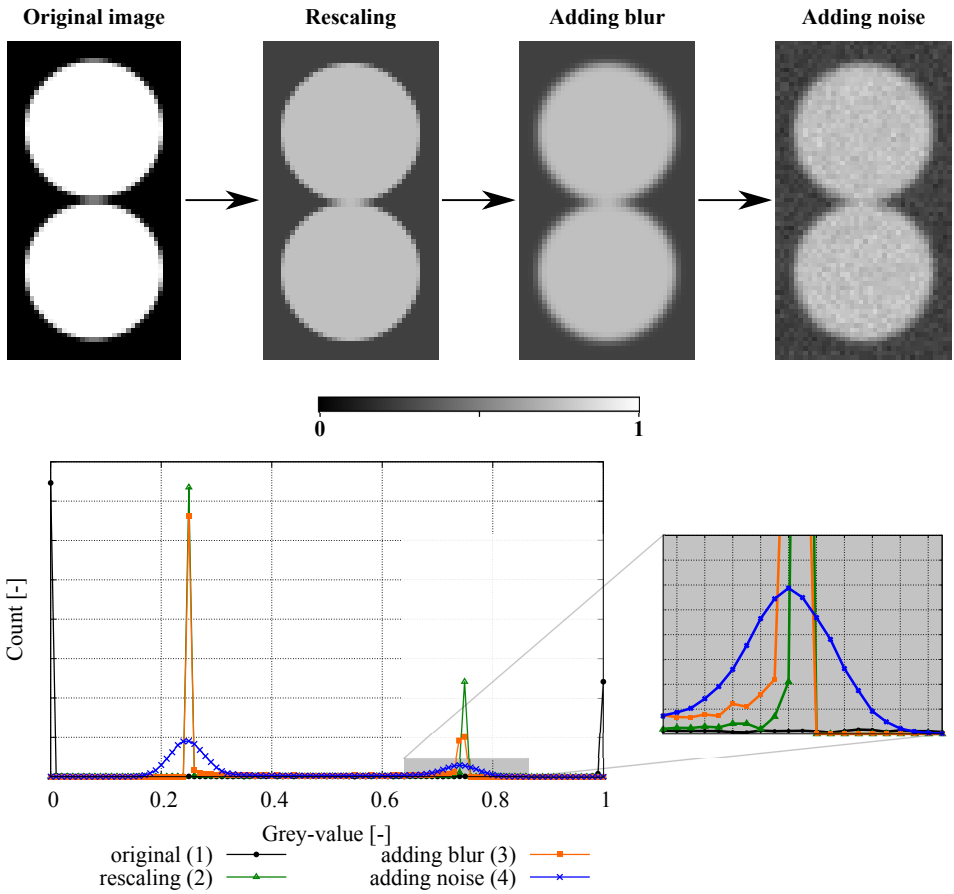

Figure 7.3: Incorporating image defects in synthetic images of spheres with a diameter of 30 pixel. Top: Slices through the 3D synthetic images – from the initial Kalisphera spheres (1) to rescaling the image (2) to adding blur (3) and noise (4). Bottom: Histogram showing the change in grey-values of the images with a zoom in on the solid part.

raphy (01) of the experiment HNMWTC03[1], a triaxial compression test on Hostun sand, a material that is used in many experiments of this work. To consider only the grain and void phases, a subset is extracted from the center of the image.

[1]The experiment is described in section 12.4

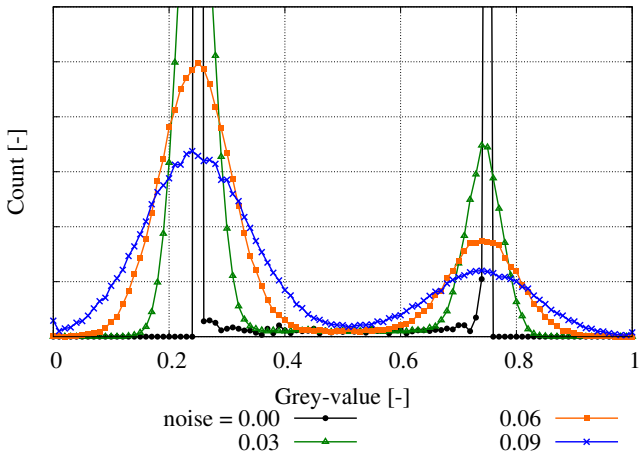

Figure 7.4: Histogram of grey-levels in synthetic images with different level of Gaussian noise. The spheres for this study have a diameter of 30 pixel.

The data type of the acquired tomgraphies is 16-bit unsigned integer[2]. To compare them with the 32-bit floating point images from Kalisphera, the grey-value of each individual voxel is transferred to a 32-bit value by dividing it with 65,535, which is the maximum value of the 16-bit unsigned integer range:

$$x_{32b} = \frac{x_{16b}}{65535} \tag{7.13}$$

with x_{type} being the grey-values of the voxels at a given data type. A histogram of the grey-values for this experiment is plotted in Figure 7.5a in the range of [0.;1.]. The void and the solid phase are identified in the histogram and Gaussian functions are fitted to the distinct phases. For the chosen image HNMWTC03-01, the solid phase is characterised by a mean value of $\mu_s = 0.75$ with a standard deviation of $\sigma_s = 0.031$. The fitting of the Gaussian function to the void phase yields $\mu_v = 0.12$ and $\sigma_v = 0.036$. Generally, the mean grey-values of the void and solid phase in the real tomographies are not similar to the synthetic images at 0.25 and 0.75, respectively. In order to consistently compare the histograms of the synthetic and the real images, the grey-values of the real image are distorted such that both phases are represented by similar mean values. Using the difference of the mean values in the real tomography $\Delta\mu_{real} = 0.63$, of the

[2]16-bit unsigned integer values can range from 0 to 65,535

Table 7.1: Standard deviations of the solid and void phase of subsets of chosen experiments. The values are determined on the histograms of the grey-values of the images.

Experiment	Material	μ_s	σ_s	μ_v	σ_v
HNMWOD01	Hostun sand	0.75	0.021	0.25	0.028
HNMWTC02	Hostun sand	0.75	0.019	0.25	0.024
HNMWTC03	Hostun sand	0.75	0.025	0.25	0.026
HNMWTC04	Hostun sand	0.75	0.021	0.25	0.026
TT70_Lenti_06	Lentils	0.75	0.021	0.25	0.022
HNEA01	Hostun sand	0.75	0.55	0.25	0.091
HNCO01	Caicos ooids	0.75	0.028	0.25	0.047

synthetic image $\Delta\mu_{syn}$ and the resulting offset of the void phase (in this case 0.155), the distortion is given by:

$$x_{32b,dist} = x_{32b} \cdot \frac{\Delta\mu_{syn}}{\Delta\mu_{real}} + 0.155 = x_{32b} \cdot \frac{0.5}{0.63} + 0.155 \tag{7.14}$$

After the distortion, the standard deviations of the solid and void phases are $\sigma_s = 0.025$ and $\sigma_v = 0.026$. Figure 7.5b shows the histogram after the distortion of grey-values. This normalisation of histograms is performed on other experiments that are part of this work and the results are summarised in Table 7.1. The experiments in the upper part of the table are experiments that were conducted within this work whereas the experiments in the lower part are from the thesis of Edward Andò [And13]. The apparent level of noise, that is estimated by the standard deviation of the void and the solid phase, is lower in the new experiments. This is due to improvements in the imaging system in Laboratoire 3SR and in the software for the reconstructions. Thus, the level of noise that is used repeatedly in this work is set to 0.03.

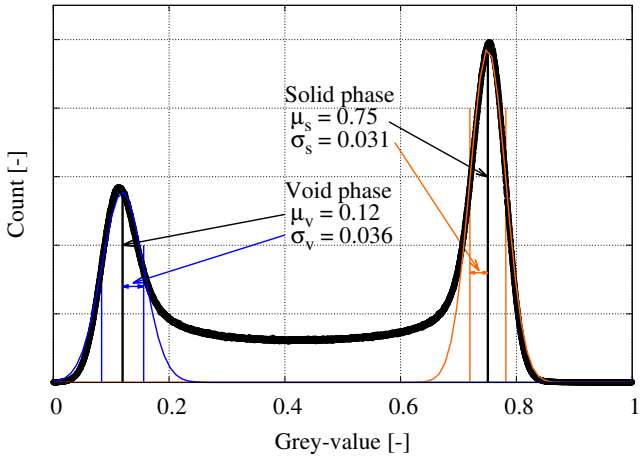

(a) Histogram in the 32-bit floating point range of $[0.; 1.]$

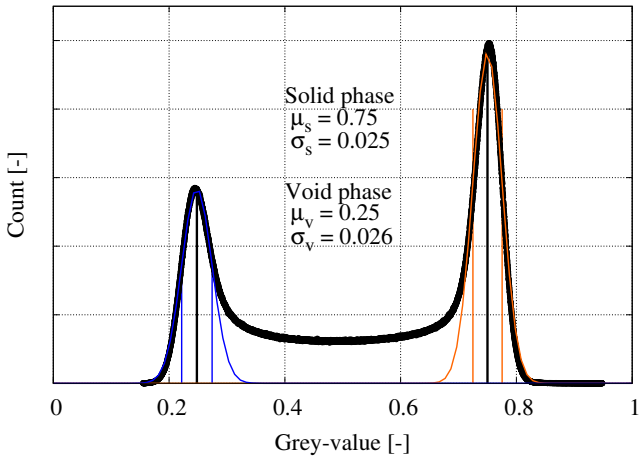

(b) Histogram of distorted grey-values to yield comparable void and solid phases to the synthetic images

Figure 7.5: Histograms of grey-values of a subset from the tomography HNMWTC03-01.

8 Metrology of individual contacts

8.1 Study on synthetic images

8.1.1 Reference configurations

The analysis on the individual contacts has to cover different configurations of two spheres. For spheres these orientations are identical to the direction of the branch vector, that connects the centres of the spheres. The set of orientations can either be created randomly or systematically. If the number of orientations (realisations) N is sufficiently large, a random set should cover most orientations. Additionally to the inherent nature of a systematic analysis, it might be easier to identify a possible bias later using a systematic set. Thus, a systematic set of orientations is used here.

Distributing points equally on a sphere is a mathematical problem and has no analytical solution. One of the approaches to this problem, is to define a spiral on the surface of the sphere and equally space points on this spiral [RSZ94]. Using the spherical coordinates, $\phi \in 0 \leq \phi \leq 2\pi$ as the azimuthal angle and $\theta \in 0 \leq \theta \leq \pi$ as the inclination, the formulas giving the points on the spiral are slightly modified from [RSZ94, SK97]:

$$\theta_k = \arccos(h_k) \tag{8.1}$$

$$h_k = 1 - \frac{2 \cdot k - 1}{2 \cdot N} \tag{8.2}$$

$$\phi_k = \phi_{k-1} + \frac{3{,}6}{\sqrt{2N}} \frac{1}{1 - h_k^2} \tag{8.3}$$

with N being the number of realisations and $k \in N$. Distributing points equally on a sphere has been discussed after these contributions regarding the optimisation of such algorithms, but it does not matter in this analysis

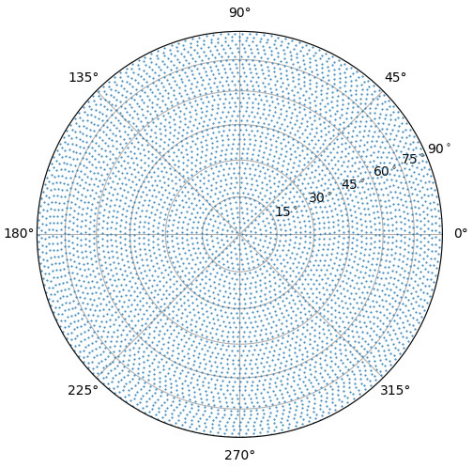

Figure 8.1: Reference set of orientations for the study on the metrology of contacts. The orientations are plotted with the Lambert azimuthal equal area projection.

how accurate these points are distributed. It is sufficient to consider a semi-sphere and always flip one axis, the vertical axis in this work, because the contact orientations are only oriented along a vector, but have no direction. 5,000 realisations of distributed orientations on a semi-sphere are chosen as the reference set for the analysis of contact fabric. Figure 8.1 shows a Lambert azimuthal equal area projection of the reference orientations.

8.1.2 Creation of a synthetic image of two touching spheres

In order to create an image with two particles in contact, their geometry, *i.e.*, the diameter of each sphere d and their orientation $\mathbf{o}$ to each other, has to be defined, The orientation is defined as described in section 8.1.1. With the orientation systematically varying in the systematic set, the branch vector $\mathbf{b}$, that is aligned with the contact orientation in the case of spherical particles, can be expressed as:

$$\mathbf{b} = \mathbf{o} \cdot d \tag{8.4}$$

In the situation that the contact between the spheres consists geometrically of only a single point, the centres of the spheres $\mathbf{c}_i$ are defined as:

$$\mathbf{c}_i = \mathbf{c}_{image} \pm \frac{1}{2} \cdot \mathbf{b} \tag{8.5}$$

with $\mathbf{c}_{image}$ being the center of the image. The size of the image is chosen to be cubic with every dimension being as big as the size of the two spheres in contact plus an empty buffer space, *i.e.*, $dim_i = 2 \cdot d +$ buffer. The images of the spheres are created individually and then merged by simply summing the values of each pixel of the two images. At a contact this might lead to pixels with values higher than 1, which are identified and set back to 1 because 1 is already defined as the highest value for a solid. As described in section 7.4, the values of the voxels, initially having the range $[0; 1]$, are translated to lie in a range of $[0.25; 0.75]$. This allows the application of noise as a typical image defect to transition to more realistic images later. Figure 4.2 shows the creation of two touching spheres, both with a diameter of 30 pixel.

8.1.3 Contact detection

One of the questions, that arise from the discussion in section 4.1.1 and Figure 4.2, is whether two spheres appear in contact in the image if they are not touching but close. The starting point for every configuration, *i.e.*, fixed size and orientation of the spheres and their branch vector, respectively, is the single point contact. A grey-scale image is created as described in the previous section. This image is transformed into a binary image by applying a global threshold of 0.5, which is the physically correct threshold dividing void and solid phase. If these spheres appear in contact in the binary image, the binary phase, consisting of all non-zero voxels, has to be connected. This means, that only one object can be identified in the binary image. In order to check that, the binary image is labelled with the `scipy.ndimage.measurements.label` function from the scipy library [JOP+]. A structural element s defining the connectivity of the binary phase is necessary for the labelling in order to decide whether the voxels are connected or not. Here, we employ a 3x3x3 element with all diagonal elements set to zero, *i.e.*, an element with a squared connectivity of one. This element s is given by:

$$\text{in 2D} \qquad s = \begin{bmatrix} 0 & 1 & 0 \\ 1 & 1 & 1 \\ 0 & 1 & 0 \end{bmatrix} \tag{8.6}$$

$$\text{in 3D} \qquad s = \left[\begin{bmatrix} 0 & 0 & 0 \\ 0 & 1 & 0 \\ 0 & 0 & 0 \end{bmatrix}, \begin{bmatrix} 0 & 1 & 0 \\ 1 & 1 & 1 \\ 0 & 1 & 0 \end{bmatrix}, \begin{bmatrix} 0 & 0 & 0 \\ 0 & 1 & 0 \\ 0 & 0 & 0 \end{bmatrix} \right] \tag{8.7}$$

The structural element is centred on every voxel and it is checked whether neighbours exist at the places where s has a value of one. Fonseca et al [FNRA+16] proposed an enhanced structural element for the detection of contacts and state that it would result in less bias in the orientations. A full connectivity, *i.e.*, all elements of s have a value of 1, is therefore also assessed in this study.

After this condition is checked and if the two spheres, that are imposed to be in contact geometrically, also appear to be in contact in the image, the distance between the spheres is increased. For the creation of the images, Equation (8.4) giving the branch vector has to be extended to include a distance dis between both spheres:

$$\mathbf{b} = \mathbf{o} \cdot d + dis \tag{8.8}$$

Geometrically, both spheres are not in contact, but due to the partial volume effect, they might appear as such. The check whether a contact exists in the image is performed in the same way as described above, by binarising and labelling the image and counting the separate objects in the labelled image. The distance between the particles is increased subsequently as long as a contact appears to exist in the image. As the results will differ with varying orientations of the branch vector due to the pixel nature of the image, the analysis is carried out on all 5000 reference orientations and different diameters of the spheres. The workflow of the analysis on contact detection is pictured in Figure 4.6.

At a fixed diameter of the spheres, most configurations have a different maximum distance between the spheres for which a contact still appears in the image. The results are therefore presented with the probability of finding a contact for a given distance, which is calculated by relating the number of configurations at which a contact appears to the total number of the 5000 reference configurations. The probability of finding contacts at increasing distances is shown in Figure 8.2a for different diameters of the spheres.

A perfect detection, *i.e.*, a contact only appears in the image in the way it is imposed geometrically, would exactly be one point at full probability of finding a contact at zero distance and zero at all other distances as indicated in the figure. The diameters for the spheres range from 16 to 100 pixel. All curves have a plateau at 100 % probability of finding a contact until decreasing to 0 %. The entirety of these curves, but the first point, represent an

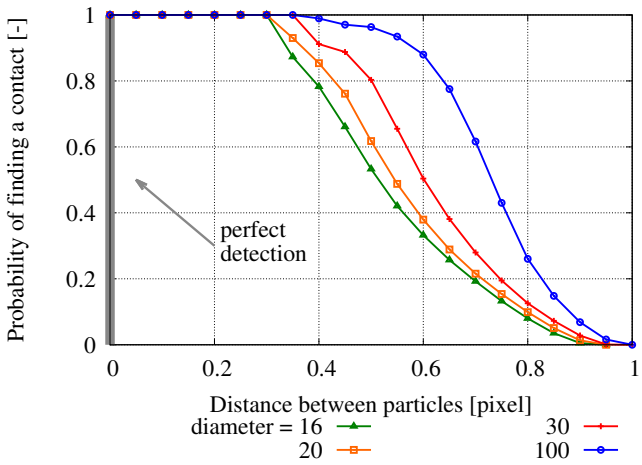

(a) Effect of the diameters of the spheres.

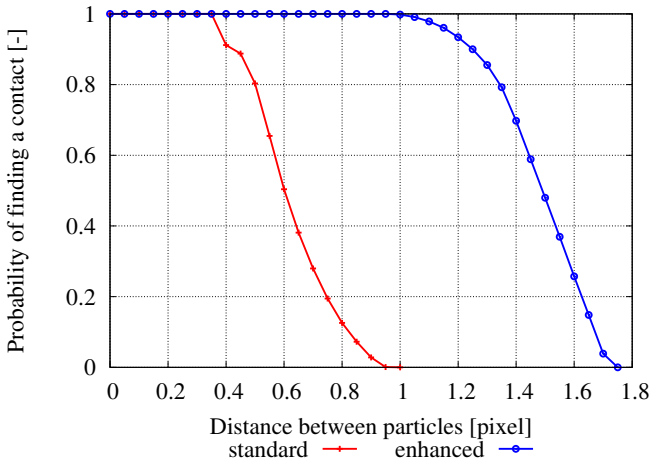

(b) Effect of different connectivity elements.

Figure 8.2: Results of the analysis on contact detection studying the influence of particle size and the connectivity elements. Contacts are detected at a physically correct threshold of 0.5. Top: Varying diameter of the spheres. The standard connectivity element from (8.7) is used. Bottom: Comparison of the standard and the enhanced connectivity element. The diameter of the spheres is 30 pixel.

error because contacts are detected although they geometrically do not exist. This error will be called *over-detection distance*. The diameter does not have a strong influence on this over-detection distance, as almost all curves start decreasing from 1 and stop at 0 probability at similar distances. The major influence is the shape of the curves – smaller spheres have a lower over-detection distance in the transition from 1 to 0 probability. Contacts can be detected up to a distance of 1 pixel between the spheres at all diameters. This represents not only a systematic, but due to the amount, also a serious error. When measuring kinematics from tomographies of granular materials with image correlation techniques an error smaller than 0.1 pixel can be reached [And13].

In the following part of the analysis, only spheres with a diameter of 30 pixel are discussed to reduce the complexity of the problem when more image defects are added. Furthermore, this diameter corresponds to the range of pixel sizes at which tomographies of mechanical experiments of thousands of particles are acquired in the x-ray CT in Laboratoire 3SR; *e.g.*, Caicos ooids, rather round sand grains used in many experimental studies in Grenoble, have $d_{50} = 420\,\mu m$ and are imaged at a pixel size of $15\,\mu m$ in a triaxial test and thus, are imaged at a ratio of $d_{50}/\text{pixel size} = 28$ pixel. The effect of the structural element on the detection of contacts is investigated by studying the standard connectivity element presented in Equation (8.7) and an enhanced element as proposed in [FNRA+16]. Both results are plotted in Figure 8.2b. It is evident that using an enhanced connectivity element increases the *over-detection distance*, *i.e.*, the error, substantially. Therefore, the standard connectivity is employed throughout this work.

In order to get more realistic but only include one image defect at a time, the analysis is repeated for increasing levels of blur. A Gaussian filter with different standard deviations (called levels of blur here) is applied on the initially perfect image with no defects as described in section 7.4. The results are displayed in Figure 8.3a in the same way as before. The probability of finding a contact for the perfect image (red line) is compared with blurred images for the levels of blur of 0.8 (green line) and 1.6 (blue line). The curve at 0.0 blur is the same as the one for a diameter of 30 pixel in Figure 8.2a as this diameter is chosen as a reference. It is obvious that the over-detection distance is increasing strongly with increasing blur. Furthermore, the drop of the probability gets steeper with increasing blur. At the representative level of blur of the x-ray imaging system in Laboratoire 3SR (Grenoble) of 0.8 [TA15] a contact is always detected up to a distance of 1 pixel

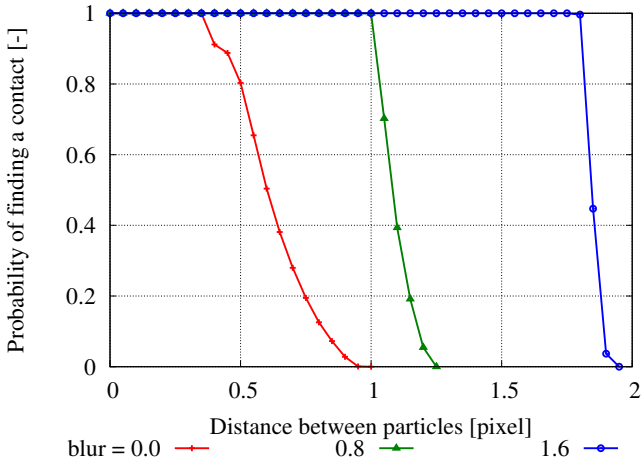

(a) Results of the analysis on contact detection for images at different levels of blur.

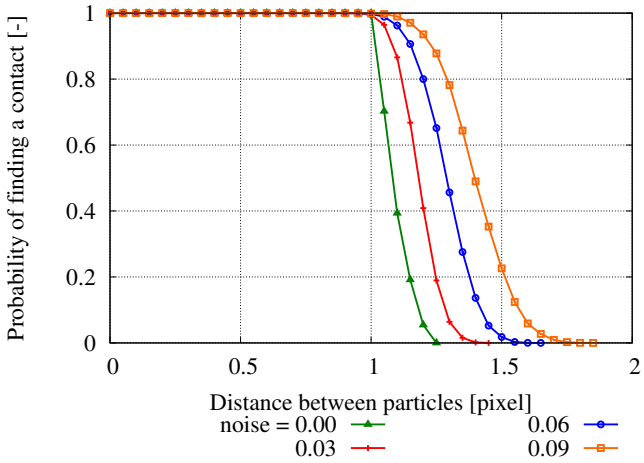

(b) Results of the analysis on contact detection for images at different levels of noise at a fixed level of blur of 0.8.

Figure 8.3: Results of the analysis on contact detection including image defects. The diameter of the spheres is 30 pixel. Contacts are detected at a physically correct threshold of 0.5.

The next and last image defect that is included in this analysis is noise. In order to incorporate noise and discuss only its specific effect on the detection of contacts, the diameter of the spheres and the level of blur of the image are fixed to their reference values of 30 pixel and 0.8, respectively. Random noise based on a Gaussian distribution is applied as described in 7.4. The effect of the noise is studied on four different levels of noise: 0.030.060.09. Figure 8.3b displays the probability of finding contacts for these noise levels and the noiseless reference that is identical to the green curve in Figure 8.3a. An increase of the noise level in the images leads to an increase of the over-detection distance. For the reference values of blur and noise, estimated in 7.4 to 0.8 and 0.03, respectively, contacts are over-detected up to a maximum distance of 1.45 pixel.

8.1.4 Influence of the image grid on contact detection

As described in section 8.1.2, the contact point or the middle of the branch vector between the two centres of the spheres is always located in the centre of the image. The dimensions of the synthetic images are chosen to be even. Thus, the contact point is always located exactly at the edges of 8 voxels. All results presented in 8.1.3 are obtained on images with the same position of the contact point relative to the image grid for each configuration. Thus, this relative contact position is varied here to see whether it affects the over-detection distance.

Figure 8.4 depicts this fixed geometric problem. The position of the contact point is shown with respect to the image grid in red for the study on contact detection. On the right side of the figure, images of two identical configurations are shown – both at a distance of 1 pixel, with a diameter of 30 pixel and no image defects, such as blur or noise. The position of the contact in the upper image is the one used in the study on the detection and is shown as a red cross in the schematic on the left side of the figure – both spheres appear in contact as the grey level in the contacting voxels is higher than 0.5, *i.e.*, the physically correct global threshold. The spheres in the lower image, with a contact point that is displaced by $\Delta x = 0.5$ pixel, do not appear to be in contact. Thus, the position relative to the image grid does matter.

Exploiting the symmetry, it is sufficient to investigate changes of the geometric centre with respect to the centre of the image in the range of $[0.; 0.5]$ for the coordinate axes $\Delta x, \Delta y, \Delta z$. In order to facilitate the analysis and

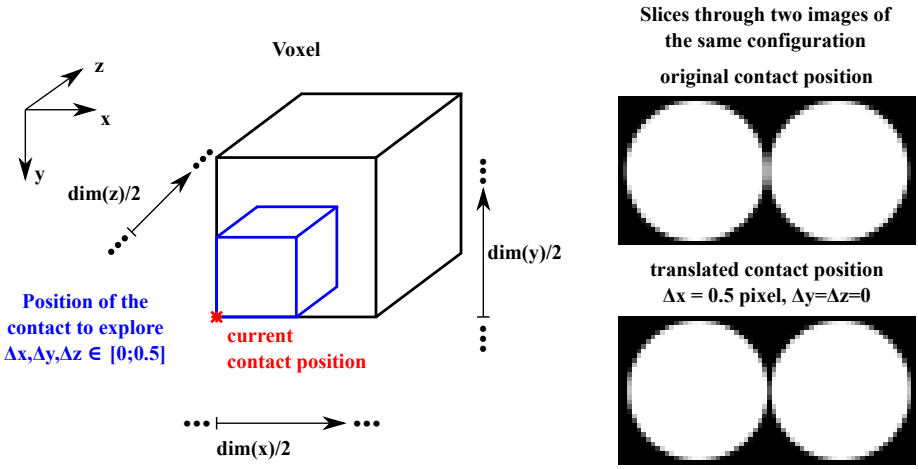

Figure 8.4: Influence of the position of the contact points on the detection. Left: Schematic of the contact position within a voxel in the centre of the image. Red – the original position. Blue – the range of positions that is explored here. Right: 2D Slices through the 3D images of spheres at a distance of 1 pixel. Due to their different positions relative to the grid, they appear in contact in the upper image and not in contact in the lower image.

again, exploiting symmetry of the particles and the imaging grid, only 3 representative changes are presented here:

- (1) $\Delta x = \Delta y = \Delta z = 0.5$
- (2) $\Delta x = \Delta y = 0.5; \Delta z = 0.$
- (3) $\Delta x = 0.5; \Delta y = \Delta z = 0.$

The analysis on contact detection is conducted using these centres between the spheres with a diameter of 30 pixel for the creation of the synthetic images of the 5000 reference configurations. The images are otherwise perfect as no image defects are considered to keep the analysis free from these partially random defects. The results of changing the centre position between the spheres with respect to the image grid is plotted in Figure 8.5. The influence of this change on the over-detection distance for the 5000 reference configurations is negligible.

The influence of the imaging grid on individual configurations, however, is important, as Figure 8.4 clearly shows. In order to show that, the configurations that are still detected as a contact are evaluated for the distances

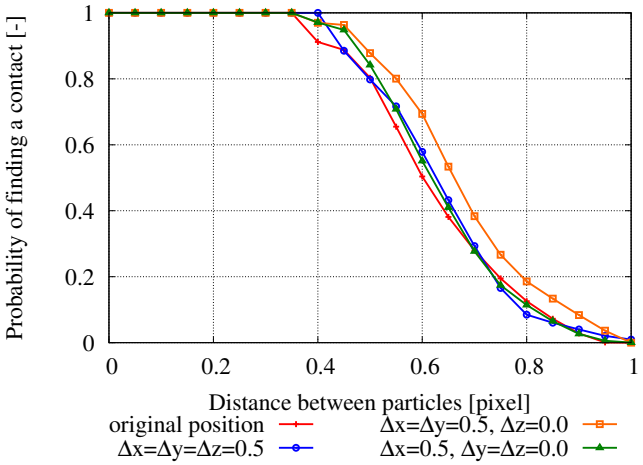

Figure 8.5: Results of the analysis on contact detection for synthetic images of spheres with a diameter of 30 pixel. Influence of the position of the spheres with respect to the image grid. No image defects are considered. A physically correct global threshold of 0.5 is applied.

of 0.6 and 0.9 pixel between the spheres for the original position as well as the position changed by $\Delta x = \Delta y = \Delta z = 0.5$. These orientations are shown in Figure 8.6 with a reference to Figure 8.5. It is obvious that the over-detection distance of a specific configuration is strongly dependent on its position in the image grid. The statistical over-detection distance, however, is not influenced by the the relative position of the spheres in the grid. Thus, it will not be considered further in this analysis.

8.1.5 Locally adaptive thresholding

In addition to the developed approach of local thresholding in this work as described in section 4.1.1, another locally adaptive threshold is assessed. This approach directly influences the binarisation process instead of working only on the detected contacts after the initial image processing. An individual threshold is applied to each voxel based on the grey-value distribution of its neighbourhood. This neighbourhood can be defined in different ways. In this small test of the approach, it is defined by a Gaussian distribution centred at each voxel with a given standard deviation σ_{gauss}. Based on this Gaussian, a weighted mean value is calculated for each voxel. This value is

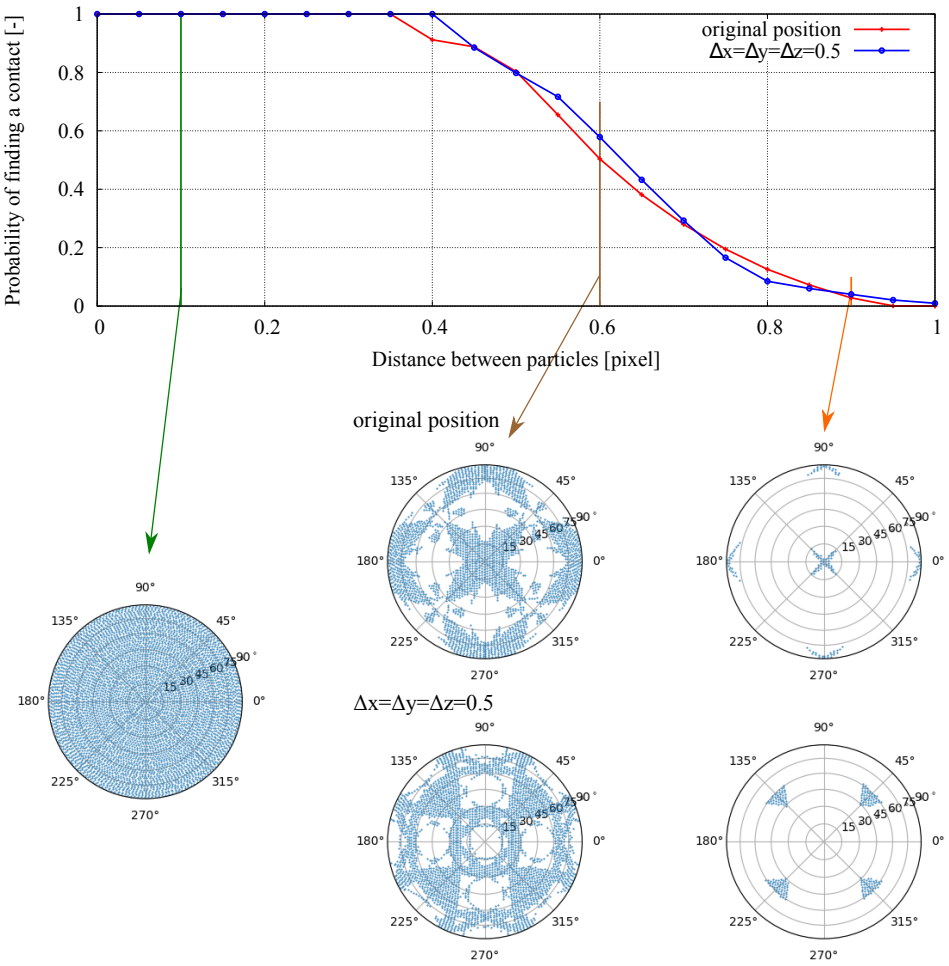

Figure 8.6: Results of the analysis on contact detection for synthetic images of spheres with a diameter of 30 pixel. No image defects are considered. A physically correct global threshold of 0.5 is applied. Top: Influence of the position of the spheres with respect to the image grid. Bottom: The orientations that appear as contacts at the distances 0.6 and 0.9 pixel for the original and one changed ($\Delta x = \Delta y = \Delta z = 0.5$) centre position of the two spheres.

then used as the threshold for the binarisation of the grey-scale image.

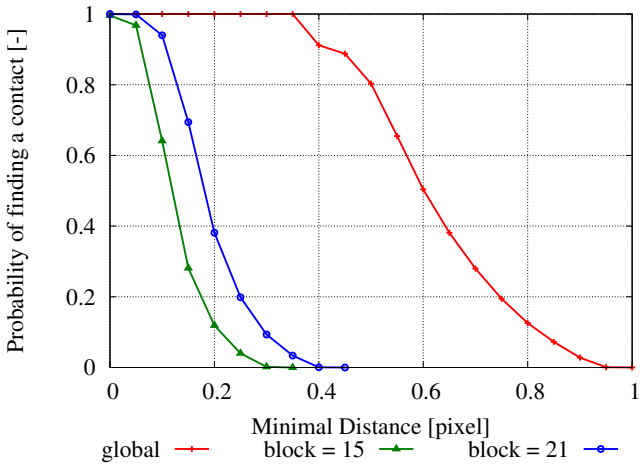

Figure 8.7: Contact detection on perfect images of spheres using a locally adaptive threshold. The area used for the local threshold is defined by the `block_size`.

This approach is implemented as the function `threshold_adaptive()` in the scikit-image python package [vdWSN+14] which is used for testing here. The size of the area to take into account for the calculation of the thresholds is captured in the variable `block_size`. This determines the shape of the Gaussian by $\sigma_{gauss} = (\texttt{block\_size} - 1)/6.0$. The approach is tested on perfect images of spheres with a diameter of 30 pixel using the same methodology as before. The results are displayed in Figure 8.7. The over-detection distance of the global threshold is again plotted using the red lines[1]. Applying the locally adaptive threshold results in similar improvements to the over-detection distance as the developed local re-thresholding. It, however, requires a thorough calibration which depends on the conditions of the image, *i.e.*, blur and noise, and the size of the particles. For blurred images the optimal block size decreases. Thus, this approach does not seem to be advantageous over the local re-thresholding developed in this work.

[1] It is identical to the red line in Figure 8.3a and to the green line in Figure 4.7a.

8.1.6 Contact orientations

To assess the accuracy of determining contact orientations, a similar procedure as in the study on the detection is developed. In this analysis, the synthetic images are created such that the two spheres are geometrically touching each other at exactly one point for every configuration that is considered, as described in section 8.1.2. The configurations that are studied are described by the reference orientations as defined in section 8.1.1, different sizes of spheres and the image defects, blur and noise. Unlike in the previous analysis, the error can be directly determined in the study on the orientations. Due to the particles being spheres, the direction of the branch vector, that is imposed in the creation of the synthetic images, is identical to the contact orientation. Thus, the orientations $\mathbf{o}$ that are determined by the image analysis can be compared with the imposed branch vectors. The error δ is defined as the angle between both orientations:

$$\delta = \arccos\left(\frac{\mathbf{b}\cdot\mathbf{o}}{|\mathbf{b}|\cdot|\mathbf{o}|}\right) \tag{8.9}$$

Two different watersheds are compared here: a common interpixel topological watershed [MB90] and a power watershed, called the random walker [Gra06]. The main difference between the two watersheds is the resulting image: the topological watershed results in a segmented image whereas the output of the random walker is a probability map. The contact orientation can be determined on the segmented image from the topological watershed by detecting the voxels in the contact area. To detect these voxels, a pixel search is run on the labelled image, that identifies voxels of one label that are touching voxels of the other label using a structural element as described in section 8.1.3. Since it is found to perform better than a full connectivity, the element from Equation 8.7 is employed here. A plane can be fitted onto the point cloud defined by these voxels using a principal component analysis (PCA): a covariance matrix is calculated for the point cloud whose eigenvectors and eigenvalues can be used for the geometric description. The eigenvector corresponding to the minimal eigenvalue describes the direction of the smallest extent of the point cloud and thus, the normal to a possible plane. This vector is considered as the contact orientation.

The random walker assigns a probability to each voxel of belonging to a specific marker. For an image of two spheres, where two markers are determined from the maxima of the euclidean distance map, the random walker

will determine two probability maps: each giving the probability of belonging to either marker 1 or 2. In this way, the contact can be described by the surface of 50 % probability of belonging to either one of the markers. The image can be labelled based on the probability map and the contacting voxels can be detected. The first step to define this surface is to identify the neighbouring voxels in the same way as for the topological watershed. The 50 % probability surface is then determined by linearly interpolating the probability values of the neighbouring voxels. The contact normal is calculated by applying the PCA on the set of points defining the surface. Figure 4.10 depicts the way of determining the contact surface from these two different watersheds.

The analysis described above is applied to all reference configurations, *i.e.*, all reference orientations per size of the spheres, per level of blur and per level of noise. The results are plotted as mean error for all 5000 reference orientations versus the diameter of the spheres in contact in Figures 8.8. The complete and the dotted lines depict the mean errors for the topological watershed and the random walker, respectively. The orange lines in Figure 8.8a show the error for the perfect images with no defects. Generally, an increasing size of the spheres leads to a lower error. This is not surprising as the diameter of the spheres corresponds to the pixel size in the images. The accuracy of the random walker is higher than of the topological watershed due to the improved spacial resolution of the contact surface. Figure 8.8a also shows the influence of blur for the levels of 0.8 and 1.6. Surprisingly, the accuracy increases with increasing this image defect. That is due to the increased contact surface which leads to a larger point cloud and thus, a more accurate fit with the PCA. On the other hand, noise does not seem to have an influence on the determination of the orientations as plotted in Figure 8.8b. The level of blur for the study on the influence of noise is set to 0.8, the representative value of the imaging system of Laboratoire 3SR, Grenoble.

In order to analyse the accuracy in more detail, a specific reference set of configurations is selected: a diameter of 30 pixel with the levels of blur and noise set to 0.8 and 0.03, respectively. A histogram of the errors of the contact orientations for both watersheds is plotted in Figure 8.9. The distribution of the errors can be represented with a Gaussian distribution in both cases. Not only the mean error but also the spread (given by the standard deviation of the Gaussian) is substantially smaller when determining the orientations from the probability map. The mean value determined by

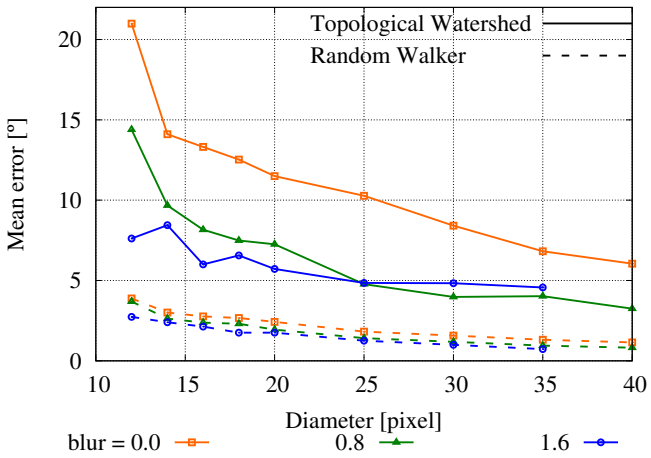

(a) Results of the analysis on contact orientations for images at different levels of blur. No noise is added to the synthetic images.

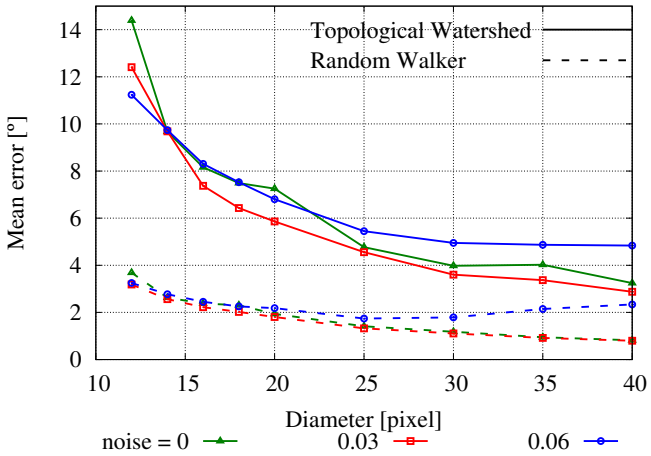

(b) Results of the analysis on contact orientations for images at different levels of noise at a fixed level of blur of 0.8.

Figure 8.8: Results of the analysis on contact orientations including image defects. Comparison of a standard topological watershed and the random walker segmentation for various sizes of touching spheres.

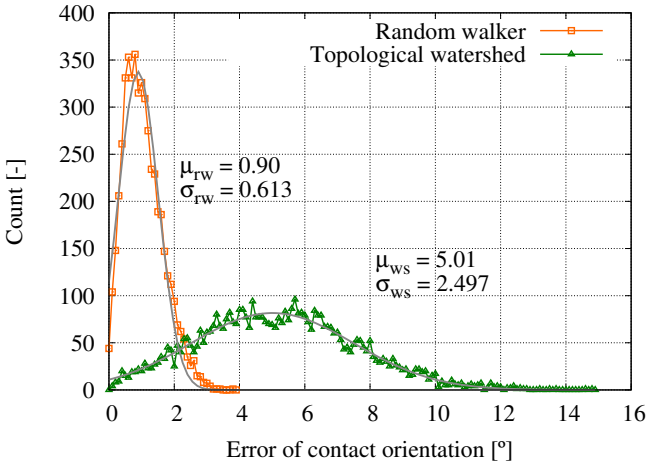

Figure 8.9: Histogram of the error of contact orientations determined on images of spheres with a diameter of 30 pixel and levels of blur and noise of 0.8 and 0.03.

the fit of the Gaussian onto the histogram is slightly lower than the statistical mean value determined on the data: for the random walker, the mean value of the Gaussian is $\mu_{RW} = 0.90$ whereas the statistical mean is $\mu_{RW} = 1.097$. The statistical mean values, however, are used for the analysis on all configurations.

Figure 8.10 shows the individual results for the chosen set of configurations in Lambert projections. The topological watershed introduces a bias towards diagonal axes, *i.e.*, axes having an angle of 45° with respect to the cartesian axes. That can be observed from the concentration of points along the azimuthal values of 45°, 135°, 225° and 315° as well along the inclination of 45°. On the other hand, no clear bias can be observed in the plot of the results from the random walker.

8.1.7 Using levels set for contact orientations

Level sets are a highly promising approach to extract information from images of granular materials as presented in [VAVA13]. This approach is assessed here to complement the study on the metrology of inter-particle contacts. Reid Kawamoto from Caltech (at that time), which is the group that pushes the level set method in granular material research, supplied

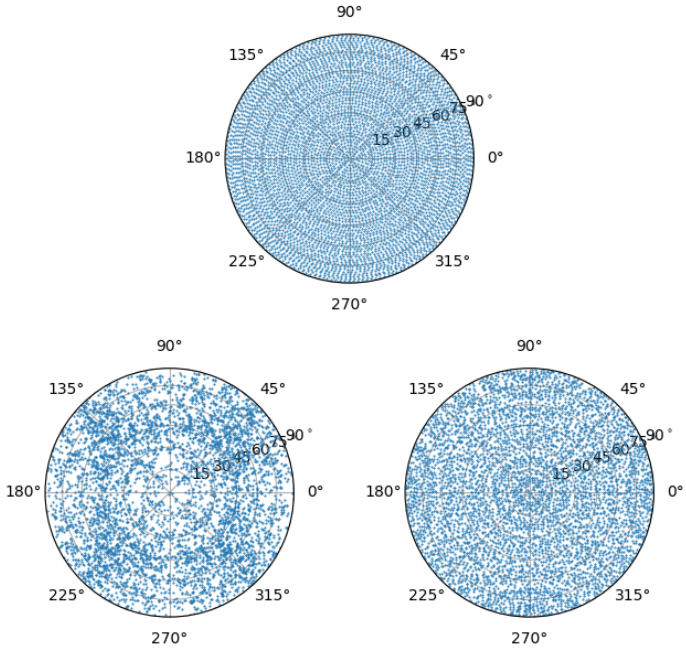

Figure 8.10: Lambert azimuthal equal area projections of the orientations for the reference set of configurations. The synthetic images have spheres of a diameter of 30 pixel with a level of blur and noise of 0.8 and 0.03, respectively. Top: Reference set. Bottom left: Orientations from the topological watershed. Bottom right: Orientations from the random walker.

us the matlab routines. These are fitting a level set to each particle and then determine the contact orientation between two presumably touching particles. The complete approach is outlined in [VAVA13] and only briefly described here. In order to fit a level set to each particle, the particles first have to be identified. Therefore, the standard approach described in section 9 is employed to binarise, segment and label the image. The binary image of each grain is eroded several times and serves as the initial guess of the level set. This level set then grows based on the original grey-value image mainly driven by the image gradient such that the boundary of the final level set agrees with the largest gradient, *i.e.*, the boundary of the particle. Unfortunately, at the time of implementation, the routine did not use a convergence criterion and thus, requires a distinct amount of iterations to obtain the final level set. This number needs to be calibrated and tested on the images. The level set is basically a distance map with the zero

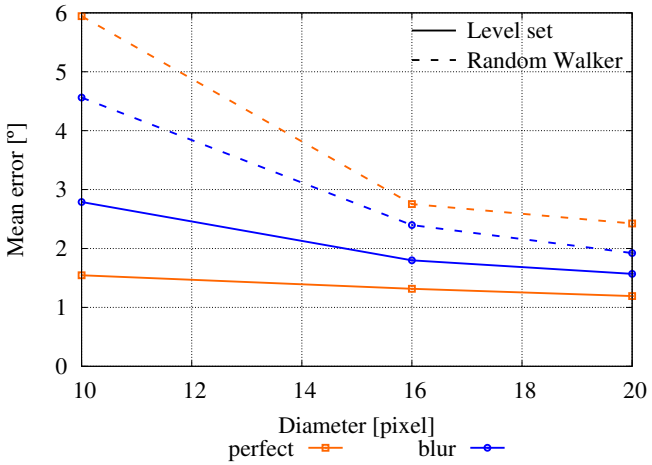

Figure 8.11: Results of the metrological study on contact orientations of individual contacts using level sets. Level sets are compared to the random walker watershed for perfect and blurred synthetic images of spheres of varying diameters.

contour being the surface of the particle that is described. This property is exploited to determine the contact orientation by overlaying the level sets of both particles and thus, finding the area of the apparent contact. The orientations itself is then calculated from the gradient of the level sets in this area.

This approach is applied to the systematic analysis on contact orientation using Kalisphera and the reference set of orientations as presented in 8.1.6. The matlab routines for the use of the level sets are coupled with the python code written for this analysis using the `oct2py` routine [S$^+$]. The results for perfect and blurred images and for different sizes of spheres are plotted in Figure 8.11 for both, the level set method and the random walker. The level sets yield more accurate orientations than the random walker which is already improving the standard topological watershed considerably. With increasing diameter of the spheres, the errors of both methods quickly get close to each other. The computational cost, however, is substantially higher for the level sets. In the case of the supplied matlab routine the computation with level sets took 50 times as long for a diameter of 20 pixel and otherwise perfect images, *i.e.*, no blur or noise, as the random walker.

8.2 Study on high resolution tomographies

In contrary to the synthetic images in the first part of this study, the ground truth for any of the measures that are used in this work cannot be known from real images. Thus, images of selected materials were acquired at a low pixel size in a nano focus x-ray imaging system.

8.2.1 Acquisition of high resolution tomographies

These images were acquired with the imaging system of Laboratoire SIMaP[2] in Grenoble. Grains of different materials are part of this imaging campaign, of which only Hostun sand and manufactured spheres are included in this work. The Hostun sand grains have an average diameter $d_{50} = 380\,\mu m$[3] whereas the manufactured spheres all have a diameter of $d = 400\,\mu m$. These spheres were created by *Sandoz Fils SA*[4] with a tolerance of $0.125\,\mu m$ on sphericity and $1\,\mu m$ on the diameter. To study contacts between touching particles, grains were filled in a glass capillary with an inner diameter of 1.57 mm allowing for several contacts to develop also along the radial direction.

Images of a part of the filled capillaries were then acquired at the settings: 2 s exposure time, low gain, 50 kV and 100 µA. The 3D image was reconstructed using the commercial software X-Act from 1200 radiographs recorded at 4 complete turns of the specimen (4 times 360°). Originally, these tomographies are 16-bit images and thus, each tomography has a size of 9 GB. In order to carry out this metrological analysis considering available computer memory and processing speed, the images are transformed to 8-bit images still yielding tomographies of 4.5 GB. The tomographies are binarised with Otsu's threshold [Ots79] and segmented using the topological watershed that is implemented in the commercial software Visilog [BFNS11]. This initial segmentation, however, results in a high degree of over-segmentation[5], *i.e.*, particles themselves are split into multiple pieces. As the images consist of a limited number of particles, the over-segmentation is corrected manually by merging labels that belong to the same particle.

[2] SIMaP is the Laboratoire Science et Ingenierie des Materiaux et Procedes – simap.grenoble-inp.fr

[3] This is the diameter at a 50 % passing of the grain size distribution.

[4] http://www.sandoz.ch/

[5] The over-detection is visualised in Figure 9.3 in section 9.4.

(a) Glass capillary

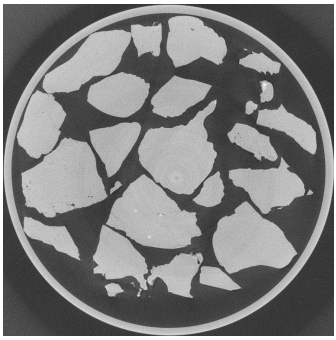

(b) Grey-scale image

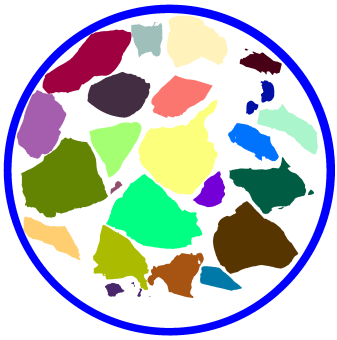

(c) Labelled image

Figure 8.12: Acquisition and pre-processing of the high resolution tomographies of Hostun sand grains.

Due to the low pixel size, the optical identification of over-segmented particles is sufficient for this correction.

8.2.2 Treatment of the high resolution tomographies

The analyses of the contact fabric on the high resolution tomographies have to be carried out in a comparable manner as the analysis on synthetic images. The main challenge for a comparable analysis, however, is that the ground truth of the contact fabric is not known a priori as in the case of synthetic images. Thus, the reference quantities have to be defined on these original images.

The topological watershed implemented in Visilog segments the image by deleting the pixels that define boundaries between touching regions – these boundaries are called watershed lines. They are determined by subtracting the segmented image from the not segmented binary image. The watershed lines are labelled in order to create a list of contacts assigning particles to each contact. A pixel search is carried out on each watershed line using a structural element as in Equation (8.7) to detect all labels that are touching any of the voxels of the respective watershed line. A contact is registered

only in the case in which there are two labels touching a watershed line. This procedure was developed in [And13] and is described there in more detail. 137 and 196 contacts are detected in the images of the manufactured spheres and Hostun sand grains, respectively.

As these images do not comprise the complete glass capillary, the grains on the bottom and top end of the image are only included partially. Dealing with the grains that only partially lie in the image is problematic as the full field of information of the grains is needed and thus, these grains are excluded from the analysis and deleted in the images. After excluding these grains, 99 and 135 contacts are detected in the images of the manufactured spheres and sand grains.

The reference for both analyses is determined on the images at the original pixel size of 1 µm. The analyses itself, however, is carried out on images at larger pixel sizes to determine the accuracy on spatial resolutions that are typical for tomographies of representative specimens in mechanical tests. This downscaling of the gold standard images has to consider realistic image properties in a similar way as already described in section 7.4. Only a pair of contacting particles is downscaled at a time in the analysis. This pair is fetched from the image based on the list of contacts. To fetch a pair from the original image, a binary image of only the two particles representing the pair is applied onto the original grey-scale image as a mask. To safe time and memory , this operation is run on subsets of both the binary and the grey-scale image that are determined by finding a bounding box that includes both particles. The resulting image only has the grey-scale information from the particles with the void phase being set to zero due to the application of the mask. In order to consider the image properties similarly to the synthetic images, the grey level is shifted such that the mean grey value of the solid phase is close to 191, which is equal to 0.75 in a 32-bit image with a range of [0.; 1.], and thus, corresponds to the reference histogram for calibration in section 7.4. To complete the image, the values of empty void voxels are set to a grey value of 64, equivalent to 0.25 in the reference range.

The images of contacting particles are downscaled with the function `scipy.ndimage.zoom`. The order of the zoom is 0, which corresponds to a binning when scaling down, *i.e.*, the mean value of the voxels in the considered array is assigned to their corresponding voxel at the lower scale. Due to the high quality tomographies at 1 µm/pixel, the apparent blur and noise is lower than for the reference images in section 7.4. That effect

becomes even stronger after the scaling to higher pixel sizes. Thus, noise and blur have to be applied on the downscaled images. In the current workflow the noise is set to 64 and due to the lack of any initial variation, an application of noise to the image after scaling impacts the solid phase more strongly than the void phase. To prevent this, noise is already applied before scaling and calibrated such that the standard deviation of both phases, solid and void, is similar after scaling. The levels of noise and blur applied to the scaled images are calibrated to consider the image properties that are set as a reference for the metrological analysis. A level of noise of 20 for the initial application before scaling is iteratively found to yield good results. After the scaling, the levels of blur and noise are set to 0.7 and 3, respectively. Note that the noise levels appear higher than for the synthetic images, but that is due to applying noise to 8-bit image with a range of values of [0;255]. As the blur is a spacial measure, it is close to the value that is applied on the synthetic images.

The procedure of downscaling can be summarized in the following steps:

1. Fetching of the particles in contact
2. Translating the grey-level of the image to yield the reference value of the solid phase
3. Setting the empty void space to a value of 64 and apply random noise
4. Downscaling the image to the desired pixel size
5. Applying image defects blur and noise

8.2.3 Contact detection

The analysis on the detection of contacts has to be slightly adapted in order to be applicable to the real tomographic images, but still be comparable in order to extent the findings from synthetic images to real images. The grains detected to be in contact in the original image at 1 µm/pixel are considered to be in contact and as such serve as the golden standard. The analysis starts with fetching two grains touching each other in this original image. The distance between the grains is subsequently increased as in the analysis on the synthetic images. For every distance, the image of the two grains under consideration is downscaled as described in the previous section. After scaling, the same approach as in section 8.1.3 is taken: the grey-scale images are binarised with the global threshold and directly labelled using

the structural element from Equation 8.7. If the number of distinct objects is one, the grains still appear as being in contact. Otherwise, no contact can be detected anymore. The distance between the grains in the original image is increased until no contact can be detected at any of the pixel sizes. After applying the global threshold of 125 and detecting the contact, the different local thresholds are tested in the same way for every imposed distance. The local thresholds that are investigated here are 140153166 for the 8-bit images with a range of $[0; 255]$ which are equivalent to 0.550.60.65 in the reference range of $[0.; 1.]$. Note that the original grey-values are translated in order to yield mean values of the void and solid phase that are comparable to the reference values defined in section 7.4.

The images are downscaled to pixel sizes of 5, 10, 15 and 20 µm in the following analyses. These are equivalent to the spatial resolutions that can be reached in the imaging system in Laboratoire 3SR, Grenoble. The oedometric and triaxial compression tests conducted within this work have pixel sizes of 10 and 15 µm, respectively.

The particles are translated from each other in the direction of the branch vector. The main reason for this decision is that the branch vector is the most accurate measure of orientation from the image for every particle shape as the centre of mass is a very reliable measure. One of the main problems of implementing this approach is the calculation of the distance between the particles after translating them from each other. This problem didn't exist in the analysis on the synthetic images as the distance between two spheres is known if the centre and the radii are known. Especially for the angular Hostun sand grains with partially convex surfaces, calculating the distance is not as simple. The easiest solution would be to calculate the distance between all voxels of one grain to all voxels of the other grain and to determine the minimum of these distances. That, however, is highly time and memory consuming as the grains consist of 20 to 50×10^6 voxel. In order to save both, time and memory, another approach is developed here. The grey-scale image of the translated particles is binarised with the global threshold. To get an image of the edges of both particles, a mask is built by eroding the binary image by 2 iteration steps. This mask is applied onto the binary image, which results in an image of both edges that is labelled afterwards. Applying an erosion with two iterations is important to identify and label the edges of each particle continuously[6]. A binary

[6]The one pixel layer, that would result from an erosion with one iteration, is usually not continuously connected and thus, causes problems for the labelling.

tree [Knu78] is built with the positions of the voxels that define one of the edges. These binary trees are very efficient in mapping data and for this particular case can also be queried for distances. This allows to look for the minimum distance between the edges of the particles by querying the tree for distances to all the voxels defining the other edge. The minimum of these distances represents the minimal distance between both particles. As the distance between the particles has to be calculated for every increment of the translation for every contact pair, the gain in speed and the smaller memory usage is worth the implementation. The implementation used for the binary tree is the function `scipy.spatial.cKDTree` from the scipy package [JOP+].

The sensitivity of the over-detection distance with the pixel size is plotted in Figure 8.13 for both materials. The detection of contacts in both materials, the spheres and the Hostun sand grains, does not seem to be influenced by the pixel size. This is in contrast to the analysis on synthetic images, that shows a light influence of the size of spheres on the over-detection distance, see Figure 8.2a. The synthetic spheres are tested for diameters of 16, 20, 30 and 100 pixel. To cover a similar spatial resolution, the pixel size of manufactured spheres are scaled to 5, 10, 15 and 20 µm which corresponds to 80, 40, 26.7 and 20 pixel along the diameter of 400 µm. Although similar ranges are investigated, the analysis on real tomographies of spheres does not show an influence of the pixel size for the standard contact detection with the global threshold. The same scaling results in 67.6, 33.8, 22.5 and 16.9 pixel along the average diameter of the Hostun sand grains. The over-detection is slightly influenced by the spatial resolution of the images, see Figure 8.13b. The lowest pixel size yields the highest over-detection distance. This is in light accordance to the results obtained on synthetic images.

Overall, the systematic over-detection of contacts is apparent in both materials. The extent is higher for the spheres than for the angular Hostun sand. This can be represented by the distance at 50 % probability of finding a contact, which is 1 pixel for the spheres and varies from 0.5 to 0.6 pixel for the Hostun sand grains. As the images are prepared in order to have almost identical properties after the scaling, the only difference is the shape of the surface of the particles. Especially the shape in the vicinity of the contacts must be responsible for these results. Angular shapes might yield very singular contacts which are not as susceptible to over-detection as the round surfaces of spheres.

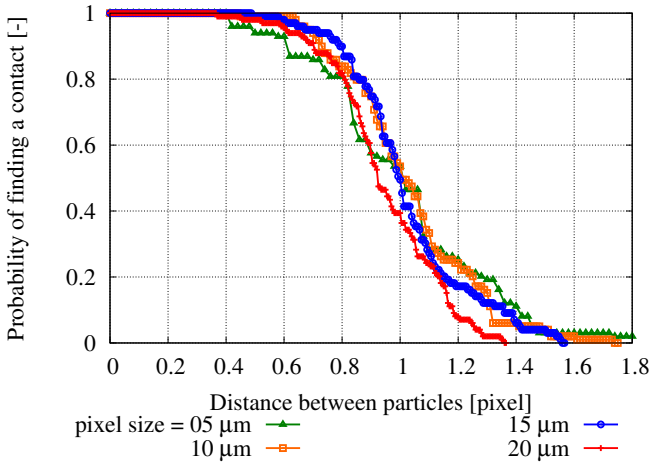

(a) Contact detection for manufactured spheres at varying pixel sizes.

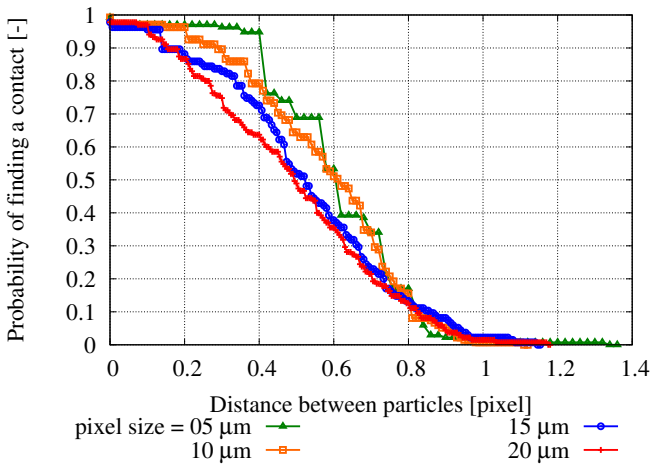

(b) Contact detection for Hostun sand at varying pixel sizes.

Figure 8.13: Results of the study on contact detection on the high resolution tomographies. Influence of the pixel size on the over-detection distance. To detect contacts only the global threshold is applied on the scaled grey-scale images.

8.2.4 Contact orientations

The metrological analysis of contact orientations on the high resolution tomographies is carried out in the same spirit as on the synthetic images. At first, the reference orientations for every contact has to be determined. As the manufactured spheres were created with a low tolerance on their sphericity, their geometric shape can be exploited: the branch vector is calculated based on the centre of mass of both particles in contact and normalised to give the reference contact orientation. This measure is very reliable due to the centre of mass being determinable to a very high accuracy.

Due to their irregular shape, the reference orientation of contacts in Hostun sand cannot be determined from the corresponding branch vector. Thus, the golden standard is deduced from the image processing of the original tomography at 1 µm/pixel. A PCA is run on the positions defining the watershed line that segments the particles in contact. The eigenvector corresponding to the minimum eigenvalue is considered to be the normal to the contact plane and thus, the reference orientation.

Each pair of contacting particles is fetched from the complete tomography as described in 8.2.2. The images are scaled to pixel sizes of 8, 10, 12, 14, 16, 18 and 20 µm considering the reference image defects calibrated in section 7.4. The same analysis as for the synthetic images described in section 8.1.6 is carried out at these lower scales: the grey-scale image of the contact pair is binarised and the Euclidean distance map (EDM) of this binary image is calculated. Based on the EDM, the markers are selected for the two watershed approaches that are investigated in this study: the topological interpixel watershed and the random walker. The contact orientation is calculated from either the position of contacting labels or from an interpolation of the probability map for the topological watershed and the random walker, respectively. The angle between these calculated orientations at the respective pixel size and the reference orientation is considered to be the error of the measurement.

Figures 8.14 show the results in terms of the mean error versus the size of the contacting particles. The size is displayed as the number of pixels along the diameter for the spheres and along the average diameter d_{50} for Hostun sand. In general and in accordance with the results on the synthetic images, the accuracy of determining contact orientations using the labelled image of the topological watershed is lower than when using the probability map from the random walker. In the case of the spheres, the mean error

of the topological watershed reduces linearly with the spatial resolution. That is, however, not true for the random walker which seems to yield orientations that are almost independent of the pixel size. This seems to not be in accordance with the results on synthetic images in Figure 8.8. The reduction in mean error for the synthetic images is however only small with increasing resolution. Due to the restricted number of investigated contacts, the slightly increasing trend from the high resolution images can still be associated with the results on synthetic images.

Contacts in Hostun sand show a substantially higher mean error of up to 27° for the topological watershed and 18° for the random walker as plotted in 8.14b. Multiple reasons for this high error can be identified from the images due to several scaling effects: (1) the creation of artificial contacts, (2) the enlargement of existing or artificial contacts and (3) the merging of originally distinct contacts. They are visualised on two examples in Figure 4.12 and explained in section 4.1.2

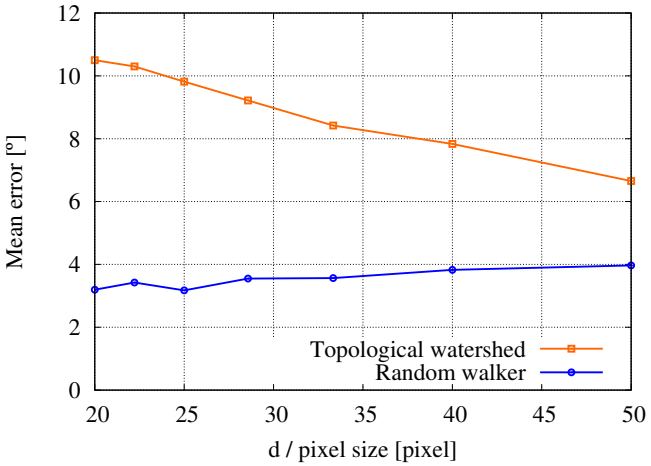

(a) Contact orientations studied on spheres.

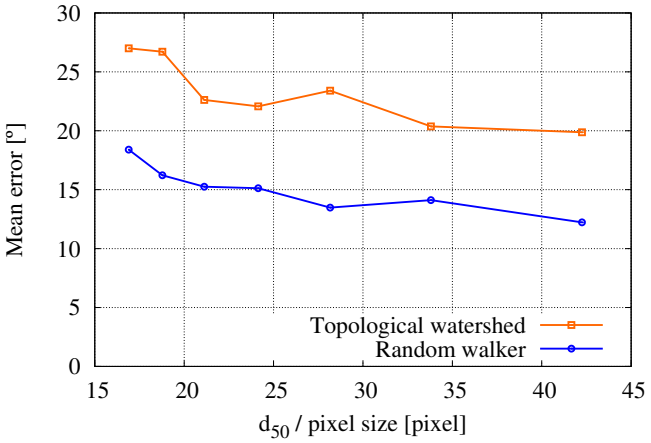

(b) Contact orientations studied on Hostun sand.

Figure 8.14: Accuracy of contact orientations studied on high resolution tomographies. The accuracy is plotted via the mean error from all investigated contacts in the respective materials. The size of the contacting particles is presented as the number of pixels across the diameter of the spheres and across the d_{50} for Hostun sand.

9 Image analysis toolbox

This chapter covers the image analysis tools that are used within this work. The toolbox that is developed relies on some standard image processing steps that are presented in the first part of this chapter. This is followed by a description of the implementation of the refinements and improvements suggested in the metrological study on individual contacts. To save computation time and memory for the analysis of assemblies, the implementation of these refinements has to be adapted to large amounts of contacts. Due to image defects such as noise, there are some tricks that improve the analysis and that are necessary for some parts of this implementation to work. These tricks are briefly explained as well.

The approaches developed in this work, mostly the local refinement of contacts and the determination of orientations, were implemented in a personal python code in the beginning of this work using the open source packages numpy [Oli06], scipy [JOP+] and scikit-image [vdWSN+14]. These scripts were implemented later in the open source software *spam* [ACR+], the Software for Practical Analysis of Materials, after some researchers from Grenoble, among which is Edward Andò (a supervisor of this thesis), started to develop this tool.

In order to supplement the description of the image analysis toolbox and visualise some steps, the tools are applied on an illustrative image. A synthetic, but realistic image of a numerical assembly of spheres as used in section 10.1 is utilised for this purpose. The general steps in order to extract the contact fabric mostly using the software *spam* are applied on this image. All of the scripts presented here can be applied to the images from the metrological study and can also be found in the open access archive [Wie19]. Where necessary, real tomographies of Hostun sand are used, as not all the features can be reproduced by synthetic images of spheres.

Particle orientations are not covered in this chapter, but are also part of the image analysis toolbox developed in this thesis and implemented in *spam*. The corresponding tools and their application are presented in section 12.4.8 on the triaxial compression tests.

9.1 Standard image processing

The starting point for the image analysis in this work is the reconstructed tomography. The commercial software X-Act[1] is used for the reconstruction of the tomographies from the originally recorded radiographies. The reconstruction itself, however, is not part of the analysis in this work and is thus, not discussed further. See [KC01] for a review on reconstructions of x-ray tomographies.

The reconstructed tomography is usually a 16-bit grey-scale image. The range of grey-values thus lies in the range $[0; 65{,}536]$. These images can be pre-processed if the level of noise is too high. In this work, mostly median 3D filters with a range of 2 pixel in radius are employed, because they tend to be edge preserving. There exist a huge variety of image filters to reduce the noise, but their application is generally connected to some kind of data loss. This could for example be a loss of the sharpness of edges. As some of the image analyses in the beginning of this work were carried out on servers with limited memory, these 16-bit images are scaled to 8-bit images in order to save memory during the computations. Later, 16-bit images are processed because of generous allocations of computation time on the high performance cluster of the ZIH in Dresden.

The first challenge in the image analysis is to distinguish the phases of the granular material in the image. Only dry materials are investigated in this work and thus, a binarisation is sufficient to separate the two phases, void and solid. Generally, a global threshold is defined and applied to each voxel in the image: all voxels with values above that threshold are set 1 and all others to 0. This global threshold can either be defined on the statistical distribution of grey-values in the image, *e.g.*, using Otsu's threshold [Ots79], or based on physical properties such as the mass of the specimen. If the mass is known and with the density assumed constant, the corresponding solid volume can be expressed in voxels. The threshold can then be determined from the histogram of grey-values summing all appearances starting from

[1] https://www.rxsolutions.fr/

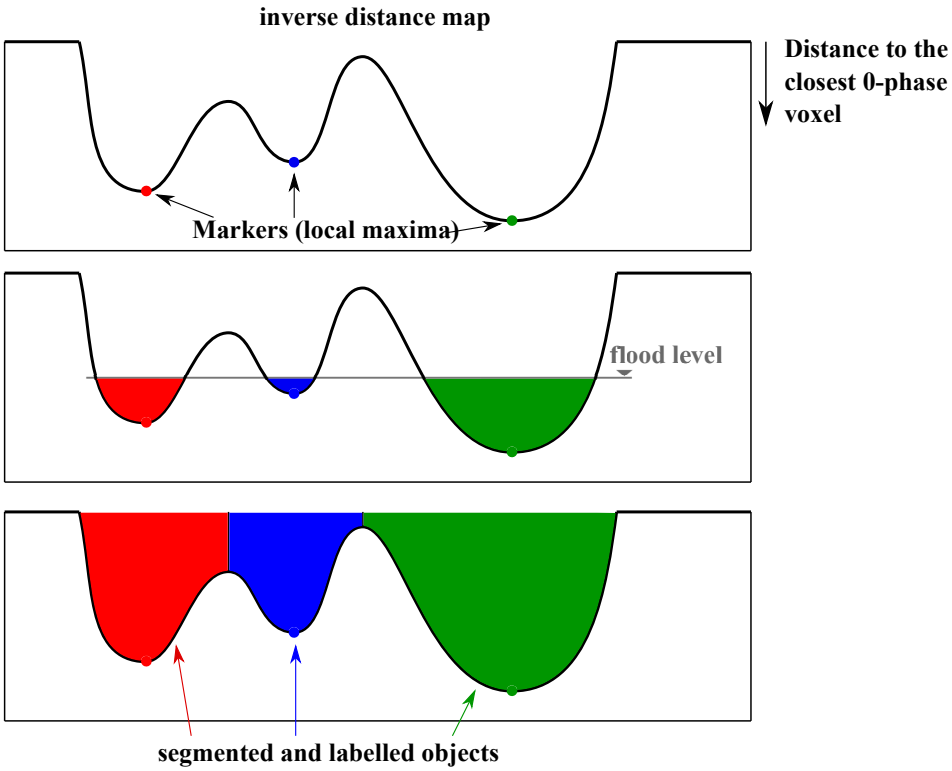

Figure 9.1: 1-D sketch of the functioning of the topological watershed. From top to bottom: The local maxima of the distance map are determined for the starting points of the watershed. The basins of the distance map are flooded starting at the markers until reaching the 0-phase of the distance map. Final segmented and labelled image.

the highest grey-level until the amount of voxels is reached. The grey-level at this state is considered to be the global threshold. In the case of our example, the physically correct threshold is known from the creation of the synthetic image, see section 7.4, and amounts to 128 for the 8-bit image.

The next crucial step is the segmentation of the individual particles. The most common approach in geomechanics and many other disciplines is a topological watershed [MB90]. The basis of most watershed approaches is a Euclidean distance map (EDM) of the binary image. These EDMs assign the distance to the closest void voxel (0) to every voxel in the solid phase (1). Local maxima are determined from the distance map and serve as markers for the watershed later. Different options can facilitate the choice

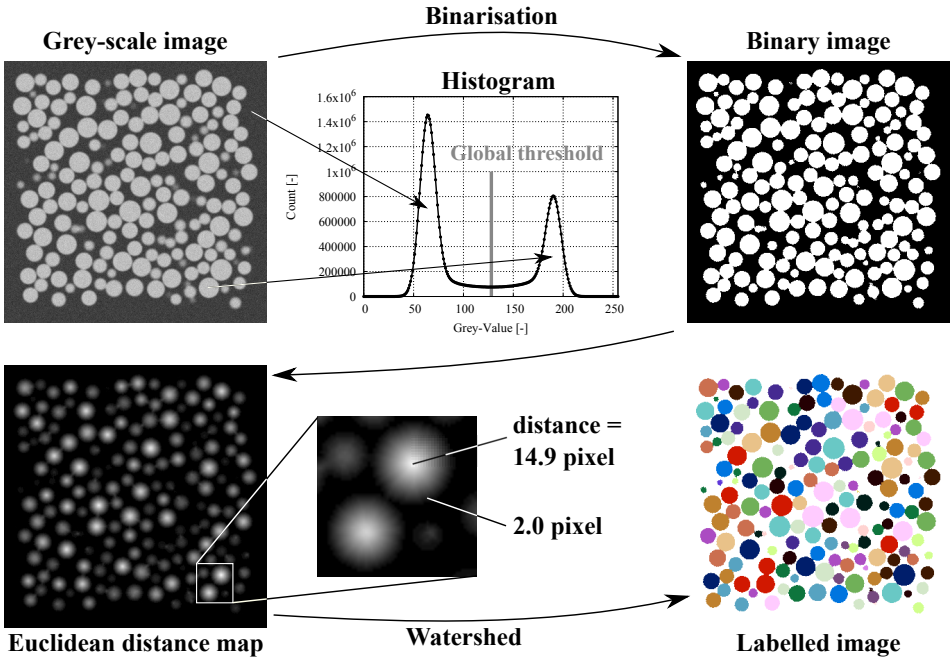

Figure 9.2: Workflow of the common image processing shown on a 2D slice of a 3D image. The grey-scale image (top left) is turned into a binary image (top right) using a global threshold (top centre). A distance map (bottom left) of the binary image is calculated and serves as input to the watershed segmentation that yields the labelled image (bottom right). A zoom-in to the distance map shows the distance of the centre and the boundary of a sphere to the nearest 0-phase (void).

of markers from the local maxima of the EDM, *e.g.*, the spacing of the markers or the amount of markers totally assigned in the image. That is especially important when concave shapes are imaged, *e.g.*, in angular grains, as the EDMs of these grains might exhibit multiple local maxima. An example is shown in section 9.4.

Each marker will define a segmented object in the final image and thus, the number of markers is equal to the number of objects after the segmentation. The distance map is inverted to serve as a valley of basins that is going to be flooded. The low point of each basin is the marker defined from the local maxima and the basins are flooded starting from these markers until the image is fully flooded and the basins are occupied. The fill of each basin is associated to its marker and given a label to distinguish it from the other

basins. An example for the application of a topological watershed on a 1-D problem is given in Figure 9.1. There are two different ways of defining the final segmented and labelled image: (1) The voxels at the boundaries of two contacting basins are not associated to the basin, but extracted and form watershed lines; (2) The voxels are always associated to a basin. These implementations are called inter-pixel watersheds. The result of both implementations of these topological watersheds are images in which the particles are given a unique label. These common image processing steps are shown on the illustrative image in Figure 9.2. The script to carry out these steps is printed in Listing 9.1. The python package *numpy* [Oli06] alongside the package *spam* is employed for this initial set up of the images.

The labelled image might be prone to errors, especially if the level of noise is high or the particles that are imaged have a complex shape. Noise can lead to patches wrongly associated to the solid phase and thus, wrongly appear as a labelled object. Irregularly shaped particles are prone to be over-segmented, *i.e.*, multiple local maxima are identified in the distance map, which causes the watershed to wrongly separate the particle in multiple pieces. Approaches to decrease these errors are described in section 9.4.

Listing 9.1: Python script using *spam* for the initial image processing of the exemplary image

```
import numpy, tifffile

import spam.label.ITKwatershed as ws
import spam.label.label as ltk

folder   = 'images/'
filename = 'triax.-1.eps=0.spheres_image_gaussian=08
    _noise=03'

# global threshold
threshold = 95

# parameter for dealing with noise patches
pixelSizeMicrons = 15 #mum
radiusThreshMicrons = 50. #mum
radiusThresh = radiusThreshMicrons/pixelSizeMicrons

greyVol = tifffile.imread(folder+filename+'.tif')
```

```
# binarisation
binVol = ((greyVol > threshold)*1).astype('uint8')
# image output
tifffile.imsave(folder+filename+'-bin.tif', binVol)

# segmentation and labelling
labVol = ws.watershed(binVol)

# dealing with noise patches
radii = ltk.equivalentRadii( labVol )
labelsToRemove = numpy.where( radii < radiusThresh )

if len(labelsToRemove[0]) > 1:
    labVol = ltk.removeLabels( labVol, labelsToRemove)
    labVol = ltk.makeLabelsSequential( labVol )

maxLabel = labVol.max()
print('\tNumber of particles identified ', maxLabel)

tifffile.imsave(folder+filename+'-lab.tif', labVol.
   astype('uint16'))
```

9.2 Detection of contacts in assemblies

Contacts are detected on the labelled image. The approach used in this thesis was developed in [And13] for watersheds that create labelled images with watershed-lines as briefly described previously. Watershed-lines have the advantage that the contacts can be detected starting from an image with watershed-lines only and zeros otherwise. The watershed lines are labelled based on structural elements, as *e.g.*, defined in Equation (8.7), and considered to be potential contacts between labelled objects. For every watershed-line, a pixel search of the neighbours of every voxel belonging to the line is run on the labelled image to detect all labels that are in contact with the watershed line. The neighbourhood is defined similar to the sparse connectivity. In this way, every contact $c \in N_c$ is assigned two particles A and B.

This approach to detect contacting particles can also be applied to labelled images from inter-pixel watersheds. The difference is that the pixel search is run for every labelled voxel in the labelled image instead of only the labelled watershed-lines. Thus, the computation time is higher for the latter watershed.

In both cases a list of contact pairs as well as a list of contacts per particle is produced. The first, called contact list in this work, is a list giving the two touching particle labels per row as shown in Table 9.1.

row number = contact label	particle labels A, B	
1	label A	label B
2	label A	label B
...		
N_c	label A	label B

Table 9.1: Layout of the contact list. The labels of both particles (A and B) per contact $c \in N_c$ are given per row.

The latter is listing all particles and the corresponding contact labels that are in contact with the particle in consideration as described in Table 9.2. It can be used for the calculation of local coordination numbers or to fetch all contacts of a given particle, *etc.* Note that this list is redundant as a contact is assigned to two particles, A and B and thus, appears in the according rows.

row number = label A	contact 1 of label A		contact 2 of label A		...
					...
label 1	label B	contact label	label B	contact label	...
label 2	label B	contact label	label B	contact label	...
		...			
label N_p	label B	contact label	label B	contact label	...

Table 9.2: Layout of the list of contacts per particle. All contacts per particle are given as tuples (label of the counterpart and label of the contact) in the respective row.

As it is shown in section 8.1.3, contacts that are detected on the basis of an image binarised with a global threshold are systematically over-detected. In order to reduce the over-detection, a local threshold is applied to every contact in the following way. A grey-scale sub-image of the pair of particles belonging to the contact in consideration is fetched from the complete image. In order to fetch an image consisting of only the two particles, the labelled image of the two particles is used as a mask and applied to the grey-scale image. Any additional noise that might appear after this operation is removed as described in section 9.4. Similar to the approach proposed and validated in section 4.1.1, the 'clean' grey-scale image is binarised with a local threshold. This local threshold must be calibrated or inferred from the study on the high resolution tomographies in section 8.2.3. The connectivity is checked in the new binary image of the apparent contact using the structural element from Equation (8.7). If more than one object is found, the contact is deleted from the contact list. As this operation must be applied to every contact, this part of the code is parallelised to save computation time.

It is possible to apply this approach only on a sub-image of the specific contact rather than on the sub-image including both particles in contact completely. A mask can be defined on the contacting voxels which is then dilated several times. This mask is applied to the complete image to get the sub-image of the contact and the local refinement can be applied on the enlarged contact area directly. This approach, however, is slightly more error-prone due to the fetching of the sub-image. It is for example harder to deal with the individual noise patches due to the actual particle being only partially present in the image. Furthermore, if the initial watershed segmented the image erroneously the contact can be located within a particle due to over-segmentation or also just slightly off the actual apparent

contact. Thus, the fetching of the contact although dilating could produce a sub-image that does not include the contact itself. As these codes are run fully automatically on the image, the first approach is implemented since it is less error-prone.

The code for the example that is accompanying this study is given with the code on the determination of the orientations in listing 9.2. A local threshold of 180 is used for the computation in the example. This value for the 8-bit image corresponds to the optimal local threshold of 0.7 found for the synthetic spheres on 32-bit image with a range of [0.;1.].

9.3 Determination of contact orientations in assemblies

The orientation of every contact from the (refined) contact list is determined in the following way. Similar to the local refinement of the contact list, a sub-image of the two grains in contact is fetched from the complete image. For this analysis, it is sufficient to fetch the binary image as well as the labelled image depending on the method chosen for the calculation. It is possible to determine the orientation from the original topological watershed or using the random walker. The latter is substantially slower, as an additional segmentation has to be performed.

There are two main steps for the calculation from the initial watershed. In order to identify the voxels in contact, a pixel search is run on every voxel belonging to label A of the respective contact using the same connectivity as before as defined in Equation (8.7). If a voxel of label B is found in the neighbourhood, the positions of both corresponding voxels in contact are recorded in a list of positions defining the contact. A principal component analysis (PCA) is performed on the set of contacting positions. The eigenvector corresponding to the third eigenvalue of the covariance matrix is considered to be the contact normal.

There are more additional steps if the orientation is chosen to be computed using the random walker. The EDM on the binary sub-image of both particles and the local maxima of this map are computed. The random walker segmentation is then run on the inverse of the distance map, starting from the defined markers. These markers are chosen from the local maxima of the distance map, but might be manipulated to account for complex parti-

cle shapes: *e.g.*, multiple local maxima can appear in a single particle in the case of concavely shaped surfaces. The result of the random walker are two probability maps that assign every voxel a probability of belonging to either one of the markers (labels)[2]. A labelled image can be created based on this map with every voxel being assigned the label for which it has a higher than 50 % probability of belonging to. The set of contacting positions is determined on this labelled image. The advantage for this method is that the probability map can be directly used to determine the contacting surface on a sub-pixel level. In order to do so, the actual values of each contact pair from the list of contacting positions are queried for their probability. These probabilities are then linearly interpolated to find the position of the 50 % probability of the contact pair. The PCA is performed on this set of points.

Similar to the detection of contacts, the determination of each contact orientation is independent from the other contacts and is parallelised for faster computation. The script for the determination of the contact fabric for the accompanying example, including both the detection and the orientation, is given in Listing 9.2. The option `RW` is chosen in the script to determine the orientation with the random walker. If they are to be determined from the initial watershed, the option has to be set to `ITK`. The orientations are saved in a list with every row consisting of a tuple for every contact. The tuples are assembled in the following way: (label A, label B, o_z, o_y, o_x, data set) with o_i being the component of the contact orientation $\mathbf{o}$ in the respective axis and the data set being the number of points supplied to the PCA.

Listing 9.2: Python script using spam for the extraction of contact fabric of the accompanying example.

```
import tifffile, numpy
import spam.label.label as ltk
import spam.label.contacts as con

folder   = 'images/'
filename = 'triax.-1.eps=0.spheres_image_gaussian=08
    _noise=03'

NumOfThreads = 3
```

[2]The probability map and its handling is visualised in Figure 4.10 in section 4.1.

```
# do you want to do local thresholding? If yes, which
    local threshold?
LOCALTHRESH = True
localThreshold = 180

# parameter for dealing with noise patches
pixelSizeMicrons = 15. #mum
radiusThreshMicrons = 50 #mum
radiusThresh = radiusThreshMicrons/pixelSizeMicrons

###############
volLab  = tifffile.imread(folder+filename+"-lab.tif")
volGrey = tifffile.imread(folder+filename+".tif")
###############

# 1 - contact List
print("\tCreating the contact list\n")
contactVolume, Z, contactsTable, contactingLabels =
    con.labelledContacts(volLab)

numpy.savetxt(folder+filename+"-contact_table.txt",
    contactsTable)
numpy.savetxt(folder+filename+"-contact_list.txt",
    contactingLabels)

# 2 - refine contact list
print("\tRefining the contact list with a threshold of
    ", localThreshold, "\n")
contactListRefined = con.localDetectionAssembly(volLab
    , volGrey, contactingLabels, localThreshold,
    radiusThresh=radiusThresh, NumberOfThreads=
    NumOfThreads)
numpy.savetxt(folder+filename+"-contact_list_local=%03
    i.txt"%(localThreshold), contactListRefined,fmt='%i
    ')

# 3 - contact orientations
print("\tDetermining contact orientations with the
    random walker\n")
```

```
contactOrientations = con.contactOrientationsAssembly(
    volLab, volGrey, contactListRefined, watershed="RW"
    , NumberOfThreads=NumOfThreads)
numpy.savetxt(folder+filename+"-local=%03
    i_orientations_rw.txt"%(localThreshold),
    contactOrientations,fmt=('%i %i %f %f %f %i'))
```

9.4 Some tricks for the analysis of real tomographies

9.4.1 Dealing with noise patches

Noise in the image among other defects can lead to elevated grey-levels. If these values are higher than the global threshold, the respective voxels are assigned to the solid phase. It is crucial to exclude these voxels from the solid phase as otherwise they will be considered in the labelling and finally impact the contact fabric. The elevated grey-values usually appear either individually or in patches. This can occur also for locally adaptive thresholding approaches although no actual value is prescribed.

One approach used in this study is to label the binary image, which might be the complete image or a sub-image of a contacting pair of grains. The connectivity used in this labelling is again the sparse structural element defined in Equation (8.7). All labels that have less than a prescribed number of voxels are set to zero and thus, excluded from the image.

An equivalent way of excluding noisy patches can be employed using some functions implemented in *spam*. The equivalent sphere radii of every label in the labelled image are determined and the labels with radii smaller than a threshold are excluded. As these approaches are applied after the initial segmentation, the labels are made sequential for a continuous assignment of labels. An illustrative code using the functions implemented in *spam* is given in listing 9.3.

In both cases the threshold for excluding small objects has to be calibrated: either as amount of voxels or as equivalent radius. The latter seems more natural in soil mechanics with the particle size distribution (PSD) being

expressed by equivalent radii and usually known before the testing the materials.

Listing 9.3: Python script using *spam* for excluding noise patches from labelled images.

```
# dealing with noise patches
radii = ltk.equivalentRadii( labVol )
labelsToRemove = numpy.where( radii < radiusThresh )

if len(labelsToRemove[0]) > 1:
    labVol = ltk.removeLabels( labVol, labelsToRemove)
    labVol = ltk.makeLabelsSequential( labVol )
```

9.4.2 Dealing with over-segmentation

Non-spherical particles tend to be over-segmented by watershed approaches. There are different ways to reduce the amount of over-segmentation, *e.g.*, by changing the watershed algorithm [FJ10] or adapting the distance map [ZH16]. In this work the implementation of the ITK watershed [YAL+02] in *spam* is employed for the segmentation, which generally yields good results. However, there are still some particles that are over-segmented.

An over-segmented particle tends to have large contact areas between the parts it was segmented into. If particles are imaged that have a relatively narrow PSD, these tend to be larger than a standard contact in the assemblies. Thus, the over-segmentation is detected by determining the size of the contact, which amounts to the number of contacting voxels, and comparing it to a calibrated threshold. If the size is bigger than the threshold, it is assumed that a particle is over-segmented and both labels involved in the apparent contact are merged. In this work, the over-segmentation only has to be dealt with in images of Hostun sand and is mostly calibrated by trial. A histogram of all contact sizes in the labelled image is used to get an initial value of this threshold. An example of over-segmentation and its successful correction is shown in Figure 9.3 for an image of Hostun sand. The code for this small example is given in Listing 9.4.

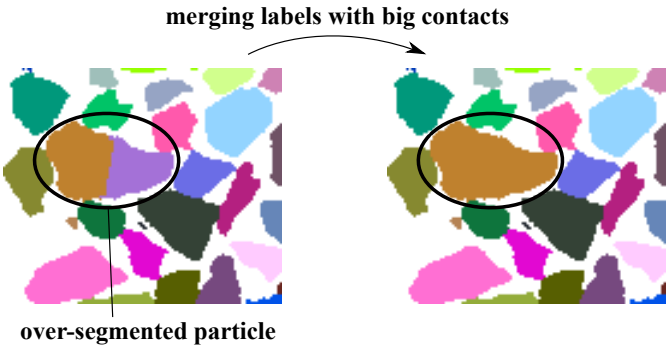

Figure 9.3: Showcase for over-segmentation of particles and the successful correction. Sub-image of the initial state of an experiment on Hostun sand (HNEA01).

Listing 9.4: Python script using *spam* for dealing with over-segmentation on Hostun sand.

```
from spam.label import contacts

threshOverseg = 300 #number of voxels

if threshOverseg!=0 :
    # fixing over-segmentation
    labVol = contacts.detectAndFixOversegmentation(
        labVol, nVoxThreshold=threshOverseg)
```

9.4.3 Choosing markers for the random walker

Especially for angular shapes, the local maxima have to be modified in some cases to supply reliable markers to the random walker segmentation. In this work, the random walker is applied to a binary sub-image consisting of two particles presumably in contact. Based on the initial labelling with the topological watershed, this sub-image is extracted from the image of the complete assembly. More than just two local maxima can appear in the Euclidean distance map for irregular shapes or if defects are present in the sub-image, *e.g.*, ring artefacts. The local maxima are determined by the function `skimage.feature.peak_local_max()` from [vdWSN+14]. It has an option to set the minimal distance between the maxima. This can

prevent to define markers that are unreasonably close and can be calibrated based on the PSD if it is sufficiently narrow. In the case that more or less than two local maxima are identified, a correction is performed: If less markers are detected, the distance between the local maxima is decreased until two markers can be found. After a pre-defined number of iterations, the detection of markers is stopped and no orientation will be calculated. If more than two maxima are identified, the distance for each set of maxima is calculated and the maxima with the highest distance are chosen to become the markers for the segmentation.

Non-spherical, elongated particles can lead to local maxima of the distance map that consist of more than one voxel. As it was found that the random walker segmentation produces more realistically labelled images when starting from markers that consists of an individual voxel, these elongated markers are shrunk. To do so the individual local maxima are uniquely identified by labelling them with a structural element that is a full (3x3x3) connectivity. The centre of mass is determined for each local maxima and serves as a marker for the segmentation.

9.5 Determination of the coordination number

The coordination number could either be calculated from the list of detected contacts or the list of contact orientations. It is defined as two times the ratio of the number of contacts N_c to the number of particles N_p as in Equation (7.9).

As some grains tend to be over-segmented, the list of contact orientations is the choice for the calculation. One output of the determination of orientations that is saved in this list, is the apparent size of the contact, *i.e.*, the number of positions that is used for the PCA. This number enables to exclude over-segmented grains, because they appear as contacts and tend to have an unreasonable large apparent contact size. The list of orientations is cleaned using the same threshold for the maximum contact size as used in the determination of orientations and the correction of the initially labelled image, see the previous section. In the case of angular grains, very small contacts of sharp surfaces are not well defined image-wise and although being apparently in contact, tend to be over-detected as shown in 8.2.3. Thus, contacts whose orientation is determined on less than two positions are excluded from the analysis as well.

Listing 9.5: Python script for the determination of the coordination number from the list of contact orientations.

```
orientations = numpy.loadtxt(folder + filename + "-
    local=180_orientations_rw.txt")
orientations_new = numpy.copy(orientations)

#exclude over-segmentation and very small contacts!
for i in range(len(orientations)):
    if (orientations[i,5] < 2) or (orientations[i,5] >
        300):
        index = numpy.where((orientations_new[:,0] ==
            orientations[i,0]) & (orientations_new[:,1]
             == orientations[i,1]))
        orientations_new = numpy.delete(
            orientations_new,index,0)

contacts = orientations_new[:,0:2]
numContacts = len(contacts)
numParticles = len(numpy.unique(contacts))
coordNumber  = 2.*float(numContacts)/float(
    numParticles)
print("Effective coord number ", coordNumber)
```

The number of particles that contribute to the contact network might be different from the number of labels in the labelled image as some might be excluded in the cleaning of the image due to an over-segmentation or due to being noise patches as described in 9.4. Thus, only labels in the modified list of contact orientations are taken into account to determine the number of particles. The coordination number is then computed using the modified number of contacts and particles. An exemplary python script that showcases these operations is included in the listing 9.5. Note that if this number is determined on a complete specimen, contacts between the membrane or the cell and the grains are not included in the coordination number which leads to a lower value. If the coordination number is calculated on a subset inside the specimen, even the contacts to the grains outside of the subset can be included. The value for the subset should, thus, be higher than for the complete specimen unless the specimen is dilating strongly inside the subset.

Another remark on the coordination number is the accuracy. As it is pointed out in the study on the metrology of the contact fabric in this work, the number of detected contacts is not reliable as contacts are systematically over-detected. Even though the number of contacts is modified using thresholds to diminish the effect of over-segmentation and over-detection, the determined values should be higher than the real ones. It is, however, complicated to estimate an error from the probabilistic over-detection of contacts.

9.6 Calculation of the void ratio

The void ratio cannot be directly measured from the experiments, because the specimens are dry. Thus, it has to be determined from the images. The strategy pointed out in [And13] on binary images is followed in this work.

The void ratio e is defined as the ratio of the pore to solid volume:

$$e = \frac{V_p}{V_s} = \frac{V - V_s}{V_s} \tag{9.1}$$

The solid volume V_s is simply determined by summing up all voxels of the binary image, because the solid phase was set to one in the binarisation step. It is, however, not simple to calculate the total volume V of the specimen as the membrane has a very low x-ray attenuation and is thus not clearly identifiable in the image. A simple filling of the solid space could not work to determine V, as the void space is interconnected throughout the specimen. Thus, the solid space is dilated several times in order to close the interconnected voids. The remaining voids are filled with a 3D algorithm of scipy [JOP$^+$]. At this stage, the binary phase of the image is not only capturing the solid and void phase but also some part on the outside of the specimen due to the dilation. In order to get rid of this part, the image is eroded by the same amount as it was dilated before. Summing up all the voxels in this image, gives the total volume V of the specimen, *i.e.*, the combined solid and void part. The void ratio is then calculated as defined above from the void volume, *i.e.*, the difference of total and solid volume, and the solid volume. The number of iterations for the erosion and dilation operations depends on the spatial resolution of the image, *i.e.*, the grain size with respect to the pixel size. An illustrative python script is shown in listing 9.6.

Listing 9.6: Python script for the determination of the void ratio from binary images.

```
binVol = tifffile.imread(folder+filename+"-lab.tif")
binVol = ((binVol > 0)*1).astype('uint8')

binVol_work = scipy.ndimage.morphology.binary_dilation
    (binVol,iterations=iterDilation).astype(binVol.
    dtype)
binVol_work = scipy.ndimage.morphology.
    binary_fill_holes(binVol_work).astype(binVol.dtype)
binVol_work = scipy.ndimage.morphology.binary_erosion(
    binVol_work,iterations=iterDilation).astype(binVol.
    dtype)

totalVol = binVol_work.sum()
solidVol = binVol.sum()

porosity  = (totalVol - solidVol)/float(totalVol)
voidRatio = (totalVol - solidVol)/float(solidVol)

print("void ratio ", voidRatio)
print("porosity   ", porosity)
```

9.6.1 Classifying the determined void ratios

As the mass of every specimen is measured after conducting the experiments, the void ratios determined on the binary images can be complemented with a physical measurement. It has to be noted, that the determination of the mass is error-prone due to the small size of the specimen. A couple of individual grains could be lost or some water might enter the specimen when removing it from the cell which might impact the measurement strongly. To diminish the effect of water that could have entered the specimen, they were dried for two days. The volume can be determined from the image by measuring the height and the diameter of the specimen. Multiple measures are taken on the original grey-scale images and averaged for the computation of the volume. The void ratio can then be calculated

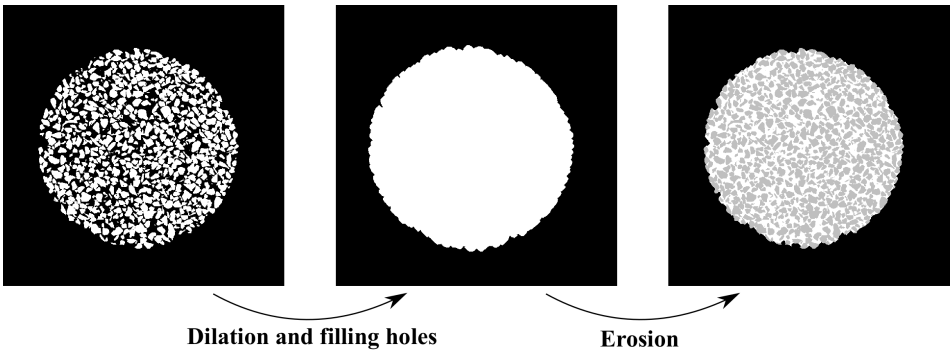

Figure 9.4: Visualisation of the determination of the void ratio from a tomography. All images show a horizontal slice through the specimen HN-MWTC04 at its initial state. Left: Binary image with the solid phase shown in white. Centre: Image after the dilation and the filling of holes. Right: Image after the erosion with an overlay showing the solid phase (from the left image).

from:

$$e = \frac{\rho_s}{\rho_d} - 1 \tag{9.2}$$

with ρ_s and ρ_d being the specific density of the grains and the dry density of the specimen, respectively. The initial void ratios of all experiments are determined using both methods and given in table 9.3.

experiment	TC02	TC03	TC04	TC05	OD01
e_0 – image	0.661	0.723	0.722	0.655	0.711
e_0 – physical measure	0.677	0.656	0.728	0.645	0.862
Δe_0	-0.016	0.067	-0.006	0.010	-0.151

Table 9.3: Comparison between the methods of determining the void ratio from the experiments. The void ratio is either computed on the binary image or from the measured physical quantities mass and volume.

The difference between both measurements lies between 0.006 and 0.016 for triaxial compression specimen. There is no bias to either side of the measurement: for some specimens the image analysis yields a lower for others a higher void ratio than the physical measurement. Only the void ratio of the experiment TC03 differs strongly by 0.067. The void ratios calculated on

the binary images yield more consistent results with the method of preparation as the specimen TC03 and TC04 have a looser initial packing than the pluviated TC02 and TC05. The preparation and the initial fabric of the specimen is described in section 12.4.1.

The measurements from the oedometric compression sample differ strongly by 0.151. The void ratio determined on the binary image seems more plausible than the physical measure as it compares well with the triaxial compression samples that are prepared similarly, *i.e.*, TC03 and TC04. Thus, the void ratio from the image analysis is used as a reference in this work.

10 Metrological study on assemblies

The starting point of the metrological analysis of contact orientations were individual contacts. These were studied through controlled synthetic images before transitioning to high resolution tomographies of idealised and natural particle shapes. To relate these findings to assemblies and determine the influence of the uncertainties on statistical expressions, a synthetic benchmark was developed based on a numerical sphere packing under loading. An experiment on glass beads in the μCT in Laboratoire 3SR is chosen as the last step to transition from these idealised images to real tomographies on natural materials.

10.1 Study on synthetic images

In the light of transparency and verification, all the scripts needed for the creation of the synthetic images and their processing including the determination of the contact fabric are collected in the open access repository Opara [Wie19]. The output from both DEM simulations is directly included in the repository.

10.1.1 Numerical simulations as a reference

For the purpose of analysing the accuracy of the image analysis tools, the DEM simulations can be relatively simple compared to simulations that investigate the actual behaviour of granular materials. Thus, the most simple contact model, the linear (Cundall) contact model [CS79] is used to control the particle interactions. It consists of a linear elastic spring in the normal as well as the tangential direction of the contact. The friction is modelled by an additional slider that operates in the tangential contact plane. The

constitutive parameters necessary for this model and used for the following simulations are a friction coefficient of $\tan\varphi = 0.4$, Young's modulus of $E = 50 \times 10^6$ Pa and a stiffness ratio of $k_t/k_n = 0.4$ with k_t and k_n being the tangential and normal components of the stiffness. The simulations are conducted on packings of spheres. The particle size distribution referring to the diameter ranges linearly from 320 to 480 μm in order to lie in range of interest of the materials investigated in this work. Periodic boundaries are employed in these simulations to minimize possible localisation phenomena.

Two simulations are conducted for this metrological analysis: a monotonic and a cyclic triaxial compression test. The initial state for both simulations is identical. 5522 spheres are created in a pre-defined box which is then isotropically compressed to a stress of 50 kPa. The isotropic compression is controlled by increasing the stress of the assembly isotropically, which might be achieved by anisotropically increasing the overall deformation field due to the discrete nature of the assembly. As long as the stress stays isotropic, the periodic boundaries can move by different extents in the 3 directions.

The triaxial compression is performed by the function `WeirdTriaxControl()` of *WooDEM*[1]. The radial stresses σ_x, σ_y are kept constant during the actual compression and the axial strain ϵ_z is increased by a defined amount. After reaching the final axial stress, the sample is unloaded to the initial isotropic stress state. That is achieved by controlling all the stresses and adjusting the deformations of the boundaries accordingly. In order to create images from the simulations for the metrological analysis, the complete fabric, *i.e.*, the positions of the particles, their radii and the contact orientations, is saved at specific stages of the loading process. After reaching these pre-defined stages, the assembly is relaxed by waiting until the unbalanced force of the system is lower than a specified value and the fabric is recorded.

Figure 10.1 shows the macroscopic response of the assembly during the monotonic triaxial compression test as well as the chosen stages at which the fabric is recorded. The initial state is created with the same friction coefficient as used in the simulation of the test. It can thus be considered as a loose initial packing, which corresponds to its response. The stress deviator keeps increasing until reaching the prescribed axial strain and the volumetric strain is compressive until 7% of axial strain. With increasing strain the assembly changes to a dilatant volumetric behaviour. At the load reversal, the sample is contracting again, which is well in agreement with actual measurements on granular materials.

[1]The manual of *WooDEM* can be accessed at https://woodem.org/

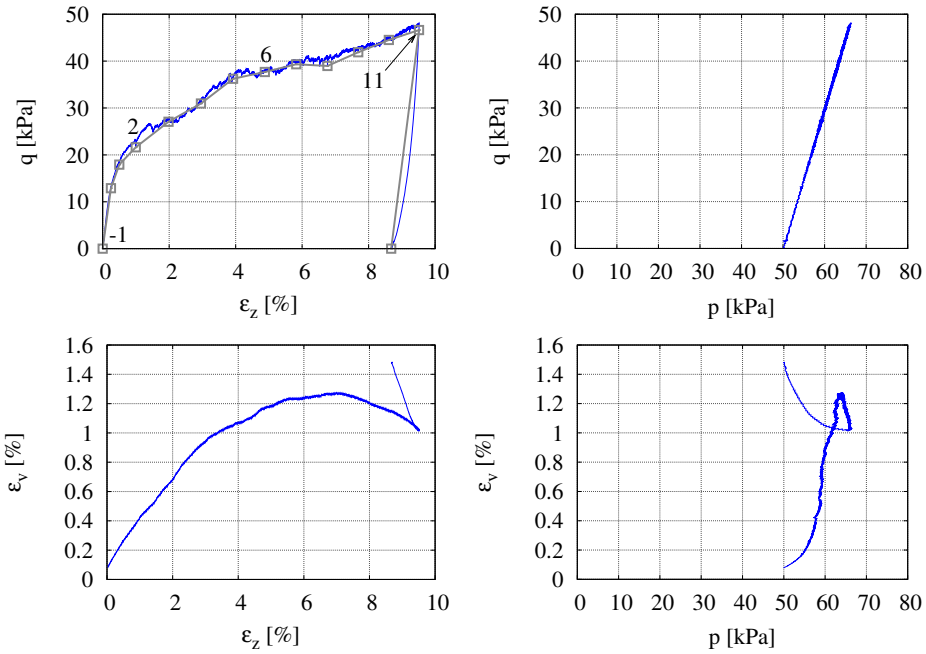

Figure 10.1: Macroscopic response of the numerical assembly to monotonic triaxial loading. Blue – actual response recorded every 100 computation steps. Grey – stages of the loading chosen for the recording of the fabric. The numbers in the subplot of $q - \epsilon_z$ refer to the states that are analysed in more detail in 10.1.4

The control of the cyclic triaxial compression test is conducted similarly to the monotonic test. Unloading and reloading cycles are added at chosen deformation states of the axial loading, beginning at rather small strains and being repeated until reaching the final axial strain. The sample is again unloaded to the initial isotropic stress state by servo controlling all stresses. The reloading is performed in the same manner as the actual loading by keeping the radial stresses constant and increasing the axial strain until it reaches its value from the start of the cycle.

The macroscopic response of the sample to the cyclic loading is plotted in Figure 10.2. This simulation is carried out until reaching an axial strain of 18% and thus, a much higher strain than in the monotonic test. The evolution of the deviatoric stress is similar to the monotonic simulation, but the volumetric behaviour deviates due to the cycles. Every unloading-

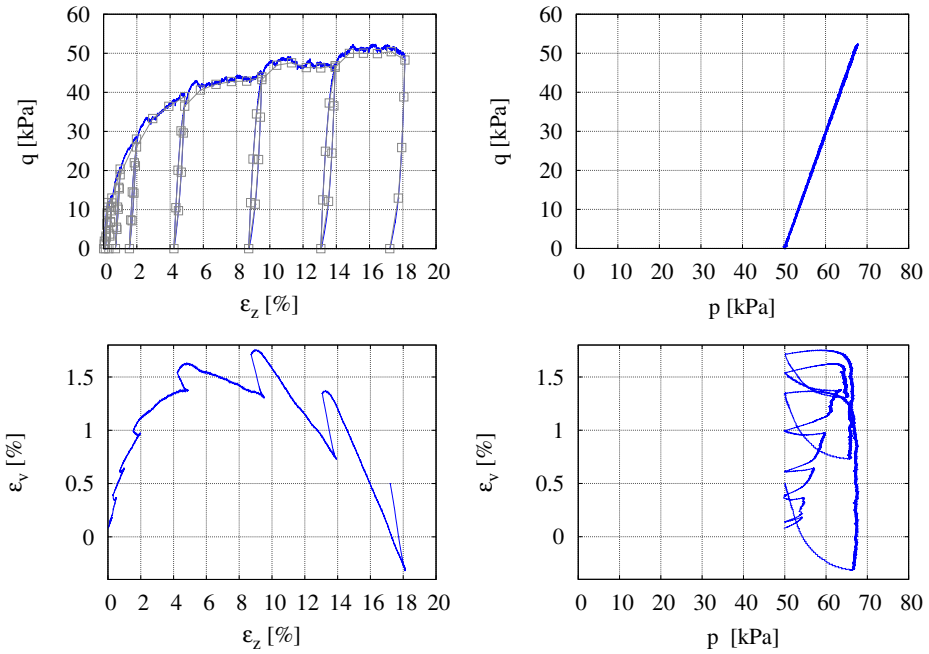

Figure 10.2: Macroscopic response of the numerical assembly to cyclic triaxial loading. Blue – actual response recorded every 100 computation steps. Grey – stages of the loading chosen for the recording of the fabric.

reloading cycle leads to an increase of volume, in the compressive as well as the dilatant part of the behaviour. Overall, the volumetric behaviour agrees to the monotonic test qualitatively as it switches from compressive to dilatant at around the same axial strain.

10.1.2 Transforming numerical assemblies into images

The numerical assemblies have to be transformed into realistic images, featuring the most important image properties and defects, such as the partial volume effect, blur and noise. To create the images, the positions and the radii of the spheres are extracted from the recordings of the fabric at the chosen loading stages. As these data are recorded in [meter], they are divided by the pixel size in order to translate them into image coordinates, which are given in [pixel]. The pixel size is chosen to 15 µm, corresponding to the majority of experiments conducted in this work. The average

diameter $d_{50} = 4 \times 10^{-4}$ m is translated to 26.67 pixel and lies in the range studied in the analysis on the metrology of individual contacts, see section 8. The python code for reading the input from the output files creating with *WooDEM* and translating the measures, that are in the metric system [meter] to the image system [pixel], is given in Listing 10.1.

Listing 10.1: Python script for the creation of a synthetic image from a *WooDEM* packing: reading the input and translating the measures into pixel.

```
import numpy, math, tifffile, scipy.ndimage
import spam.kalisphera as kali

filename     = "triax.-1.eps=0.spheres"

num_lines = sum(1 for line in open("positions/"+
    filename+".txt"))
pixel_size = 15.e-6 #m/pixel
gaussian   = 0.8    #std dev
noise      = 0.03   #std dev

# loading the dem file
box_size_dem = numpy.genfromtxt(folder+"positions/"+
    filename+".txt",skip_footer=(num_lines-1),comments=
    '%',usecols=(1,2,3))
centres    = numpy.loadtxt(folder+"positions/"+filename
    +".txt",skiprows=0,usecols=(4,3,2))
radii      = numpy.loadtxt(folder+"positions/"+filename
    +".txt",skiprows=0,usecols=(5))

# get maximum radius to pad our image (periodic
    boundaries...)
r_max          = numpy.amax(radii)
box_size       = box_size_dem + 3*r_max
# move the positions to the new center of the image
centres[:,:]   = centres[:,:] + 1.5*r_max

# turn the mm measures into pixels
box_size = numpy.array([math.ceil(box_size[0]/
    pixel_size), math.ceil(box_size[1]/pixel_size),
    math.ceil(box_size[2]/pixel_size)])
```

```
box_size = int(numpy.amax(box_size))

centres = centres/pixel_size
radii   = radii/pixel_size
```

Initially an empty 32-bit image is created using the boundaries of the box defined in the numerical simulation with a range of grey-values of $[0; 1]$. The boundaries are padded by 3 times the maximum diameter of the spheres in the assembly in order to compensate for the periodic boundary conditions in the simulation, which allow particles to leave one side of the box and enter the corresponding other side. The centres of the spheres are translated accordingly by 0.5 times of this padding in order for the assembly to be centred in the image. Using Kalisphera [TA15] to incorporate the partial volume effect, a box of the same size is created for each sphere. These images are then subsequently added to the empty image. Due to this adding and the inherent overlap of spheres in the DEM simulation, some voxels in overlapping areas can obtain values higher than 1. These voxels are set back to values of 1, which is the highest possible value for the solid phase. In order to allow for a realistic addition of noise, the grey values are shifted to the range of $[0.25; 0.75]$ the mean values of the void and solid phase, respectively. Blur and noise are added to the otherwise perfect image with the calibrated levels of 0.8 and 0.03^2, respectively. The process of creating synthetic images from the numerical assemblies considering the properties and defects of real tomographies is shown in Figure 4.14. Finally, the images are transformed to 8-bit images as most common real tomographies are treated as 8-bit images rather than the memory intensive 32-bit images[3]. The whole process of creating the image using kalisphera and deteriorating it by adding blur and noise is shown in the python script in Listing 10.2.

[2] These values were calibrated to be representative of the real tomographies of the specimens used for the experiments. The calibration is described in section 7.4

[3] Note that 16-bit tomographies are also common but cost double the amount of memory when loading the initial images and more when working on them. In this work, the tomographies are mostly acquired as 16-bit unsigned integer type images. At the beginning of this work, these were downgraded to 8-bit images to analyse them on a local server with limited available memory. With the possibility of computing on the high performance cluster taurus at the centre for information services and high performance computing (ZIH) of the TU Dresden, some experiments are analysed using the original 16-bit images.

Listing 10.2: Python script for the creation of a synthetic image from a *WooDEM* packing: creating the image.

```
# create the big image
Box = numpy.zeros( (box_size, box_size, box_size),
    dtype="<f8")

# create the whole assembly
kali.makeSphere(Box, centres, radii)

# some voxels at the contact will get a value higher
# than 1.0 due to the overlap of the spheres reset
    these values to 1.0
Box[numpy.where(Box > 1.0)] = 1.0
Box[numpy.where(Box < 0.0)] = 0.0

Box = Box * 0.5
Box = Box + 0.25

# apply blur
if gaussian!=0:
    Box = scipy.ndimage.filters.gaussian_filter(Box,
        sigma=gaussian)

# apply noise
if noise!=0:
    Box = numpy.random.normal(Box,scale=noise)

# convert to 8bit image
Box = numpy.rint(Box*255)

tifffile.imsave( "images/"+filename+"_image_gaussian
    =%02i"%(gaussian*10)+"_noise=%02i.tif"%(noise*100)
    , Box.astype('uint8') )
```

10.1.3 Contact detection in assemblies

The synthetic images are processed using the tools described in chapter 9. The 8-bit grey-scale images are binarised with a global threshold of 128 which corresponds to the physically correct threshold of 0.5 for the 32-bit floating point images used in section 8.1.3. The binary image is then segmented and labelled using the ITK watershed [BL06] as implemented in *spam*. Due to the noise applied when creating the synthetic images, some patches of elevated grey-values might develop in the void space. If their grey-value is higher than the global threshold, these patches will be segmented and labelled and wrongly be associated to the solid phase. In order to exclude these noise patches, labelled objects with an equivalent diameter of less than 50 µm are excluded from the labelled image. Note that the minimal diameter of the spheres is 21.3 pixel and this threshold corresponds to 3.33 pixel. The image is relabelled sequentially afterwards to facilitate the following image analysis.

The list of contacts is initially created by the algorithm described in section 9.2 and implemented in *spam* [ACR$^+$] on the labelled image. As found in section 8.1.3, contacts between spheres are systematically over-detected. A local refinement of the original contact list is thus, applied to reduce this error. The local threshold employed here is 180, which corresponds to the value of 0.7 for 32-bit images with a range of [0.; 1.] that is found to yield acceptable results[4]. These two approaches to the detection of contacts, the common global and the locally refined one, are compared using the average coordination number CN as defined in Equation 7.9[5].

The coordination numbers for the global and local approach can be directly computed from the list of contacts and the number of labels in the image. In order to determine the reference from the DEM simulation, the periodic boundaries must be taken into account. Due to this boundary condition, contacts between spheres that are located on the one boundary might be in contact with spheres located on the corresponding opposite boundary of the numerical specimen. These contacts are detected by searching for spheres that are in contact but whose distance is further apart than their summed radii. They are excluded from this metrological analysis.

[4] This was analysed in section 4.1.1.

[5] Note that this definition of the coordination number is debatable for poly-disperse materials and there exist other definitions that account for more than just the raw numbers.

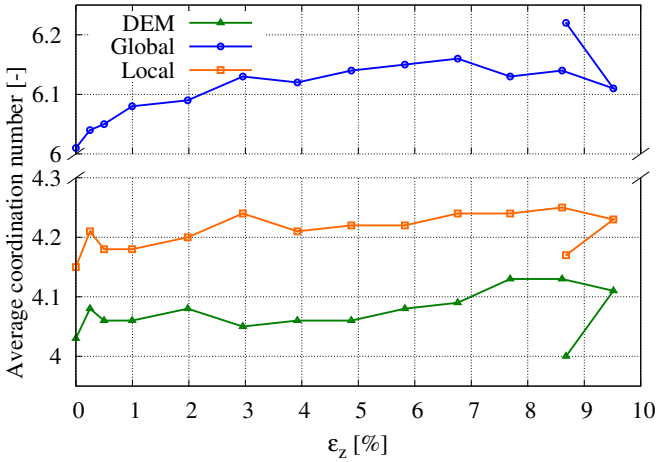

Figure 10.3: Evolution of the average coordination number in the monotonic test given by the numerical reference values (green) and determined by the global (blue) and local (orange) image analysis approaches. Note the broken vertical axis that separates the actual values due to the big differences.

Figure 10.3 shows the evolution of the average coordination numbers with the axial strain. The systematic over-detection of contacts clearly manifests in this benchmark test with the coordination number from the global approach being 50 % higher than the reference value from the numerical simulation. Furthermore, the evolution even qualitatively shows a wrong trend upon the final unloading. After refining the globally detected contacts with the local threshold, the coordination number and its evolution agree qualitatively and quantitatively with the reference showing a mean deviation of 3 %. The approach still shows more detected contacts than actually existing, which is in agreement with the study on the detection in section 4.1.1. As the local threshold is calibrated to not loose existing contacts, some particles that are close still appear as being in contact, see Figure 4.7b.

10.1.4 Contact orientations in assemblies

The orientations are determined with the locally refined contact list. Both approaches, the more commonly used topological watershed and the random walker [Gra06], are compared here. It has to be noted, that the determina-

tion of the orientations from the initial topological watershed is substantially faster because the labelled image can be used directly. The random walker has to be applied on each contact pair in order to fit the contact normal on the resulting probability map. The workflow and implementation are described in section 9.3.

The orientations are presented in two different ways here: by capturing them individually and by describing their statistical distribution. The individual orientations are plotted in Figure 10.4 using Lambert azimuthal equal area plots[6]. The bins are normalised by the average count of orientations per bin to facilitate comparing the projections and use the same legend and color scheme for all plots. The IDs −12611 indicate the stages of the loading at which the fabric is analysed and are referred to in Figure 10.1. The reference orientations appear to be isotropically distributed in the initial state. With ongoing loading the orientations align with the major principal stress direction, the vertical direction (z-axis) that is the centre in these projections.

The orientations from the topological watershed are denominated by ITK watershed following their implementation [BL06] and are plotted in the middle row. They are strongly deviating from the reference orientations in the upper row. As found in section 8.1.6 on the equally distributed orientations and in [JAVT13], there is a bias due to fitting the contact plane on the pixel information from the labelled image. For this ITK watershed, the orientations align by 45° with the major axes of the image as shown in Figure 8.10. This bias emerges even stronger in this benchmark. The distribution of orientations from the random walker in the lower row agrees qualitatively with the reference. The reason for the better agreement is the fit on the probability map which enables an interpolation of the contact plane on sub-pixel level[7].

This visual comparison needs a quantitative basis. As described in 9.2, contacts are identified by the labels of the two contacting particles. The relation from contacts in the reference DEM simulation to the images is not straightforward, because the labels are assigned in different order. Each label is topographically mapped from the DEM simulation to the respective image based on its position in the assembly. Although the labels do not change in the numerical simulation, the mapping has to be repeated for every loading state as the labels in the images might be assigned differently.

[6] These projections are described in detail in 7.2.1.
[7] See section 4.1.2 for an explanation of the probability map.

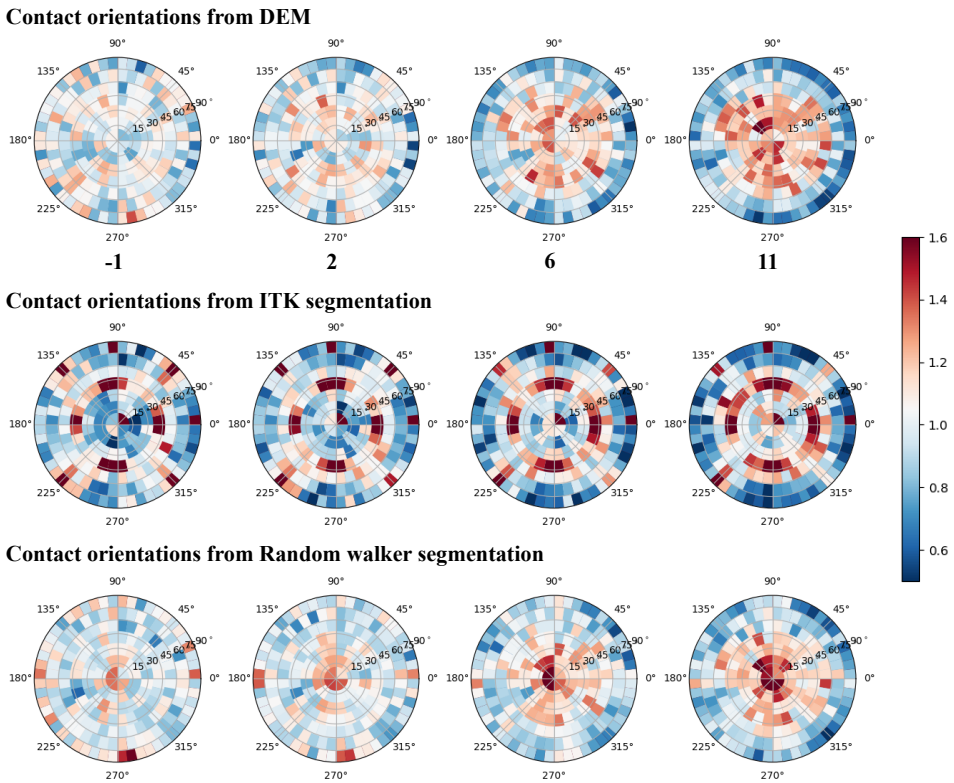

Figure 10.4: Plots of the orientations from the monotonic benchmark test using Lambert azimuthal equal area projection. The chosen loading stages are indicated and referred to in the plot of the macroscopic response, Figure 10.1. The orientations from the reference DEM simulation and the image processing by the ITK segmentation and the random walker are plotted along the respective rows. The bins are normalised by the average count of orientations per bin.

With labels being mapped between reference and images, the contact orientations from the image analysis can be compared with their corresponding reference. As in the metrological analysis on individual contacts in section 8.1.6, the error is defined as the angle between the two orientations. A histogram of all individual errors from both approaches is plotted in Figure 10.5 for loading state 6. The histograms are similar for all the loading states in the monotonic test. As found in section 8.1.6 and as obvious from Figure 10.1.4, the random walker yields more accurate results that the topological watershed. The statistical mean error of the random walker and

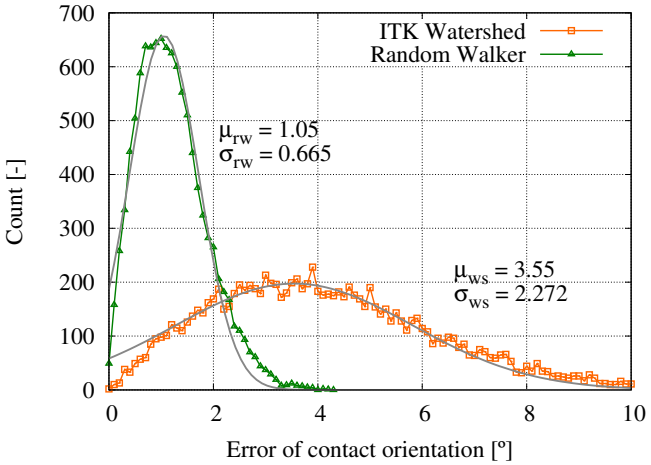

Figure 10.5: Histogram of the error of contact orientations determined with the random walker and the ITK watershed for state 6 of the monotonic simulation. The grey lines and the μ and σ values represent a fit of a Gaussian on the data.

the topological watershed are approximately 1.26° and 4.18° for all states, respectively, and compare well to the mean errors found in the study on individual contacts in synthetic images. These amount to 1.32° and 4.56° for the random walker and the topological watershed as extracted from Figure 8.8b (red lines) for spheres with a mean diameter of 26.67 pixel. Note that the statistical error does not agree with μ of the Gaussian fit to the data as given in the plot.

Scalar measures can enable a quantitative comparison of the evolution between the reference and the results from the image analysis. A possible measure is the inclination θ, *i.e.*, the angle between the orientation and the vertical axis, as the orientations are aligning in the direction of the major principal stress and only negligibly reorientate in the radial direction. The inclination is determined by:

$$\theta = \arccos\left(\frac{z}{\sqrt{x^2+y^2+z^2}}\right) \tag{10.1}$$

The mean inclination over all contacts is plotted in Figure 10.6a for the reference and well as the two image analysis techniques. The qualitative trend of the realignment of the orientations with the vertical axis is quantified in this representation. The mean inclination is decreasing from an

initial 57° to 53° at the final strain level. Note that the orientation is more aligned with the vertical axis, the lower the inclination is. In contrast to the individual orientations, the same trend is observed from the inclination determined from the results of the ITK watershed and the random walker. The deviations from both image approaches with respect to the reference amount up to a maximum of 0.7°.

The most common way of statistically capturing the distribution of orientations is the use of a fabric tensor as described in section 7.1. A second order fabric tensor and the scalar anisotropy factor as defined in Equations (1.2), (7.7) and (7.8) are employed to capture the distributions and the anisotropy, respectively. The evolution of the anisotropy with the macroscopic loading is plotted in Figure 10.6b. As the observation on the Lambert projections suggests, the orientations are distributed isotropically in the initial state. With increasing loading, the anisotropy is also increasing due to the alignment with the direction of the major principal stress. Both anisotropies based on the image processing agree qualitatively with the reference and show only minor deviations.

There are several reasons for the agreement of the statistical values determined from the results of the ITK watershed to the reference that showed a strong bias when observing solely individual orientations. The first is the degree of approximation: a second order fabric tensor is employed in this analysis, which is unable to reproduce more complicated distributions, see [KI84]. Secondly, the distributions are aligning in the vertical direction, which is one of coordinate axes. This realignment is symmetric and although there is a strong bias, the orientations are aligning further to the vertical direction with ongoing loading. The vertical alignment and not the bias towards the 45° of the image axes is captured by definition by both the inclination and the anisotropy.

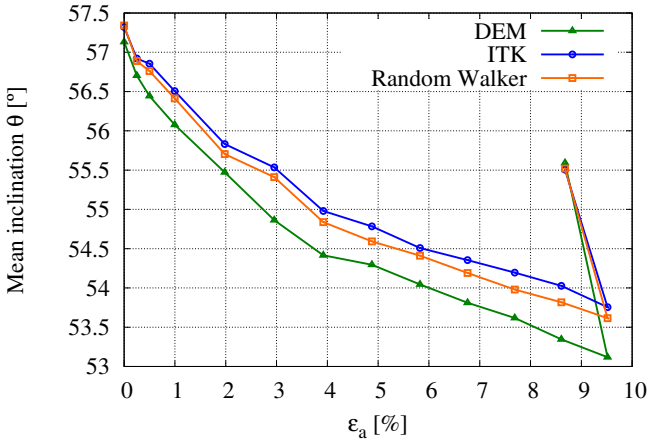

(a) Evolution of the mean inclination.

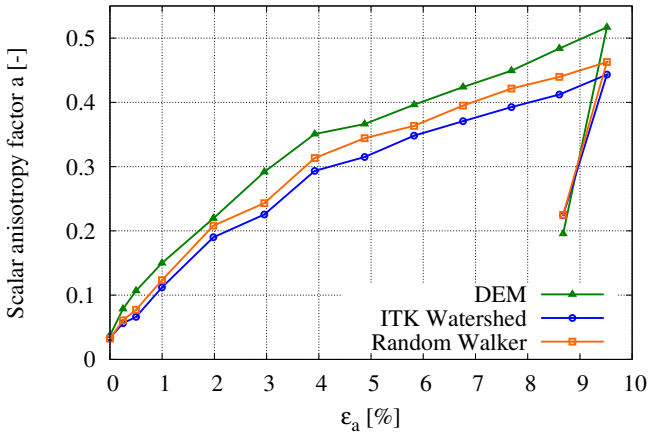

(b) Evolution of the anisotropy.

Figure 10.6: Evolution of the mean inclination and the anisotropy of the second order fabric tensor with the macroscopic loading in the monotonic benchmark test. Comparison of the reference from the DEM simulation with the results from the image analysis using the ITK watershed and the random walker.

10.2 An experiment on glass beads

The experiment is a triaxial compression test with several load-unload cycles to complement the numerical benchmark and the experiments on natural sand. A similar set-up as outlined later in section 12.4.1 is used for this test. The glass beads consist mainly of silica and are ordered from Whitehouse Scientific Ltd[8]. They have a particle size range from 150 to 650 µm and should thus, be in the range of Hostun sand with a $d_{50} = 338\,\mu m$. It must be noted that few of the particles are not highly spherical, but show deviations as visible in the zoom in Figure 10.7. As only a limited amount of particles is purchased, the specimen is prepared by what is introduced as piling in section 12.4.1: the particles are put on a spoon and filled in a funnel that is based on the bottom cap of the specimen. Several attempts for the preparation are carried out, because the spheres tended to segregate if the particles were piled either too slow or too fast. The aim, however, was to achieve a mixing of the particles and thus, a rather homogeneous distribution in the specimen.

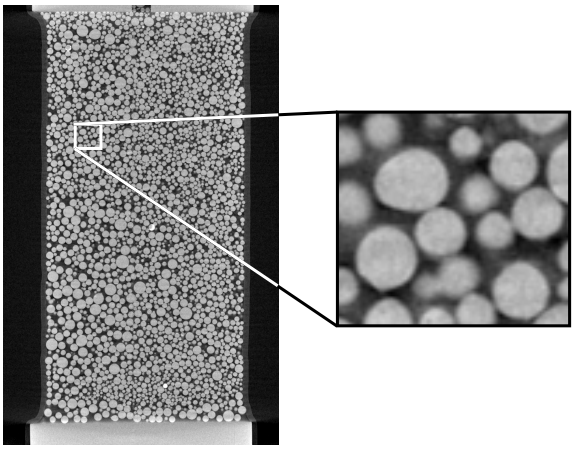

Figure 10.7: Vertical slice through the tomography of the glass beads specimen of the initial state. The zoom shows a particle that is not perfectly spherical.

The macroscopic response of the sphere packing to the cyclic triaxial compression is plotted in Figure 10.8. As the specimen is dry, the void ratio cannot be determined directly from the experimental set-up, but only from

[8] https://www.whitehousescientific.com/

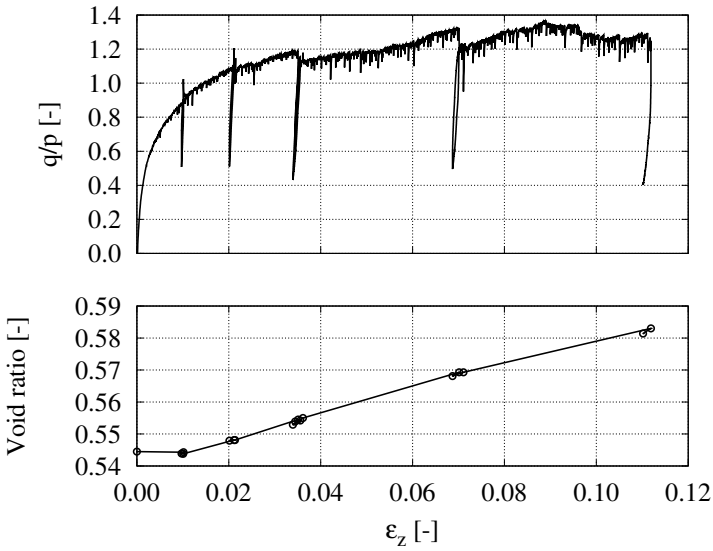

Figure 10.8: Macroscopic response of the triaxial compression test on a glass beads specimen.

the images as described in section 9.6. The amount of iterations for this procedure (6) is lower than the calibrated one (10) for the experiments on Hostun sand, as the spatial resolution is different. The tomographies are acquired at chosen stages of the loading, *i.e.*, before a change of the loading direction to un-, re- or further loading, at a pixel size of 15 µm.

10.2.1 Image processing and problems

The images are processed as described in section 9. At first, the 16-bit grey-scale images are binarised using a global threshold to distinguish between the solid and the void phase. As there are slight shifts in the grey level distributions throughout the image series, this threshold is calibrated for each image in the series taking these changes into account. The basic global threshold is determined on the image statistics using Otsu's method [Ots79]. The ITK watershed [YAL+02] is applied on the binary images to separate and label the individual particles. As the contacts that are identified directly on the labelled image are systematically over-detected, the contact list is refined using a local threshold on every contact as described in section 4.1. This local threshold is chosen lower than the optimum calibrated in

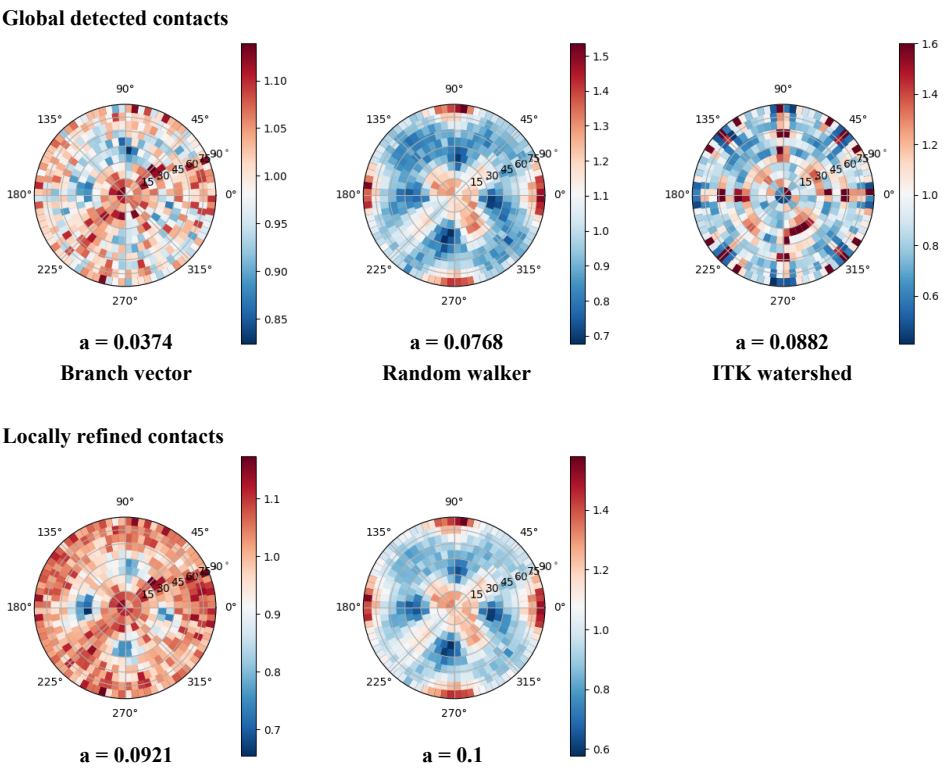

Figure 10.9: Contact orientations of state 01 in the experiment on Glass spheres GSMWTC02. Comparison of the orientations determined from the branch vectors, the random walker and the ITK watershed based on the globally detected contacts as well as the locally refined contacts. The scalar anisotropy factor a from a second order fabric tensor is calculated and given for each distribution.

section 4.1 because the particles are not perfect spheres and the optimal threshold was shown to decrease with increasing non-sphericity. The contact orientations are then computed using both, the ITK watershed and the random walker, for the global as well as the locally refined list of contacts. Although the glass beads are not perfectly spherical, the branch vectors are considered to be the reference orientations as the deviation from the ground truth should not be significant.

All the individual orientations determined in these ways, *i.e.*, three methods on two sets of contacts (global and local), are plotted in Figure 10.9 for the initial state of the specimen. The branch vectors are shown in the left

side for the global and local list of contacts. They are distributed roughly isotropically for the global contact list with only small regions that have less than average contacts. When locally refining the contacts, these small regions are strongly pronounced and the orientations show a bias in the Cartesian x-y axes with an inclination of 45°. The contact orientations determined with the random walker already show the same bias without locally refining the contacts list. This bias seems very artificial as it is aligned with the coordinate axis of the image. There are two possible reasons for this: (1) the spatial resolution that is on the lower end of the metrological study and substantially lower than for the other experiments in this work. (2) it seems that the local threshold has a tendency to exclude contacts with specific orientations and pronounce slight biases.

(1) The actual particle size distribution in the specimen can be determined from the labelled image by determining the equivalent diameter (or radius) of each object. This function is, among many other useful functions, implemented in *spam* [ACR+]: `ltk.equivalentRadii()`. It is plotted in Figure 10.10a. The diameters range from 8 to 52 pixel, which would on average be similar to the sizes investigated in this work. The problem, however, is that the large majority of the particles has a diameter from 10 to 16 pixel. This might already introduce a bias in the orientations when not calculated from the branch vectors as the centre of mass is a very accurate measure.

To explore both possible reasons, the first state of the numerical benchmark is imaged again at a lower pixel size. Otherwise, the image is created in the same way as described in section 10.1.2. At the original pixel size of 15 µm, no bias is apparently created: nor by the spatial resolution neither the local thresholding. The pixel size is chosen to 26.7 µm such that the smallest particles from the numerical packing are also imaged at approximately 12 pixel. It must be noted that the particle size range is smaller in the numerical sample. The image analysis is carried out in exactly the same way as described for the benchmark.

Figure 10.11 shows the reference contact orientations (left) as well as the results of the calculation with the random walker on the global and locally refined contact list. Contrary to the analysis on the images with the pixel size of 15 µm, the random walker introduces a bias that is aligned with all Cartesian axes, *i.e.*, the edges and the centre of the projection plots. This is further pronounced by locally refining the detection of contacts. Thus, it can be concluded that both suspected reasons, *i.e.*, the low spatial resolution in combination with the local thresholding are responsible for the strong

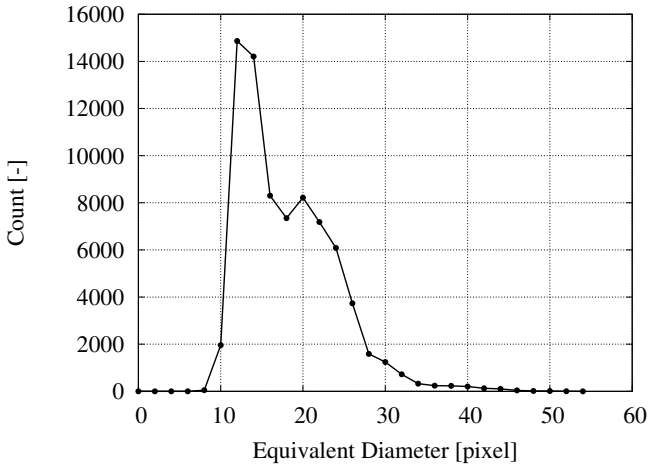

(a) Particle size distribution.

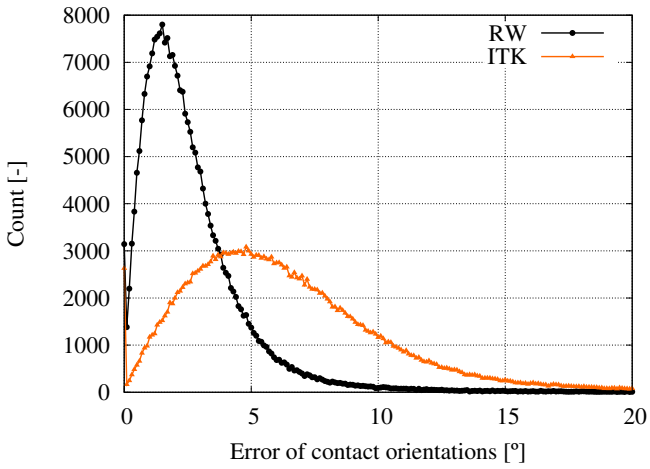

(b) Errors of orientations.

Figure 10.10: Histograms of the equivalent diameter (left) and the errors of the orientations (right).

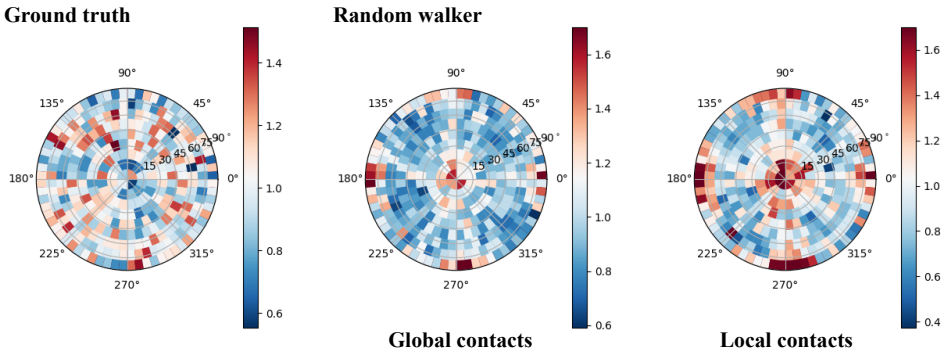

Figure 10.11: Contact orientations for the initial state of the numerical benchmark presented in section 4.2. Left: Reference orientations from the simulation. Centre and right: Contact orientations determined with the random walker on the global and local set of contacts, respectively.

bias in orientations. This manifests also in the statistical description of the distribution of contacts. The anisotropy as calculated from a second order fabric tensor in section 7.1 is substantially different for the distributions shown in Figure 10.9 as given in the Figure.

10.2.2 Contact fabric evolution

Due to the substantial problems of the image analysis at the spatial resolution of the tomographies, the experiment is evaluated only with the basic analysis. As both, the local refinement of the set of contacts as well as the watershed analyses, introduced a strong bias, the contacts are detected globally and their orientations are determined as the normalised branch vectors. Most of the particles are close to perfect spheres and only few to ellipsoids, which should still make the branch vector a viable measure for the contact fabric. The distribution of the normalised branch vectors is statistically captured by a second order tensor and a scalar anisotropy factor as defined in Equations (1.2) and (7.8), respectively. The coordination number is also calculated throughout the image series although the local contact refinement is not applied to these images. The error should not be as high as found in the benchmark analysis, as the over-detection distance is slightly lower for smaller spatial resolutions[9]. Furthermore, the

[9]This can be observed in Figure 8.2a in section 8.1.3.

over-detection is systematic which means that qualitative observation on the contact density are still meaningful.

The evolution of the coordination number is plotted in Figure 10.12a on top of the void ratio. Both measures show that the specimen is dilating during the shearing. The coordination number evolves at a higher rate than the void ratio which starts to decrease around 7 % axial strain. It can be seen a precursor to the evolution of the void ratio, as only very small motion is required for a loss of contact whereas a larger motion is required for volumetric changes. In this experiment, the coordination number seems to converge to a value larger than six. The coordination number for monodisperse sphere packings at the random loose packing limit, however, was found to take values between four and six for very rough to frictionless spheres, respectively [SWM08]. This difference is due to the *systematic over-dection*, that was not corrected here as pointed out above, as well as the particle shapes, that are not perfectly spherical.

Figure 10.12b shows the evolution of the anisotropy on top of the stress ratio. It does continually increase until 7 % of axial strain after which it stays constant. The rate is low at the beginning of the shear before picking up the loading. This is similar in both measures: the contacts need a small amount of loading before rearranging and adapting to the loading.

During the load reversals, the contact fabric changes only very slightly. It appears as if the contact fabric is locked for the amount of unloading, that the specimen is undergoing in this experiment. This is in contrast to the numerical simulations either carried out in literature [OC09, JZL19] or in the benchmark in this work in section 10.1.1. In these DEM simulations, the contact fabric does reflect the change in the loading direction significantly. This difference in contact fabric could either be generated by the low spatial resolution and the accompanying problems or the employed contact models and basics of the DEM that do not reflect the behaviour accurately. As the image analysis tools are shown to be able to pick up any changes, large or small, in such cyclic numerical simulations in section 4.2, the problem is likely to be the discrete simulations.

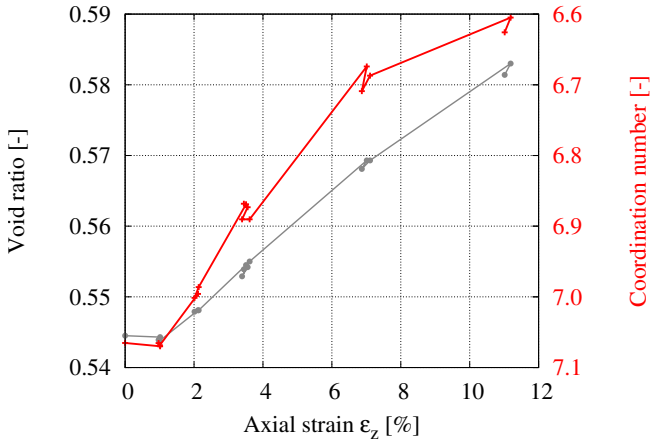

(a) Coordination number

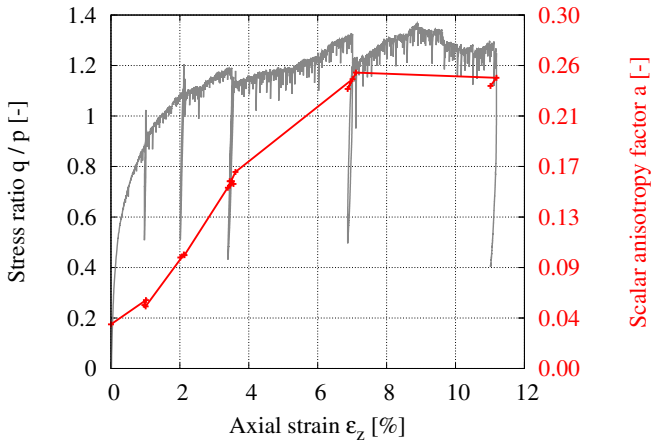

(b) Fabric anisotropy.

Figure 10.12: Response of the contact fabric in the triaxial compression test on Glass beads. Left: coordination number as determined on the global list of contacts. Right: fabric anisotropy calculated on the distribution of the normalised branch vectors.

10.3 Error propagation

The actual values of the uncertainty for the orientations **o** are determined based on the analysis on individual contacts using the high resolution tomographies in section 4.1.2. In this analysis, the errors are only evaluated in terms of angles, but not components. To specify the error, the deviation of each component $[o_z, o_y, o_x]$ is determined for each contact by subtraction from the reference orientation and taking the absolute. The uncertainty is then determined by taking the average deviation of each component $[\delta o_x, \delta o_y, \delta o_z]$. This is repeated for the all studied pixel sizes.

The uncertainty has to be propagated from the individual orientations to the aimed fabric variable, *e.g.*, the fabric tensor or the scalar anisotropy factor. There are many calculation steps that are necessary for the propagation of an uncertain vector to a tensor variable and via tensor operations to a scalar value, such as the anisotropy. The basic steps are outlined in section 7.1. In this work, the python package uncertainties [Leb] is employed to propagate this error. As it is formulated on top of numpy [Oli06], it is able to translate the error directly through matrix calculations. A simple implementation of propagating the error for the determination of the fabric tensor and the anisotropy is given in Listing 10.3. In the case of the given example, the uncertainties for the components of the orientations are taken from the metrological study on Hostun sand at a pixel size of 15 µm. Propagating these trough all the operations for ≈ 135,000 orientations as in the case of the triaxial compression tests in this study, yields an uncertainty for the anisotropy of ≈ 0.004.

Listing 10.3: Python script to determine the fabric tensor using the uncertainties package.

```
import numpy
import uncertainties
from uncertainties import unumpy
from uncertainties import umath

filename = "..."

#define uncertainties
dz = 0.132 #e.g. for Hostun sand at 15 mum/pixel
dy = 0.132
dx = 0.132

contacts = numpy.loadtxt(filename, usecols=(4,3,2))
numContacts = numpy.shape(contacts)[0]
print(numContacts)

#initiating N
null = unumpy.uarray([[0,0,0]], [[0,0,0]])
N = null*null.T

for i in range (0, (numContacts-1)):
    #define the orientation and assign an uncertainty
        to each component
    orientationUncert = unumpy.uarray([[contacts[i,0],
        contacts[i,1], contacts[i,2]]], [[dz, dy, dx
        ]])

    tensorProduct = orientationUncert*
        orientationUncert.T
    N = N + tensorProduct

#Fabric tensor
F = N/numContacts
print("Fabric tensor \n", F)

#Deviatoric part of the fabric tensor
devF = ( F - ((F[0,0] +F[1,1] + F[2,2])* (1./3.)) *
```

```
    numpy.eye(3,3) )* (15./2.)

# scalar anisotropy factor
double_contraction = devF*devF.T

a_r = umath.sqrt(3./2. * (double_contraction[0,0] +
    double_contraction[0,1] + double_contraction[0,2] +
     double_contraction[1,0] + double_contraction[1,1]
    + double_contraction[1,2] + double_contraction[2,0]
     + double_contraction[2,1] + double_contraction
    [2,2]))

print("Value of a \t= ", uncertainties.nominal_value(
    a_r))
print("Uncertainty of a \t= ", uncertainties.std_dev(
    a_r))
```

11 Metrology of particle orientations

Particle orientations are the second fabric entity discussed in this work. As they are also extracted from the tomographies, the accuracy of the image analysis approach has to be investigated. The initial work to study the particle orientation is carried out on an individual Hostun sand grain that is imaged at a very high spatial resolution. To complement and extent the results on this individual grain, several grains are imaged at a slightly higher pixel size and their orientations are studied at varying scales. The principal particle orientations are considered to be the eigenvectors of the moment of inertia tensor (MOI) of each particle as described in section 4.3.

11.1 Studying particle orientations with an individual Hostun grain scan

To acquire the image of an individual Hostun sand grain, one representative grain is chosen and glued to a stick. The stick is then placed in the chamber of the nano focus x-ray tomograph of Laboratoire SiMaP, Grenoble. Using this set-up allowed to obtain a tomography with a pixel size of 350 nm. Due to this high spatial resolution, many features that are otherwise not accessible are visible and complicate a binarisation of the image. The threshold is chosen by Ostu's method [Ots79]. At certain areas in the image, the glue has to be manually erased to refine the binary image. A 3D rendering of the Hostun sand grain and its eigenvectors is depicted in Figure 4.19.

11.1.1 Procedure to study the accuracy

In order to study the accuracy of this approach, a reference image of the Hostun sand grain is rotated. In contrary to the study on contact orienta-

tions, in which the orientations are chosen systematically, a series of random rotations is applied here. The main reason is the computation time, as there are 4 parameters for a rotation instead of 3 in the case of the contact orientations. The rotation is given by the axis $u = [x, y, z]$ (three components in 3D) and the angle α by which the image is rotated around this axis.

A grid of the coordinates of the image is created with the centre of mass of the particle being the origin as the pivot point of the rotation. This grid assigns a position vector to every voxel in the image. Rodrigues rotation formula [Rod40] offers one possibility of rotating the image. The matrix for a rotation $[R]$ by α around $[u]$ reads:

$$[R] = [I] + \alpha \cdot [N] + (1 - \cos\alpha) \cdot [N]^2 \tag{11.1}$$

with $[I]$ being the identity matrix and $[N]$ defined as:

$$[N] = \begin{bmatrix} 0 & z & -y \\ -z & 0 & x \\ y & -x & 0 \end{bmatrix} \tag{11.2}$$

Note that clockwise rotations are chosen to be positive for this definition of $[N]$. Each position vector from the image grid is rotated by applying the rotation matrix:

$$[v]_{rot} = [R] \cdot [v] \tag{11.3}$$

The golden standard (the reference) is calculated on the particle orientations that are determined on the binary image of the Hostun sand grain at a pixel size of 350 nm. These three eigenvectors of the MOI tensor are rotated using Equation (11.3) and serve as the reference orientation for the random rotation. The eigenvectors are always sorted depending on their corresponding eigenvalues: the highest labelled as the first and the lowest as the third eigenvector.

The analysis starts with the grey-scale image scaled to 0.5^3, which is equivalent to pixel size of 2.8 µm. This saves memory and computation time as the initial image amounts to 3.1 GB and is in accordance with an initial study that showed that the first times of scaling the image by 0.5^i yield a negligible error in particle orientations for this specific grain shape. 4000 random rotations are investigated, each being created as a random angle $\alpha \in [0; 2\pi]$ and a rotation axis $[u]$ with three independently generated components. The following steps are carried out for every rotation:

the undeformed grey-scale image is rotated at a first order interpolation using the scipy [JOP+] function `scipy.ndimage.map_coordinates`. This rotated grey-scale image is binarised with Otsu's threshold [Ots79]. The MOI tensor and its eigenvectors are calculated on the binary image. Each eigenvector is compared to its corresponding reference with the angle between both serving as the error of the computation. These steps are repeated for decreasing scales 0.5^i with $i \in [3; 4; 5; 6; 7]$, *i.e.*, increasing pixel sizes from 2.8 to 44.8 µm. The grey-scale image is scaled using the function `scipy.ndimage.interpolation.zoom` with a linear interpolation which is sufficient as only steps of 0.5 (binning) are used. In this way, the error of determining particle orientations from the MOI is evaluated for increasing pixel sizes.

The statistical mean error of all principal particle orientations is plotted in Figure 11.1a for increasing pixel sizes. It is obvious that the error of all three eigenvectors increases with increasing pixel size. The error seems to increase dramatically for pixel sizes larger than 20 µm. For the images acquired in this work, *i.e.*, pixel sizes of 10 to 15 µm, the errors of all eigenvectors are lower than 1°. Eigenvectors 1 and 2 experience similar errors that are consistently higher than the error of the third eigenvector. That is due to the particular shape of the grain. From simply looking at the 3D rendering of the grain in Figure 4.19, it is obvious that the most distinguishable axis of this grain is its long axis, which corresponds to eigenvector 3. Respecting the orthonormality condition of the eigenvectors, the short and intermediate axis are very similar in extent. This is also obvious from the eigenvalues of the MOI tensor: The eigenvalues of the first, intermediate and third eigenvector amount to approximately 907, 800 and 488×10^{-9} µm^5, respectively. These values coincide with the visual inspection and show that the third eigenvector is the most distinguishable orientation which thus, can be determined with the highest accuracy. In this way, the differences of the eigenvalues can be taken into account for choosing the most unique particle orientation for a specific material automatically.

Figure 11.1b shows a histogram of the errors at a pixel size of 11.2 µm, *i.e.*, the most relevant pixel size for the experiments analysed in this work. Any particle orientation can be reliably determined for this particular shape as even the maximum errors for these 4000 random rotations are lower than 1°. This analysis is, however, restricted to a particular Hostun sand grain and needs to be extended to more shapes of the same material in order to reliably prove these results.

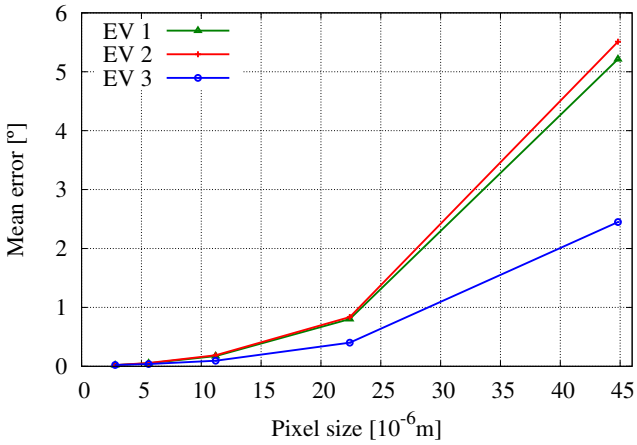

(a) Mean errors of the eigenvectors of the moment of inertia tensor.

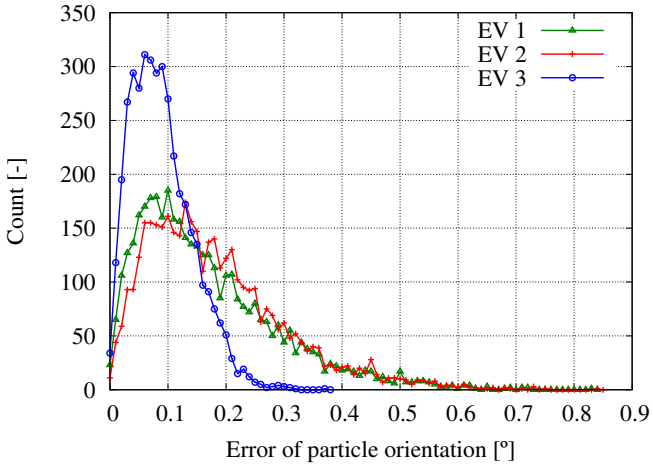

(b) Histogram of the error distribution at a pixelsize of 11.2 µm.

Figure 11.1: Accuracy of the determination of principal particle orientations from the moment of inertia tensor. The single Hostun sand grain is rotated 4000 times by a random angle around a randomly chosen axis and scaled to increasing pixel sizes. The reference image is acquired at a pixel size of 350 nm.

11.2 Study on many Hostun sand particles

To extend the previous analysis, the high resolution tomography of Hostun sand grains, acquired initially for the metrological study of contacts, is used

here. This tomography is acquired at a pixel size of 1 µm in order to image a small assembly of grains as described in section 8.2.1. In this analysis, only grains that are located completely in the image are taken into account. The images of these 53 grains are fetched from the labelled and the grey-scale image, similar to the analysis on individual contacts in section 8.2.2.

These images are then processed similarly to the analysis on the individual Hostun sand grain, as described before. The reference particle orientations are determined on the lowest pixel size in the fetched images, *i.e.*, 1 µm. The image is therefore binarised and the MOI tensor is calculated on the binary image. In the previous analysis, the MOI tensor is calculated with a python function. Here, the C++ version of this function is used as it is implemented in the label toolkit in *spam*: `ltk.momentOfInertia()`. Furthermore, the images are scaled more realistically than in the previous analysis. The image properties blur and noise are applied to the images before and after scaling as explained and calibrated in sections 8.2.2 and 7.4, respectively.

Every grain is randomly rotated 4000 times and scaled to the pixel sizes 4, 8, 12, 16, 20 and 24 µm. The average errors for all grains at the specific pixel sizes are plotted in Figure 4.20a. As observed on the single grain in Figure 11.1a, the mean error increases with increasing pixel size. The actual errors, however, are higher. That is for two reasons: (1) the incorporation of blur and noise in this analysis. (2) the variety of shapes that are mostly less well defined than the individual grain. Furthermore, the first and the third eigenvector yield rather similar errors instead of the third being the best measure in the previous analysis. The reason is, again, the variety of shapes for which the longest axis is not necessarily the best defined one.

In the following, three grains with very different shapes are investigated closer. The 3D renderings are drawn in Figure 11.2 in an attempt to grasp the shape as clear as possible. To simplify this complex task, the shape is described using the eigenvalues in this analysis. Grain (19) has a lentil-like shape. It has two long axes and a very distinct short axis. The ratios of the eigenvectors are used to describe the shape here. The first and the third EV are related to the intermediate one: ratio12 = EV1/EV2 and ratio23 = EV2/EV3. The ratio12 is higher than the ratio23 for this grain having values of 1.6 and 1.4, respectively. The histogram of the errors for a pixel size of 12 µm is plotted in Figure 11.3a. The error distribution is bi-modal for the different eigenvectors: the first eigenvector, corresponding to the shortest axis, is the least error-prone. This supports the observation on the image as well as from the eigenvalues. For the lentil-like shape, the shortest

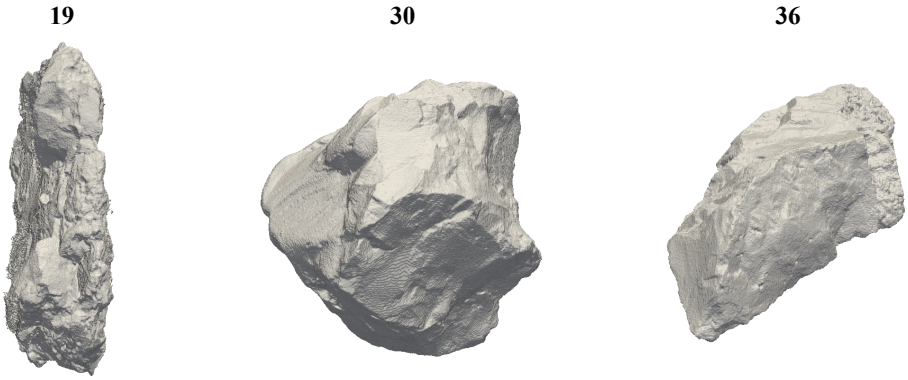

Figure 11.2: 3D renderings of three very different particles: (19) flat, lentil-like shape; (30) compact shape without a very distinct longest or shortest axis; (36) shape with a clear long axis.

axis is the best defined axis and the ratio of EV1/EV2 is highest.

Grain (30) is the most compact grain of this assembly. No axis is very distinct from the others. This is well captured by the eigenvalues having a ratio12 of 1.2 and ratio23 of 1.0. As these are very close or equal to 1, the axes are not well defined. Figure 11.3b shows the distribution of the error again at a pixel size of 12 µm. For this shape, the distributions are not as different for the eigenvectors as for the other two shapes. Nevertheless, the first eigenvector yields the best accuracy. Again this can be observed from the ratio of the eigenvalues with the ratio12 being the largest and thus, EV's 1 and 2 being the most distinct axes.

Grain (36) has a similar shape to the individual sand grain from the previous study with one, very clear long axis. In this case, the ratio12 of 1.2 is far lower than the ratio23 with a value of 4.6. The distribution of the error for this shape at 12 µm is plotted in Figure 11.3c. Similar to the observation on the individual sand grain on Figure 11.1b, the third eigenvector is the most accurate to determine as it corresponds to the very distinct long axis of the grain.

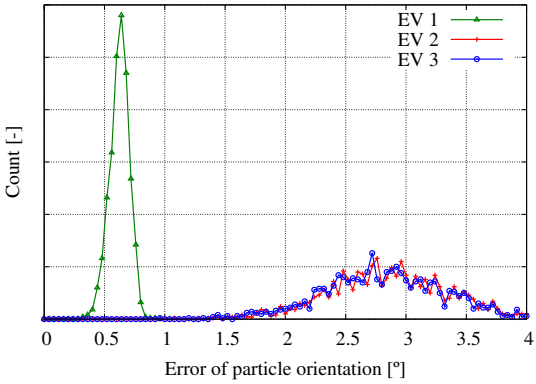

(a) Grain 19.

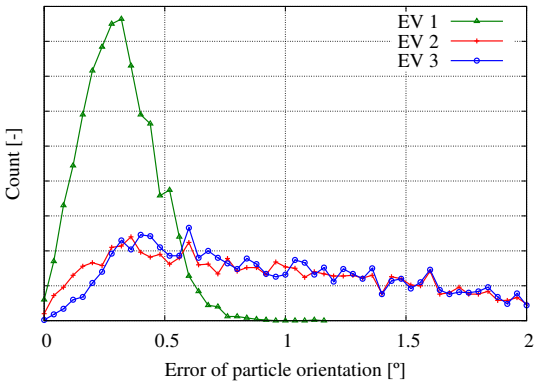

(b) Grain 30.

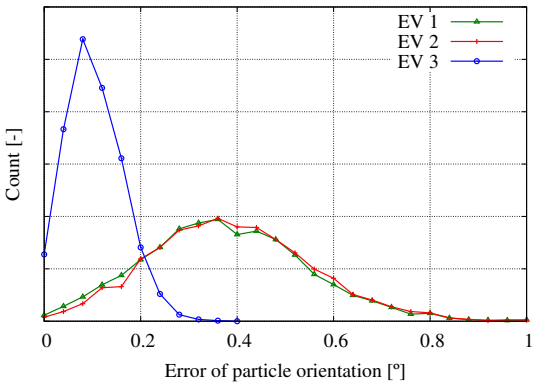

(c) Grain 36.

Figure 11.3: Histogram of the error distribution of each eigenvector for different Hostun sand grains at a pixelsize of 12 µm. The three different grains are displayed in Figure 11.2.

12 Experimental campaign

12.1 Materials used in this work

The experiments in this work are almost exclusively conducted on Hostun sand specimens. There is, however, a study on experiments that were carried out in the thesis of Edward Andò [And13] that involve an additional material, Caicos ooids. Both materials are briefly described here[1].

Hostun sand is silica sand that is obtained from a quarry close to Hostun in France. The sand grains are rather angular as they were created by crushing from rock and then slightly cemented by kaolin. They are washed after the quarrying to remove the kaolin and sorted by grain sizes. The experiments in this work are carried out on grains with a narrow size distribution and an average equivalent grain diameter of $d_{50} = 338\ \mu$m as given by the manufacturer Sibelco France. Multiple investigations on the characteristics and the behaviour of assemblies of Hostun sand grains were conducted in the past, *e.g.*, in the Laboratoire 3SR in Grenoble as it became one of the standard materials for experimental studies there [CD86, FDP90, Com98]. The minimum and maximum dry density of Hostun sand specimens were determined to $\gamma_{d,min} = 13.489 \pm 0.033\,\mathrm{kN/m^3}$ and $\gamma_{d,max} = 16.191 \pm 0.037\,\mathrm{kN/m^3}$ in the most recent of the aforementioned studies [Com98]. The minimum and maximum void ratio can be estimated to $e_{min} = 0.606$ and $e_{max} = 0.928$ using the specific density of the grains of $\rho_s = 2.65\,\mathrm{g/cm^3}$ [FDP90] via:

$$e_{max} = \frac{\rho_s}{\rho_{d,min}} - 1 \qquad \text{and} \qquad e_{min} = \frac{\rho_s}{\rho_{d,max}} - 1 \tag{12.1}$$

This is in slight disagreement with the values determined in [CD86] of $e_{min} = 0.656$ and $e_{max} = 1{,}000$, but the latter might have used a dif-

[1] See [And13] for a more detailed description.

ferent category of Hostun sand grains as this study is a decade older than [Com98].

Caicos ooids are round, carbonate grains consisting mostly of aragonite ($> 96\,\%$). The material was collected on the Caicos platform, north-east of Cuba, and was given to Laboratoire 3SR by ExxonMobile. The limited amount of material did not allow for a systematic study (dense and loose packings, *etc.*) and was used for experiments in the x-ray scanner. The d_{50} of these grains is $420\,\mu m$. In contrast to the Hostun sand, these ooids are created by growing from small seeds in the marine environment either by physical attachment or by precipitation. As reported in [And13], the specimen of Caicos ooids can mobilize a higher peak friction angle (45-48°) than the Hostun sand (46°) and show a strongly pronounced stress peak in triaxial compression tests. The friction angles reported here are from triaxial compression tests at 100 kPa cell pressure.

12.2 Subset analysis on existing experiments

The first real mechanical experiments chosen for the determination of contact fabric were carried out within the dissertation of Edward Andò [And13]. Two monotonic triaxial compression tests at 100 kPa cell pressure are chosen to be studied here, one on Hostun sand (HNEA01) and one on Caicos ooids (COEA01). These they have already been thoroughly analysed regarding their kinematic evolution in [AHV12a]. The focus there was to identify the forming of a localised shear band using Digital Image Correlation and a particle tracking approach [AHV+12b]. The following analysis on the contact fabric and its evolution is aimed at complementing these results.

The most important information on the experiments and the main results of the image analysis are described in section 5.1. The details on the image analysis as well as some complementing results to the ones shown in the main part are given here. Some slices through the specimens are shown in Figure 12.1. The states that are imaged are the same as referred to later in this analysis. They represent different stages of the loading: (01) the initial state, (04) and (08) a pre- and a post stress peak state and a state at large axial strain (16). See Figure 5.1 for a reference to the macroscopic response. The slices are chosen in a direction that is orthogonal to the forming shear band in order to visualise it. It is observable that a shear band develops in both specimens after the stress peak. Using DIC or particle tracking

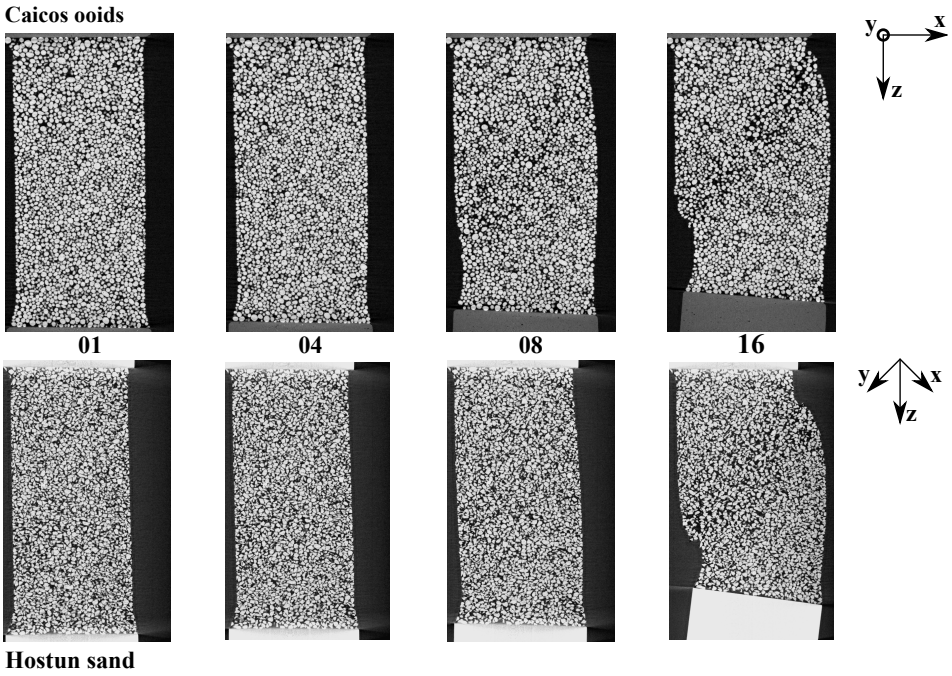

Figure 12.1: Vertical slices through the tomographies of Caicos ooids and Hostun sand in the triaxial compression tests. The states are marked in the macroscopic answer of the specimen in Figure 5.1.

revealed that the onset of the localisation appears slightly before the stress peak [AHV12a, AHV$^+$12b].

12.2.1 Image analysis

In accordance to the previous analysis of these images, the thresholds for the binarisation of the 8-bit grey-scale images[2] are chosen to be 123 and 96 for the Caicos ooids and Hostun sand specimen, respectively. These were applied to every tomography in the image series. As described in section 5.1, two observation windows are extracted from the tomographies: one inside and one outside of the developing shear band. This allows to distinguish the fabric evolution for different zones in the specimen. After

[2]Generally, 16-bit images are processed in this work in contrast to the 8-bit images here. This, however, does not impact the determination of the contact fabric significantly as shown in section 12.4.3.

initially segmenting the image and labelling the grains, the grains located directly on the boundary of the image are identified and deleted from the image. This is done to avoid problems with the labelling as particles that are only partly included in the image tend to be segmented wrongly and thus, impact the detection and orientation of the contacts. For a faster computation, the image is relabelled sequentially afterwards to account for the deleted labels. In the window outside of the shear band, ≈1400 particles are detected in both experiments throughout the loading. The window inside the developing the shear band hosts 1800 to 1400 grains in the Hostun sand specimen and ≈1900 in the Caicos ooids specimen. The local thresholding is only applied to the images of Caicos ooids, because the irregular shapes of the Hostun sand are not as affected by the over-detection of contacts[3]. The original histogram of the observation window inside the shear band is shown in Figure 12.2a. In order to apply the local threshold, the grey-values of the image are first translated to 32-bit and the data range of [0.,1.] and then distorted to the normalised distribution with peaks at 0.25 and 0.75 for the void and solid phase, respectively. This normalisation of the histogram is explained in section 7.4 for a 16-bit images, but works similarly here. The translated and distorted histogram is plotted in Figure 12.2b. The optimal threshold for the manufactured spheres is estimated to 0.65 in section 4.1.1. As the ooids are not perfectly spherical and have slightly rougher surfaces than the spheres, the local threshold is set to 0.6. It is known to reduce the more angular a shape gets, thus reducing it seemed an appropriate guess as a complete metrological analysis on the Caicos ooids is not carried out in this work. This value corresponds to 160 in the 8-bit data range with $[0; 255]$, which is calculated by reversing the distortion to the original image settings.

The initial analysis was performed using the thresholds determined on the initial image of each experiment. These thresholds are applied to every image of the series. Some results, however, appeared to oscillate around possibly constant values, which could be caused by a difference of the image properties of the series as the analysis was otherwise carried out similarly for every image. Thus, histograms of the grey-value distribution for each image are evaluated in the same way as described above and shown in Figure 12.2a. The mean values for the solid and void phases as well as the resulting global threshold are given in Table 12.1 for the observation windows inside the shear band in the Caicos Ooids specimen. Using the shift of the mean values for solid and void phase, the global and local thresholds determined

[3]This is observed in the metrological study on contact detection in section 4.1.

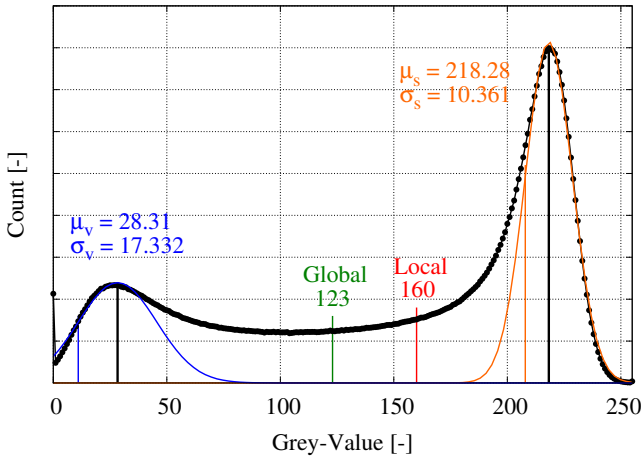

(a) 8-bit range

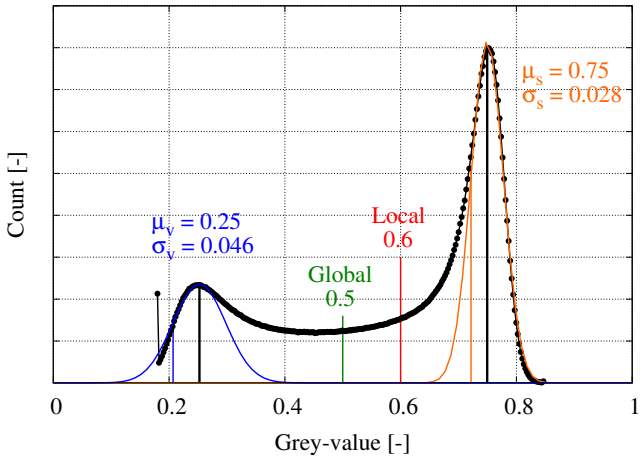

(b) 32-bit range

Figure 12.2: Histogram of the tomography of Caicos ooids at the initial state (01) of COEA01 determined on the observation window inside the shear band. The histogram is determined on the 8-bit image and translated to the 32-bit data range $[0; 1]$ in order to relate it to the metrological analysis. The solid and void phases are fitted with Gaussian distributions and plotted in orange and blue, respectively. The global and local thresholds for the analysis are marked.

Table 12.1: Mean values and standard deviations of the solid and void phase in the observation window inside the shear band in the Caicos ooids specimen. The values are determined on the histograms of the grey-values of the images.

Image	μ_s	σ_s	μ_v	σ_v	global	local
01	218.3	10.4	28.3	17.3	123	160
02	216.6	10.4	28.7	18.1	122	159
03	219.6	10.6	28.3	17	124	161
04	213.9	10.4	29.2	20	121	157
05	215.8	10.3	27.2	18.5	121	158
06	216	9.9	23.9	16.9	120	157
07	217.8	10.2	21.4	17.4	119	158
08	208.4	8.7	17.5	18	113	150
09	218.9	10.5	15.7	19.2	117	157
10	213.8	10.1	14.1	22.1	114	153
11	210.2	9	11.4	21.1	110	149
12	214.3	10.3	13.2	21.8	113	153
13	216.1	10.4	12.6	21.6	114	154
14	217.2	10.4	12.8	20.2	115	154
15	213.1	9.7	12.7	20.6	113	152
16	214.9	10	12.9	20.2	114	153
17	216.7	10.4	13.4	19.8	115	154

on the initial image (threshold_{ref}) can be translated to each observation window (threshold_i) in the following way:

$$\text{threshold}_i = \text{threshold}_{ref} \cdot \frac{\Delta\mu_i}{\Delta\mu_{ref}} + \text{offset} \tag{12.2}$$

with $\Delta\mu$ being the difference of the mean values for the solid of void phase. The red lines for the images 01 and 08 in Table 12.1 highlight the big shift for some images. The differences of the obtained results with and without considering this shift in grey values are shown and examined in 12.2.4.

As the observation windows are processed independent of their surroundings, the coordination number that is calculated based on the list of contacts will be too low. Contacts that grains share with the outside of the observation window have to be neglected here[4]. The actual coordination number, however, is also impacted by the systematic over-detection of contacts,

[4]These cannot be considered, because only the observation windows are processed.

which leads to a higher value. Thus, the coordination number is only referred to as a qualitative value to follow its evolution. The evolution should not be affected strongly by this approach as both deviations are systematic errors. After detecting the contacts, the random walker is applied to the every pair of contacting grains to determine the contact orientations.

12.2.2 Individual contact orientations

The contact orientations in both observation windows, inside and outside the developing shear band, are plotted in Figure 12.3 for the experiment on Hostun sand[5] using Lambert azimuthal equal area plots[6]. As described in section 7.2.1, Lambert azimuthal equal area plots are employed for the plotting. The orientations from the experiment on Caicos ooids and Hostun sand are plotted in the upper and lower part of the Figure, respectively. The different states chosen for this demonstration are visualised in Figure 12.1. See Figure 5.1 for a reference to the corresponding macroscopic states.

In contrast to the experiment on ooids, the contacts in the Hostun sand specimen do have a stronger preference towards the vertical direction in the initial state. The behaviour in the first increment (01-04), however, is similar to COEA01: the contacts in both windows align stronger with the major principal stress axis in both windows. After state (04), the subset outside of the forming shear band seems to revert to the initial fabric state and appears to stay in this state until the end of the experiment. The orientations inside the shear band align further to the vertical direction with ongoing shear. The distribution of orientations, however, appears to be less anisotropic than in the experiment on Caicos ooids.

As discussed in section 10.1.4, the mean inclination of all orientations is a scalar measure that can be used to show an evolution of the contact fabric. It is defined as the statistical mean of the inclination, *i.e.*, the angle between the orientation and the vertical axis as defined in Equation (10.1). The inclination is plotted for both experiments and both observation windows in Figure 12.4. In the first four imaged states of the experiment

Note that this is not the case for the triaxial compression tests in section 12.4. The contacts to the outside of the window can be considered there, because the complete specimen is processed. This is described in section 12.4.7.

[5]Note that the orientations in the experiments on Caicos ooids are shown in Figure 5.4 and analysed in the corresponding section 5.1.

[6]These projections are explained in section 7.2.1.

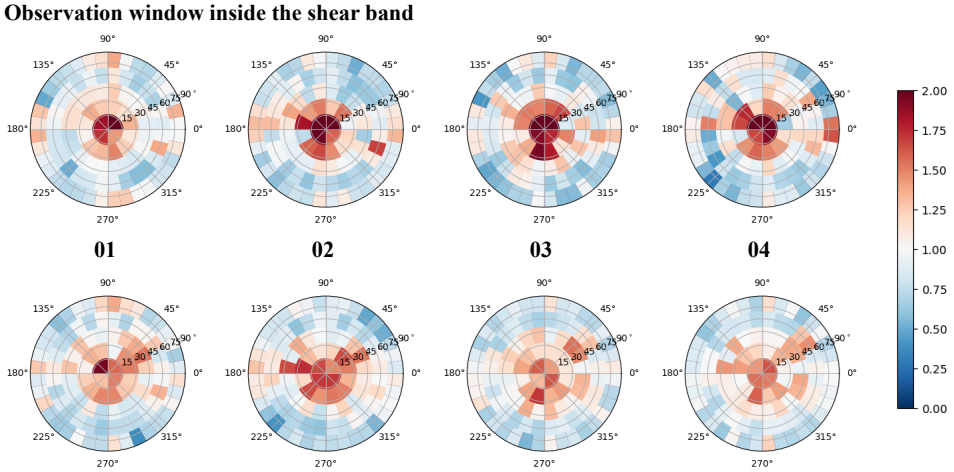

Figure 12.3: Lambert azimuthal equal area projections of the contact orientations for the triaxial compression test on Hostun sand (HNEA01) in two observation windows of the specimen: inside and outside the developing shear band. The orientations are plotted for four chosen states of the macroscopic loading. For a reference of these states see Figure 5.1. The bins are normalised by the average number of orientations per bin.

on Caicois ooids, the inclination decreases similarly in both observation windows. Afterwards, the structure in both windows evolves differently: the inclination inside the shear decreases further until reaching a peak and increases again to what might be a steady state at larger strains. Outside the shear band, the inclination does not change significantly and stays almost constant. This is consistent with the observations on the projections of the orientations in Figure 5.4: as the orientations align more with the vertical direction, the inclination must decrease.

A similar, but much less pronounced evolution can be observed on the Hostun sand specimen in Figure 12.4b. The inclination in both windows agrees, before branching off each other. Inside the shear band, it decreases until reaching a flat peak. Outside, the inclination increases again to its initial state and stays relatively constant.

The inclination inside the shear band in both tests qualitatively follows the stress ratio. The more pronounced stress peak in the test on Caicos ooids is reflected in the more pronounced peak of the inclination.

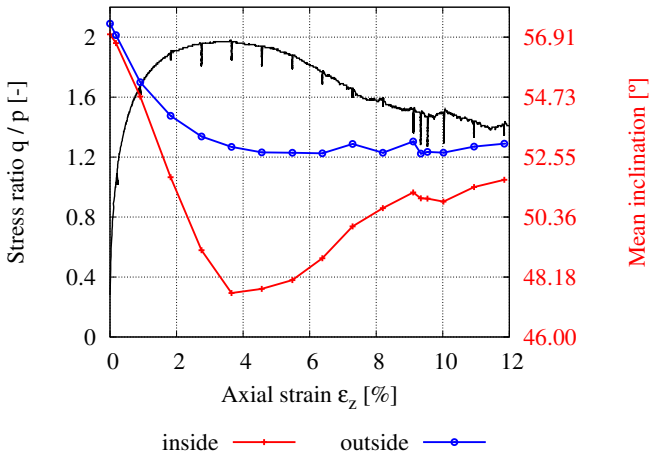

(a) Caicos Ooids (COEA01)

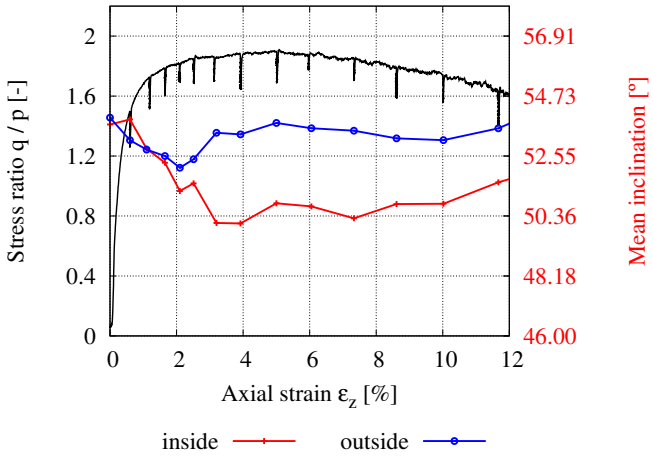

(b) Hostun sand (HNEA01)

Figure 12.4: Evolution of the mean inclination in triaxial compression tests on Caicos ooids (COEA01) and Hostun sand (HNEA01) in two observation windows of the specimen: inside and outside of the forming shear band.

12.2.3 Evolution of the fabric tensor

Figure 12.5 shows the surface of the fabric tensor for the same states in HNEA01 as analysed in the previous section[7]. A similar, but far less pronounced evolution is observed in the plots of the fabric tensor in the Hostun sand specimen compared to the Caicos oods specimen. The initial state in both subsets is less isotropic than in the ooids specimen, which coincides with the orientation plots. Outside of the shear band, the shape of the tensor undergoes no major changes: it starts at an inclined state and changes towards the vertical direction, *i.e.*, the major stress direction. At the peak stress state it becomes slightly more anisotropic, *i.e.*, peanut-shaped, before reverting to a similar shape as in the initial state. It always stays aligned with the vertical axis. The fabric inside the shear band clearly becomes peanut-shaped, but stays less anisotropic than for the Caicos ooids specimen. The extent of the anisotropy does not appear to change as strongly, but the direction fluctuates. This might be due to the higher uncertainty of the measurement of contact orientations in the irregularly shaped Hostun sand grains. In the last state, the tensor inside the shear band appears to be aligned in the axis of the shear band, which forms in a plane that is orientated along the horizontal diagonal and the vertical axis.

To capture the evolution of the anisotropy with the loading, the scalar anisotropy factor as defined in Equation (7.8) is plotted in Figure 5.6. The error bars are determined from the error of the individual orientations as quantified in Equations 8.1.6 and 8.2.4 and propagated via the fabric tensor to the anisotropy fabric. As explained in section 10.3, the propagation of the error through the fabric tensor requires the input of the error in terms of the three spatial components. These are determined based on the analysis on the high resolution tomographies of the manufactured spheres and Hostun sand in section 4.1.2. As there is not a specific study on Caicos ooids to determine the error and the shape is very rounded, the error determined on the spheres is adopted. The mean error of the components $\delta o_z, \delta o_y, \delta o_x$ of the Hostun sand and the Caicos ooids that are propagated are 0.132 and 0.03, respectively. This results in an uncertainty of the scalar anisotropy factor δa for the observation windows of about up to 0.03 in Hostun sand and 0.006 in Caicois ooids. Note that the uncertainty depends on the actual number of orientations that contributes to the fabric tensor and as such varies with the contact density.

[7]The surface of the fabric tensor for COEA01 is analysed in section 5.1 plotted in Figure 5.5.

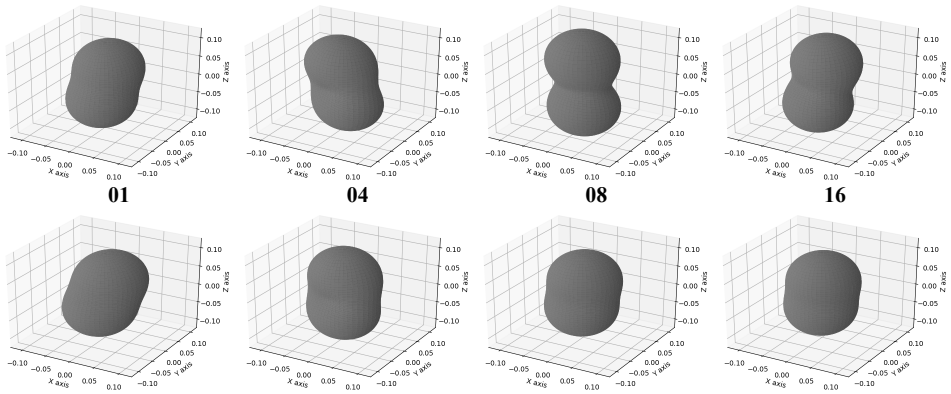

Figure 12.5: Surface plots of the fabric tensor for the triaxial compression test on Hostun sand in two observation windows of the specimen: inside and outside the developing shear band. The tensor is plotted for four chosen states of the macroscopic loading. See Figure 5.1 for a reference of these states.

The evolution of the anisotropy in both experiments in plotted in Figure 5.6 and discussed in section 5.1. It must be noted that the anisotropy and the mean inclination (in Figure 12.4) follow highly similar trends. The inclination is controlled by the alignment of the orientations with the major principal stress, i.e. the vertical axis (z-axis). The anisotropy on the other hand does not depend on the major principal stress or an alignment, but only the actual spread of the distribution. As the orientations align with the vertical axis and thus, the spread decreases, the anisotropy increases and the inclination decreases. This, however, does not make one of the two measures dispensable.

12.2.4 Importance of considering changes in an image series

As mentioned before, the grey-value distribution changes substantially in the image series of the experiment on the Caicos ooids specimen (COEA01). The effect of these changes on the resulting contact fabric is discussed here. In the initial analysis of the image series the predecessor of *spam* is used to determine the contact fabric. The shifts in the grey-levels are not considered in this initial analysis and all images are processed with the same global and

local threshold that is determined in the initial image as described in Figure 12.2.

Figure 12.6a shows the evolution of the coordination number for the analysis with constant thresholds (initial) with dashed lines and for the analysis with adapted thresholds (*spam*) with solid lines for both subsets. The general trend, especially in the beginning of the test, is similar, which is consistent with the distribution of grey-values, which change insignificantly, see Table 12.1. The initial processing yields strong oscillations from 5 % of axial strain onwards. This behaviour could have either been due to the high uncertainty of the measurement or a change in the image properties which was the reason for this analysis. Considering the shift in grey-values and re-running the image analysis with *spam* yields a substantially smoother evolution.

The effect of the shifting grey-values is considerably lower on the scalar anisotropy factor. Its evolution is plotted in Figure 12.6b. This means, that the quality of the calibration of the thresholds for binarisation and contact detection has a major impact on detecting contacts, but not on their distribution. The reason for this little impact is the error propagation that can minimize an otherwise huge error on an individual orientation to a low uncertainty of a bulk value if propagated often. The error propagation is explained in section 10.3.

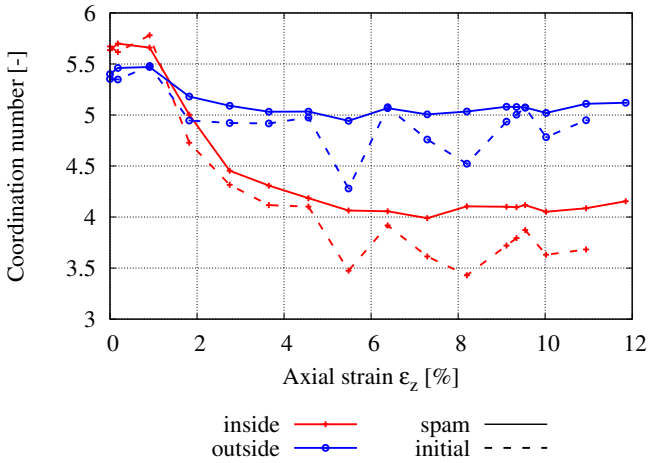

(a) Coordination number

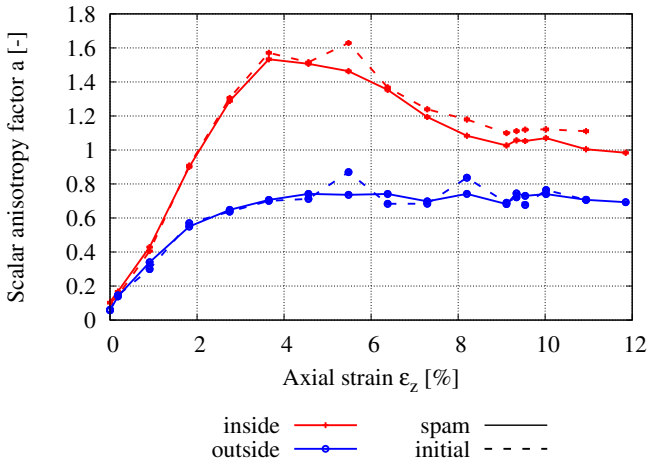

(b) Anisotropy

Figure 12.6: Showing the effect of calibrating the thresholds (global and local) carefully. The initial analysis (dashed lines) use constant thresholds for the complete image series whereas a more careful analysis with *spam* (solid lines) calibrated the thresholds for every image of the series separately. The comparison is shown on the coordination number and the scalar anisotropy factor.

12.3 Oedometric compression test

12.3.1 Experimental set-up and macroscopic response

The experimental apparatus for oedometric compression tests in the x-ray scanner in Laboratoire 3SR was developed by Zeynep Karatza [Kar17]. It was created to study grain breakage of a specific material, Zeolites. Poly Ether Ether Ketone (PEEK), an organic polymer, was chosen as the material of the cell to provide a sufficient stiffness at a low attenuation of x-rays. Two cells are available with inner diameters of 45 and 15 mm 45 and 15 mm. The latter one is used in this work in order to allow a higher spatial resolution of the grains when imaging the complete specimen. As the specimen is prepared with Hostun sand, the diameter of the cell is equivalent to 44 times the d_{50}. The chosen size of the cell allowed to acquire images at a pixel size of 10 µm which means that the d_{50} is resolved by 33 pixel.

The specimen is prepared in order to have a rather loose initial state. A funnel is installed on a tube with a smaller outer diameter than the inner diameter of the oedometer cell. The tube is put on the bottom of the cell and filled with the sand through the funnel. It is then pulled slowly upwards to fill the cell with the sand. After installing the specimen in the loading system in the tomography chamber, an initial low quality scan is performed to ensure a sufficient quality of the specimen, *e.g.*, to correct a possible tilt of the loading platen or to ensure rough homogeneity. As the test is performed on a dry specimen, no o-ring is placed between the loading ram and the loading stage. In order to decrease the friction further, the loading ram is greased.

The oedometric compression test is displacement controlled due to the loading system that is installed in the tomography chamber. The loading and unloading speed are calibrated in an initial experiment to account for rate effects and are set to 0.02 µm/s. The maximum load of this test has to account for two problematic points: crushing of the particles and the deformation of the cell that was originally developed for very soft and fragile materials. Crushing could become a problem due to the production of fines and smaller particles: Fines might not be resolvable by the pixel size of the tomography and small particles pose problems in the determination of the contact fabric, see *e.g.*, section 8.2.4. It was found in [CD86], that Hostun sand starts breaking well before 10 MPa in oedometric compression – at 10 MPa the mass of grains that have an equivalent diameter of less than the

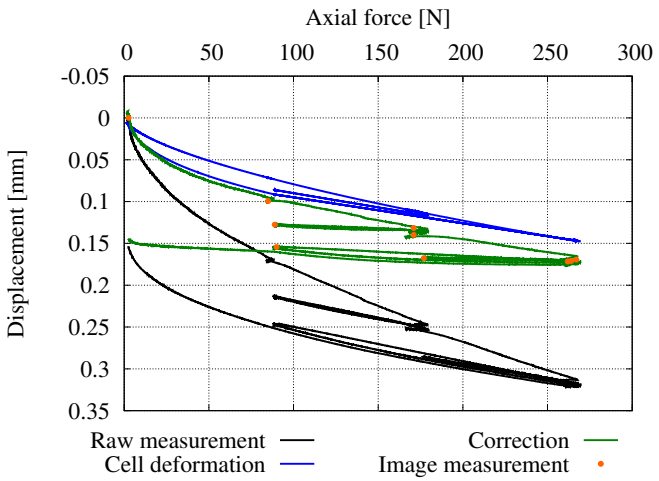

Figure 12.7: Calibration of the measured macroscopic response of Hostun sand in the oedometric compression test HNMWOD01 with unloading-reloading cycles. The raw measurements were corrected by the deformation of the oedometric cell. This calibration is tuned to correspond with the displacement as measured from the tomographies.

initial d_{10} has already doubled. The maximum load for this experiment is set to 1.5 MPa, respecting these restrictions. Three unloading-reloading cycles are carried out: the first at 1000 kPa unloading by 500 kPa, the second at 1500 kPa unloading again by 500 kPa and the third again at 1500 kPa unloading by 1000 kPa to reach the same stress state after unloading as in the first cycle. At chosen macroscopic states, the experiment is halted and a tomography of the specimen is acquired. This is generally done before unloading, after unloading and after the reloading to try to capture the structural changes that are only due to the unloading-reloading cycles. The measured macroscopic response is plotted in Figure 12.7 labelled as the raw measurement.

It was apparent from previous experiments that the apparatus is rather soft which requires a correction of the measured displacements. In this chosen set-up, the displacement of the specimen is measured by an LVDT and additionally by the motor that controls the experiment. To calibrate the oedometer cell, it is loaded in exactly the same manner as during the experiment, but without a specimen between the top and bottom platen. The calibration had to be done on a different acquisition machine outside the x-ray scanner, which corrupted that data slightly although the same

sensors are used. The measurements from the LVDT and the motor do not agree in this setup although they do agree in the set-up in the experiment. The deformation of the cell measured by the LVDT is plotted in Figure 12.7. The different loading paths can be described by the following functions:

$$d(F) = a \cdot F^b \tag{12.3}$$

$$d(F) = a \cdot F^b + c \tag{12.4}$$

$$d(F) = a \cdot F + c \tag{12.5}$$

with d being the displacement, F the force, and a,b,c the fitting parameters. The loading, the unload-reload cycles and the final unloading are fitted by equations (12.3), (12.5) and (12.4), respectively. To check these corrections, the displacements of the specimen are directly measured from the tomographies at the imaged loading states. In the images, the height of the specimen is measured as the average distance of the top platen to the bottom platen in two orthogonal vertical slices. These displacement from the images do not agree totally to the calibrated displacements. As the measurements from the images must be more accurate due to the selected pixel size and the observable changes of the height of the specimen, the calibration functions (12.3)-(12.5) are corrected to yield the displacement measured from the images. The final iteration of this calibration is shown in the main part of this work in Figure 5.7.

12.3.2 Image processing

The image processing steps are described in detail and on an example in section 9. Thus, only the crucial steps and the calibration of these image analysis tools are described briefly here. The tomographies are reconstructed to 16-bit images and processed as such in order to keep the original data range. As the cell of the oedometer consists of PEEK, its grey values are closer to the void space than the solid grains and it is automatically excluded after the images are binarised. To calibrate the global threshold, a subset from the centre of the image of the initial state is fetched. For this image, Otsu's method [Ots79] yields a more reliable threshold compared to the physically calibrated one.

The grains that are close to the top and the bottom of the specimen have slightly elevated grey-values and are excluded from the image analysis by setting the affected slices to zero. All images of the oedometric compression test are binarised with a grey-value of 30.812. The ITK watershed

[YAL+02] implemented in *spam* is applied to the binary images to segment and label the solid phase. As some grains are over-segmented and noise in the images might be assigned to the solid phase, the tricks described in 9.4 are applied to the labelled images. To exclude noise patches, labels with an equivalent radius of less than 5 pixel are excluded. The over-segmentation is reduced by merging touching labels that have a contact area that is larger than 450 pixel. Due to the exclusion of the bottom and the top layer of the specimen, some grains are not completely captured in the images. These might cause problems when calculating the contact orientations as the segmentation is problematic. Thus, these grains are identified and set to zero, *i.e.*, erased and assigned to the void phase. After cleaning the labelled images, they are relabelled sequentially to facilitate the post-processing.

Contacts are detected globally on the labelled images as described in section 9.2. As the Hostun sand grains are angular and thus, not as prone to the systematic over-detection, a local thresholding is not necessary and might exclude real existing contacts from the contact list. Nevertheless, the local thresholding code is applied to the images in order to refine the global list of contacts. In order to not loose contacts, the global threshold is employed for the local refinement. Both approaches yield slightly different results with the local refinement being more accurate. Finally, the contacts are determined using the random walker segmentation. The coordination number is calculated based on this list of contact orientations as described in section 9.5.

Some of the resulting orientations are error-prone and in order to only include the more reliable orientations in the fabric analysis, they are excluded from the fabric. The random walker as the ITK watershed might over-segment grains and the orientations determined on over-segmented grains are excluded based on the number of positions used for the PCA. This number is identical to the threshold for over-segmentation applied to the initially labelled images. Very small contacts are also very unreliable in this kind of analysis. Thus, contacts that are determined based on less than 11 positions are excluded from the contact fabric. This number, however, is not dependent on the pixel size, but calibrated on the results of the PCA and thus, similar for the images of the triaxial compression tests.

12.3.3 Contact fabric evolution in an observation window

The contact fabric anisotropy of the complete specimen does change very little by about $\Delta a \approx 0.01$ as explained in section 5.2.1 and plotted in Figure 5.9. In fact, this change cannot be used quantitatively because the error is partially larger than the fabric changes during the cycles. Therefore, the fabric in an observation window is determined following the analysis in section 5.1. In this analysis, the fabric changed more clearly in a zone where the deformation localised. Analysing the complete specimen is, thus, blurring the fabric. As the radial walls and the top platen are fixed in this oedometer cell, most deformation occurs from the bottom platen to the centre of the specimen.

The rectangular observation window is chosen to be in the centre of the specimen with a width of 700 pixel and a height of 400 pixel. This results in about 5.200 particles that are located in this window. The complete specimen has approximately 26.500 particles, although the real number is slightly higher as some grains on the boundary are excluded from the image processing to avoid dealing with artefacts. The fabric is determined differently than in the monotonic experiments with shear banding explained in section 12.2.1. As the complete specimen is already processed and the fabric is determined, only the respective orientations and particles have to be extracted. The particles located in the observation window are identified by their centre of mass (COM). If the COM is inside the window, the labels are recorded and all orientations associated to these labels are extracted from the list of contact orientations of the complete specimen. The contact fabric tensor is then calculated based on these orientations. The coordination number, however, is calculated differently compared to the complete specimen or the aforementioned analysis on observation windows. As mentioned in the corresponding sections, the coordination number is slightly lower than the real existing one, as contacts to the outside, *i.e.*, the cell or the membrane, are not considered. In the case of the observation window, this is possible: all orientations associated with the particles in the window are accounted for in the number of contacts, which includes the ones to the outside. Only the particles inside the window constitute the number of particles. This necessarily leads to a higher coordination number than found for the complete specimen. The resulting evolutions of the observation windows are plotted in Figure 12.8.

Apart from the higher value of the coordination number in the observation

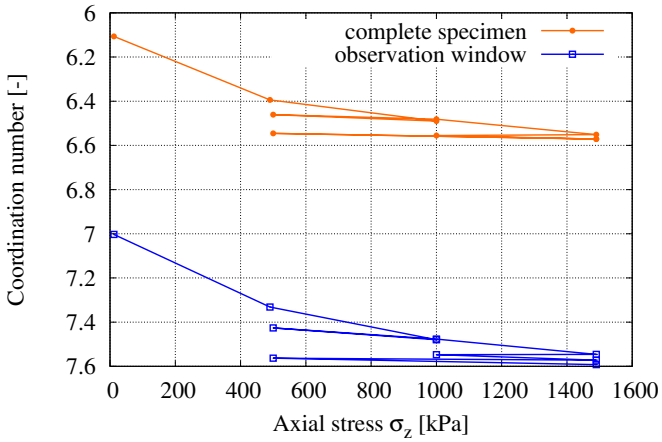

(a) Coordination number

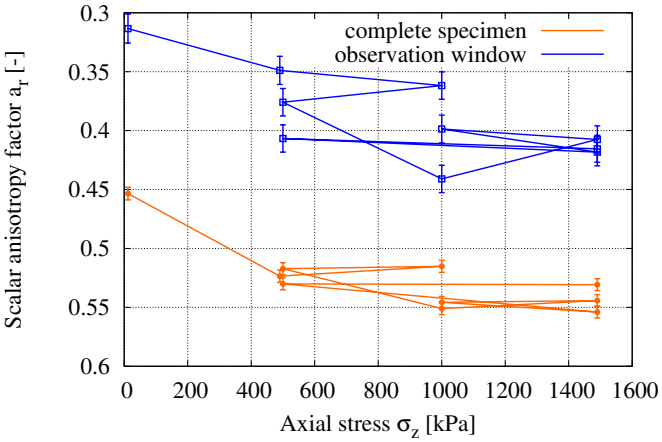

(b) Anisotropy

Figure 12.8: Fabric evolution in an observation window in the oedometric compression test HNMWOD01. The observation window is located in the centre of the specimen.

window, its evolution is very similar to the complete specimen. It is slightly more pronounced with a range that is larger by about $\Delta CN = 0.1$. The contact fabric in the window is substantially less anisotropic than in the complete specimen, which means that the fabric on the boundaries of the specimen must be very anisotropic in comparison. The evolution of the

anisotropy is covering a larger range, but it is also more defective. The error of the fabric in the observation window is higher as fewer orientations are used to built the fabric tensor. Thus, although the evolution of the anisotropy is more pronounced in the window, it is still too low compared to the uncertainty from the employed image analysis tools.

12.3.4 A simple DEM simulation of an oedometric compression test

A simple DEM simulation is carried out to complement the image analysis of the oedometric compression test. The idea is to check how large the evolution of the contact fabric is in these perfect conditions. The simulation is carried out in a similar way as described for the benchmarking in section 10.1.1. The main difference is the application of the loading in this oedometric compression compared to the triaxial compression test. Periodic boundary conditions are also used in this simulation. A simple linear (Cundall) contact model is used that consists of an elastic spring in the contact normal and a frictional slider in the tangential direction with the following parameters: Young's modulus of 300 MPa, a ratio of tangential to normal stiffness of $k_t/k_n = 0.4$ and a friction of $\tan\varphi = 0.6$. These parameters are empirically chosen to result in a comparable stress-strain response as the experiment, *i.e.*, approximately 2.5 % axial strain at 1500 kPa axial stress. A random packing of spheres with a linear particle size distribution ranging from 320 to 480 µm is created and isotropically compressed to 10 kPa. To create a rather loose initial state, as it was done for the experiment, the friction is set to $\tan\varphi = 1$ in the preparation step. The lateral boundaries are kept at a constant position for the actual simulation after the initial state is created. The loading is applied by compressing the vertical boundaries at a constant velocity similar to the set-up of the experiment. At chosen states of the experiments, the contact fabric and the positions of all spheres are recorded and the coordination number as well as the fabric tensor and its anisotropy are computed similar to the real experiment. The evolution of these values are plotted on top of the macroscopic response in Figure 5.10 and briefly discussed in section 5.2.1.

12.4 Triaxial compression test

12.4.1 Experimental set-up and macroscopic response

The triaxial apparatus from Laboratoire 3SR is used in this work to perform the triaxial compression tests. It was developed by Nicolas Lenoir and Pierre Bésuelles and is described in detail in [Len06] and [And13]. In contrast to the standard set-up, this apparatus has no tie bars in order to allow a proper acquisition of x-ray radiographs during the test. The reaction forces are carried by the cell itself. The cell is composed of Poly-Methyl-Methacrylate (PMMA) as this material has a low x-ray attenuation coefficient. The cell with the specimen is installed on the rotation stage of the x-ray scanner. The motor for the application of the axial loading is hanging from the rotation stage to allow the rotation of the stage during the experiment. The bottom and the top platen that comprise the specimen are made of ceramic. Their axial surfaces have a very low friction coefficient to decrease the influence of these plates on the deformation of the specimen. Two different loading rams are available: one having a spherical and the other a flat tip. The spherical tip is employed for every experiment in this work. To seal the cell, an o-ring is placed between the bottom plate and the loading ram. The ram is greased to reduce the friction. The set-up inside the tomography chamber is shown in Figure 3.2.

The specimens are rather small in this experimental set-up because tomographies of the complete specimen are acquired at a pixel size that is sufficient to identify each individual grain. The choice of these small dimensions is a trade-off between the pixel size of the tomography and the representativeness of the specimens: a specimen consisting of too few grains would not yield a representative continuum answer, but a specimen consisting of too many grains could not be imaged at a sufficient pixel size [AVHD13]. The size of the specimen is $\approx 11\,\text{mm}$ in diameter and $\approx 22\,\text{mm}$ in height, which amounts to roughly 50,000 grains.

In order to prepare a specimen, the membrane is installed in a mould with one of the loading platen in place. The membrane is then dragged to the walls of the mould by applying a suction. The specimens are created to have an initially loose or dense state. To achieve a dense initial state, the sand is pluviated as described in [And13]: a 1 m long tube is placed above the mould and the sand is slowly dropped through this tube. The tube is slowly pulled upwards to roughly keep the same drop height during the

preparation. This method of preparation is used to create the specimen HNMWTC02 and HNMWTC05[8]. The loose initial state is created in the same way as for the oedometric compression test: a tube that has a smaller diameter than the final specimen is placed on the bottom of the mould and filled with sand. The tube is slowly pulled upwards to reduce impact effects on the package. This method is used to prepare the specimen TC03 and TC04 and will be referred to as *piling* in this work. A ceramic plate is then put on top of the specimen and the membrane is folded over the plate to close the specimen. The other plate has a hole in order to create a suction inside the specimen. After this suction is applied, the suction applied to hold the membrane is released and the specimen is installed in the loading system. The cell is then slowly filled with water. To check the quality of the specimen, *i.e.*, the homogeneity and the perpendicularity of the specimen, a fast low-quality tomography is acquired. If the specimen has a sufficient quality, a pressure is applied to the water in the cell and the suction inside the specimen is released. If the quality is not sufficient, a new specimen is prepared in the same way. Finally, the loading ram is driven into contact with the bottom platen.

Depending on the specific experiment, the specimen is loaded in compression and undergoes several unloading-reloading cycles, similar to the oedometric compression test. All experiments are conducted on Hostun sand. The loading speed is 0.3 µm/s. The cycles are carried out with a lower speed of 0.1 µm/s for both paths, unloading and reloading. All four experiments were carried out with latex membranes. For every preparation method, pluviation and piling, two different cell pressures were applied to the specimens, 100 kPa and 400 kPa.

As the specimens are dry, there is no possibility to directly record the volumetric strain of the whole specimen during the experiment, which is usually done through the expelled or retracted water. To measure the volumetric behaviour, the void ratio is determined from the binary images of the acquired tomographies as described in section 9.6. The initial settings of each specimen, such as geometry and void ratio, are reported in Table 12.2[9].

[8]The experiments are named by the following convention: The two first letter refer to the material, the second pair to the experimentalist and the last two to the test. In this case it is HN for Hostun sand, MW for Max Wiebicke, TC for triaxial compression test. As these are similar for all experiments in this section, only the last pair and the number (ID) will be used for identification here.

[9]The relative density I_D given in this table is determined by $I_D = (e_{max} - e) / (e_{max} - e_{min})$. The minimum and maximum void ratios are given in sec-

test	preparation	$h_0\,[mm]$	$d_0\,[mm]$	cell pressure
HNMWTC02	pluviation	22.965	10.515	100 kPa
HNMWTC03	piling	23.910	10.305	100 kPa
HNMWTC04	piling	24.015	10.35	400 kPa
HNMWTC05	pluviation	23.145	10.47	400 kPa

	$e_0(I_D)$	tilt [°]
HNMWTC02	0.661 (83 %)	0.582
HNMWTC03	0.723 (64 %)	1.035
HNMWTC04	0.722 (64 %)	2.105
HNMWTC05	0.655 (85 %)	1.484

Table 12.2: Initial settings of the triaxial compression tests. h_0, d_0, e_0, I_D being the initial height, diameter, void ratio and relative density.

The initial void ratios show that the second method of preparation, piling, is not reliable and far from creating loose specimens. The two specimens TC03 and TC04 do have lower void ratios than the pluviated samples, but their relative densities can still be considered as medium-dense.

The macroscopic responses of the specimens are plotted in terms of the stress and void ratio in Figure 12.9 . The experiments are sorted by the applied cell pressure: 100 kPa in Figure 12.9a and 400 kPa in Figure 12.9b. The evolution of the void ratio agrees with the calculated initial relative densities. The pluviated samples with lower void ratios dilate substantially whereas the experiments created by piling show a different evolution. The loosest sample, TC04, is compressing while the void space of TC03 is almost constant throughout the loading.

Although the stress-strain evolution was measured continuously in experiment TC05, the controlling machine did not record the data. The force and displacement at every acquisition of a tomography were, fortunately, entered in a log file of the experiment and the stress response is recreated from these values.

tion 12.1.

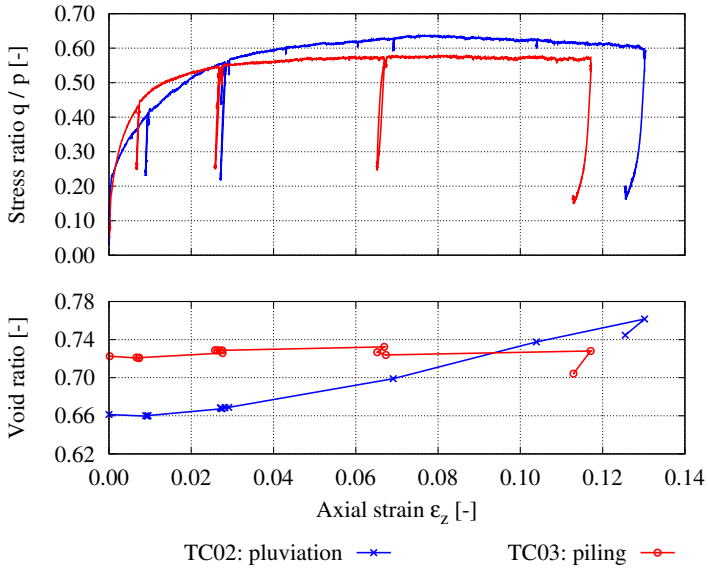

(a) Triaxial compression tests at 100 kPa.

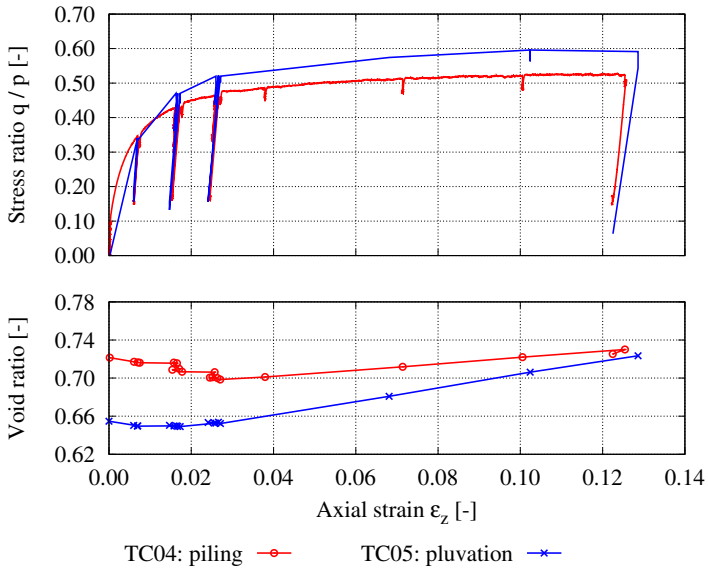

(b) Triaxial compression tests at 400 kPa.

Figure 12.9: Macroscopic response of the triaxial compression tests. The experiments TC01-03 are conducted at 100 kPa cell pressure and TC04-05 at 400 kPa. The specimens TC03 and TC04 are prepared by piling and TC02 and TC05 by pluviation.

12.4.2 Image processing

The images of the experiments TC02 - TC05 are processed in the same manner because they have very similar properties due to the experimental set up. For brevity, only the processing of the experiment TC03 is described here.

Due to the higher density of the caps, the grey-values of the specimen are elevated close to the top and the bottom cap. To process the images similarly all over the specimen, these elevated regions are identified and excluded from the image. These regions cover only 1-2 grains in height and can thus, be excluded without loosing important data to describe the fabric. Note that these regions can be influenced strongly by the boundary conditions. Similarly, an area of several grain diameters from the specimen boundary is regularly excluded in the analysis of DEM simulations [ASS05, SNS+15]. The latex membrane does not have to be addressed specifically as it has a very low x-ray attenuation coefficient compared to the grains and is automatically excluded when binarising the image with a suitable threshold.

Generally, the reconstructed 16-bit images are directly processed without rescaling them to 8-bit images as done in section 12.2. The threshold for the binarisation, *i.e.*, the distinguishing between solid and void voxels, is selected using the statistical method of Otsu [Ots79]. This is done on a subset in the centre of the specimen with a size of 400x400x400 voxel^3, such that the least amount of image artefacts influence the grey-level of the voxels. Initially, the thresholds were only chosen based on the distribution of grey-values in the tomography of the initial state. As found for monotonic experiments in section 5.1, these distributions sometimes shift even during an image series with no apparent changes to the imaging procedure. This also concerned the image series of the experiments 03, 04 and 05. The thresholds for binarisation and contact detection are therefore calibrated on each image specifically using Otsu's threshold. The methodology and the impact are similar to those of the anaylsis on the monotonic experiments and are therefore only described in sections 12.2.1 and 12.2.4, respectively. The binary image is then segmented and labelled with the ITK watershed [BL06] that is implemented in *spam*. To clean the image of noisy voxels and over-segmentation, the following steps are applied to the image as described in section 9.4. In order to remove labels that are not assigned to particles but rather to noisy patches in the image, the equivalent radius of each

label in the image is determined and labels with a radius smaller than a defined threshold are set to zero and, thus, excluded from the analysis. As the Hostun sand grains have an angular shape, over-segmentation can be a problem. To decrease this over-segmentation, the number of voxels of the contacting surfaces of each pair of labels is calculated. If this number is larger than a set threshold, the labels are merged as they are considered to be originally one single grain that has been over-segmented. For the analyses of Hostun sand grains at a pixel size of 15 µm, the limits are set to 3.33 voxel and 300 voxel for the equivalent radius and the contact surface, respectively. As the images are cut close to the top and the bottom cap, particles lying on that boundary are only partially included in the image. These particles might cause problems in the later processing of the image and are thus, excluded from the labelled image. After excluding the labels that meet all these criteria, the image is relabelled sequentially.

The contact fabric is determined as described in sections 9.2 and 9.3. No local thresholding is applied to the images because angular particles are not as prone to over-detection of contacts as round particles and contacts might be lost easily when locally refining the contact list. The local thresholding algorithm is however applied to the image using the global threshold to exclude some wrongly detected contacts. The orientations are determined using the random walker segmentation on the contact pairs. As the orientations are calculated by running a PCA on the probability map from the random walker, the quality of an orientation can be estimated by the number of positions involved in the fit. In this work, orientations that are determined from less than 11 positions are excluded from the later analysis as they are very error-prone. Furthermore, the complete analysis is automated and the individual segmentation success of either the initial segmentation of the ITK watershed or of the random walker is checked visually. Thus, over-segmentation can become a problem as described in section 9.4. To decrease the influence of over-segmentation of the random walker, orientations that are determined based on an amount of positions involved in the fit that is larger than a calibrated threshold are excluded. This threshold is set to 300 voxel for Hostun sand at a pixel size of 15 µm/pixel.

12.4.3 16-bit versus 8-bit analysis

The first analyses are conducted on 8-bit images in this work. The reason for this choice was the availability of computational resources, mainly the

memory. Thus, 8-bit images of the experiments HNEA01 and COEA01 in section 12.2 are processed after rescaling the 16-bit images. After getting access to the clusters of the centre for high performance computations (HPC) at the TUD, the processing of 16-bit images of complete samples was feasible and the majority of experiments are processed as 16-bit images.

The range of grey-values is substantially smaller in unsigned 8-bit images $[0; 255]$ compared to the 16-bit images $[0; 65{,}535]$ that are produced by the reconstruction process. The contact detection and orientation are sensitive to a change of grey-values as shown in section 8. As the range of deciding whether a voxel belongs to the solid or void phase is considerably lower, the type of the image is expected to have a strong influence on the computed contact fabric.

To check this influence, the contact fabric of the initial state (01) and the state at the highest shear strain (13) of the experiment HNMWTC03 is determined on the original 16-bit as well as the downscaled 8-bit images. The images are processed as described in the previous section. The threshold for the binarisation of the 16-bit images is calculated with Otsu's method to 28,508. Its corresponding value of 111 is used for the 8-bit images.

The coordination number is computed as described in section 9.5 to check the effect on the detection of contacts. It must be noted, that this is not a quantitatively reliable estimation of the coordination number and that such an estimation directly from the images is hardly possible. At the initial state, the coordination number is 7.367 for the 16-bit image and 7.363 for the 8-bit image. The coordination number for state (13) are 6.747 and 6.745 for the 16-bit and 8-bit images, respectively. This change of 0.05 % is negligible.

The contact orientations of state (13) are plotted in Figure 12.10. It is clear that the type of the images has roughly no visible influence on the distribution of the orientations. A second order fabric tensor is computed on the basis of these orientations to determine the anisotropy for both states. The scalar anisotropy factor for the first state is 0.103 for the 16-bit image and 0.104 for the 8-bit image. For state (13) the anisotropy amounts to the 0.560 for both image types, when expressed to the third digit. As the number of orientations is in the same order in both states, the uncertainty of the scalar anisotropy factor is $\delta a \pm 0.004$ for all states and image types. Thus, the anisotropy is almost identical and well within the uncertainty interval of the calculation itself. Due to these reasons, the processing of the

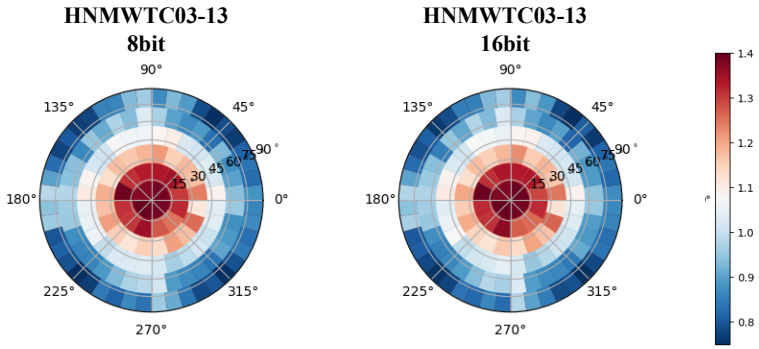

Figure 12.10: Contact orientations of state 13 of the triaxial compression test HNMWTC03. Comparison of the results of an analysis on the original 16bit and the scaled 8bit images. The orientations are plotted using the Lambert azimuthal equal area projection as described in 7.2.1.

images that were already evaluated (HNEA01, COEA01) is not repeated with their original 16-bit data range.

12.4.4 Reproducibility of the tomographies and the image processing

In order to test the reproducibility of the acquisition of the 3D images as well as the image processing, two tomographies of the initial state of specimen HNMWTC02 are acquired. Both tomographies are acquired at the same settings and the second one is started directly after the first one is finished. The contact fabric is determined as described in section 12.4.2 in exactly the same way in both images. As this comparison is part of an early study in this work, the images are scaled from 16-bit to 8-bit in order to save memory. The impact of downscaling, however, should be negligible as shown in the previous section.

The coordination numbers amount to 7.613 and 7.616, for the first and the second image, respectively. The agreement of these values appears close, especially as this measurement is error-prone and sensitive to image defects as shown in section 8.2.3. The contact fabric anisotropy of both states is determined to 0.154 and 0.149 with an uncertainty of $\delta a \pm 0.004$ in both images. In terms of the contact fabric, the acquisition and the image processing of selected states is reproducible.

12.4.5 Initial contact fabric

The first topic that is addressed here is the initial state. The specimens are prepared in two different ways: by pluviation from a specific drop height to create a dense initial packing (pluviation) and by filling the specimen slowly from the bottom to the top to achieve a looser initial packing (piling). Two questions that can be asked in terms of the contact fabric are: (1) how reproducible are the initial states and (2) to what extent do the two different methods differ?

The experiments can be distinguished clearly by their initial coordination number which is given in Table 12.3. The specimen that are created by pluviation have an initial coordination number of 7.61 (TC02) and 7.66 (TC05). This number is slightly higher for the test carried out at 400 kPa (TC05). The experiments prepared by piling start with coordination numbers of 7.19 (TC03), 7.25 (TC04). The methods of preparation are well captured and engrained in the structure of the specimen with the higher coordination numbers corresponding to the pluviated sample and the lower ones to the piling. The reproducibility in terms of the coordination number is given as well with only slight changes. These slight changes could be in the same order as the error in the determination of the actual contacts as investigated in section 8.2.3. It is, however, difficult to directly relate the over-detection to an error of the actual detection of contacts.

The distribution of orientations for all initial states is plotted in Figure 12.11. All specimen have a contact fabric that is at least slightly aligned with the vertical direction, *i.e.*, the direction of creating the specimen. To compare the anisotropy, a second order fabric tensors and its anisotropy as defined in Equations (1.2) and (7.8). As all initial states have the same order of the number of contacts, the uncertainty of the anisotropy is almost similar and amounts to $\delta a = \pm 0.004$. The anisotropy of the pluviated samples

Measure	TC02	TC03	TC04	TC05
coordination number	7.61	7.19	7.25	7.66
anisotropy	0.158	0.103	0.241	0.181

Table 12.3: Initial contact fabric of the triaxial compression tests. Mean coordination number and scalar anisotropy factor from the second order fabric tensor as described in section 7.1

.

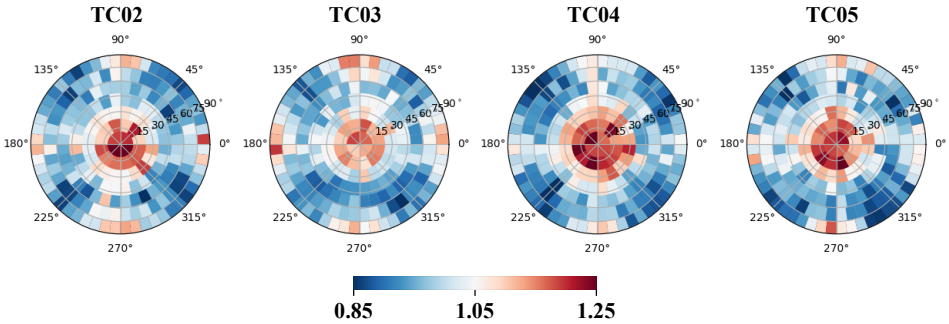

Figure 12.11: Contact orientations at the initial state of the triaxial compression tests. The orientations are plotted using the Lambert azimuthal equal area projection as described in section 7.2.1.

ranges from 0.158 to 0.181 whereas the specimen prepared by slow filling experience a substantially higher range of anisotropies ranging from 0.103 to 0.241, as given in Table 12.3. That might be due to the controllability of the preparation: as the slow dropping is done very crudely by hand, it is far more influenced by the experimentalist than the pluviation with the grains dropping from a set drop height. In order to carefully quantify the reproducibility of the specimen, more tests need to be included in this analysis.

12.4.6 Response of the contact fabric

The evolution of the contact fabric is depicted in Figure 12.13. Both measures, the coordination number and the anisotropy as defined in section 7.1, are plotted individually for the experiments at 100 kPa and 400 kPa cell pressure.

As contacts are systematically over-detected, the apparent coordination number is larger than the existing one[10]. This number, however, is evaluated on the complete specimen and contacts to the boundary of the specimen, *i.e.*, contacts with the membrane or the top and bottom caps, cannot be included. Thus, the apparent coordination number is reduced.

The coordination number follows a similar evolution in all experiments. It decreases throughout the macroscopic loading after a small initial compression. The extent is consistent with the change of the void ratio: it is

[10] See sections 4.1 and 8.2.3 for more information from the metrological study.

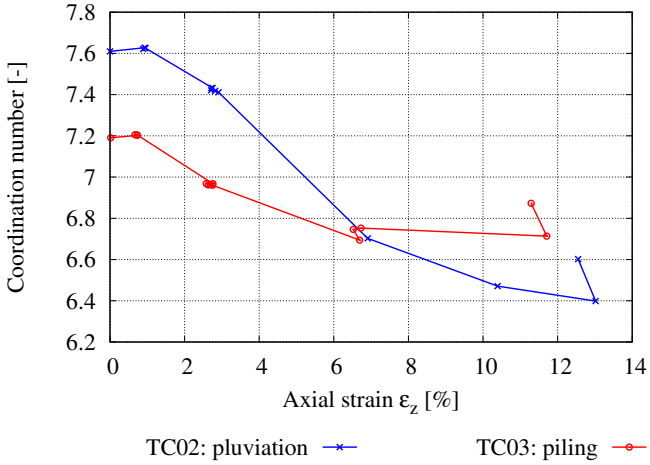

(a) Tests at 100 kPa cell pressure.

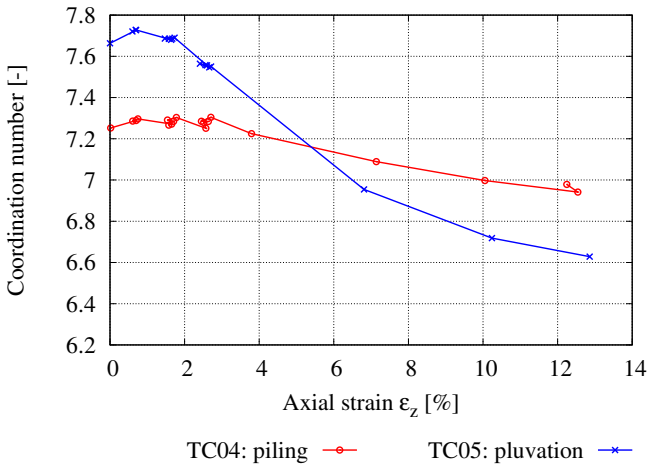

(b) Tests at 400 kPa cell pressure.

Figure 12.12: Evolution of the coordination number in the triaxial compression tests. The specimens TC03 and TC04 are prepared by piling and TC02 and TC05 by pluviation.

higher for the specimen that are pluviated (TC02, TC05) and lower for the specimen that are piled. Specimen 04 experiences the lowest change of the coordination number although it has a similar initial void ratio and coordination number to TC03. Only the cell pressure is significantly different, which might lead to an almost constant contact density.

The main point of this analysis, however, is the reaction of the contact fabric to the load-unload cycles. The coordination number changes only very slightly during the load cycles. It generally increases during unloading and decreases during the reloading. For the dense specimens (blue lines) these changes remain on the same path as the initial loading, whereas the medium dense specimens (red lines) experience a slightly more unique change. It stays almost constant at the third cycle for TC03 and reacts significantly for the 4th cycle. Specimen TC04 experiences the most significant change during the load reversals with the main changes, however, happen at unloading where the contact density always increases.

Very similar observations can be made on the anisotropy of the fabric tensor as defined in section 7.1. The anisotropy increases for every specimen with the general loading, disregarding the cycles. It increases substantially more for the dense specimen (blue lines) than for the medium-dense ones (red lines). The cell pressure does not seem to have a significant impact on the evolution of the anisotropy. At least not in these tests, as the range of anisotropy is higher for TC05 at 400 kPa compared to TC02 at 100 kPa for the dense specimens. This, however, does not apply for the medium-dense specimens, as the range is smaller for TC04 at 400 kPa than for TC03 at 100 kPa[11].

Comparable to the contact density, the anisotropy of the specimen at lower cell pressure (TC02 and TC03) does not change significantly at the load cycles. It does decrease very little at the first cycle of experiment TC02 and the fourth of TC03, but stays relatively constant otherwise. The specimen at higher cell pressure, react stronger to the cycles. It decreases consistently at every unloading and stays increases during the reloading. Especially for the dense specimen, the fabric changes stay on the same path as for the initial loading, comparable to the evolution of the coordination number.

[11] This can be observed in Figure 12.13. The absolute values for the changes in anisotropy and coordination number are given in Table 12.4

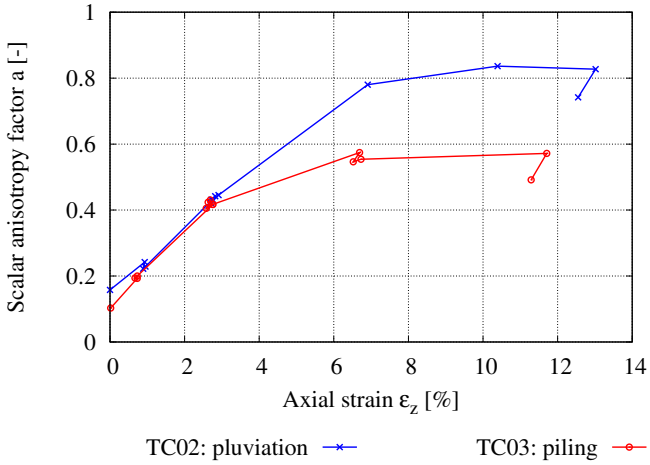

(a) Tests at 100 kPa cell pressure.

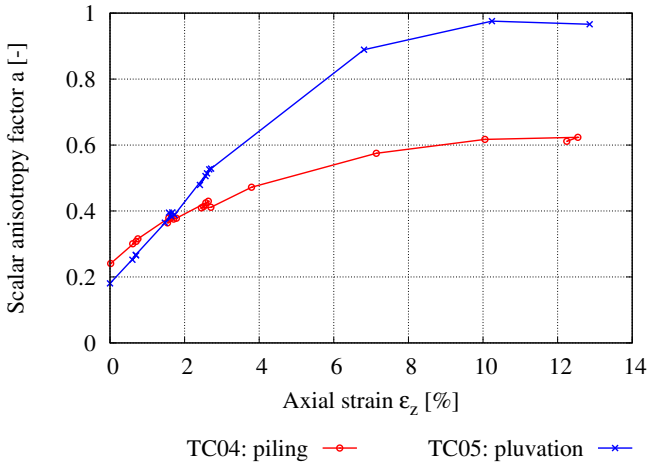

(b) Tests at 400 kPa cell pressure.

Figure 12.13: Evolution of the contact fabric anisotropy in the triaxial compression tests. The specimens TC03 and TC04 are prepared by piling and TC02 and TC05 by pluviation.

12.4.7 Fabric analysis of observation windows in the triaxial compression specimens

Analogously to the analysis of the experiments on Hostun sand and Caicos ooids in section 12.2, the contact fabric is evaluated in chosen observation windows in the cyclic triaxial compression tests. A window, that is fixed in space, is chosen in each test such that it contains the developing shear band. It is located in the centre of the specimen and spans 300x300x300 pixel^3. In contrary to the approach in section 12.2, the windows are not extracted as sub-images from the complete image. The results from the analysis of the complete images, *i.e.*, the lists of contacts and orientations, are the basis here.

The grains that are located inside the shear band are identified in the labelled image of the complete specimen by their centre of mass (COM). If the COM is located in the prescribed volume, the corresponding labels are considered as part of the observation window. When extracting the data, contacts to the outside of the window can be included in the measure as well.

In order to also include the orientations to the outside of the observation window, any orientation that is associated to at least one label that lies within the window is included in the new list of orientations of the window. The coordination number is determined differently than on the complete specimen in order to include all contacts. The number of contacts is composed of the internal contacts and the contacts to the outside of the window. The number of particles, however, is only determined by the labels that lie within the observation window. Thus, the coordination number is higher for the windows than for the complete specimen. The fabric tensor is calculated as usual on the whole set of contacts, *i.e.*, internal and external ones. To deal with over-segmentation and noise, the same thresholds as described in sections 9.4 and 12.4.2 are employed.

The results of the contact fabric analysis in the windows of all specimens are displayed in Figure 12.15. The coordination number of the window evolves qualitatively similar to the complete specimen. The two quantitative differences are the actual values and the rate of change. The coordination number is larger in the windows because external contacts are also considered as described above. The range of the coordination number, however, is also larger in the windows, *i.e.*, the evolution is more pronounced in the shear band.

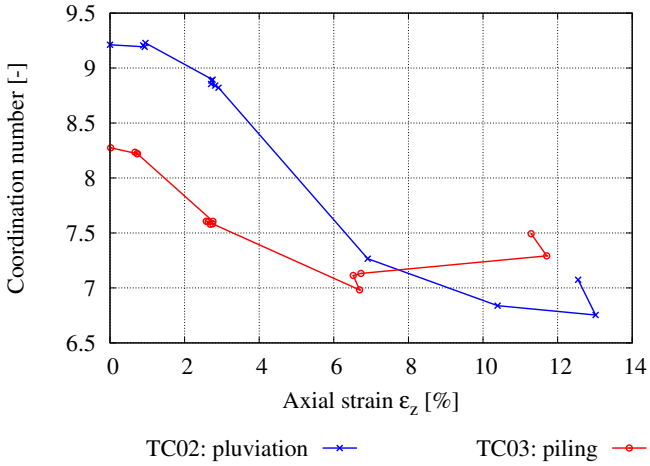

(a) Tests at 100 kPa cell pressure.

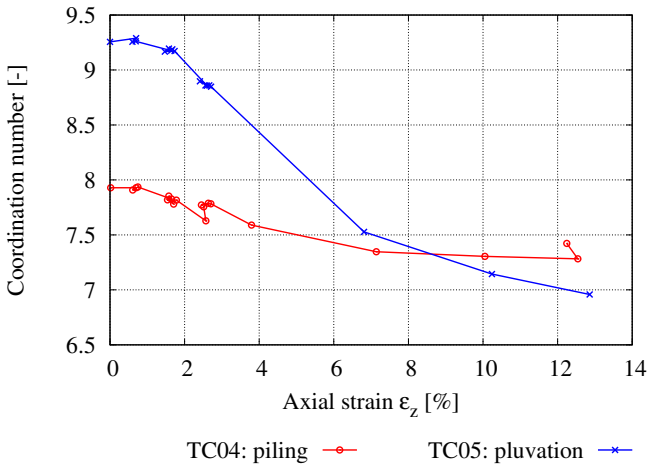

(b) Tests at 400 kPa cell pressure.

Figure 12.14: Evolution of the coordination number in observation windows in the triaxial compression tests. The windows are fixed in space and contain the evolving shear band. The specimens TC03 and TC04 are prepared by piling and TC02 and TC05 by pluviation.

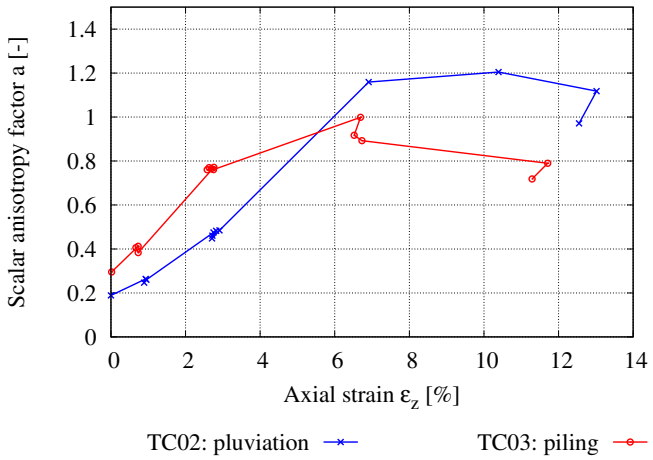

(a) Tests at 100 kPa cell pressure.

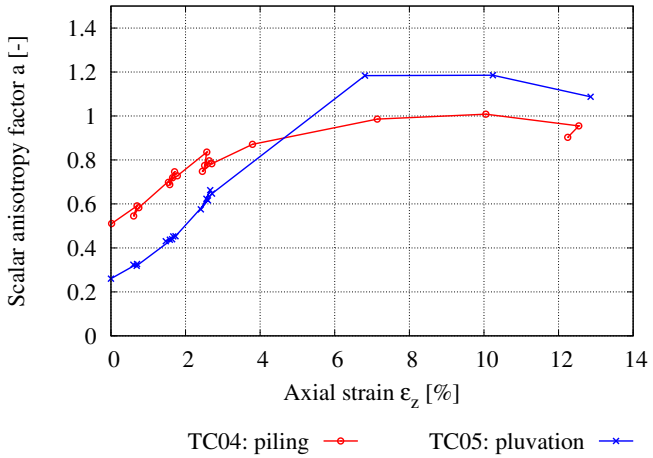

(b) Tests at 400 kPa cell pressure.

Figure 12.15: Evolution of the contact fabric anisotropy in observation windows in the triaxial compression tests. The windows are fixed in space and contain the evolving shear band. The specimens TC03 and TC04 are prepared by piling and TC02 and TC05 by pluviation.

Measure	Set	TC02	TC03	TC04	TC05
Δ coordination number	complete	1.23	0.51	0.36	1.1
Δ coordination number	window	2.47	1.29	0.65	2.33
Δ anisotropy	complete	0.68	0.47	0.38	0.80
Δ anisotropy	window	1.02	0.70	0.50	0.93

Table 12.4: Range of the fabric measures inside the observation windows and in the complete specimen of the cyclic triaxial compression tests. The measures displayed are the coordination number and the scalar anisotropy factor determined on the second order fabric tensor as defined in section 7.1.

The anisotropy of the contact fabric tensor is not affected by including the external contacts as the tensor is normalised by the number of contacts instead of the number of particles. The evolution of the anisotropy inside the observation window is stronger than in the complete specimen. This is in agreement with the findings of the analysis in section 12.2: the fabric inside the shear band evolved more pronounced than outside. Thus, it leads to an overall fabric evolution that is similar but less strong than the evolution inside the shear band as it gets smeared by the zones in which the fabric is only slowly evolving.

Both fabric measures, the coordination number and the contact fabric anisotropy, evolve more pronounced in the observation window that contains the shear band than in the complete specimen. The range of values of the coordination number and anisotropy of all tests within the window as well as in the complete specimen are given in Table 12.4.

12.4.8 Response of the particle fabric

Most of the analysis in this work is on the evolution of the contact fabric. In order to complement these measures, the triaxial compression tests are also analysed in terms of another fabric entity, the particle orientation. There are three principal particle axes which are defined on the eigenvectors from the moment of inertia tensor (MOI) as described in section 4.3. As Hostun sand has a variety of shapes and no distinct axes could be identified using the 53 grains from the high resolution tomographies in section 11.2, two axes are regarded here. The particle fabric tensor is determined based on either the eigenvector corresponding to the maximum and or to the minimum

eigenvalue, *i.e.*, the shortest and longest axis of the grain, respectively.

The principal particle directions can be determined from the labelled images using *spam* [ACR+] in the following way:

```
import tifffile, numpy
import spam.label.label as ltk
volLab = tifffile.imread(folder+filename+"-lab.tif")
eVal, eVec = ltk.momentOfInertia(volLab)
```

This function calculates the MOI tensor for every label in the range of the minimum and maximum label in the image. Several labels, however, might not exist anymore due to the image treatment, which is why no MOI can be calculated and the function returns a vector filled with zeros. These need to be excluded from the list of particle orientations before using them to determine the fabric tensor. This can for example be done using the following loop:

```
for i in range(len(eVal)):
    if (eVal[i,0]!=0):
        #write to file....
```

To visualise an evolution of the particle fabric, the anisotropy is calculated from the deviatoric part of the fabric tensor as defined in Equation (7.8). In *spam* this is achieved by using the following function:

```
orientations = numpy.loadtxt( folder+filename+"-
    particleOrientations_exclude.txt", usecols
    =(11,10,9) )
N, D, a = ltk.fabricTensor(orientations)
```

The anisotropy of the tensor built from the long particle axis is plotted in Figure 12.16a. The evolution of the anisotropy is very similar for all specimens. They start at different initial values, but increase at almost the same rate during the loading. The anisotropy determined on the short axes of the particles shows a slightly different response as displayed in Figure 12.16b. The rate of increase is slightly different for all specimen. It seems that specimen with a higher initial density experience a faster increase in anisotropy. The extreme case is specimen TC04: it starts at the highest particle fabric anisotropy and increases at a substantially slower rate than the other tests.

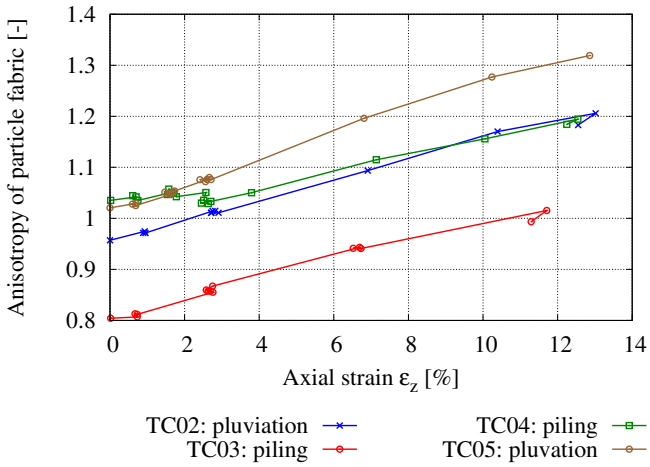

(a) Anisotropy of minimum eigenvectors.

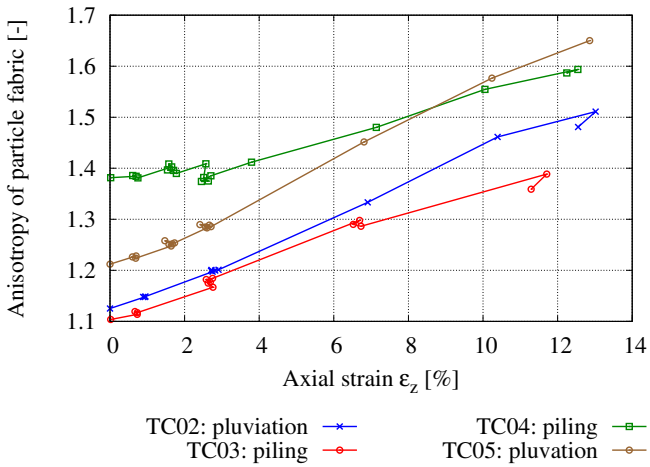

(b) Anisotropy of maximum eigenvectors.

Figure 12.16: Evolution of the particle fabric anisotropy. Specimens TC03 and TC04 are prepared by piling and TC02 and TC05 by pluviation.

The particle fabric in general, *i.e.*, for the minimum and maximum eigenvalues, does not react to the load cycles. Only very small changes can be observed, but these do not show systematic response. Furthermore, the evolution of the anisotropy does not seem to slow down or peak or show any features that might be used to draw conclusions on the macroscopic behaviour. For more distinct shapes, such as lentils, the particle fabric shows a characteristic evolution. An experiment on lentils is described and analysed in the next section.

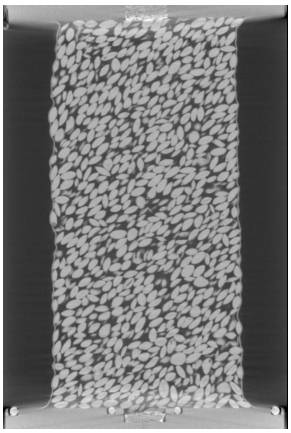

Figure 12.17: Vertical slice through the tomography of the initial state of the lentils specimen.

12.5 Cyclic triaxial compression test on lentils

Within the framework of another research project that is driven by Jacques Desrues from Laboratoire 3SR in Grenoble, a triaxial compression test on lentils is carried out. There are mainly two reasons why it is included in this work: (1) The specimen undergoes several load cycles during the experiment. (2) The very distinct shape of the lentils is suspected to cause a more pronounced response of the particle fabric. The specimen is prepared to have a highly anisotropic initial state because the aim of the other project is to investigate the influence of inherent anisotropy on the evolution of fabric and the macroscopic response. This is also the reason why lentils are chosen as they facilitate the creation of such an anisotropic initial state. The lentils are commercial lentils that are sold in the supermarket. They have a long axis of approximately 6.6 mm and are therefore substantially larger than the sand grains that are used for the other experiments in this work. Thus, a cell, that was developed by Jacques Desrues et al [DAB+17] for bigger specimen, has to be used to test a specimen consisting of these lentils.

The initial anisotropy is created by layering the particles such that their short axis is inclined by 45° to the vertical direction, *i.e.*, the main loading direction. The initial state is visualised by the vertical slice in Figure 12.17. This is done by spooning the lentils into the mould that is tilted by that angle. After sealing the specimen with the top cap and applying a vacuum,

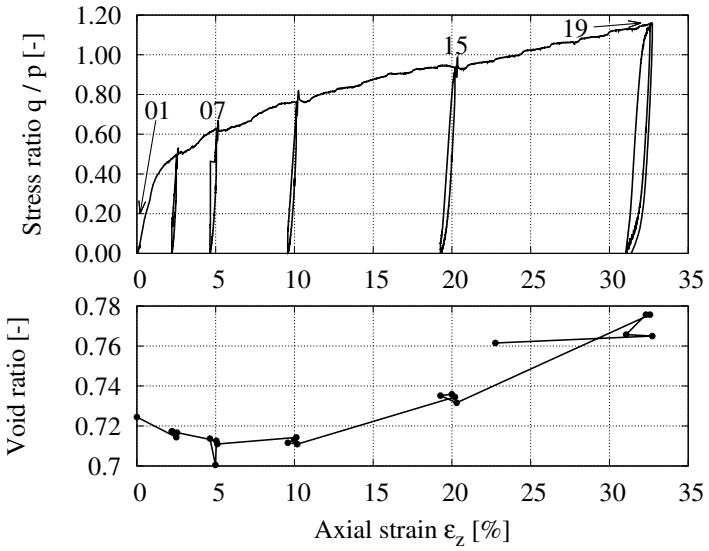

Figure 12.18: Macroscopic response of the lentils specimen in a triaxial compression test.

it is installed in the triaxial loading system in the tomograph of Laboratoire 3SR. The specimen has a diameter of 68 mm and a height of 140 mm. The loading is then applied in the same way as for the other triaxial experiments in this study. The cell pressure for the experiment is 50 kPa. The specimen is unloaded and reloaded at chosen stages of the general loading and tomographies are acquired before each change of the loading direction. Due to the size of the specimen, the pixel size of the tomographies is relatively large with 180 µm. The long axis is still resolved by approximately 37 pixel, since the lentils are an order of magnitude larger than the Hostun sand grains. The macroscopic response is plotted in Figure 12.18. Unlike the other triaxial compression tests, no tendency towards an asymptotic state can be observed within an axial strain of 32 %.

12.5.1 Image processing

The images are generally processed as described in section 9 and similar to the other image series of triaxial compression tests. As visible in the vertical slice in Figure 12.17, the regions of the specimen that are close to the caps are subject to an elevated grey-level. The images are capped at these

regions and the particles that lie on the chosen boundary are erased in the labelled image and thus, excluded from the analysis. Due to the high spatial resolution of the particles, the images are binned and transformed from 16-bit to 8-bit to save computation time and memory. The global threshold for the binarisation is chosen to 144 using Otsu's method [Ots79]. The image is then segmented using the ITK watershed [BL06] as implemented in *spam* [ACR+].

As the lentils are very well rounded, the optimal local threshold from the metrological study on the manufactured spheres is applied to locally refine the contact list as explained in section 9.2. The histogram of the grey-values is therefore distorted to the normalised histogram in which the peaks for solid and void phase are located at 0.75 and 0.25 in the range of [0.,1.]. Using this distortion, the optimal threshold of 0.65 as found in Figure 4.9a is translated to a local threshold of 156 for the original 8-bit images. The process of distorting the histogram of grey-values is also described in section 7.4. The orientations of the refined contacts are determined by applying the random walker [Gra06] to each contact pair as described in sections 4.1.2 and 9.3.

The particle orientations are calculated from the labelled image by calculating the MOI tensor for each grain and determining its eigenvectors. The methodology and the processing are described in sections 4.3 and 12.4.8, respectively. Some code snippets are given in the latter, explaining the usage of *spam* [ACR+]. Lentils have two long and one short axis. The eigenvector corresponding to the maximum eigenvalue, that points in the direction of the short axis, is therefore used to describe the particle orientations.

12.5.2 Fabric response

Both, the orientations of the contacts and the particles are shown in Figure 12.19. They are plotted using Lambert azimuthal equal area-projections[12]. The particle orientations of the initial state (in the upper left figure) show that the intended anisotropic state is successfully created as the vast majority of orientations lies on the 45° inclination line. There is also a strong alignment with the azimuth of 90° which originates from the preparation by spooning. The particles settle with their short axis in the vertical direction during the preparation. This initial anisotropy is also manifested in

[12]These projections are introduced in section 7.2.1.

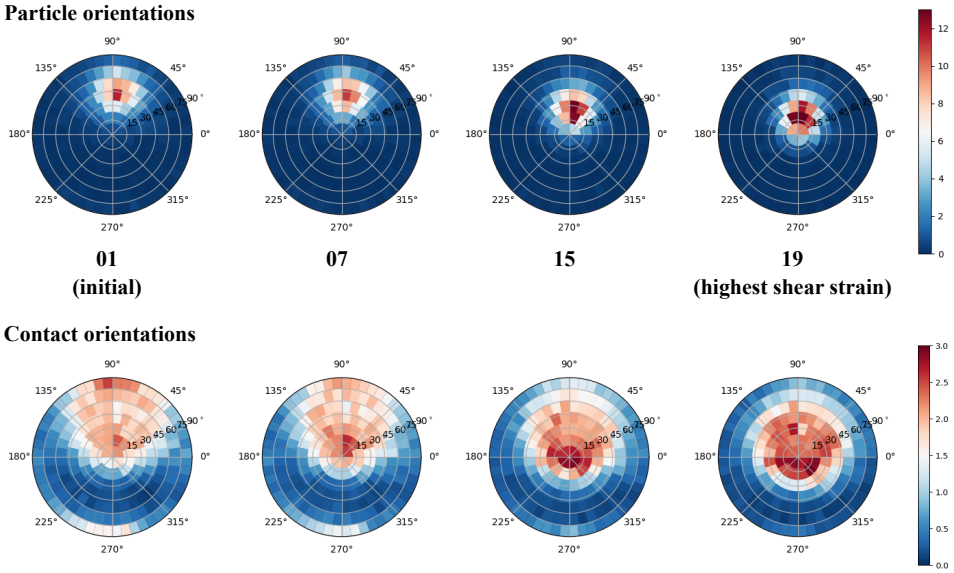

Figure 12.19: Particle and contact orientations in four chosen stages of the loading. They are represented by the Lambert azimuthal equal-area projection and binned. The plot is also used in [WAHV19].

the contact orientations. They mostly lie in a cone (in the projected plot) that is centred at the major particle orientation. The spread of the contact orientations must be larger as the contacts have to support the particles at more places than just the direction of the intended bias. The fabric would otherwise be unstable.

The particle orientations then evolve continuously with the loading by aligning with the vertical direction, *i.e.*, the major principal stress direction. They do not quite reach the vertical axis, however. It also seems that the spread of the orientations is slightly decreasing. The contact orientations undergo a similar evolution and align further with the vertical axis. The spread of the distribution necessarily remains larger than for the particle orientations but decreases with ongoing loading.

A second order fabric tensor is again used to statistically capture the distribution of both fabric entities. Its anisotropy is plotted in Figure 12.20 for both, the particle and the contact fabric. Initially, both anisotropies start at an, within this work, unusually high value as intended by the preparation

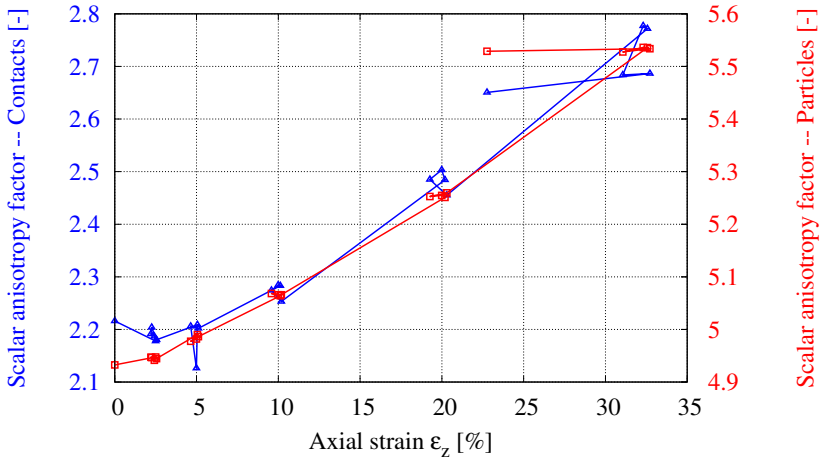

Figure 12.20: Fabric anisotropy response to the cyclic triaxial compression test on lentils. It is represented for the contact and particle fabric of the complete specimen.

of the specimen[13]. The contact fabric slightly decreases initially before generally increasing. The slope, however, is flexed differently compared to the experiments on Hostun sand, Caicos ooids or synthetic sphere packings. It increases stronger with higher shear strain in the tested strain range. The response of the contact anisotropy to the unload and reload cycles is not clear. There is a small evolution, but the contacts appear to be locked. The particle anisotropy is steadily increasing with ongoing shear and stays almost perfectly constant at the load cycles. It is completely locked which is similar to the response of the particle fabric in the Hostun sand specimen described in section 12.4.8. Surprisingly, the fabric evolution of particle and contact orientations is almost completely similar, when disregarding the actual value. The anisotropy is mobilised at a similar rate in both cases. The higher uncertainty of contact orientations might be the reason for the small deviations.

[13]Due to the formulation of the scalar anisotropy factor in section 7.1, the anisotropy can maximally reach 7.5 and amounts to 0 for an isotropic distribution.

Bibliography

[AA11] J. E. Andrade and C. F. Avila. Granular element method (GEM): linking inter-particle forces with macroscopic loading. *Granular Matter*, 14(1):51–61, dec 2011. doi:10.1007/s10035-011-0298-8.

[ABD+17] A. Amon, P. Born, K. E. Daniels, J. A. Dijksman, K. Huang, D. Parker, M. Schröter, R. Stannarius, and A. Wierschem. Preface: Focus on imaging methods in granular physics. *Review of Scientific Instruments*, 88(5), 2017, 1703.02928. doi:10.1063/1.4983052.

[ACR+] E. Andò, R. Cailletaud, E. Roubin, O. Stamati, and the spam contributors. spam: The software for the practical analysis of materials. `https://ttk.gricad-pages.univ-grenoble-alpes.fr/spam/`, 2017–.

[ADAAA77] J. R. Arthur, T. Dunstan, Q. A. Al-Ani, and A. Assadi. Plastic deformation and failure in granular media. *Geotechnique*, 27(1):53–74, 1977. doi:10.1680/geot.1977.27.1.53.

[ADC77] J. R. F. Arthur, T. Dunstan, and K. S. Chua. Induced anisotropy in a sand. *Géotechnique*, 27(1):13–30, 1977. doi:10.1680/geot.1977.27.1.13.

[AH08] K. A. Alshibli and A. Hasan. Spatial variation of void ratio and shear band thickness in sand using x-ray computed tomography. *Géotechnique*, 58(4):249–257, 2008. doi:10.1680/geot.2008.58.4.249.

[AHV12a] E. Andò, S. A. Hall, and G. Viggiani. Experimental micromechanics: grain-scale observation of sand de-

formation. *Géotechnique Letters*, 2(3):107–112, 2012. doi:10.1680/geolett.12.00027.

[AHV+12b] E. Andò, S. A. Hall, G. Viggiani, J. Desrues, and P. Bésuelle. Grain-scale experimental investigation of localised deformation in sand: a discrete particle tracking approach. *Acta Geotechnica*, 2012. doi:10.1007/s11440-011-0151-6.

[AM72] J. Arthur and B. Menzies. Inherent anisotropy in a sand. *Geotechnique*, (1):115–128, 1972.

[AMH04] F. Alonso-Marroquín and H. J. Herrmann. Ratcheting of Granular Materials. *Physical Review Letters*, 92(5):4, 2004, 0305043. doi:10.1103/PhysRevLett.92.054301.

[AMLHV05] F. Alonso-Marroquín, S. Luding, H. J. Herrmann, and I. Vardoulakis. Role of anisotropy in the elastoplastic response of a polygonal packing. *Physical Review E - Statistical, Nonlinear, and Soft Matter Physics*, 71(5):1–18, 2005, arXiv:1011.1669v3. doi:10.1103/PhysRevE.71.051304.

[And13] E. Andò. *Experimental investigation of microstructural changes in deforming granular media using x-ray tomography*. PhD thesis, Université de Grenoble, 2013.

[ASC+00] K. Alshibli, S. Sture, N. Costes, M. Frank, M. Lankton, S. Batiste, and R. Swanson. Assessment of localized deformations in sand using x-ray computed tomography. *Geotechnical Testing Journal*, 23:274, 09 2000. doi:10.1520/GTJ11051J.

[ASS05] T. Aste, M. Saadatfar, and T. J. Senden. Geometrical structure of disordered sphere packings. *Physical Review E*, 71, 2005, 0502016. doi:10.1016/j.physa.2004.03.034.

[ASS06] T. Aste, M. Saadatfar, and T. J. Senden. Local and global relations between the number of contacts and density in monodisperse sphere packs. *Journal of Statistical Mechanics: Theory and Experiment*, (7), 2006, 0709.3141. doi:10.1088/1742-5468/2006/07/P07010.

[AVHD13] E. Andò, G. Viggiani, S. A. Hall, and J. Desrues. Experimental micro-mechanics of granular media studied by x-ray tomography: recent results and challenges. *Géotechnique Letters*, 3:142–146, 2013. doi:10.1680/geolett.13.00036.

[BBM00] J. Baruchel, J.-Y. Buffiere, and E. Maire. *X-ray tomography in material science*. 2000.

[BFNS11] L. Bernard, S. Fave, E. Noirfalise, and A. Saragaglia. Visilog 7 reference guide, 2011. Manual.

[BH19a] B. Bacic and I. Herle. Laboratory evaluation of liquefaction potential for coarse-grained soils. In *The XVII European Conference on Soil Mechanics and Geotechnical Engineering*, number September, 2019. doi:10.32075/17ECSMGE-2019-0101.

[BH19b] B. Bacic and I. Herle. Soil liquefaction as an identification test. In *E3S Web of Conferences*, volume 92, 2019. doi:10.1051/e3sconf/20199208008.

[BL06] R. Beare and G. Lehmann. The watershed transform in itk-discussion and new developments. *The Insight Journal*, 92:1–24, 2006.

[BW62] J. Biarez and K. Wiendieck. Remarque sur l'élasticité et l'anisotropie des matériaux pulvérulents. *Comptes Rendus Hebdomadaires des Séances de l'Académie des Sciences*, 254:2712–2714, 1962. doi:10.1016/S0764-4469(99)80063-8.

[BW63] J. Biarez and K. Wiendieck. La comparaison qualitative entre l'anisotropie mécanique et l'anisotropie de structure des milieux pulvérulents. *Comptes Rendus Hebdomadaires des Séances de l'Académie des Sciences*, 256:1217–1220, 1963. doi:10.1016/S0764-4469(99)80063-8.

[Cas44] A. Casagrande. Shear failure of anisotropic materials. *Proc. Boston Soc. Civ. Engrs*, 31:74–87, 1944.

[CB13] V. Cnudde and M. N. Boone. High-resolution X-ray computed tomography in geosciences: A review of the current technology and applications. *Earth-Science Reviews*, 123:1–17, 2013. doi:10.1016/j.earscirev.2013.04.003.

[CCL97] F. Calvetti, G. Combe, and J. Lanier. Experimental micromechanical analysis of a 2d granular material: relation between structure evolution and loading path. *Mechanics of Cohesive-frictional Materials*, 2:121–163,

1997. doi:10.1002/(SICI)1099-1484(199704)2:2<121::AID-CFM27>3.0.CO;2-2.

[CD86] J.-L. Colliat-Dangus. *Comportement des matériaux granulaires sous fortes contraintes - Influence de la nature minéralogique du matériau étudié*. Phd, L'Université scientifique et médical; L'Institut national polytechnique de Grenoble, 1986.

[CMNN81] J. Christoffersen, M. M. Mehrabadi, and S. Nemat-Nasser. A micromechanical description of granular material behavior. *Journal of Applied Mechanics, Transactions ASME*, 48(2):339–344, 1981. doi:10.1115/1.3157619.

[Com98] A.-L. Combe. Comportement du sable d'Hostun S28 au triaxial axisymétrique. Comparaison avec le sable d'Hostun RF. Master's thesis, Université Joseph Fourier, 1998.

[Com16] T. P. Company. tochnog. `https://www.tochnogprofessional.nl/`, Version 2019-09-16.

[CS79] P. A. Cundall and O. D. L. Strack. A discrete numerical model for granular assemblies. *Géotechnique*, 29(1):47–65, 1979. doi:10.1680/geot.1980.30.3.331.

[CSV12] R. Conti, L. Sanctis, and G. M. B. Viggiani. Numerical modelling of installation effects for diaphragm walls in sand. *Acta Geotechnica*, 7(3):219–237, jan 2012. doi:10.1007/s11440-011-0157-0.

[CW18] Z. Cheng and J. Wang. Experimental investigation of interparticle contact evolution of sheared granular materials using X-ray micro-tomography. *Soils and Foundations*, 58(6):1492–1510, 2018. doi:10.1016/j.sandf.2018.08.008.

[CW19] Z. Cheng and J. Wang. Investigation of the fabric evolution and the stress-transmission behaviour of sands based on X-ray μCT images. *Advanced Powder Technology*, 30(9):1858–1869, 2019. doi:10.1016/j.apt.2019.06.003.

[DAAR16] A. M. Druckrey, K. A. Alshibli, and R. I. Al-Raoush. 3d characterization of sand particle-to-particle contact and morphology. *Computers and Geotechnics*, 74:26–35, 2016. doi:10.1016/j.compgeo.2015.12.014.

[DAB+17] J. J. M. Desrues, E. Andò, P. Bésuelle, G. Viggiani, L. Debove, P. Charrier, and J. Toni. Localisation precursors in geomaterials? In *International Workshop on Bifurcation and Degradation in Geomaterials*, number April, pages 3–10. Springer, 2017. doi:10.1007/978-3-319-56397-8_1.

[DCMM96] J. Desrues, R. Chambon, M. Mokni, and F. Mazerolle. Void ratio evolution inside shear bands in triaxial sand specimens studied by computed tomography. *Géotechnique*, 46(3):529–546, 1996. doi:10.1680/geot.1996.46.3.529.

[Dd72] A. Drescher and G. de Josselin de Jong. Photoelastic verification of a mechanical model for the flow of a granular material. *Journal of the Mechanics and Physics of Solids*, 20(5):337–340, 1972. doi:10.1016/0022-5096(72)90029-4.

[DM04] Y. F. Dafalias and M. T. Manzari. Simple Plasticity Sand Model Accounting for Fabric Change Effects. *Journal of engineering mechanics*, 130(6):622–634, 2004.

[DM18] J. Doreau Malioche. *Grain-scale investigation of sand-pile interface under axial loading conditions using x-ray tomography*. PhD thesis, Université Grenoble Alpes, 2018.

[DPL04] Y. F. Dafalias, A. G. Papadimitriou, and X. S. Li. Sand Plasticity Model Accounting for Inherent Fabric Anisotropy. *Journal of Engineering Mechanics*, 130(11):1319–1333, 2004. doi:10.1061/(ASCE)0733-9399(2004)130:11(1319).

[DV04] J. Desrues and G. Viggiani. Strain localization in sand: an overview of the experimental results obtained in Grenoble using stereophotogrammetry. *International Journal for Numerical and Analytical Methods in Geomechanics*, 28(4):279–321, 2004. doi:10.1002/nag.338.

[DVB06] J. Desrues, G. Viggiani, and P. Bésuelle. *Advances in X-ray Tomography for Geomaterials*. ISTE. Wiley, 2006.

[Edw98] S. F. Edwards. The equations of stress in a granular material. *Physica A: Statistical Mechanics and its Applications*, 249(1-4):226–231, 1998. doi:10.1016/S0378-4371(97)00469-X.

[FD11] P. Fu and Y. F. Dafalias. Fabric evolution within shear bands of granular materials and its relation to critical state theory.

International Journal for Numerical and Analytical Methods in Geomechanics, 35(18):1918—-1948, 2011. doi:10.1002/nag.

[FDK84] L. A. Feldkamp, L. C. Davis, and J. W. Kress. Practical cone-beam algorithm. *J. Opt. Soc. Am. A*, 1(6):612–619, Jun 1984. doi:10.1364/JOSAA.1.000612.

[FDP90] E. Flavigny, J. Desrues, and B. Palayer. Note technique - le sable d'Hostun «RF». Technical Report 53, 1990.

[FJ10] M. Faessel and D. Jeulin. Segmentation of 3D microtomographic images of granular materials with the stochastic watershed. *Journal of Microscopy*, 239(1):17–31, 2010. doi:10.1111/j.1365-2818.2009.03349.x.

[FNRA+16] J. Fonseca, S. Nadimi, C. C. Reyes-Aldasoro, C. O'Sullivan, and M. R. Coop. Image-based investigation into the primary fabric of stress-transmitting particles in sand. *Soils and Foundations*, 56(5):818–834, 2016. doi:10.1016/j.sandf.2016.08.007.

[FOCL12] J. Fonseca, C. O'Sullivan, M. R. Coop, and P. D. Lee. Non-invasive characterization of particle morphology of natural sands. *Soils and Foundations*, 52(4):712–722, 2012. doi:10.1016/j.sandf.2012.07.011.

[FOCL13] J. Fonseca, C. O'Sullivan, M. Coop, and P. Lee. Quantifying the evolution of soil fabric during shearing using directional parameters. *Géotechnique*, 63(6):487–499, may 2013. doi:10.1680/geot.12.P.003.

[Fon11] J. Fonseca. *The evolution of morphology and fabric of a sand during shearing*. PhD thesis, Imperial College London, University of London, 2011.

[GDL10] F. Göncü, O. Durán, and S. Luding. Constitutive relations for the isotropic deformation of frictionless packings of polydisperse spheres. *Comptes Rendus - Mecanique*, 338(10-11):570–586, 2010. doi:10.1016/j.crme.2010.10.004.

[GHH17] X. Gu, J. Hu, and M. Huang. Anisotropy of elasticity and fabric of granular soils. *Granular Matter*, 19(2):1–15, 2017. doi:10.1007/s10035-017-0717-6.

[Gra06] L. Grady. Random walks for image segmentation. In *IEEE Transactions on Pattern Analysis and Machine Intelligence*, volume 28, 2006.

[GZ13] N. Guo and J. Zhao. The signature of shear-induced anisotropy in granular media. *Computers and Geotechnics*, 47:1–15, 2013. doi:10.1016/j.compgeo.2012.07.002.

[GZLD13] Z. Gao, J. Zhao, X. Li, and Y. Dafalias. A critical state sand plasticity model accounting for fabric evolution. *International Journal for Numerical and Analytical Methods in Geomechanics*, 38(July 2013):370–390, 2013. doi:10.1002/nag.

[Han81] K. M. Hanson. Noise and contrast discrimination in computed tomography. *Radiology of the Skull and Brain*, 5(1):3941–3955, 1981.

[HBD+10] S. Hall, M. Bornert, J. Desrues, Y. Pannier, N. Lenoir, G. Viggiani, and P. Bésuelle. Discrete and continuum analysis of localised deformation in sand using X-ray μCT and volumetric digital image correlation. *Géotechnique*, 60(5):315–322, 2010. doi:10.1680/geot.2010.60.5.315.

[HM09] I. Herle and P. M. Mayer. Calculation of deformations of an underwater excavation using parameters of Berlin sand from a hypoplastic model. *Bautechnik*, 86(Special issue 2009 – Geotechnical Engineering):74–85, 2009. doi:10.1002/bate.200990007.

[HMRA14] R. Hurley, E. Marteau, G. Ravichandran, and J. E. Andrade. Extracting inter-particle forces in opaque granular materials: Beyond photoelasticity. *Journal of the Mechanics and Physics of Solids*, 63:154–166, feb 2014. doi:10.1016/j.jmps.2013.09.013.

[Hun07] J. D. Hunter. Matplotlib: A 2d graphics environment. *Computing in Science & Engineering*, 9(3):90–95, 2007. doi:10.1109/MCSE.2007.55.

[IDA18] W. H. Imseeh, A. M. Druckrey, and K. A. Alshibli. 3D experimental quantification of fabric and fabric evolution of sheared granular materials using synchrotron micro-computed tomog-

raphy. *Granular Matter*, 2018. doi:10.1007/s10035-018-0798-x.

[IGT09] P. Iassonov, T. Gebrenegus, and M. Tuller. Segmentation of X-ray computed tomography images of porous materials: A crucial step for characterization and quantitative analysis of pore structures. *Water Resources Research*, 45(9):1–12, 2009. doi:10.1029/2009WR008087.

[IO99] K. Iwashita and M. Oda. *Mechanics of granular materials: an introduction*. CRC press, 1999.

[IO00] K. Iwashita and M. Oda. Micro-deformation mechanism of shear banding process based on modified distinct element method. *Powder Technology*, 109:192–205, 2000.

[JAVT13] C. Jaquet, E. Andó, G. Viggiani, and H. Talbot. Estimation of Separating Planes between Touching 3D Objects Using Power Watershed. In *International Symposium on Mathematical Morphology*, volume 11, pages 452–463, 2013.

[JCY15] R. Jiménez, C. Comps, and J. A. Yagüe. An Optimized Segmentation Algorithm for the Surface Extraction in Computed Tomography for Metrology Applications. *Procedia Engineering*, 132:804–810, 2015. doi:10.1016/j.proeng.2015.12.563.

[JL09] Y. Jiang and M. Liu. Granular solid hydrodynamics. *Granular Matter*, 11(3):139–156, apr 2009. doi:10.1007/s10035-009-0137-3.

[JLDF92] H. Joer, J. Lanier, J. Desrues, and E. Flavigny. $1\gamma 2\epsilon$: A new shear apparatus to study the behavior of granular materials. *Geotechnical Testing Journal*, 15(2):129–137, 1992.

[JOP$^+$] E. Jones, T. Oliphant, P. Peterson, et al. SciPy: Open source scientific tools for Python, 2001–. URL `http://www.scipy.org/`.

[JZL19] M. Jiang, A. Zhang, and T. Li. Distinct element analysis of the microstructure evolution in granular soils under cyclic loading. *Granular Matter*, 21(2), 2019. doi:10.1007/s10035-019-0892-8.

[Kar17] Z. Karatza. *A study of temporal and spatial evolution of deformation and breakage of dry granular materials using x-ray computed tomography and the discrete element method.* PhD thesis, The university of Edinburgh, 2017.

[KC01] R. A. Ketcham and W. D. Carlson. Acquisition, optimization and interpretation of x-ray computed tomographic imagery: Applications to the geosciences. *Computers and Geosciences*, 27(4):381–400, 2001. doi:10.1016/S0098-3004(00)00116-3.

[KCK+99] H. Kawakata, A. Cho, T. Kiyama, T. Yanagidani, K. Kusunose, and M. Shimada. Three-dimensional observations of faulting process in Westerly granite under uniaxial and triaxial conditions by X-ray CT scan. *Tectonophysics*, 313(3):293–305, 1999. doi:10.1016/S0040-1951(99)00205-X.

[KI84] K. K.-I. Distribution of directional data and fabric tensors. *International Journal of Engineering Science*, 22(2):149 – 164, 1984. doi:https://doi.org/10.1016/0020-7225(84)90090-9.

[Knu78] D. E. Knuth. The art of computer programming. vol. 1: Fundamental algorithms. *Atmospheric Chemistry & Physics*, 1978.

[Kol91] D. Kolymbas. An outline of hypoplasticity. *Archive of applied mechanics*, 61(3):143–151, 1991.

[KSV+08] G. Kerckhofs, J. Schrooten, T. Van Cleynenbreugel, S. V. Lomov, and M. Wevers. Validation of x-ray microfocus computed tomography as an imaging tool for porous structures. *Review of Scientific Instruments*, 79(1), 2008. doi:10.1063/1.2838584.

[LBD+07] N. Lenoir, M. Bornert, J. J. M. Desrues, P. Bésuelle, and G. Viggiani. Volumetric Digital Image Correlation Applied to X-ray Microtomography Images from Triaxial Compression Tests on Argillaceous Rock. *Strain*, 43:193–205, 2007.

[LD75] P. V. Lade and J. M. Duncan. Elastoplastic stress-strain theory for cohesionless soil. *Journal of Geotechnical and Geoenvironmental Engineering*, 101(ASCE# 11670 Proceeding), 1975.

[LD11] X. S. Li and Y. F. Dafalias. Anisotropic critical state theory: Role of fabric. *Journal of Engineering Mechanics*, 138(3):263–275, 2011. doi:10.1061/(asce)em.1943-7889.0000324.

[Leb] E. O. Lebigot. Uncertainties: a python package for calculations with uncertainties. URL `http://pythonhosted.org/uncertainties/`.

[Len06] N. Lenoir. *Comportement mécanique et rupture dans les roches argileuses étudiés par micro tomographie à rayons X*. PhD thesis, Université de Grenoble, 2006.

[Mašín] D. Mašín. A hypoplastic constitutive model for clays. *International Journal for Numerical and Analytical Methods in Geomechanics*, 29(4):311–336, apr 2005. doi:10.1002/nag.416.

[MB90] F. Meyer and S. Beucher. Morphological segmentation. *Journal of Visual Communication and Image Representation*, 1(1):21 – 46, 1990. doi:https://doi.org/10.1016/1047-3203(90)90014-M.

[MB05] T. S. Majmudar and R. P. Behringer. Contact force measurements and stress-induced anisotropy in granular materials. *Nature*, 435(7045):1079–1082, 2005. doi:10.1038/nature03805.

[MCT14] N. H. Minh, Y. P. Cheng, and C. Thornton. Strong force networks in granular mixtures. *Granular Matter*, 16(1):69–78, 2014. doi:10.1007/s10035-013-0455-3.

[MKU+06] T. Matsushima, J. Katagiri, K. Uesugi, T. Nakano, and A. Tsuchiyama. Micro X-ray CT at SPring-8 for Granular Mechanics. In *Soil Stress-Strain Behavior: Measurement, Modeling and Analysis*, pages 1–10, 2006. doi:10.1007/978-1-4020-6146-2.

[MSGJ03] F. Mees, R. Swennen, M. V. Geet, and P. Jacobs. Applications of X-ray Computed Tomography in the Geosciences. *Geological Society, London, Special Publications*, 215:1–6, 2003.

[MTLL04] M. Madadi, O. Tsoungui, M. Lätzel, and S. Luding. On the fabric tensor of polydisperse granular materials in 2D. *International Journal of Solids and*

Structures, 41(9-10):2563–2580, 2004, arXiv:1011.1669v3. doi:10.1016/j.ijsolstr.2003.12.005.

[NH97] A. Niemunis and I. Herle. Hypoplastic model for cohesionless soils with elastic strain range. *Mechanics of cohesive - frictional Materials*, 2(March 1996):279–299, 1997.

[Nit16] K. Nitzsche. *Verschiebungsmuster in Böschungen während Aushubvorgängen*. PhD thesis, Technische Universität Dresden, 2016.

[NN00] S. Nemat-Nasser. Micromechanically-based constitutive model for frictional deformation of granular materials. *Journal of the Mechanics and Physics of Solids*, 48(6):1541–1563, 2000. doi:10.1016/S0022-5096(99)00089-7.

[OC09] C. O'Sullivan and L. Cui. Micromechanics of granular material response during load reversals: Combined DEM and experimental study. *Powder Technology*, 193(3):289–302, aug 2009. doi:10.1016/j.powtec.2009.03.003.

[Oda72a] M. Oda. Initial fabrics and their relations to mechanical properties of granular material. *Soils and Foundations*, 12(1):17–36, 1972.

[Oda72b] M. Oda. The mechanism of fabric changes during compressional deformation of sand. *Soils and foundations*, 12(2):1–18, 1972. doi:10.1038/143865a0.

[OKNN80] M. Oda, J. Konishi, and S. Nemat-Nasser. Some experimentally based fundamental results on the mechanical behaviour of granular materials. *Geotechnique*, (4), 1980.

[Old78] W. H. Oldendorf. The quest for an image of brain. *Neurology*, 28(6):517–517, 1978. doi:10.1212/WNL.28.6.517.

[Oli06] T. E. Oliphant. A guide to numpy. USA: Trelgol Publishing, 2006.

[OMO00] J. Otani, T. Mukunoki, and Y. Obara. Application of x-ray CT method for characterization of failure in soils. *Soils and Foundations*, 40(2):111–118, 2000.

[OMO02] J. Otani, T. Mukunoki, and Y. Obara. Characterization of failure in sand under triaxial compression using an industrial

x-ray CT scanner. *International Journal of Physical Modelling in Geotechnics*, 1:15–22, 2002.

[ONMM82] M. Oda, S. Nemat-Masser, and M. M. Mehrabadi. A statistical study of fabric in a random assembly of spherical granules. *International Journal for Numerical and Analytical Methods in Geomechanics*, 6(1):77–94, 1982. doi:10.1002/nag.1610060106.

[ONNK85] M. Oda, S. Nemat-Nasser, and J. Konishi. Stress-induced anisotropy in granular masses. *Soils and Foundations*, 25(3):85–97, 1985.

[OO04] J. Otani and Y. Obara. *Xray CT for Geomaterials: Soils, Concrete, Rocks – International Workshop on Xray CT for Geomaterials, Kumamoto, Japan.* CRC Press, 2004.

[OR01] H. Ouadfel and L. Rothenburg. 'Stress-force-fabric' relationship for assemblies of ellipsoids. *Mechanics of Materials*, 33(4):201–221, 2001. doi:10.1016/S0167-6636(00)00057-0.

[Ots79] N. Otsu. A Threshold Selection Method from Gray-Level Histograms. *IEEE Transactions on Systems, Man, and Cybernetics*, 9:62–66, 1979. doi:10.1109/TSMC.1979.4310076.

[OTT04] M. Oda, T. Takemura, and M. Takashi. Microstructure in shear band observed by microfocus X-ray computed tomography. *Géotechnique*, 54(8):539–542, 2004.

[OYJB13] S. Ontiveros, J. A. Yagüe, R. Jiménez, and F. Brosed. Computer tomography 3D edge detection comparative for metrology applications. *Procedia Engineering*, 63(2010):710–719, 2013. doi:10.1016/j.proeng.2013.08.263.

[PDP19] A. L. Petalas, Y. F. Dafalias, and A. G. Papadimitriou. SANISAND-FN: An evolving fabric-based sand model accounting for stress principal axes rotation. *International Journal for Numerical and Analytical Methods in Geomechanics*, 43(1):97–123, 2019. doi:10.1002/nag.2855.

[PKW18] M. Pouragha, N. P. Kruyt, and R. Wan. Fabric response to strain probing in granular materials: Two-dimensional, isotropic systems. *International Journal of Solids and Structures*, pages 1–12, 2018. doi:10.1016/j.ijsolstr.2018.08.020.

[PPP+80] D. R. Pickens, R. R. Price, J. A. Patton, J. J. Erickson, F. D. Rollo, and A. B. Brill. Focal-plane tomography image reconstruction. *IEEE Transactions on Nuclear Science*, 27(1):489–492, Feb 1980. doi:10.1109/TNS.1980.4330874.

[RÖ95] W. C. Röntgen. Über eine neue art von strahlen. In *Aus den Sitzungsberichten der Würzburger Physik.-medic. Gesellschaft 1985*, volume 5, page 380–440, 1895.

[RB01] D. Robertson and M. Bolton. DEM simulation of crushable grains and soils. In *Powders & Grains 2001*, 2001.

[RC78] T. Ridler and S. Calvard. Picture Thresholding Using an Iterative Selection Method. *IEEE Transactions on Systems, Man and Cybernetics*, smc-8(8):630–632, 1978.

[RFM+89] S. Raynaud, D. Fabre, F. Mazerolle, Y. Geraud, and H. J. Latière. Analysis of the internal structure of rocks and characterization of mechanical deformation by a non-destructive method: X-ray tomodensitometry. *Tectonophysics*, 159(1):149 – 159, 1989. doi:https://doi.org/10.1016/0040-1951(89)90176-5.

[RJMR96] F. Radjai, M. Jean, J.-J. Moreau, and S. Roux. Force distributions in dense two-dimensional granular systems. *Physical Review Letters*, 77(2):274–277, 1996. doi:10.1007/BF02787434.

[Rod40] O. Rodrigues. Des lois géometriques qui regissent les déplacements d' un systéme solide dans l'espace, et de la variation des coordonnées provenant de ces déplacement considérées indépendant des causes qui peuvent les produire. *J. Math. Pures Appl.*, 5:380–440, 1840.

[Ros70] K. H. Roscoe. The influence of strains in soil mechanics. *Geotechnique*, 20(2):129–170, 1970. doi:10.1680/geot.1970.20.2.129.

[RRD17] F. Radjai, J.-N. Roux, and A. Daouadji. Modeling Granular Materials: Century-Long Research across Scales. *J. Eng. Mech.*, 143(4):04017002, 2017. doi:10.1061/(ASCE)EM.1943-7889.0001196.

[RSZ94] E. A. Rakhmanov, E. B. Saff, and Y. M. Zhou. Minimal Discrete Energy on the Sphere. *Mathematical Research Letters*, 1(6):647–662, 1994. doi:10.4310/MRL.1994.v1.n6.a3.

[RVB+17] J. Reimann, J. Vicente, E. Brun, C. Ferrero, Y. Gan, and A. Rack. X-ray tomography investigations of mono-sized sphere packing structures in cylindrical containers. *Powder Technology*, 318(July):471–483, 2017. doi:10.1016/j.powtec.2017.05.033.

[S+] S. Silvester et al. Oct2py, 2011–. URL `https://pypi.org/project/oct2py/`.

[SEG+02] L. E. Silbert, D. Ertaş, G. S. Grest, T. C. Halsey, and D. Levine. Geometry of frictionless and frictional sphere packings. *Physical Review E - Statistical Physics, Plasmas, Fluids, and Related Interdisciplinary Topics*, 65(3):1–6, 2002. doi:10.1103/PhysRevE.65.031304.

[SK97] E. Saff and A. Kuijlaars. Distributing many points on a sphere. *The mathematical intelligencer*, 19(1):5–11, 1997.

[SNS+13] F. M. Schaller, M. Neudecker, M. Saadatfar, G. Delaney, K. Mecke, G. E. Schröder-Turk, and M. Schröter. Tomographic analysis of jammed ellipsoid packings. *AIP Conference Proceedings*, 1542(June 2013):377–380, 2013. doi:10.1063/1.4811946.

[SNS+15] F. M. Schaller, M. Neudecker, M. Saadatfar, G. W. Delaney, G. E. Schröder-Turk, and M. Schröter. Local origin of global contact numbers in frictional ellipsoid packings. *Physical Review Letters*, 114(15):1–5, 2015, 1312.1327. doi:10.1103/PhysRevLett.114.158001.

[SSBW14] S. Schlüter, A. Sheppard, K. Brown, and D. Wildenschild. Image processing of multiphase images obtained via X-ray microtomography: A review. *Water Resources Research*, 50(4):3615–3639, 2014. doi:10.1002/2014WR015256.

[SV09] T. G. Sitharam and J. S. Vinod. Critical state behaviour of granular materials from isotropic and rebounded paths: DEM simulations. *Granular Matter*, 11(1):33–42, 2009. doi:10.1007/s10035-008-0113-3.

[SW68] A. Schofield and C. Wroth. *Critical State Soil Mechanics*. McGraw-Hill, 1968.

[SWM08] C. Song, P. Wang, and H. A. Makse. A phase diagram for jammed matter. *nature letters*, 453(May):629–632, 2008. doi:10.1038/nature06981.

[TA15] A. Tengattini and E. Andò. Kalisphera: an analytical tool to reproduce the partial volume effect of spheres imaged in 3D. *Measurement Science and Technology*, 26(9), 2015. doi:10.1088/0957-0233/26/9/095606.

[TB86] C. Thornton and D. J. Barnes. Computer simulated deformation of compact granular assemblies. *Acta Mechanica*, 64(1-2):45–61, 1986. doi:10.1007/BF01180097.

[Tho00] C. Thornton. Numerical simulations of deviatoric shear deformation of granular media. *Géotechnique*, 50(1):43–53, 2000. doi:10.1680/geot.2000.50.1.43.

[TVD17] A. I. Theocharis, E. Vairaktaris, and Y. F. Dafalias. Scan line void fabric anisotropy tensors of granular media. *Granular Matter*, 19(4):1–12, 2017. doi:10.1007/s10035-017-0752-3.

[TVDP16] A. I. Theocharis, E. Vairaktaris, Y. F. Dafalias, and A. G. Papadimitriou. Proof of incompleteness of critical state theory in granular mechanics and its remedy. *Journal of Engineering Mechanics*, 143(2):04016117, 2016. doi:10.1061/(ASCE)EM.1943-7889.0001166.

[TZ10] C. Thornton and L. Zhang. On the evolution of stress and microstructure during general 3d deviatoric straining of granular media. *Géotechnique*, 60(5):333–341, jan 2010. doi:10.1680/geot.2010.60.5.333.

[VATS14] G. Viggiani, E. Andò, D. Takano, and J. Santamarina. Laboratory x-ray tomography: a valuable experimental tool for revealing processes in soils. *Geotechnical Testing Journal*, 38(1):61–71, 2014. doi:10.1520/GTJ20140060.

[VAVA13] I. Vlahinić, E. Andò, G. Viggiani, and J. E. Andrade. Towards a more accurate characterization of granular media: extracting quantitative descriptors from tomographic images.

Granular Matter, 16(1):9–21, dec 2013. doi:10.1007/s10035-013-0460-6.

[VDW91] H. J. Vinegar, J. A. De Waal, and S. L. Wellington. CT studies of brittle failure in castlegate sandstone. *International Journal of Rock Mechanics and Mining Sciences and Geom.*, 28(5):441–450, 1991. doi:10.1016/0148-9062(91)90082-W.

[vdWSN+14] S. van der Walt, J. L. Schönberger, J. Nunez-Iglesias, F. Boulogne, J. D. Warner, N. Yager, E. Gouillart, T. Yu, and the scikit-image contributors. scikit-image: image processing in Python. *PeerJ*, 2:e453, 6 2014. doi:10.7717/peerj.453.

[Š16] V. Šmilauer. *Woo Documentation*. 2016. https://woodem.org.

[vT20] K. von Terzaghi. Old earth-pressure theories and new test results. *Engineering News-Record*, 85(14):632–637, 1920.

[vW96] P. von Wolffersdorff. A hypoplastic relation for granular materials with a predefined limit state surface. *Mechanics of Cohesive-frictional Materials*, 1(March), 1996.

[WAHV17] M. Wiebicke, E. Andò, I. Herle, and G. Viggiani. On the metrology of interparticle contacts in sand from x-ray tomography images. *Measurement Science and Technology*, 28(12):124007, 2017. doi:https://doi.org/10.1088/1361-6501/aa8dbf.

[WAHV19] M. Wiebicke, E. Andò, I. Herle, and G. Viggiani. Measuring the fabric evolution of particulate media during load reversals in triaxial tests. In *E3S Web of Conferences*, volume 92, page 03001. EDP Sciences, 2019.

[WAŠ+19] M. Wiebicke, E. Andò, V. Šmilauer, I. Herle, and G. Viggiani. A benchmark strategy for the experimental measurement of contact fabric. *Granular Matter*, 21(3):54, 2019. doi:10.1007/s10035-019-0902-x.

[Weg13] D. Wegener. *Ermittlung bleibender Bodenverformungen infolge dynamischer Belastung mittels numerischer Verfahren*. Phd, Technische Universität Dresden, 2013.

[WG99] M. Wood and A. Gajo. Severn–Trent sand: a kinematic-hardening constitutive model: the q–p formulation. *Géotechnique*, 49(5):595–614, 1999. doi:10.1680/geot.1999.49.5.595.

[Wic19] T. Wichtmann. Soils Under High- and Low-Cycle Loading - Experiments vs. Predictions by Constitutive Models. In *Desiderata Geotechnica - in honor of Prof. Gudehus' 80th birthday. Proceedings of the Special Session held during the China-Europe Conference on Geotechnical Engineering, Wien.*, pages 211–220, 2019. doi:10.1007/978-3-030-14987-1_25.

[Wie67] K. Wiendieck. Zur Struktur körniger Medien. *Die Bautechnik*, 6:196–199, 1967.

[Wie12] M. Wiebicke. Accessing forces between elastic grains using 2d digital image correlation. Master's thesis, Université Joseph Fourrier, Grenoble INP, 2012.

[Wie19] M. Wiebicke. Benchmark analysis of synthetical images – source code and example dem data. `http://dx.doi.org/10.25532/OPARA-26`, 2019.

[WS17] S. Weis and M. Schröter. Analyzing X-Ray tomographies of granular packings. *Review of Scientific Instruments*, (88), 2017, 1612.06639. doi:10.1063/1.4983051.

[WT04] T. Wichtmann and T. Triantafyllidis. Influence of a cyclic and dynamic loading history on dynamic properties of dry sand, part II: Cyclic axial preloading. *Soil Dynamics and Earthquake Engineering*, 24(11):789–803, 2004. doi:10.1016/j.soildyn.2004.05.002.

[WTCZ17] T. Wichtmann, T. Triantafyllidis, S. Chrisopoulos, and H. Zachert. Prediction of long-term deformations of offshore wind power plant foundations using HCA-based engineer-oriented models. *International Journal of Offshore and Polar Engineering*, 27(4):346–356, 2017. doi:10.17736/ijope.2017.fv05.

[YAL+02] T. S. Yoo, M. J. Ackerman, W. E. Lorensen, W. Schroeder, V. Chalana, S. Aylward, D. Metaxas, and R. Whitaker. Engineering and algorithm design for an image processing api:

a technical report on itk-the insight toolkit. *Studies in health technology and informatics*, pages 586–592, 2002.

[ZG13] J. Zhao and N. Guo. Unique critical state characteristics in granular media considering fabric anisotropy. *Géotechnique*, 63(8):695–704, 2013. doi:10.1680/geot.12.P.040.

[ZG15] J. Zhao and N. Guo. The interplay between anisotropy and strain localisation in granular soils : a multiscale insight. *Geotechnique*, 65(8):642–656, 2015.

[ZH16] J. Zheng and R. D. Hryciw. Segmentation of contacting soil particles in images by modified watershed analysis. *Computers and Geotechnics*, 73:142–152, 2016. doi:10.1016/j.compgeo.2015.11.025.

[ZT15] M. Zeghal and C. Tsigginos. A micromechanical analysis of the effect of fabric on low-strain stiffness of granular soils. *Soil Dynamics and Earthquake Engineering*, 70:153–165, 2015. doi:10.1016/j.soildyn.2014.12.018.

Mitteilungen - Institut für Geotechnik, Technische Universität Dresden

ISSN 1434-3053

Herausgeber: Univ.-Prof. Dr.-Ing. habil. Dietrich Franke

Heft 1	Franke, D. (Hrsg.)	1992	Das Institut für Geotechnik an der TU Dresden + Die Veröffentlichungen Johann Ohdes
Heft 2	Franke, D. (Hrsg.)	1995	OHDE-Kolloquium 1993
Heft 3	Franke, D. (Hrsg.)	1995	Festschrift zum 60. Geburtstag von Prof. Dr.-Ing. habil. Dietrich Franke
Heft 4	Franke, D. (Hrsg.)	1997	OHDE-Kolloquium 1997
Heft 5	Engel, J.	1998	Entwicklung von Datenstrukturen für bodenmechanische Anwendungen
Heft 6	Vogt, L.	1998	Untersuchungen zum Tragverhalten und zur Verbesserung der Standsicherheit von Stützmauern
Heft 7	al Diban, I.	2000	Das Tragverhalten horizontal belasteter, in nichtbindigem Boden eingespannter starrer Träger, in ebenem und geböschtem Gelände
Heft 8	Winkler, A.	2001	Ermittlung des Erddrucks im Bruchzustand bei Drehung einer Wand um den Kopfpunkt
Heft 9	Franke, D. (Hrsg.)	2001	OHDE-Kolloquium 2001
Heft 10	Engel, J.	2002	Verfahren zur Festlegung von Kennwerten für bodenmechanische Nachweise
Heft 11	Neuberg, C.	2002	Ein Verfahren zur Berechnung des räumlichen passiven Erddrucks vor parallel verschobenen Trägern

Herausgeber: Univ.-Prof. Dr.-Ing. habil. Ivo Herle

Heft 12	Bartl, U.	2004	Zur Mobilisierung des passiven Erddrucks in kohäsionslosem Boden
Heft 13	Arnold, M.	2004	Zur Berechnung des Erd- und Auflastdrucks auf Winkelstützwände im Gebrauchszustand
Heft 14	Al-Akel, S.	2005	Beitrag zur Berechnung von eingespannten starren Stützkonstruktionen in kohäsionslosem Boden
Heft 15	Herle, I. (Hrsg.)	2005	OHDE-Kolloquium 2005
Heft 16	Herle, I. (Hrsg.)	2009	OHDE-Kolloquium 2009
Heft 17	Wegener, D.	2013	Ermittlung bleibender Bodenverformungen infolge dynamischer Belastung mittels numerischer Verfahren
Heft 18	Gajári, G.	2013	Modellierung bleibender Verformungen des Asphalts mit einem hypoplastischen Stoffmodell der Bodenmechanik
Heft 19	Herle, I. (Hrsg.)	2014	OHDE-Kolloquium 2014
Heft 20	Shi, X.	2016	Verformungsverhalten von Kippenböden mit Multiporosität
Heft 21	Nitzsche, K.	2016	Verschiebungsmuster in Böschungen während Aushubvorgängen
Heft 22	Hleibieh, J.	2017	Anwendung der Hypoplastizität bei numerischen Berechnungen von bodendynamischen Problemen
Heft 23	Schwiteilo, E.	2018	Bestimmung bodenmechanischer Parameter nach fortgeschrittenen Methoden
Heft 24	Herle, I. (Hrsg.)	2018	OHDE-Kolloquium 2018

Heft 25	Pankrath, H.	2019	Beitrag zur Fallgewichtsverdichtung in sandigem Boden
Heft 26	Bergholz, K.	2020	An extended bounding surface model for the application to general stress paths in sand
Heft 27	Wiebicke, M.	2020	Experimental analysis of the evolution of fabric in granular soils upon monotonic loading and load reversals